# Prediction of Fire Growth on Furniture Using CFD

by
Richard Pehrson

A Dissertation
Submitted to the Faculty
of the
WORCESTER POLYTECHNIC INSTITUTE
in partial fulfillment of the requirements
for the
Degree of Doctor of Philosophy
Fire Protection Engineering
by

---

APPROVED:

---
Professor J. R. Barnett  Major Advisor

---
Professor N. A. Dembsey  Advisor

---
Professor B. J. Savilonis  Advisor

---
Professor D. A. Lucht  Department Head

Professor H. W. Emmons
(Committee Member 1994-1998)

**Abstract**

A fire growth calculation method has been developed that couples a computational fluid dynamics (CFD) model with bench scale cone calorimeter test data for predicting the rate of flame spread on compartment contents such as furniture. The commercial CFD code TASCflow has been applied to solve time averaged conservation equations using an algebraic multigrid solver with mass weighted skewed upstream differencing for advection. Closure models include $k - \epsilon$ for turbulence, eddy breakup for combustion following a single step irreversible reaction with Arrhenius rate constant, finite difference radiation transfer, and conjugate heat transfer. Radiation properties are determined from concentrations of soot, $CO_2$ and $H_2O$ using the narrow band model of Grosshandler and exponential wide band curve fit model of Modak. The growth in pyrolyzing area is predicted by treating flame spread as a series of piloted ignitions based on coupled gas-fluid boundary conditions. The mass loss rate from a given surface element follows the bench scale test data for input to the combustion prediction. The fire growth model has been tested against foam-fabric mattresses and chairs burned in the furniture calorimeter. In general, agreement between model and experiment for peak heat release rate (HRR), time to peak HRR, and total energy lost is within $\pm 20\%$. Used as a proxy for the flame spread velocity, the slope of the HRR curve predicted by model agreed with experiment within $\pm 20\%$ for all but one case.

# Acknowledgements

This dissertation would not be possible without the support, encouragement and instruction provided by Professor Jonathan Barnett and Professor David Lucht of the Worcester Polytechnic Institute, Center for Firesafety Studies. Your kind words and years of enthusiasm and guidance mean very much to me. I would also like to thank Professor Brian Savilonis and Professor Nicholas Dembsey for their words of encouragement shown during my tenure at WPI.

As the last Ph.D. student working under Professor Howard Emmons, I am truly honored to have been involved with his work. As a committee member until the time of his recent death, his vision and instruction added immeasurably to my work and knowledge of fire. His wisdom and guidance have touched countless students, and I am proud to have been one of them.

My years at WPI would have certainly been fewer in number had it not been for the distractions created by the resident firefighters at the West Station in Auburn, Massachusetts. While many of the residents have gone on to honest work as Fire Marshals, I must report that others have found their niche in the world of consulting. Few will forget driving the ambulance to NYC, all of those hazardous material incidents with C-O-O, Dave's 2X4, the grease trap, and the pole of light. Also, if it were not for The Force, there would unquestionably be more dents in all of the apparatus under our care. I hereby apologize for all lost bets when I did not move from the station to Auburn Manor across the field.

Certainly one of my biggest supporters during the last few years has been Katherine Peterson. When she is not performing her duties as a stoker on the back of a tandem, she finds time to do a little singing and poetry. Without her proofreading, the text that follows would certainly contain many more split infinitives (oops, did it again). The Katerator XL 2000, as she is known in certain circles, has written a haiku for me that even an engineer can understand:

*Fluid Dynamics*
*Bits and bits of dataflow*
*Electric water*

Finally, I must thank my parents for all their love and belief in me. Without their almost inhuman stores of patience and understanding, I could long ago have been relegated to a life of wandering, searching for someone who would calmly and sincerely answer the question "But, Mommy, why it do that?" - at least 20 times an hour. And thanks for the tool kit for my 3rd birthday - without which I might never have been able to start answering this question for myself.

# Contents


**1 Introduction** **1**
- 1.1 Rationale . . . 2
- 1.2 The Process . . . 3

**2 Flame Spread** **6**
- 2.1 Qualitative Description of Ignition . . . 7
- 2.2 Quantitative Description of Ignition . . . 9
  - 2.2.1 Ignition Temperature . . . 9
  - 2.2.2 Critical Flux for Ignition . . . 11
  - 2.2.3 Critical Mass Flux . . . 12
  - 2.2.4 Flux Time Product . . . 13
  - 2.2.5 More Detailed Predictions . . . 14
- 2.3 Flame Spread . . . 16
  - 2.3.1 Mechanisms Controlling Flame Spread . . . 17
  - 2.3.2 Concurrent Spread with Forced Flow . . . 18
  - 2.3.3 Concurrent Spread over Horizontal Surfaces . . . 18
  - 2.3.4 Downward, Lateral and Opposed Flow Flame Spread . . . 20
- 2.4 Thermal Flame Spread Models . . . 21
  - 2.4.1 Submodels . . . 23
  - 2.4.2 Model of Markstein and deRis . . . 26
  - 2.4.3 Model of Orloff . . . 27
  - 2.4.4 Models for Opposed Flow . . . 28

**3 Predicting Fire Growth** **31**
- 3.1 Classification Models . . . 31
- 3.2 Thermal Models using Bench Scale HRRs . . . 34
  - 3.2.1 Model of Saito, Quintiere and Williams . . . 34
  - 3.2.2 Model of Karlsson . . . 37
  - 3.2.3 Model of Grant . . . 38
- 3.3 Fire Growth Incorporated in Zone Models . . . 40
  - 3.3.1 Model of Smith . . . 41
  - 3.3.2 Model of Mitler . . . 42
  - 3.3.3 Dietenberger Furniture Fire Model . . . 43
- 3.4 Fire Growth Incorporated in CFD Models . . . 46

3.4.1 Model of Opstad . . . 46
3.4.2 Model of Yan . . . 48
3.5 Furniture Reaction to Fire . . . 49
3.5.1 Test Methods . . . 49
3.6 Experimental Furniture Test Data . . . 51
3.6.1 Furniture Component Testing . . . 51
3.6.2 Full Scale Furniture Testing . . . 53
3.6.3 CBUF Test Series . . . 55
3.7 Scaling . . . 61

**4 Computational Fluid Dynamics 66**
4.1 Governing Equations for Fluid Dynamics . . . 66
4.1.1 Conservation of Mass . . . 67
4.1.2 Conservation of Momentum . . . 67
4.1.3 Conservation of Energy . . . 69
4.1.4 Conservation of Species . . . 70
4.1.5 Equation of State . . . 71
4.2 Discretization . . . 71
4.2.1 Finite Element Geometry Specification . . . 73
4.2.2 Physical Processes and Discretization . . . 76
4.2.3 Discretized Form of the Conservation Equations . . . 80
4.3 Numerical Solution . . . 80
4.4 Closure Models Used in CFD Calculations . . . 83
4.4.1 Time Averaging and Turbulence Modeling . . . 83
4.4.2 Wall Functions . . . 90
4.4.3 Radiation Transfer . . . 92
4.4.4 Radiation Properties . . . 97
4.4.5 Soot Production . . . 100
4.4.6 Combustion . . . 102
4.4.7 Conjugate Heat Transfer . . . 104
4.5 CFD Modeling of Fire . . . 105
4.5.1 Comparison with Experiment . . . 105
4.5.2 Fire Reconstruction and Design . . . 107
4.5.3 Suppression . . . 107

**5 Numerical Simulation of Furniture Fires 108**
5.1 Numerical Model Treatment of Physics . . . 108
5.1.1 Fluid Flow . . . 109
5.1.2 Solid Heat Transfer . . . 110
5.1.3 Transport Processes . . . 111
5.1.4 Source Terms . . . 112
5.1.5 General Boundary Conditions . . . 113
5.1.6 Coupling of Gas and Solid Energy Boundary Conditions . . . 116
5.1.7 Source Term Calculation . . . 120

5.1.8 Combustion and Species Production . . . 123
5.1.9 Convergence Criteria . . . 125
5.1.10 Summary of Physics Treatment . . . 125
5.2 Fire Growth Routine . . . 129
5.2.1 Start of Run . . . 132
5.2.2 Nodal Solution Procedure . . . 137
5.2.3 Physics Not Addressed in the Model . . . 139

**6 Results of Numerical Experiments 141**
6.1 Problem Specification . . . 142
6.2 Results . . . 152
6.2.1 CBUF Mattress 1:21 . . . 152
6.2.2 CBUF Mattress 1:22 . . . 169
6.2.3 CBUF Mattress 1:23 . . . 180
6.2.4 CBUF Mattress 1:24 . . . 191
6.2.5 CBUF Chair 3:13 . . . 202

**7 Conclusions 213**
7.1 Summary of Results . . . 213
7.2 Accomplishments . . . 216
7.3 Future Work . . . 219

**A Thermal Physical Properties 239**
A.1 Foam and Fabric Properties . . . 239

**B User Source Code Routines 242**
B.1 usrsrc.f . . . 242
B.2 flame.dat . . . 267
B.3 flame.hrr . . . 268
B.4 flame.out . . . 269
B.5 flame.sum . . . 270
B.6 flame.com . . . 271
B.7 propb.f . . . 272
B.8 propf.f . . . 274
B.9 propq.f . . . 277
B.10 propr.f . . . 279
B.11 propt.f . . . 283
B.12 prpfvr.f . . . 290

# Nomenclature

| | |
|---|---|
| $A$ | Arrhenius rate equation pre-exponential factor ($\frac{1}{s}$), area ($m^2$) |
| $A_o$ | original burning area ($m^2$), area behind the burner ($m^2$) |
| $A_s$ | area for solid pyrolysis ($m^2$) |
| $A_{s,p}$ | surface area of control volume $p$ ($m^2$) |
| $A_v$ | area of ventilation opening ($m^2$) |
| $\dot{A}$ | time rate of change in burning area ($\frac{m^2}{s}$) |
| $a$ | empirical coefficient, absorption coefficient ($\frac{1}{m}$), constant(-), acceleration ($\frac{m}{s^2}$) |
| $a_g$ | absorptivity of gas (-) |
| $a_s$ | absorptivity of soot (-) |
| $B$ | Spalding Mass Transfer Number (-) |
| $B_d$ | mean line-width to spacing ratio |
| $b$ | empirical coefficient, constant (-) |
| $b_i$ | binomial fit constant |
| $C$ | constant, pre-exponential factor, viscous sublayer thickness ($m$) |
| $C_D$ | turbulence model constant |
| $C_o$ | constant |
| $C_s$ | mass concentration of soot per unit volume ($\frac{kg}{m^3}$) |
| $C_{\epsilon 1}$ | turbulence model constant |
| $C_{\epsilon 2}$ | turbulence model constant |
| $C_\mu$ | constant term in eddy viscosity equation |
| $\bar{c}$ | average coefficient of particulate extinction(-) |
| $c_f$ | fuel specific constant |
| $c_o$ | curve fit constant |
| $c_p$ | specific heat ($\frac{J}{kg\ K}$) |
| $c_s$ | specific heat of solid ($\frac{J}{kg\ K}$) |
| $c_1$ | Planck's first constant ($3.742X10^{-16}\ Wm^2$) |
| $c_2$ | Planck's second constant ($0.01439\ m\ K$) |
| $d$ | spectral line spacing, filling constant |
| $d_i$ | turbulent wall function closure constant |
| $ds^*$ | optical depth |
| $E$ | activation energy from Arrhenius equation ($\frac{J}{mol}$), internal energy ($J$) |
| $F$ | force ($N$) |
| $f_i$ | body force ($N$) |
| $f_v$ | soot volume fraction (-) |
| $g$ | acceleration due to gravity ($\frac{m}{s^2}$) |
| $g_i$ | acceleration vector ($\frac{m}{s^2}$) |
| $H_o$ | height of ventilation opening ($m$) |
| $h$ | enthalpy ($\frac{kJ}{kg}$), heat transfer coefficient ($\frac{W}{m^2\ K}$) |
| $h_c$ | convective heat transfer coefficient ($\frac{W}{m^2\ K}$) |
| $h_k$ | effective heat transfer coefficient ($\frac{W}{m^2\ K}$) |
| $h_l$ | linearized heat transfer coefficient ($\frac{W}{m^2\ K}$) |
| $h_\alpha$ | enthalpy of species $\alpha$ ($\frac{kJ}{kg}$) |

| | |
|---|---|
| $I$ | intensity $(\frac{W}{m^2})$ |
| $I_o$ | incident intensity $(\frac{W}{m^2})$ |
| $I'_\lambda$ | radiation intensity source function |
| $i$ | x direction unit vector |
| $i'$ | incident radiation intensity $(\frac{W}{m^2})$ |
| $i'_b$ | blackbody radiation intensity $(\frac{W}{m^2})$ |
| $J_{\alpha j}$ | species $\alpha$ mass diffusion flux |
| $j$ | y direction unit vector |
| $K$ | power law empirical constant, extinction coefficient $(a + \sigma)$ $(\frac{1}{m})$ |
| $k$ | turbulent kinetic energy, thermal conductivity $(\frac{W}{m\ K})$ |
| | z direction unit vector |
| $k_e$ | extinction coefficient $(\frac{1}{m})$ |
| $k_o$ | soot concentration $(\frac{kg}{m^3})$ |
| $k_{\text{rate}}$ | reaction rate constant |
| $k_s$ | thermal conductivity of solid $(\frac{W}{m\ K})$ |
| $k_t$ | apparent (eddy) turbulent conductivity |
| $k_{tke}$ | turbulent kinetic energy |
| $L$ | length scale $(m)$ |
| $L_\epsilon$ | turbulent length scale $(m)$ |
| $l$ | path length $(m)$ |
| $l_{mix}$ | mixing length $(m)$ |
| $\ell_b$ | burnout length $x_p - x_b$ $(m)$ |
| $\ell_d$ | downstream heating distance $(m)$ |
| $\ell_f$ | flame tip length, $x_f - x_p$ $(m)$ |
| $\ell_p$ | pyrolysis length, $x_p - x_b$ $(m)$ |
| $\ell_u$ | upstream heating distance $(m)$ |
| $M$ | molecular weight $(\frac{kg}{kmol})$ |
| $m$ | mass $(kg)$ |
| $m_o$ | initial mass $(kg)$ |
| $m_{\text{soft}}$ | mass of upholstery material $(kg)$ |
| $\dot{m}$ | mass flow rate $(\frac{kg}{s})$, mass loss rate $(\frac{kg}{s})$ |
| $\dot{m}_f$ | fuel mass loss rate $(\frac{kg}{m})$ |
| $\dot{m}''$ | regression rate $(\frac{kg}{s})$ or $(\frac{mm}{s})$, mass flux $(\frac{kg}{m^2 s})$ |
| $\dot{m}''_{bs}$ | bench scale mass loss rate $(\frac{kg}{m^2 s})$ |
| $\dot{m}''_{bs,tot}$ | bench scale total mass loss $(\frac{kg}{m^2})$ |
| $\dot{m}''_{cr}$ | critical mass flux from surface for ignition $(\frac{kg}{m^2 s})$ |
| $\dot{m}''_o$ | initial mass loss rate $(\frac{kg}{m^2 s})$ |
| $\dot{m}''_{\text{peak}}$ | peak mass loss rate $(\frac{kg}{m^2 s})$ |
| $N$ | time increment (-) |
| $N_i$ | shape function (-) |
| $n$ | power law exponent (-) |
| $n^+$ | non-dimensional distance from wall (-) |
| $\vec{n_j}$ | outward normal surface vector (-) |
| $P$ | pressure $(Pa)$ |

| | |
|---|---|
| $P_e$ | spectral line broadening pressure correction |
| Pr | Prandtl number (-) |
| $\mathrm{Pr}_k$ | turbulent Prandtl number (-) |
| $p$ | (partial) pressure $(Pa)$ |
| $p_c$ | partial pressure of $CO_2$ $(Pa)$ |
| $p_f$ | partial pressure of fuel $(Pa)$ |
| $p_w$ | partial pressure of $H_2O$ $(Pa)$ |
| $p_\infty$ | ambient pressure $(Pa)$ |
| $Q$ | heat $(kJ)$ |
| $\dot{Q}$ | total heat release rate $(kW)$ |
| $\dot{Q}_b$ | burner heat release rate $(kW)$ |
| $\dot{Q}_{bs}$ | bench scale heat release rate $(kW)$ |
| $\dot{Q}_{bs,pk}$ | bench scale peak heat release rate $(kW)$ |
| $\dot{Q}_{fs}$ | full scale heat release rate $(kW)$ |
| $\dot{Q}_{fs,pk}$ | full scale peak heat release rate $(kW)$ |
| $\dot{Q}_{tot}$ | total heat release rate $(kW)$ |
| $\dot{Q}_{tp}$ | total heat released during peak HRR period $(kJ)$ |
| $Q_{300}$ | total heat released during first 300 seconds $(kJ)$ |
| $\dot{Q}'$ | heat release rate per unit width $(\frac{kW}{m})$ |
| $\dot{Q}'_b$ | burner heat release rate per unit width $(\frac{kW}{m})$ |
| $\dot{Q}''$ | heat release rate per unit area $(\frac{kW}{m^2})$ |
| $\dot{Q}''_c$ | heat release rate from spread area $(\frac{kW}{m^2})$ |
| $\dot{Q}''_{co}$ | heat release rate from ceiling $(\frac{kW}{m^2})$ |
| $\dot{Q}''_{max}$ | maximum HRR $(kW)$ |
| $\dot{Q}''_w$ | wall heat release rate $(\frac{kW}{m^2})$ |
| $q_j$ | flux (convective) $(\frac{kW}{m^2})$ |
| $\dot{q}''_c$ | convective flux $(\frac{kW}{m^2})$, convective heat loss $(\frac{kW}{m^2})$ |
| $\dot{q}''_{cr}$ | critical external flux for ignition $(\frac{kW}{m^2})$ |
| $\dot{q}''_e$ | external flux $(\frac{kW}{m^2})$ |
| $\dot{q}''_f$ | forward heat flux $(\frac{kW}{m^2})$, flame heat flux $(\frac{kW}{m^2})$ |
| $\dot{q}''_{fo}$ | wall heat flux at pyrolysis front $(\frac{kW}{m^2})$ |
| $\dot{q}''_{ign}$ | critical flux for ignition $(\frac{kW}{m^2})$ |
| $\dot{q}''_k$ | heat flux at element $k$ $(\frac{kW}{m^2})$ |
| $\dot{q}''_{min}$ | minimum external flux for ignition $(\frac{kW}{m^2})$ |
| $\dot{q}''_{net}$ | net heat flux to surface $= \dot{q}''_e - \dot{q}''_{rr}$ $(\frac{kW}{m^2})$ |
| $\dot{q}''_r$ | radiant flux $(\frac{kW}{m^2})$ |
| $\dot{q}''_{rr}$ | re-radiated energy flux from surface $(\frac{kW}{m^2})$ |
| $\dot{q}''_w$ | wall heat flux $(\frac{kW}{m^2})$ |
| $\dot{q}''^{N-i}$ | bench scale heat release rate at step $N-i$ |
| $\dot{q}^R_j$ | radiative flux $(\frac{kW}{m^2})$ |
| $R$ | universal gas law constant $(\frac{kJ}{kmol\ K})$ |
| $Re_x$ | free stream Reynolds number (-) |
| $r$ | surface reflectivity (-), stoichiometric oxygen to fuel mass ratio (-) |

| | |
|---|---|
| $r_f$ | heating distance $(m)$ |
| $r_p$ | flame foot distance $(m)$ |
| $\vec{r}$ | direction of flame spread (-) |
| $S$ | source-sink term, solid thickness $(m)$, pathlength or distance along beam of radiation $(m)$, mean spectral line intensity, fire point equation constant |
| $S_b$ | bouyancy source term |
| $S_f$ | fuel source term |
| $S_E$ | energy source term |
| $S_k$ | Sutherland conductivity constant |
| $S_m$ | mass source term |
| $S_p$ | product source term |
| $S_T$ | energy source term for thermal conduction |
| $S_u$ | momentum source term |
| $S_\alpha$ | species source term |
| $S_\mu$ | Sutherland viscosity constant |
| $S_\phi$ | scalar $\phi$ source term |
| $s$ | stoichiometric oxygen requirement of fuel (-) |
| $s_e$ | flame heating distance $(m)$ |
| $T$ | temperature $(K)$ |
| $T_b$ | blackbody temperature $(K)$ |
| $T_f$ | flame temperature $(K)$ |
| $T_g$ | gas temperature $(K)$ |
| $T_{ign}$ | ignition temperature $(K)$ |
| $T_o$ | ambient, original or starting temperature $(K)$ |
| $T_p$ | piloted ignition (pyrolysis) temperature $(K)$ |
| $T_s$ | source (wall) temperature $(K)$, surface temperature $(K)$ |
| $T_u$ | turbulent intensity (-) |
| $T_w$ | wall temperature $(K)$ |
| $T_\infty$ | ambient temperature $(K)$ |
| $T^+$ | non-dimensional temperature |
| $t$ | time $(s)$, non-orthogonal local coordinate (-) |
| $t_b$ | burnout time $(s)$ |
| $t_c$ | characteristic combustion time for charring materials $(s)$ |
| $t_{fo}$ | time for flashover $(s)$ |
| $t_{ign}$ | ignition time $(s)$ |
| $t_o$ | initial time $(s)$ |
| $t_p$ | dummy variable of integration |
| $u$ | x direction velocity $(\frac{m}{s})$, non-orthogonal local coordinate (-) |
| $u_{ip}$ | integration point velocity $(\frac{m}{s})$ |
| $u_o$ | initial velocity $(\frac{m}{s})$ |
| $u_\tau$ | shear (friction) velocity $(\frac{m}{s})$ |
| $u_\infty$ | free stream velocity $(\frac{m}{s})$ |
| $\bar{u}_t$ | mean velocity tangent to wall $(\frac{m}{s})$ |
| $u^+$ | non-dimensional velocity, $\frac{\bar{u}_t}{u_\tau}$ (-) |

| | |
|---|---|
| $u'/U$ | turbulent intensity $(m)$ |
| $\dot{V}$ | volumetric flow rate $(\frac{m^3}{s})$ |
| $V$ | volume $(m^3)$ |
| $V_f$ | lateral flame spread rate measured in LIFT test $(\frac{m}{s})$ |
| $V_p$ | flame (pyrolysis) front velocity $(\frac{m}{s})$ |
| $v$ | y direction velocity $(\frac{m}{s})$ |
| $v_T$ | turbulent mixing velocity $(\frac{m}{s})$ |
| $W$ | work $(kJ)$ |
| $w$ | z direction velocity $(\frac{m}{s})$ |
| $X$ | partial pressure pathlenth product $(atm-m, Pa-m)$ |
| $x$ | Cartesian coordinate, distance from leading edge $(m)$ |
| $x_b$ | x coordinate for burnout location $(m)$ |
| $x_f$ | x coordinate for flame tip location $(m)$ |
| $x_{fo}$ | initial flame height $(m)$ |
| $x_p$ | x coordinate for pyrolysis front location $(m)$ |
| $x_{po}$ | height of initial pyrolyzing region due to burner $(m)$ |
| $x_1$ | correction factor |
| $x_2$ | correction factor |
| $Y$ | mass fraction (-) |
| $Y_f$ | fuel mass fraction (-) |
| $Y_o$ | oxygen mass fraction (-) |
| $Y_p$ | product mass fraction (-) |
| $Y_s$ | soot mass fraction (-) |
| $Y_\alpha$ | mass fraction of species $\alpha$ (-) |
| $\bar{Y}_f$ | mean fuel mass fraction (-) |
| $\bar{Y}_o$ | mean oxygen mass fraction (-) |
| $\bar{Y}_p$ | mean product mass fraction (-) |
| $Y_{o,\infty}$ | ambient oxygen mass fraction (-) |
| $(\bar{Y}_f')^2$ | variance of fuel mass fraction fluctuation |
| $y$ | Cartesian coordinate, horizontal distance $(m)$, distance into solid $(m)$ |
| $z$ | Cartesian coordinate |

## Greek Letters

| | |
|---|---|
| $\Gamma$ | exchange coefficient, species mass diffusion coefficient $(\frac{m^2}{s})$ |
| $\Gamma_f$ | fuel mass diffusion coefficient $(\frac{m^2}{s})$ |
| $\Gamma_o$ | oxidizer mass diffusion coefficient $(\frac{m^2}{s})$ |
| $\Gamma_\alpha$ | diffusion coefficient for species $\alpha$ $(\frac{m^2}{s})$ |
| $\Gamma_\phi$ | eddy diffusion coefficient |
| $\Delta$ | heating distance $(m)$, change |
| $\Delta H_{air}$ | heat of combustion per unit mass of air consumed $(\frac{kJ}{kg})$ |
| $\Delta H_c$ | heat of combustion $(\frac{kJ}{kg})$ |
| $\Delta H_f$ | heat of formation $(\frac{kJ}{kg})$ |

| | |
|---|---|
| $\Delta H_o$ | heat of combustion per unit mass of $O_2$ consumed ($\frac{kJ}{kg}$) |
| $\Delta H_p$ | heat of pyrolysis ($\frac{kJ}{kg}$) |
| $\Delta H_v$ | heat of vaporization ($\frac{kJ}{kg}$) |
| $\Delta n$ | distance of first node away from wall ($m$) |
| $\Delta T$ | temperature difference ($K$) |
| $\Delta t$ | time step ($s$) |
| $\Delta x$ | distance ($m$) |
| $\Delta y$ | distance ($m$) |
| $\Delta \nu$ | wavelength interval for narrow band model ($\mu m$) |
| $\nabla$ | divergence vector operator |
| $\Phi$ | lateral flame spread (LIFT) constant |
| $\Omega$ | albedo for scattering |
| $\alpha$ | absorptivity (-), thermal diffusivity $\frac{k}{\rho c}$ ($\frac{m^2}{s}$) |
| $\beta$ | in-depth radiation absorption coefficient (-), fraction of upper zone flow leaving the compartment (-), coefficient of volumetric expansion correction factor accounting for additional flux reaching fuel surface (-) |
| $\delta_{ij}$ | Kronecker delta (-) |
| $\delta_s$ | thickness of solid ($m$) |
| $\delta_s^*$ | optical length ($m$) |
| $\epsilon$ | emissivity (-), dissipation rate of turbulent kinetic energy |
| $\epsilon_g$ | gas emissivity (-) |
| $\epsilon_s$ | soot emissivity (-) |
| $\zeta$ | fraction of water vapor $\frac{p_w}{p_w+p_c}$ (-) |
| $\kappa$ | optical path length ($m$), coefficient of bulk viscosity, von Karman constant |
| $\kappa_\lambda$ | optical depth ($m$) |
| $\kappa^*$ | dummy variable of integration for optical path length |
| $\lambda$ | HRR exponential approximation decay constant, wavelength ($\mu m$), stoichiometric coefficient(-) |
| $\mu$ | viscosity ($\frac{N\ s}{m^2}$) |
| $\mu_l$ | laminar viscosity ($\frac{N\ s}{m^2}$) |
| $\mu_o$ | reference viscosity ($\frac{N\ s}{m^2}$) |
| $\mu_T$ | turbulent viscosity ($\frac{N\ s}{m^2}$) |
| $\mu'$ | second coefficient of viscosity |
| $\nu$ | kinematic viscosity ($\frac{m^2}{s}$), frequency ($\frac{1}{s}$) |
| $\rho$ | density ($\frac{kg}{m^3}$) |
| $\rho_g$ | gas density ($\frac{kg}{m^3}$) |
| $\rho_o$ | reference density ($\frac{kg}{m^3}$) |
| $\rho_s$ | density of solid ($\frac{kg}{m^3}$) |
| $\rho_\infty$ | ambient density ($\frac{kg}{m^3}$) |
| $\sigma$ | Prandtl/Schmidt number (-), Stefan-Boltzmann constant ($5.67X10^{-8}\ \frac{W}{m^2K^4}$) |
| $\sigma_f$ | specific extinction area ($\frac{m^2}{kg}$) |
| $\sigma_{ij}$ | stress tensor |
| $\sigma_s$ | soot scattering coefficient ($\frac{m^2}{kg}$), specific extinction area |

| | |
|---|---|
| | per unit mass of soot ($\frac{m^2}{kg}$) |
| $\sigma_\alpha$ | Schmidt Number (-) |
| $\tau$ | shear stress, ignition time constant, preheat time ($s$), ignition delay time ($s$) |
| $\tau_b$ | burnout time ($s$) |
| $\tau_c$ | characteristic time for diffusion flame reaction ($s$) |
| $\tau_g$ | physical mixing time ($s$) |
| $\tau_{ign}$ | non-dimensional ignition time (-) |
| $\tau_t$ | tangent stress |
| $\tau_w$ | shear stress at wall |
| $\phi$ | dependent (general) variable, forward heat flux parameter, scattering phase function, azimuthal angle (radians), local equivalence ratio maximum fraction of flame heat loss resulting in extinction (-) |
| $\phi^o$ | value of $\phi$ at the old (previous) time step |
| $\bar{\phi}$ | time mean value of $\bar{\phi}$ |
| $\phi'$ | fluctuating component of $\phi$ |
| $\varphi$ | global equivalence ratio (-) |
| $\psi$ | species yield (-) |
| $\psi_s$ | soot yield (-) |
| $\psi^3$ | pentagamma function |
| $\omega$ | solid angle (steradians) |

## Subscripts

| | |
|---|---|
| $f$ | fuel |
| $g$ | gas |
| $i$ | Cartesian coordinate x direction |
| $ign$ | ignition |
| $ip$ | integration point |
| $j$ | Cartesian coordinate y direction |
| $k$ | Cartesian coordinate z direction |
| $l$ | laminar |
| $o$ | ambient, atmospheric |
| $ox$ | oxygen |
| $s$ | solid, scattering, soot |
| $t$ | turbulent |
| $tot$ | total |
| $w$ | wall |
| $\lambda$ | wavelength (spectral) |

## Acronyms

| | |
|---|---|
| ACM | Additive Correction Multigrid |
| AMG | Algebraic Multigrid Method |
| EBU | Eddy Break-up |
| EDC | Eddy Dissipation Concept |
| FCFD | Furniture Computation Fluid Dynamics Model |
| FFM | Furniture Fire Model |
| FRPU | Flame Retardant Polyurethane |
| FTP | Flux Time Product |
| GER | Global Equivalence Ratio |
| HRR | Heat Release Rate |
| IPV | Incremental Plume Volume |
| MWS | Mass Weighted Skew Upstream Differencing |
| PAC | Physical Advection Correction |
| PDF | Probability Density Function |
| PU | Polyurethane |
| RHS | Right Hand Side |
| SPF | Self Propagating Flux |
| TKE | Turbulent Kinetic Energy |
| TUHC | Total Unburned Hydrocarbons |
| VOL | Volume |

# Chapter 1

# Introduction

The effectiveness of deterministic fire models for the prediction of fire spread and smoke movement has traditionally been limited by the lack of suitable methods to quantify the growth rate of fire. Much of the modeler's time is spent on fire specification in an effort to overcome the unknowns involved in this portion of the problem input. Currently a significant effort is being made internationally to improve the ability to predict compartment fire growth on contents and surface linings based on bench scale heat release data. The ability to estimate the rate of fire spread using reaction to fire measurements and material properties would provide a quantitative risk assessment tool that can be used for setting fire regulations, design and reconstruction.

This dissertation describes research leading to the development of a computational fluid dynamics (CFD) model to include a fire growth rate calculation method. The goal is to allow the use of bench scale cone calorimeter test data and material properties in a general purpose CFD code for predicting the rate of fire growth on compartment contents such as furniture. The direct result will be to free the model user from having to define the heat release rate of the fire. Instead the fire growth rate is determined by the model based on the fuel, radiant flux level, geometry, compartment environment and burning history.

Results of five different comparisons between experiment and model will be presented. Tested configurations include two solid mattresses, two interior spring mattresses, and a simple chair design without arms. The range of combustion behavior includes both slowly propagating flame retardant to rapid spreading foam-fabric combinations. Results show that the current model provides reasonable estimates for flame spreading periods of fire growth when the fuels are not highly fire retardant. In most cases, model results for the peak HRR, time to peak HRR, and slope of the HRR curve are within 25% of experiment. The model was less successful predicting the behavior of highly fire retardant fuels.

## 1.1 Rationale

When a user specifies the source for combustion, a deterministic fire model principally functions to predict the energy and fluid flow through the domain resulting from the source. For problems such as furnaces and engines, the mass rate of fuel entering the domain is a known value, so a user specified source is appropriate. When one wants to look at fires inside compartments, the fuel production rate is not known *a priori*, so a user specified source term for pyrolysis, although an option, is a less rigorous treatment. The more appropriate approach is to use the model to calculate the source terms based on surface pyrolysis rates that are a function of the local environment. The compartment conditions therefore control the source terms or fire growth.

Additionally, as countries move closer to performance based engineering, development of standardized design fires will be an important component of the evolution from prescriptive building regulations. A tested fire growth model for contents and linings coupled with CFD can, and will, assist in the creation and testing of design fire scenarios.

A recent review on the state of fire models for use as fire safety engineering tools discusses the significant shortfall in the treatment of fire dynamics that limits the applicability of current models [1]. Six main areas of deficient fire chemistry and physics treatment common to all publicly available fire models were indicated:

- No flame spread
- No heat release rate
- Absence of realistic layer mixing
- No fire chemistry - CO generation
- No smoke chemistry
- No suppression

Before fire modeling can truly be applied to general fire protection engineering problems, research effort must go into improving our understanding in each area.

This work will serve to apply CFD and bench scale test results to address the first three items. The growth in the pyrolyzing area will be predicted by treating flame spread as a series of piloted ignitions. The mass loss rate from a given surface element is based on the cone calorimeter test data and serves as the fuel mass inflow boundary condition. A combustion model then provides for distributed combustion based on the rate of mixing between fuel and oxidizer. By adding the energy contributions of each element, the heat release rate is determined.

Except for the most basic gaseous fuels, multiple step reactions for combustion of pyrolysis products are not available. For the near future, experimental data will continue to be used to predict the heat release rate (HRR) and species generation without first principle calculation of the actual production.

As a result of the way they are formulated, zone models can not easily predict the mixing between the two layers without some form of empirical approximation. CFD, however, does not suffer this inherent weakness and should provide more realistic predictions for mixing and entrainment than is available from zone models. A number of simplifications and approximations such as turbulence modeling, however, are still necessary for a closed solution of the conservation equations.

## 1.2 The Process

Current state of the art computational fluid flow and heat transfer models can provide reasonably accurate predictions for velocity, energy distribution and species transport. Fires add the complication of reacting species and radiation heat transfer. When specified by the user, a fire source in terms of HRR or mass loss rate does not incorporate local conditions that influence the rate of fire growth. Most fire predictions with CFD simply track the movement of smoke resulting from a user specified input fire. For many problems of engineering interest to fire safety, this is sufficient since incomplete information is known about the source fuels to predict a growing fire that is interacting with its environment, Figure 1.1.

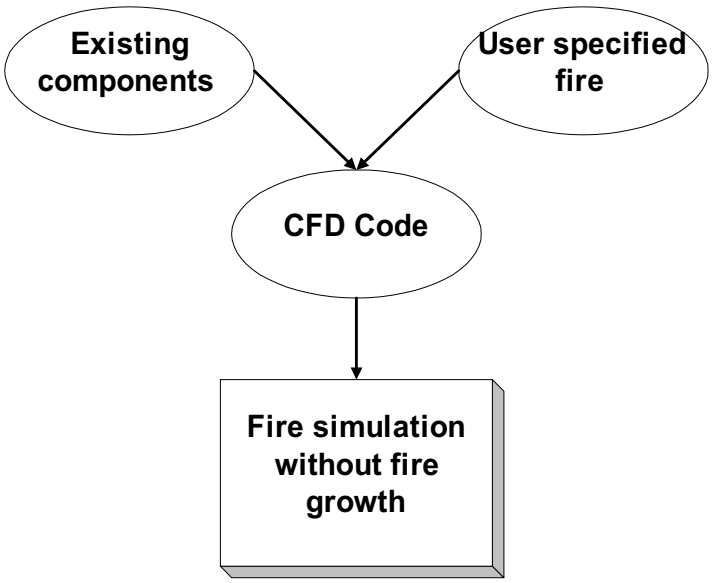


Figure 1.1: CFD predictions without fire growth.

The problem of fire growth prediction differs from other forms of combustion modeling (furnaces, engines, power generation etc.) in the prior knowledge about fuel supply. For most combustion situations, the fuel composition and flow rate is known, if not controlled, by the process, simplifying input for the numerical modeler. Contrast this to the situation where the heat feedback from the fire itself controls the rate of fuel generation in a compartment, the composition of which is not well defined or known in advance.

A CFD code with an accurate radiation transfer routine and combustion model can provide fluid flow and heat transfer information to a pyrolysis model when the two are coupled. Existing CFD component submodels for heat transfer, turbulence, combustion and species transport are able to provide boundary condition information at the surface of a fuel. A flame spread routine can use this information to predict pyrolysis, flame spread and ultimately fire growth rate using bench scale and material property data as input. By applying source terms to the conservation equations for mass, momentum, energy and species, a furniture fire model has been developed to interface with the CFD code TASCflow to predict the rate of fire growth, Figure 1.2.

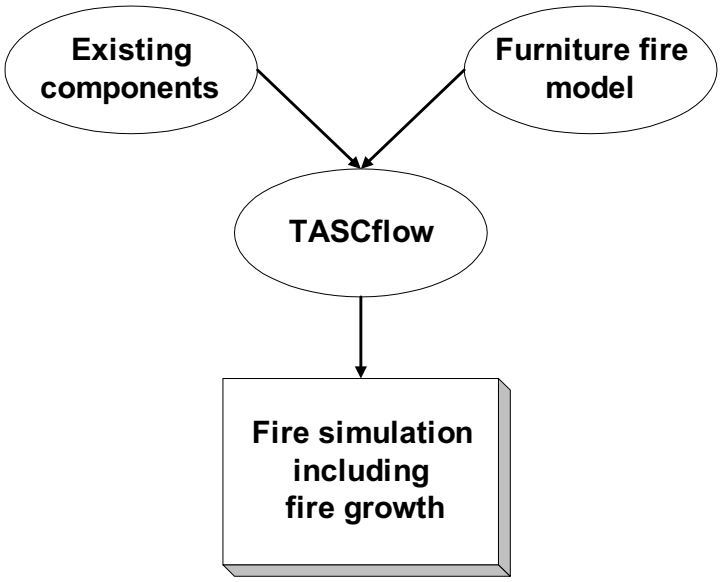


Figure 1.2: CFD predictions with fire growth.

One of the most commonly encountered furniture items in the residential setting, the polyurethane (PU) foam "easy chair", is also a frequently burned fuel package in the laboratory. Chairs typically have a foam seat and back, along with armrests, and are sometimes decorated with buttons, welt cord edging and possibly skirting around the base. A number of geometric irregularities such as crevices and gaps are formed which complicate the prediction of how the furniture will burn, and due to construction techniques, can vary from piece to piece for the same design. Experimental data show that such irregularities can have a profound effect on how a chair will burn, especially close to the ignition source. During a fire, furniture can be expected to burn with local regions of high temperature, velocity and species gradients, a range of time and length scales, and unknown intermediate chemical reactions, all adding more complications to quantification efforts.

The ability to gather useful experimental data for modeling has grown significantly over the last 15 years with the refinement of oxygen consumption calorimetry [2]. It is the goal of this work to apply more detailed quantification techniques toward predicting fire growth on furniture as shown in Figure 1.3, and includes:

- Development of an engineering prediction tool for flame spread on simple furniture geometries.
- Coupling this tool with a commercial CFD package to generate the basic grid, fluid flow, heat transfer and combustion solutions.
- Incorporation of bench scale test results as an engineering approach to provide boundary conditions between the solid fuel and gas phase for the physics such as pyrolysis that are difficult to quantify.
- Evaluate the effectiveness of the model to predict fire growth on simple furniture mockups composed of mattresses and simple chair designs.
- Simulate numerically the developing fire as measured in the furniture calorimeter to allow comparisons to be made with laboratory results for mass loss rate, HRR and radiant flux.

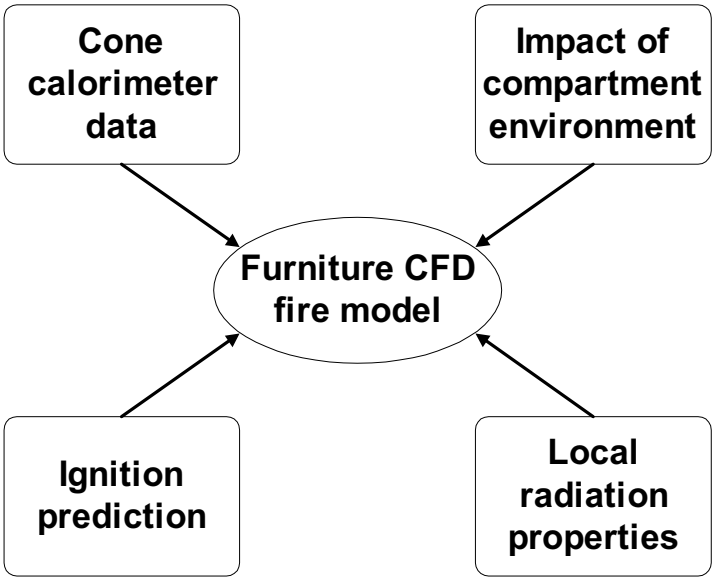


Figure 1.3: Fire growth model components.

Because it is critical to an accurate prediction of fire growth, ignition and flame spread over solids will be discussed first in Chapter 2. Chapter 3 covers the topic of fire growth and furniture. A brief overview of computational fluid dynamics (CFD), and more importantly the use of CFD for the modeling of fire, will be given in Chapter 4. Ignition, flame spread, CFD and fire growth will then be united in Chapter 5, where the details of the current research on modeling of furniture fire growth are presented. Results of numerical experiments and conclusions then follow.

# Chapter 2

# Flame Spread

This chapter will lay the theoretical foundation to the problem of predicting growth of fire in compartments. Flame spread in each direction over the surface of a solid will be evaluated with the increase in area involved providing the growth in heat release rate. For fuel near the pyrolysis front, ignition will result in additional burning area, i.e. flame spread.

Since the process of flame spread will be viewed as a series of piloted ignitions, the success in predicting flame spread will depend on the determination of when ignition occurs. In this context, piloted ignition will be discussed almost exclusively since the advancing flame front provides the necessary ignition source. The discussion will be generally limited to diffusion flames, although mention is made of premixed combustion.

Theoretical calculations of ignition will be presented along with experimentally determined ignitability data measured during heat release rate testing. Modeling the ignition process is a complex task requiring a coupled solution for unsteady physical and chemical processes in both the gas and solid phases. Physical properties are highly variable and the resulting coupled conservation equations non-linear with time and length scales covering several orders of magnitude. Current models for ignition utilize extensive assumptions and approximations to make analytical or numerical solutions possible.

Because of its importance, piloted ignition of solid fuel surfaces will be discussed first along with possible measures of the ignition process and prediction models. Mechanisms and types of flame spread are covered next, followed by thermal flame spread theory and models that attempt to predict flame spread by treating the fuel as an inert solid and include bench scale data as the fuel mass loss boundary condition. Because the literature covering the growth of fire on furniture is limited, much of the current discussion will include reference to the more abundant work on flame spread over compartment lining materials.

## 2.1 Qualitative Description of Ignition

Ignition defines the initiation of flaming combustion. For most solids, this requires an external flux to the fuel sufficient to heat the surface to a level such that the irreversible process of pyrolysis is able to produce an adequate flow of volatiles to support flaming combustion. Figure 2.1 is a schematic of the basic one-dimensional model that will be used for the bulk of the ignition discussion. For a given material,

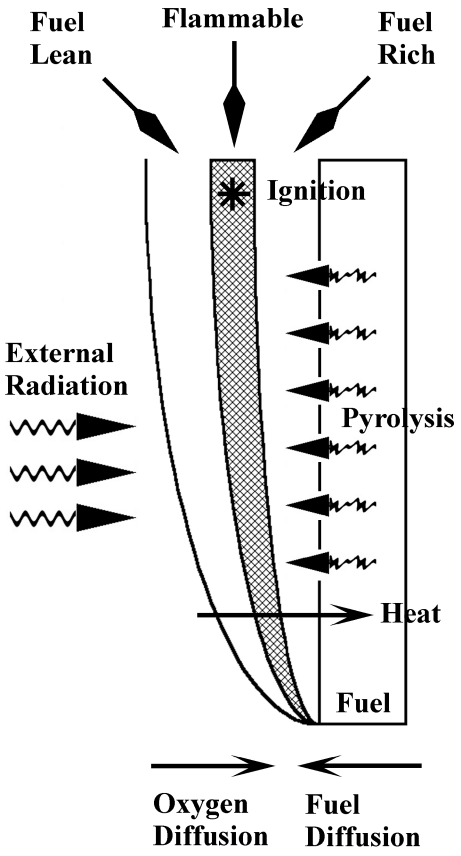


Figure 2.1: Ignition model with one-dimensional heat transfer.

piloted ignition is primarily controlled by the external heat flux reaching the solid surface. The critical flux for piloted ignition must raise the surface temperature sufficiently to produce the necessary flow of pyrolysis products to create a region near the pilot that is above the lower flammable limit for premixed flames.

Ignition delay time as a function of flow velocity, temperature and oxygen concentration was studied by Niioka for spontaneous ignition of polymers in a high temperature stagnant point oxidizing gas flow [3]. It was found that as the flow velocity increases, the ignition time decreases and then reaches a minimum. With further increases in the flow velocity, the ignition time begins to lengthen, demonstrating competing mechanisms between the solid phase and gas phase reactions. At low flow velocities, the heat transfer to the surface is enhanced, which reduces the time

necessary to obtain a sufficient flow of volatiles from the surface. As flow velocities are increased, additional heat is transferred to the surface. At the same time, the residence time for the volatiles and oxidizer above the fuel surface decreases, inhibiting the chemical reaction and delaying ignition. When gas temperature and oxygen concentrations are increased, the time for ignition decreases as expected. The total ignition time was found to be the sum of the solid pyrolysis time and the gas phase reaction (induction) time as shown in Figure 2.2 [4].

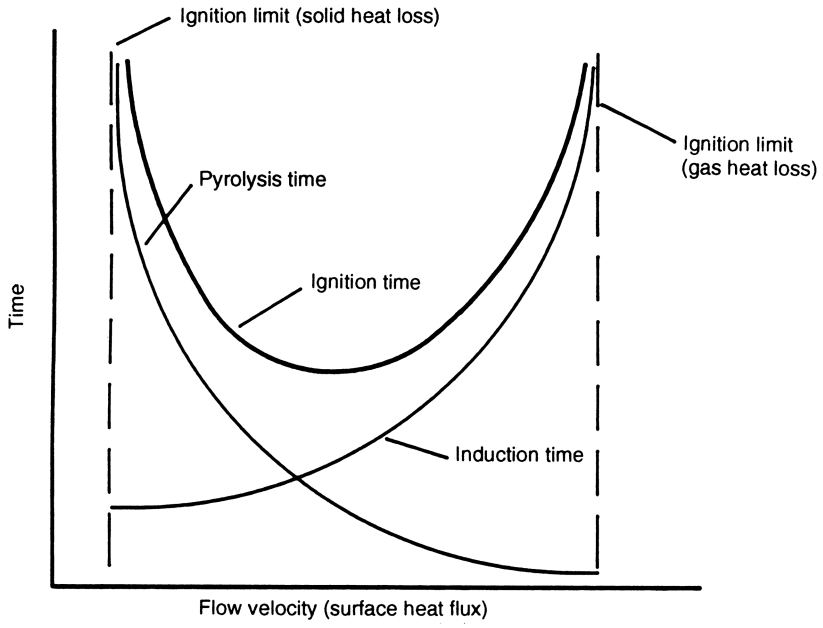


Figure 2.2: Ignition time as a function of solid pyrolysis and induction times [4] .

In terms of material properties, a large latent heat of vaporization, $L_v$, thermal conductivity, $k$, specific heat, $c_s$, or density, $\rho$, will result in a material that is harder to ignite. Similarly, if the volatiles from the solid have a low heat of combustion, maintaining a flame will be more difficult since there is a smaller heat source to counteract losses from the surface via convection and radiation. For cellulosic materials, moisture content influences the ignition process both by changing the thermal properties of the solid ($k\rho c$) and more importantly, changing the energy input required to pyrolyze the solid [5].

Flame retardant treatments will also influence the ignition properties of a solid. A given retardant can increase the surface temperature or the critical flux necessary for ignition, while decreasing the mass flux of volatiles from the surface due to char formation. The thermal inertia of the solid could be increased, along with an accompanying decrease in the heat of combustion. Janssens provides an excellent review of experimental conditions that influence the measurement of piloted ignition [5]. Time to ignition was found to be affected by flow conditions near the sample caused by drafts and change in sample orientation. Generally, piloted ignition times were insensitive to pilot type, strength and location.

## 2.2 Quantitative Description of Ignition

The most common criteria for piloted ignition of solids is surface temperature, critical external flux to the surface or critical mass flux from the surface. Correlations of bench scale piloted ignition data are also used for determining ignition, where the most common is the Flux Time Product (FTP). Additional measures include a reversal in the direction of the temperature gradient of the gas phase boundary layer above the surface of the solid, sufficiently high rate of increase in temperature of the gas phase (indication of an exothermic reaction), and a critical reaction rate in the gas phase [5].

This section will highlight the different indicators of ignition to determine suitability for inclusion in a fire model. A good measure of ignition for experimental work may, however, not be appropriate for modeling.

### 2.2.1 Ignition Temperature

Drysdale describes the firepoint of a solid similar to the common definition for liquids and gases where it represents a temperature high enough to produce a sufficient flow of volatiles to allow ignition [6]. For solid fuels, it represents a surface temperature, as opposed to a bulk temperature when associated with fluids. For most engineering purposes, the fire point temperature can be considered equal to the ignition temperature.

When experimentally measuring the firepoint temperature over a range of external irradiances, accuracy at lower flux levels tends to suffer due to problems with thermocouple detachment. Rapid temperature changes between pilot flame application at high flux levels can also lead to errors. The measured value of ignition temperature was found to be apparatus independent when the Edinburgh University apparatus results were compared to those from the ISO apparatus [6]. It is also pointed out that the use of a firepoint temperature for flux exposures below the minimum for ignition (critical) may lead to errors if the fuel is consumed or a char layer develops. Similarly at high heat fluxes where the gas reaction times are on the same order as the solid heating time, determination of ignition based on a firepoint temperature can result in errors. Boundary layer flow conditions may exist that inhibit ignition by removing fuel from the reaction zone.

In general, when the external flux is nearly constant, the firepoint temperature is satisfactory for engineering purposes [7]. At this temperature, the solid is able to produce a sufficient mass flow of volatiles to allow the formation of a persistent diffusion flame above the surface. Thomson and Drysdale found the firepoint temperature to be very sensitive to boundary conditions at the surface during piloted ignition tests with polymers [8].

Given a solid exposed to a constant external heat flux, a surface energy balance allows development of relations between the time to ignition and external flux based on a firepoint temperature. The solid is assumed inert, such that mass and energy interactions during pyrolysis before and after ignition are ignored. Complications

of variable radiative energy absorption in depth through the solid are avoided by evaluating radiation at the surface. Gas phase radiation absorption, boundary layer effects and the chemical reaction among species are not considered. Determining the surface temperature becomes an exercise in calculation of the solid phase energy diffusion (conduction).

Fernandez-Pello [4] describes a simplified ignition model based on the spontaneous ignition of a solid in a hot stagnant point oxidizer flow. Ignition of a solid fuel at an initially uniform temperature is determined for exposure to a constant heat flux from the hot flow. As the solid pyrolyzes, the fuel mixes with the oxidizer stream above the surface to form a premixed gas volume. The fuel concentration increases until it is above the lower flammable limit, at which time it can be ignited by the hot gas flow.

Looking at the solid phase heating and pyrolysis production at a surface temperature, $T_s$, the rate of mass loss from the surface due to pyrolysis, $\dot{m}''$, can be described by a zero order Arrhenius law equation

$$\dot{m}'' = A\rho \exp\left(-\frac{E}{RT_s}\right) \tag{2.1}$$

Considering constant material properties and no charring, an energy balance at the surface yields

$$\rho_s c_s \frac{\partial T_s}{\partial t} + \rho_s c_s \frac{d\delta_s}{dt}\frac{\partial T_s}{\partial y} = k_s \frac{\partial^2 T_s}{\partial y^2} - \dot{m}''\Delta H_v \tag{2.2}$$

where the subscript $s$ represents solid material properties, $\Delta H_v$ the latent heat of vaporization, $\delta_s$ the solid thickness, $y$ the coordinate direction normal to the solid surface, and $k_s$, $c_s$, and $\rho_s$ the thermal conductivity, specific heat and density for the solid. A material can be considered thermally thick if $\frac{\delta_s}{\sqrt{\alpha t}} \gg 1$ and thermally thin for $\frac{\delta_s}{\sqrt{\alpha t}} \ll 1$, where the thermal diffusivity, $\alpha$, is equal to $\frac{k_s}{\rho_s c_s}$.

Except in the limit of high flow velocities and low temperatures or oxygen concentrations, the rate of pyrolysis is dependent on the rate of surface heating. If the solid is considered inert and heating can be treated as one-dimensional and constant, Equation 2.2 simplifies to

$$\rho_s c_s \frac{\partial T_s}{\partial t} = k_s \frac{\partial^2 T_s}{\partial y^2} \tag{2.3}$$

Carslaw and Jaeger [9] give solutions to Equation 2.3 for the limiting cases of thermally thick and thin behavior. For a thermally thick solid exposed to a constant heat flux, $\dot{q}''_{net}$, the time to ignition, $t_{ign}$, based on raising the solid from the initial temperature, $T_\infty$, to the piloted ignition temperature, $T_{ign}$, is:

$$t_{ign} = \frac{\pi \rho_s c_s k_s (T_{ign} - T_\infty)^2}{4(\dot{q}''_{net})^{\,2}} \tag{2.4}$$

The net heat flux to the surface equals the externally applied flux minus the energy

re-radiated from the surface, $\dot{q}''_{net} = \dot{q}''_e - \dot{q}''_{rr}$. For thermally thin materials

$$t_{ign} = \frac{\rho_s c_s \delta_s (T_{ign} - T_\infty)}{\dot{q}''_{net}} \tag{2.5}$$

Inclusion of the gas phase requires consideration of mass, momentum, energy, species and chemical rate equations for the fluid above the surface. A recent review has been completed by Janssens [5].

### 2.2.2 Critical Flux for Ignition

Measurements of ignitability can be made during radiant heating in the cone calorimeter as part of heat release rate testing or in the lift apparatus during lateral flame spread measurements. The time to ignition under different levels of external flux is usually reported based on visual observation. By running multiple tests with the flux level reduced after each test, the minimum external radiant flux necessary for piloted ignition can be measured. Time to ignition has been related to externally applied flux levels by many researchers including Janssens [10] and Mikkola [11].

Krasny looked at ignitability predictions between the cone calorimeter and small flaming pilot sources for upholstered furniture fabric and padding mockups [12]. The cone calorimeter was used for large external radiant flux tests, while the piloted tests were completed with methenamine pill and propane jet flame sources. Agreement for screening purposes was found between ignitability in the cone calorimeter and piloted sources. Measurements in the cone calorimeter, however, were found to be superior since data on mass loss as a function of time are available and can be used to supplement visual ignition observations.

Similar relations for ignition time were found using a non-linear heat loss boundary condition and an integral solution. Mikkola took ignition data from a host of researchers and correlated $\dot{q}''$ versus $t^{-\frac{1}{2}}$ with excellent results. By extrapolating $\dot{q}''$ as $t \to \infty$, then $t_{ign}^{-\frac{1}{2}} \to 0$, and the minimum external flux necessary for ignition, $\dot{q}''_{min}$, can be found.

Mikkola [11] shows $\dot{q}'' \propto t_{ign}^{-.5}$ for piloted ignition under an external flux. Shields [13] looked at ignition of vertical and horizontal cellulosic samples and came up with a similar relation with a slightly different exponent (-0.553). Janssens recommends plotting ignition test data as $t_{ign}^{-0.547}$ versus $\dot{q}''_e$ from which the critical flux for ignition and the apparent thermal inertia, $(k\rho c)$, can be found from the intercept and slope respectively.

Thomson and Drysdale [14] point out that while the fire point temperature could be considered a material property, the critical flux for ignition can not, since the heat transfer environment above and behind the sample are important. Depending on the convective fraction, the critical flux for ignition may be sensitive to surface orientation unless radiation dominates [7]. Experimental values for the minimum heat flux resulting in ignition from bench scale tests are often slightly higher than the values obtained by correlating test data or by calculation using simple thermal

models.

### 2.2.3 Critical Mass Flux

A fundamentally more basic method of measuring ignition is based on the flow rate of pyrolysis products necessary to allow the ignition and subsequent formation of a diffusion flame. At the critical mass flux for ignition, enough fuel is produced from the solid, such that the flame is able to provide sufficient energy to the surface for pyrolysis, allowing for losses due to re-radiation and convection. Since the mass generation rate of volatiles from the surface depends upon the flux reaching the surface and the total energy exposure history, the critical mass flux should be a more accurate indicator of ignition than a surface temperature value. The mass generation rate of volatiles from a burning surface, or mass loss rate, is given by

$$\dot{m}'' = \frac{\dot{q}''_e + \dot{q}''_f - \dot{q}''_c - \dot{q}''_{rr}}{L_v} \tag{2.6}$$

where $\dot{q}''_e$ is the externally applied flux, $\dot{q}''_f$ is the flux from the flame, $\dot{q}''_c$ is the convective heat loss from the surface and $\dot{q}''_{rr}$ is the energy re-radiated from the surface. Using a critical mass flux from the surface for ignition, $\dot{m}''_{cr}$, Equation 2.6 can be expressed in a form suitable for determining ignition

$$(\phi \Delta H_c - L_v)\dot{m}''_{cr} + \dot{q}''_e - \dot{q}''_c - \dot{q}''_{rr} = S \tag{2.7}$$

which is termed the firepoint equation by Drysdale [7]. $\phi$ is the maximum fraction of the heat of combustion that the diffusion flame can lose to the pyrolyzing fuel surface without flame extinction occurring. When $S$ is larger than zero, ignition is possible and the flame will grow due to the net positive flow of energy to the fuel surface, whereas no ignition or flame extinction is indicated for $S$ less than zero.

Rasbash stated that surface temperature alone is not a sufficient indicator of ignition, but that the mass flux of volatiles from the surface must also be known to determine if a diffusion flame will be formed above a solid's surface [15]. He also suggested that Spalding's mass transfer number could be used to determine an approximate $\dot{m}''_{cr}$.

Thomson and Drysdale [8] measured the critical mass flux at the firepoint temperature for eight plastics oriented in the horizontal configuration when subject to an external irradiance of $12 - 35\ \frac{kW}{m^2}$. The data showed that the critical mass flux for ignition is independent of the ignition source, and for non-fire retardant plastics, relatively insensitive to the level of external flux over the range tested. $\dot{m}''_{cr}$ values were, however, found to depend on the sample size. Also, any disturbances in the airflow around the sample during testing changed the results [16].

The results of this and earlier work using bench scale ignition testing apparatus have shown that the critical mass flux necessary for ignition is also sensitive to the experimental apparatus used [15]. Mass flux alone may not be sufficient to indicate ignition since flashing without sustained flame formation is possible even when

$\dot{m}'' \geq \dot{m}''_{cr}$ [15]. Thus, a surface energy balance is still necessary to determine if sufficient energy is available to vaporize the fuel and makeup losses. With this in mind, the firepoint temperature was recommended as adequate for engineering analysis of piloted ignition under a constant flux [8, 14].

### 2.2.4 Flux Time Product

As discussed by Smith [17, 18], the flux time product (FTP) is an accurate way of indicating piloted ignition of solids exposed to a varying external flux:

$$\text{FTP} = \sum(\dot{q}''_e - \text{SPF})^n \Delta t \tag{2.8}$$

The self propagating flux, SPF, is the experimentally determined minimum flux necessary for horizontal piloted flame spread. A $\text{FTP}_{\text{min}}$ can be determined for a material based on small scale tests and the results used for modeling. Bench scale heat release rate tests are run at several different flux levels above the minimum flux for piloted ignition. The test flux level, $\dot{q}''_e$, minus the minimum flux for ignition is multiplied by the time for ignition to give the $\text{FTP}_{\text{min}}$, which is averaged over several different flux levels. Since the material properties have already been taken into account during the small scale testing, thermal properties are not necessary, as they would be for surface temperature calculations. The FTP is a satisfactory method for estimating ignition when a solid is exposed to a non-constant flux, since it is better able to include the effects of varied heating levels. Piloted ignition is taken to occur when the FTP for the exposure exceeds $\text{FTP}_{\text{min}}$.

Over 50 different materials have been tested and the resulting $\text{FTP}_{\text{min}}$ values calculated. A procedure for analysis of bench scale ignition data to derive the necessary parameters for the FTP has been presented [19].The FTP was found to be a more accurate indicator of ignition than surface temperature for PVC, inorganic faced laminates, FR materials and non-thermally thick solids [18]. The FTP will produce errors, however, for samples that are exposed to a flux below $\text{FTP}_{\text{min}}$ for long periods before ignition during a "soaking period" because the assumption of constant heat loss from the surface for different flux levels breaks down [17]. The FTP in these cases will depend on flux levels and exposure time, so a constant value for the FTP can not be stated, limiting the value of the method.

Orientation and ignition mode effects on the FTP determined during testing of cellulosic materials in the cone calorimeter have been reported by Shields [13]. Based on test data, the critical flux for ignition was found to be larger for vertical sample orientation as a result of a different convective heat transfer coefficient. Calculated values of the FTP were found to be independent of the ignition mode and sample orientation.

Toal [20] found the FTP to be the most suitable method for relating incident flux level to time for ignition. A classification system for material ignitability is also proposed. The flux time product concept has also been adapted, with some modification, by Dietenberger [21] for use in determining ignition under non-constant flux conditions in the furniture fire model (FFM), to be discussed in Section 3.3.3.

Except in special cases, obtaining the necessary bench scale results for flux above critical could limit the utility of the FTP for the modeling of ignition. Determination of the SPF and correlating constant increases the difficulty for use as an engineering tool.

### 2.2.5 More Detailed Predictions

Amos [22] has investigated the auto-ignition process from pyrolysis to the formation of a steady state diffusion flame occurring over a vaporizing fuel surface in a zero gravity environment. Two cases of ignition over a flat plate were considered: no flow and a stagnation point flow field. When the fuel vapors produced during pyrolysis were considered to be non-absorbing to thermal radiation, ignition resulted from the hot surface of the fuel. If radiation absorption by the gas was included, heating of the volatilized fuel to an auto-ignition temperature was sufficient to result in ignition.

For both cases, the general process leading to the formation of a steady state diffusion flame was similar. Heating of the fuel surface results in pyrolysis, allowing the formation of a fuel rich region directly above the fuel as shown in Figure 2.1 on Page 7. Due to diffusion, a fuel and air mixture forms at the interface between fuel rich and lean regions. For vertical surfaces, a transient natural convection boundary layer may form as heat is transferred from the hot surface to the nearby gases by absorbing radiant energy from the external source. This boundary layer may benefit the ignition process by increasing mixing between the fuel and air or it may inhibit the reaction by taking away fuel vapors, thus delaying the formation of a mixture above the lower flammable limit.

At ignition, the premixed gases begin to burn near the fuel rich region and pass through a stoichiometric zone. Finally they reach a fuel lean region where the premixed flame terminates and leaves behind a diffusion flame in the stoichiometric region separating the fuel vapors from the ambient air. If the solid is exposed for an extended period to an external flux below that necessary for ignition, a char layer that inhibits the flow of volatiles necessary for ignition may begin to form.

To model this process, Amos develops energy, velocity and mass fraction conservation equations in a non-dimensional form. The conservation equations were formulated and the computational domain discretized according to Patankar [23]. As expected, numerically solving for the movement of the premixed flame was difficult due to the wide range of time and length scales involved. The finite difference method, a movable grid and the flame discontinuity method of Chorin were analyzed for applicability to the premixed problem. The last two methods were found best suited to premixed flame analysis. The finite rate kinetics associated with diffusion flames over large time and length scales could be best handled with the finite difference method [22].

Kashiwagi has developed one of the more detailed models for spontaneous ignition of a solid exposed to radiant heating that includes both solid and gas phase processes [5, 24]. Tzeng arrived at very similar equations for the analogous piloted ignition problem [25].

The model assumptions include constant pressure and constant density terms except when considering buoyancy (Boussinesq approximation). Edge effects on the solid are ignored and one-dimensional heating is considered. The surface does not re-radiate energy, but it does absorb incident radiation according to the Beer Law. Above the solid surface, the mixture of gases behaves ideally and the specific heats, molecular weights and molecular diffusivities are assumed equal for each species. A one-step irreversible stoichiometric chemical reaction with stoichiometric coefficient, $\lambda$, is assumed

$$1 \text{ kg fuel} + \lambda \text{ kg } O_2 \overset{k_{\text{rate}}}{\rightarrow} (1+\lambda) \text{ kg products} \tag{2.9}$$

Kinetics are controlled by a second-order (two molecules participating in the reaction) Arrhenius equation with reaction rate constant, $k_{\text{rate}}$,

$$k_{\text{rate}} = A \exp\left(-\frac{E}{RT}\right) \tag{2.10}$$

$E$ is the activation energy and $A$ is the pre-exponential factor for the reaction. The strength of a source or sink (of energy, species, etc.) is then

$$S = \rho_g^2 k_{\text{rate}} Y_f Y_o \tag{2.11}$$

where $Y_f$ and $Y_o$ are the fuel and oxidizer mass fractions respectively, and $\rho_g$ is the gas density. Equation 2.11 captures the source at instant in time. For a real reaction each of the variables is time dependent, and thus fluctuating. Pyrolysis of the solid occurs only at the surface, with the rate given by a single zero-order Arrhenius equation.

Conservation equations for mass, momentum and reacting species are written for the fluid. For the solid phase, all that is needed is a conservation of energy relation:

$$\rho_s c_s \frac{\partial T}{\partial t} = \frac{\partial}{\partial y}\left(k_s \frac{\partial T}{\partial x}\right) + (1-r)\dot{q}_e'' \beta \exp(-\beta y) \tag{2.12}$$

with $\beta$ the in-depth radiation absorption coefficient and $r$ the surface reflectivity. The boundary condition at the heated surface (interface between solid and gas) is

$$-k_g \frac{\partial T}{\partial y} = -k_s \frac{\partial T}{\partial y} + \sigma\epsilon\left(T^4 - T_\infty^4\right) + \dot{m}'' \Delta H_v \tag{2.13}$$

and $T = T_\infty$ at the backside (unheated surface) and throughout the solid at $t = 0$. Many of the model parameters are only approximately known, thus estimated in the model.

Solving a transformed version of Equations 2.12 to 2.13 using Crank-Nicolson on a UNIVAC 1108 computer, Kashiwagi was able to show the reaction zone moves further from the surface at higher external radiant flux levels [24]. Also, the in-depth absorption of radiation was found to be important when determining the ignition delay time. Solving a similar set of equations, Tzeng [25] found that the minimum flow rate of fuel for piloted ignition was only slightly higher than the flow rate of fuel

for extinction of a steady diffusion flame.

Park and Tien [26] have assembled a one-dimensional transient model for ignition of solid fuels that includes the effects of gas phase absorption of radiation. For high external radiation fluxes, it was found that absorption of radiation by pyrolyzed fuel is one of the critical mechanisms involved in the gas phase ignition of solids. The conservation equations and boundary conditions result in a set of coupled non-linear equations which were solved with a Crank-Nicolson method.

Currently, thermal models for ignition considering the solid phase are most appropriate for engineering work. The added complexity of the more advanced ignition models can not be justified at this time. While a model with additional detail is expected to provide improved results since more of the physics are addressed, the complexity and problems associated with determining relevant properties and constants may reduce the usefulness as an engineering tool. Realistically, ignition of solid phase fuels will occur in an atmosphere that is not yet vitiated. The chemical kinetics of the gas phase reaction are generally not the limiting process for ignition, but instead the solid phase heating and volatile generation usually control the reaction. As a result, for most modeling work, a simple thermal model will provide results nearly as accurate as more detailed models.

## 2.3 Flame Spread

The focus of this section is the spread of flame on solid surfaces, principally upward flame spread, since it can, and does, result in large spread rates that promote rapid fire growth over furniture. For each physical type of fire spread, a dominant mode of heating can be identified that will allow significant simplifications in treating the problem theoretically. While convection, conduction and radiation are present in any spreading fire, it will be shown that they contribute differently to the forward heat flux necessary for sustained spread. Many theoretical approximations of flame spread consider only a single type of heating for a given flame spread mode as required to make a solution convenient and to allow simplification of the problem. One of the goals of the current project is to provide a model for flame spread that will include a thorough consideration of heat transfer necessary to support a general treatment of the process. Such a model would be applicable to simultaneous multiple modes of spread.

In addition to thermal considerations, chemical kinetics are important during a discussion of flame spread for two reasons. First, they play a role in determining the rate at which a solid pyrolyzes, i.e. control the regression rate. For many of the flame spread models to be discussed, the solid is considered to be inert, a simplification necessary for solution of the analytical or numerical formulation. These same models, however, depend on the mass loss rate (or heat release rate) from the burning solid to determine the spread rate. Second, and probably more important, chemical kinetics control the ignition and subsequent reaction of the volatiles released from the solid surface. Classification of flame spread centers on fuel orientation (horizontal or vertical) and direction of ambient gas flow in relation to that created by the buoyancy

of the fire (concurrent or opposed).

### 2.3.1 Mechanisms Controlling Flame Spread

Concurrent flame spread occurs when a pyrolysis front on a solid travels in the direction of the bulk fluid flow above the surface. If the bulk fluid motion is the result of natural convection in an otherwise quiescent environment, then upward flame spread is considered, Figure 2.3. When an external flow (from a source other than buoyancy)

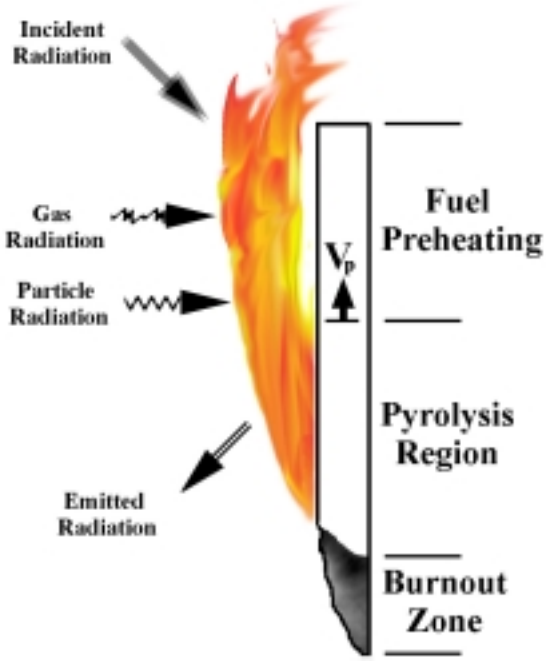


Figure 2.3: Vertical flame spread.

is applied above the surface, a forced flow condition will be assumed.

Creeping flame spread will be used to refer to the usually slower downward, lateral and horizontal flame spread, where the flow of air is induced by the flame. For opposed flow flame spread, an external velocity is imparted on the air above the surface of the fuel and the flame spreads in the direction opposite to the bulk fluid motion. Fuel concentrations further from the solid outside the flame are lean, while between the flame and solid, fuel rich conditions may be experienced.

With both natural and forced convection, the direction of flow for concurrent flame spread encourages the flame to tilt closer to the surface of the unburned fuel, which can increase heat transfer to the surface. The flux reaching the fuel surface in this case depends on the length of the flame and requires a consideration of the gas phase chemical kinetics for proper treatment [27]. While a number of papers have been presented describing experimental flame spread results, insufficient data has been published to allow for an in depth comparison between experiment and model predictions. The principle reason for the lack of experimental data on concurrent

spread is the difficulty associated with laboratory data measurement, especially for natural flow induced conditions [27, 28].

### 2.3.2 Concurrent Spread with Forced Flow

While the spread of flames within a compartment is controlled by natural convection, study of the spread of flame under a forced flow can provide insight to the process. Fernandez-Pello [29, 30] studied the spread of flame across thick sheets of PMMA under air flows of 1 to 4 $\frac{m}{sec}$ and turbulent intensities ranging from 1 to 20%. For a given forced velocity, the spread rate remained almost constant. This is thought to be a result of the competing mechanisms of flame lengthening and reduced flux reaching the surface due to flame stand-off [31]. As the forced flow velocities were increased, the flame spread rate increased almost linearly. Turbulence intensity served to increase the flame spread rate and decrease the production of products of incomplete combustion [30], while extinction was noted for velocities above 4 $\frac{m}{sec}$ [32]. Data analysis also showed that the product of the forward heat flux and the square root of the pyrolysis length, $\dot{q}''_f\sqrt{\ell_p}$, was approximately constant along the surface of the solid and varied almost linearly with flow velocity for a given turbulent intensity. Additional oxidizer in the forced flow stream increased the flame spread rate, while decreasing the concentration of CO and total unburned hydrocarbons (TUHC) in the products [30].

Schlieren photographs revealed additional entrainment and mixing of ambient air into the flame as the turbulence was increased [29, 32]. With the additional oxidizer, the reaction was completed sooner, resulting in a shorter flame. Since the forward heat flux provides the fuel preheating necessary for flame spread, a shorter flame results in a lower heat flux reaching the surface, thus slower flame spread. Any flame spread model that is intended for universal application must be able to account for effects that shorten the flame with resulting reduction in flux to the surface and flame spread rate.

Predicting soot concentrations is not as straight forward since a difference was observed with flow velocity. Unburned carbon increased with turbulence at low flow velocities, while at higher velocity soot production decreased slightly as turbulence is increased due to the enhanced reaction resulting in soot oxidation. Soot production, however, increased with additional oxygen, possibly due to a larger rate of fuel pyrolysis (a higher flux reaches the fuel surface) that is then not fully oxidized.

### 2.3.3 Concurrent Spread over Horizontal Surfaces

Zhou and Fernandez-Pello [30, 33] varied the oxygen concentration, velocity and turbulent intensity of a gas stream over thick PMMA samples to study the effect on forced flame spread rates and buoyancy. Both a ceiling and floor configuration were investigated, with the ceiling orientation being especially important since the external forced fluid flow case will give insight to the spread of flame on a ceiling exposed to a ceiling jet. To support the flame spread rate measurements, the heat flux to

the surface, the flame length, and species production were measured. Differences in spread rates were most easily explained when each mechanism was analyzed for its resulting change in forward heat flux and flame length.

The effect of stream velocity, $u_\infty$, on spread rate, $V_p$, for thick horizontal PMMA samples correlated well with

$$\frac{V_p(T_p - T_o)^2}{u_\infty(T_f - T_o)^2} = \text{constant} \tag{2.14}$$

showing that modeling the flame spread as a thermal process is expected to be possible since no gas phase kinetic effects are involved in the relation [34]. The flame spread rate was found to increase initially and then decrease with turbulence, reaching a maximum value at lower turbulence levels as velocity increased. The flame spread rate increased with oxygen concentration [35].

Buoyancy effects on ceiling flame spread were found to be dependent on flow velocity, since the heated products of combustion are pushed into a stable stratified layer against the ceiling, reducing the entrainment of oxidizer. Along with an increase in fuel pyrolysis due to the larger flux reaching the surface, a region well above stoichiometric formed near the ceiling, promoting high CO and TUHC concentrations. This trend holds as the velocity is increased to flame blow off speeds [30]. Additionally, the reduced entrainment results in a longer flame providing additional fuel preheating. At higher velocities, the increase in surface heat flux dominates, while at lower velocities, the cold wall tends to quench the reaction, as does the mixing of cool ambient air into the reaction [36]. At a given distance from the leading edge, as the velocity or turbulence intensity is increased, the mass loss also is increased [33]. As expected, for a fixed value of the turbulence intensity, the farther from the leading edge, the lower the regression rate [33].

The flat plate regression rates for laminar and turbulent flows were correlated for convective heat transfer as [33]

$$\begin{aligned} ceiling \qquad & \frac{\dot{m}''x}{\alpha\rho B} = 0.32 Re_x^{0.5}\left[1 + 1.72\left(\frac{u'}{U}\right)^{0.5}\right] \\ floor \qquad & \frac{\dot{m}''x}{\alpha\rho B} = 0.28 Re_x^{0.5}\left[1 + 3.04\left(\frac{u'}{U}\right)^{0.5}\right] \end{aligned} \tag{2.15}$$

where $\dot{m}''$ is the regression rate, $x$ is the distance on the plate from the leading edge, $\alpha$ is the thermal diffusivity of the gas (air), $\rho$ is the gas density, $B$ is the mass transfer number, $Re_x$ is the free stream Reynolds number, and $\frac{u'}{U}$ is the turbulent intensity. When flow conditions were laminar, the ceiling configuration resulted in a larger regression rate as a result of high heat transfer from the flame, but when turbulence was added, the opposite was true. The fact that the correlation worked very well for convective heating only is not surprising since the size of the solids tested were small (.3 meters long).

Generally, buoyancy is most important when velocities and oxygen concentrations are low, as shown by the more complete mixing on floor fires versus ceiling fires.

Nowhere was this more evident than in the species concentration measurements. CO and TUHC were consistently higher in the ceiling configuration due to less complete combustion as a result of less inefficient mixing. When the velocity or turbulence intensity was increased in both the floor and ceiling arrangement, concentrations of products of incomplete combustion decreased [33].

When no external velocity field is imposed, air is uniformly entrained around the perimeter of a floor fire, allowing for the creation of an axi-symmetric plume. Since the flame and plume are not tilted toward the fuel, flame radiation preheating is minimized, resulting in a slow rate of flame spread. Gas phase conduction (scale on the order of $mm$) occurs at the flame foot and depending on solid thickness, solid phase conduction both dominate the heat transfer to nonpyrolyzing fuel. The resulting forward flame flux may be insufficient to support continued spread without external heating.

### 2.3.4 Downward, Lateral and Opposed Flow Flame Spread

When the primary flow of air near a flame is in a direction opposite to the direction of flame travel, opposed flow flame spread results. Since the pyrolysis front is traveling against the bulk fluid flow making fuel preheating more difficult, the rate of propagation is much less than with upward flame spread. Figure 2.4 shows the basic mechanisms at work.

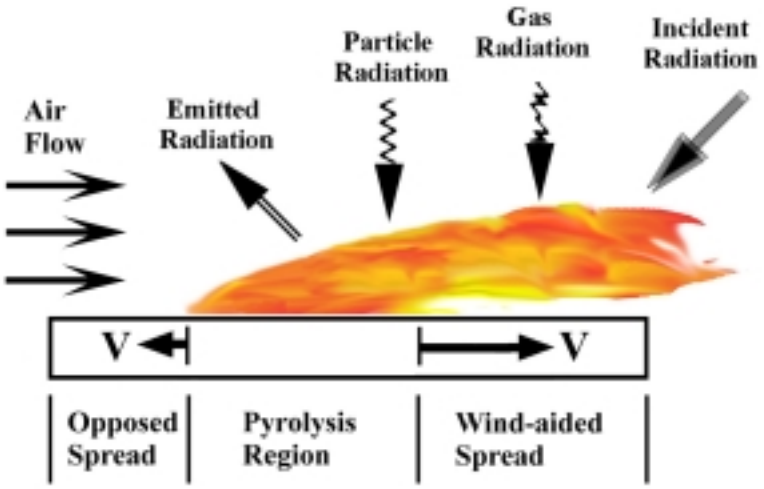


Figure 2.4: Opposed flow flame spread.

While easier to measure in the lab, opposed flow flame spread appears to be more difficult to evaluate using mathematical models. Since the overall goal of this work is to predict the rate of fire growth, opposed flow flame spread is expected to

increase the area of burning much less than upward or concurrent spread. Creeping flame spread will be used to refer to downward, lateral and horizontal flame spread, without a forced flow.

The travel rate of the pyrolysis front against the bulk fluid flow is dominated both by the rate of forward heat transfer and reaction kinetics since combustion is occurring near extinction conditions [27]. For thin solids, heat conduction in the gas phase between the flame and the solid dominates, while for thick fuels, conduction in the solid becomes more important especially as fuel thickness increases [37]. Depending on the degree of flame tilt, radiation may or may not be important based on the value of the view factor between the flame and solid. A recent review by Babrauskas shows that very little work has been done in the area of forward flame fluxes for opposed flow flame spread [38]. Horizontal spread may involve even greater reductions in radiation transfer since the flame is lifted above the surface due to buoyancy.

Fernandez covers the effect of oxygen concentration, material and fluid properties, flow velocity and external radiation on opposed flame spread in detail [27]. Upstream flow turbulence and its effect on fuel preheating and reaction kinetics have been investigated for thick and thin fuels [39, 40]. For a given velocity, an increase in the turbulent intensity decreases the pyrolysis front velocity and is attributed to convective cooling of both fuel and gas due to increased mixing and shortening of the flame. A different result than found for upward spread.

From the previous discussion, the challenges to modeling flame spread are more clear. Pyrolysis as a function of heating depends on the calculated forward heat flux that is controlled by local flow conditions and the rate of reaction.

## 2.4 Thermal Flame Spread Models

In looking at vertical fuels, upward flame spread is usually very rapid due to preheating and must be accurately predicted during modeling for enclosure lining materials. It is not until close to flashover that horizontal and downward forms of spread become important. Such is not the case with furniture. While spread up the seat back can rapidly involve a large area, the pyrolysis front usually moves across the seat and down the sides early in the fire. Any attempt to predict the growth of fire on furniture necessitates inclusion of multiple flame spread mechanisms. More complete reviews of flame spread are available in the literature [41, 42].

Heat transfer during upward flame spread is principally the result of radiant preheating of the fuel surface from the flame and buoyant plume. The net forward heat flux to the fuel that has yet to ignite, $\dot{q}''_f$, is critical in determining the rate of flame spread in an upward configuration. At the same time, it proves very difficult to predict, resulting in many of the differences seen with the following models. Figure 2.5 presents the principle features of the upward flame spread problem. Evaluation of the forward heat flux proves even more difficult for non-concurrent modes of flame spread. A radiation only solution is not usually sufficient. Depending on flow velocity, fuel thickness and orientation, gas and solid phase conduction can not be neglected.

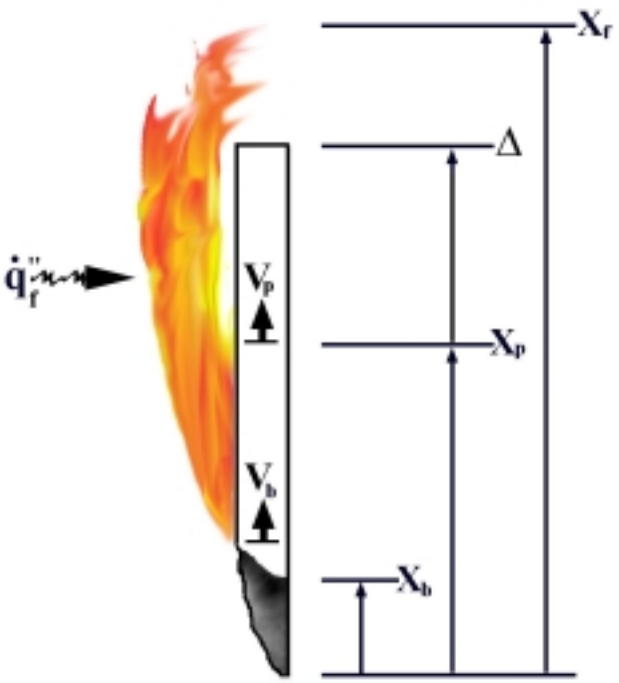


Figure 2.5: Upward flame spread model.

A significant amount of effort has gone into development of exact analytical solutions for upward flame spread, with no generally applicable solution published to date.

Most thermal models differ only in the method of determining forward heat transfer and solution. Using a firepoint temperature, a thermal model of flame spread will usually determine the pyrolysis front velocity as the rate at which the surface of the fuel ahead of the front can be heated to some critical temperature. For a constant heat flux exposure to a thermally thick solid over a heating distance, $\Delta$, an energy balance at the surface of a solid gives the pyrolysis front velocity

$$V_p = \frac{dx_p}{dt} = \frac{(\dot{q}''_f)^2 \Delta}{k_s \rho_s c_s (T_p - T_s)^2} \tag{2.16}$$

while for the thermally thin case

$$V_p = \frac{dx_p}{dt} = \frac{\dot{q}''_f \Delta}{\rho_s c_s \delta_s (T_p - T_s)} \tag{2.17}$$

with $\delta_s$ taken as the thickness of the solid in the thin case, $T_s$ the solid surface temperature, and $T_p$ the pyrolysis temperature at the flame front [42].

While the thermal models to be discussed serve as very adequate engineering approximations to a complicated problem, as conditions approach extinction, chemical kinetics increase in importance and should be included in a complete analysis [27]. This limitation of thermal models should be kept in mind during the following discussion. As the fluid and solid geometries become more complex, application of

many of these models proves more difficult, if not impossible.

### 2.4.1 Submodels

Many thermal flame spread models use the same basic approximations to allow derivation of a closed form solution. Without detailed combustion modeling, it is not possible to know exactly where the fuel produced by a pyrolyzing surface is going to burn, complicating the prediction of flame heights. Empirical correlations for flame height in the form of power laws relating heat release rate per unit width to flame height for wall fires have generally been successful. Once the flame location is obtained, the flux over the yet ignited fuel from the flame provides the boundary condition for solid heating based on heat conduction calculations. When ignited, the mass pyrolysis rate from the fuel is necessary for determining the rate of heat release. A discussion of these submodels will follow.

#### Power Law Relations for Flame Height

Most of the current flame spread models that do not include chemical kinetics or combustion rely on some form of power law to relate flame height or pyrolysis front location with time. Experimental evidence supports a relation between flame tip length, $\ell_f = x_f - x_p$, and pyrolysis length, $\ell_p = x_p - x_b$,

$$\ell_f \propto (\ell_p)^n \tag{2.18}$$

where n was found to vary from .33 to .781 for cotton fabric and PMMA sheets [43, 44]. Power law relations for velocity have also been found to fit experimental data well using

$$V_p \propto (\ell_p)^n \tag{2.19}$$

where n ranges from $\frac{1}{2}$ to $\frac{2}{3}$, with the latter being the more common value reported in the literature [43]. It is argued that since the experimental data is fit well by these simple power law relations, heat transfer from the flame to solid is the controlling mechanism regulating the flame spread rate [27].

The time for the pyrolysis front to travel from its current location, $x_p$, to the location of the flame tip, $x_f$, is defined as the preheat time, $\tau$. The distance traveled is then equal to the height of the flame, $\ell_f = x_f - x_p$. The burnout time, $\tau_b$, is defined similarly as the time required for the burnout front to travel from its current location to the pyrolysis front, $\ell_b = x_p - x_b$.

Upward flame spread velocities are frequently based on a distance traveled divided by the preheat time, $V_p \propto \frac{x_f - x_p}{\tau}$. When the flame height is correlated by $\ell_f \propto (\dot{Q}')^n$, velocity can be determined as

$$V_p \propto \frac{(\dot{Q}')^n}{\tau} \tag{2.20}$$

Unfortunately, significant differences in the prediction of extinction or acceleration

result based on the selected value of the power law coefficient [45]. For values of $n < 1$, flame spread will eventually lead to extinction, while for $n = 1$ (a value typically used with analytical solutions) the flame front will accelerate for $t > 0$. Using the models of Saito [46] and Karlsson [47], Thomas shows that including burnout can lead to indefinite propagation for $n < 1$ values.

Many compartment fires spread at conditions near extinction, yet these are the situations where power law relations begin to break down [27]. While a power law relation may be satisfactory to predict spread on a wall in the open or in the lower levels of a compartment, the local oxygen concentration must be considered when modeling flame spread and surfaces located within a vitiated upper layer. These are exactly the conditions most interesting to the fire protection engineer.

### Wall forward heat flux

A rigorous theory of flame spread will have the forward heat flux as a dependent variable, calculated based on local conditions. In the formulation of an upward flame spread model, Kulkarni [41] considers determination of the net forward heat flux to be the most challenging part of the problem. Direct substitution of experimental data has been attempted, along with a multitude of different theoretical treatments.

The upward spread of flame on 1.2 meter high samples was measured by Kim and Kulkarni to allow formulation of a correlation for the forward heat flux that can be used in models of upward flame spread [48]. The performance of four wall materials (PMMA, black PMMA, cardboard and particle board) was combined into a general relation for the exponential decay in forward heat flux as a function of height and time. Starting with the flux at the pyrolysis front, $\dot{q}''_{fo}$, the decrease toward the flame tip is given by

$$\dot{q}''_f(x) = \dot{q}''_{fo} \exp\left[c_o \left(\frac{x - x_p}{x_f - x_p}\right)\right] \tag{2.21}$$

with $c_o = -0.693$ when $\dot{q}''_{fo} = 25\ \frac{\text{kW}}{\text{m}^2}$ is used as recommended by Quintiere [49]. To improve the correlation, $\dot{q}''_{fo}$ was treated as a material property with values calculated for each sample ranging from $\dot{q}''_{fo} = 25.6\ \frac{\text{kW}}{\text{m}^2}$ for particle board to $\dot{q}''_{fo} = 34.6\ \frac{\text{kW}}{\text{m}^2}$ for PMMA. Over wall heights typically found in compartments (2.4 meters), Kulkarni found that $\dot{q}''_f(x)$ did not change significantly with height, which supports the use of constant $\dot{q}''_{fo}$ values, although $\dot{q}''_{fo}(x_p)$ could be used if data is available [48].

### Wall Heat Transfer-Conduction

One-dimensional transient heat conduction in the solid is usually used to calculate the surface temperature for ignition prediction:

$$\frac{\partial T}{\partial t} = \alpha \frac{\partial^2 T}{\partial y^2} \tag{2.22}$$

with initial condition $T(y,0) = T_\infty$, and boundary conditions for the exposed $-k\frac{\partial T}{\partial y} = \dot{q}''_f$ and unexposed $-k\frac{\partial T}{\partial y} = h(T - T_\infty)$ surfaces. The flame heat flux to the wall, $\dot{q}''_f$, may or may not be a function of time or location. The surface temperature is usually assumed to remain at $T_{ign}$ once ignition occurs. For thicker slabs when lateral and opposed flow flame spread are important, two or three dimensional calculations may be necessary to capture longitudinal conduction [48].

**Local Mass Loss Rate**

A significant number of relations based on theory and experiment for mass loss rate from solids are available. The following discussion will focus on wall fires almost exclusively, since less literature exists for furniture materials [50].

Kung numerically solved a system of coupled non-linear parabolic PDE's representing the governing equations for the pyrolysis of wood [51]. Transient heating, pyrolysis and char formation were modeled assuming thermal properties dependent on degree of pyrolysis (linear variation between virgin and char properties). Convection of energy out of the solid by the mass flux of pyrolysis products, and pyrolysis following a single first order (unimolecular process) Arrhenius relation result in

$$\frac{\partial \rho}{\partial t} = -\rho_a A e^{-\frac{E}{RT}} \tag{2.23}$$

where $\rho_a$ is the density of the material that is able to pyrolyze in the solid. With the addition of an energy relation, the conservation equations were discretized (three point central difference in both time and space) and solved via Crank-Nicolson. The pyrolysis front velocity into the slab was found to be sensitive to the thermal conductivity of the char.

A numerical solution for the heat release rate of wood that includes shrinkage of the solid during pyrolysis has been developed by Parker [52]. The solid is discretized into thin slabs parallel to the surface. The mass loss rate from each slab is calculated with an Arrhenius rate equation for each component of wood (lignin, cellulose and hemicellulose). The products of pyrolysis are assumed to instantly travel through the solid with which they are in thermal equilibrium. The mass loss rate is then determined based on a finite difference solution of the energy equation for temperature and calculation of the mass retention fraction (quantity of original mass remaining) for each slab. Included is contraction of the solid during char formation (based on user supplied experimental values).

The conservation equations are discretized in both time and space, resulting in a total of sixteen parameters that need to be specified by the user to close the problem. Some are available in the literature, but the majority require material specific experimental data. As Parker points out, many of these values are not constant, but instead vary with retention fraction and temperature. Results for douglas fir match the experimental data well for both the peak heat release rate and general curve shape, but are far from satisfactory in terms of time. Results show burnout at periods well before those seen in the test data. Parker also obtained reasonable

agreement between cone calorimeter and model results for aircraft cabin panels [53].

The effects of enclosure by a compartment on the steady mass loss rate of a vertical non-charring solid have been considered by Mitler [54, 55]. An energy balance at the surface is

$$\dot{m}''\Delta H_v = \alpha(\dot{q}''_f + \dot{q}''_e) + \dot{q}''_c - \dot{q}''_{rr} + k_s\Delta T \tag{2.24}$$

where $\dot{q}''_f$, $\dot{q}''_e$, $\dot{q}''_c$, and $\dot{q}''_{rr}$ are the flame, external, convective and reradiative fluxes respectively and $\alpha$ is the solid absorptivity. Defining an effective heat of vaporization based on experimental data as

$$\Delta H_{v,eff} = \Delta H_v + \int_{T_o}^{T_s} c_p(T)dT \tag{2.25}$$

Equations 2.24 and 2.25 give the final form for the mass loss rate

$$\dot{m}'' = \frac{[\alpha(\dot{q}''_f + \dot{q}''_e) + \dot{q}''_c - \dot{q}''_{rr}]}{\Delta H_{v,eff}} \tag{2.26}$$

A total of 14 parameters are necessary for solution, derived from the literature [56]. The compartment effects are included by summing the contributions from each zone (upper and lower). Comparison with wall fire data of Steckler was found to be very good initially, but then broke down after approximately 1200 seconds.

### 2.4.2 Model of Markstein and deRis

Upward flame spread over thin materials, such as fabric, was studied by Markstein and deRis who report both experimental results along with a semi-empirical analysis [43]. Cotton fabric samples were mounted in frames that allowed changing the orientation of the sample with respect to horizontal and permitted ignition with an electric heating coil. When sides were added to the experimental apparatus, the flame lengthened due to diminished entrainment, increasing the fuel preheating and thus the spread velocity. The spread rate was found to increase to an asymptotic value only at distances unrealistic in most compartment fires. With the sides removed, the pyrolysis front velocity obtained a constant value in a shorter distance due to the three-dimensional behavior of the flow when compared with two dimensional flow with the sides.

The model of Markstein and deRis was developed with the forward heat flux taken to be constant from the pyrolysis front to the top of the flame and zero above the flame tip [43]. The surface is thus preheated over the pyrolysis length, $\ell_f = x_f(t) - x_p(t)$ during the time, $\tau$, between arrival of the flame and arrival of the pyrolysis front (Figure 2.5). The solid is also heated in the pyrolysis region, $\ell_p = x_p(t) - x_b(t)$, during the time after ignition and up to burnout. Experimental results support the fact that $\tau$ and $\tau_b$ generally remain constant after an initial starting period. Therefore, acceleration of the spread rate is due to an increase in the lengths $\ell_f$ and $\ell_p$. Forward

heat flux was given as a function of flame height by

$$[x_f(t) - x_p(t)]\dot{q}''_f = K[x_p(t) - x_b(t)]^n \tag{2.27}$$

with $K$ and n being experimentally determined constants (not material specific). Least squares fitting of the data showed that $n = \frac{1}{2}$ provided the best fit to the fabric data. For values $n < 1$, an asymptotic spread rate theoretically should be reached, but this proved difficult to verify experimentally.

From the discussion above, the flame length is a function of the heat release rate via the length of the pyrolyzing region [27]. The preheating of the fuel over the distance covered by the flame directly determines the rate of travel by the pyrolysis front. The flame spread process itself may not directly be controlled by gas phase chemical kinetics, but the length of the flame is. Since the flame length directly controls the spread rate through the rate of surface heating, kinetics should be considered [27]. In upward flame spread experiments on PMMA, Markstein and de Ris observed an initial laminar region over the bottom 10 $cm$ of the flame where convective heating of the fuel dominates [43]. The flame rapidly became turbulent above the laminar region where radiation controlled heat transfer to the surface. Igniter strength was found to be important only during the initial flame spread until the burnout front moved from the area heated by the igniter [57]. Preheating of samples (such as from a hot upper layer), however, resulted in sustained flame spread at higher speeds.

### 2.4.3 Model of Orloff

Orloff has supported experimental work on PMMA slabs with a theory for two-dimensional upward flame spread on thermally thick materials [44]. Again $\dot{q}''_f$ is constant below $x_f$ and zero above $x_f$, which makes an analytical calculation of $V_p$ possible. The time varying flame height was found to be a function of the pyrolysis height

$$x_f(t) = K x_p^n(t) \tag{2.28}$$

Stepwise flame spread is given for fire growth at time $t + \tau$ based on the location of the pyrolysis front at time $t$,

$$x_p(t + \tau) = K x_p^n(t) \tag{2.29}$$

If $\tau$ and $n$ are only weak functions of height $x$, then the flame spread rate, $V_p$, can be determined as

$$V_p = \frac{x_p}{t_p}\left[\frac{\ln n}{n-1}\right]\ln\left(\frac{x_f}{x_p}\right) \tag{2.30}$$

with

$$n = \left(\frac{x_p}{x_f}\right)\left(\frac{dx_f}{dx_p}\right) \tag{2.31}$$

Using the relation for time to piloted ignition of a thermally thick solid given by

Equation 2.4, the velocity of spread across a thick solid is then

$$V_p = \left( \frac{4 \ln n}{\pi (n-1)} \right) \frac{x_p (\dot{q}''_f)^2 \ln(\frac{x_f}{x_p})}{\rho_s c_s k_s (T_p - T_\infty)^2} \tag{2.32}$$

Orloff also used the time for piloted ignition of a thermally thin solid given by Equation 2.5 to derive the flame spread rate for thermally thin materials

$$V_p = \left( \frac{\ln n}{n-1} \right) \frac{x_p \dot{q}''_f \ln(\frac{x_f}{x_p})}{\rho_s c_s \delta_s (T_p - T_\infty)} \tag{2.33}$$

### 2.4.4 Models for Opposed Flow

A number of thermal models that relate the opposed flow spread velocity to the rate of fuel heating ahead of the flame have been proposed in the literature. Only a few will be reviewed here, all of which either ignore radiation or use some form of empirical result, such as a fixed fraction of the combustion energy going to radiation, for closure.

The model of deRis [58] includes the effects of the gas phase to produce a coupled solution of gas and solid phase equations over both thick and thin solid fuels. As with upward flame spread models that include gas phase effects, either the Oseen approximation or a linear velocity profile is applied for the laminar fluid flow. This limits applicability, especially for compartments. Infinite reaction rates are assumed with radiation being treated as an energy gain and loss at the fuel and flame surfaces respectively. Approximate and exact analytical solutions were derived for the thin and semi-infinite fuels. For thin fuels, an inverse relation with fuel thickness, $\delta_s$, was found

$$V_p = \frac{\pi}{4} \frac{k_g}{\rho_s c_s \delta_s} \left\{ \frac{T_f - T_p}{T_p - T_\infty} \right\} \tag{2.34}$$

while for thick fuels, velocity is independent of thickness

$$V_p = \frac{u_\infty \rho_g c_g k_g}{\rho_s c_s k_s} \left\{ \frac{T_f - T_p}{T_p - T_\infty} \right\}^2 \tag{2.35}$$

A numerical solution of the thin fuel model of deRis has been published by Bhattacharjee [59]. The SIMPLE model of Patankar was used for solution with a power law treatment for advection.

A similar model was also used by Fernandez-Pello for predicting opposed flow flame spread [39, 29]. He developed an implicit numerical solution for gas phase conservation of energy and species and coupled it to the thick solid energy transport equation. Fuel pyrolysis followed a zero order Arrhenius rate equation, so that a prescribed surface temperature was not necessary. Both Oseen and Hagen-Poiseuille velocity profiles were evaluated with the uniform velocity across the section set equal to the maximum velocity in the parabolic cross section. The advantage to user specification of the velocity cross section is that it allows a solution without including

conservation of momentum. Model results show clearly that the spread rate depends on which profile is selected for a given velocity. At a profile velocity of .1 $\frac{m}{s}$, the Oseen and Hagen-Poiseuille spread results over PMMA are .02 and .06 $\frac{m}{s}$ respectively.

Di Blasi has published one of the more detailed numerical downward flame spread models [60, 61]. Finite difference formulations for the laminar momentum, energy and species conservation equations in the gas phase are formed along with separate volatile and char relations for different solid thickness values. Convective and conductive heating is included, along with finite rate combustion kinetics predicted by a second order Arrhenius rate law. A parabolic velocity profile was assumed for the opposed flow with the maximum velocity equal to that induced naturally via gravity.

Lateral flame spread data from the LIFT apparatus was correlated by Quintiere as a function of external radiant flux, $\dot{q}''_e$, and the minimum flux for piloted ignition, $\dot{q}''_{cr}$ [62]

$$V_f^{-\frac{1}{2}} = C(\dot{q}''_{cr} - \dot{q}''_e) \tag{2.36}$$

$C$ is interpreted as a material constant equal to

$$C = \left[\frac{\pi k \rho c}{4\delta_f h_{eff}^2 (\dot{q}''_f)^2}\right]^{\frac{1}{2}} \tag{2.37}$$

$h_{eff}$ is an effective surface heat transfer coefficient, $\dot{q}''_f$ is the flame heat flux, and $\delta_f$ is the distance over which the flame heat flux acts, Figure 2.6. This relation gives the maximum flame speed and is valid at steady state when the solid heating has reached equilibrium under exposure to $\dot{q}''_e$. Both $C$ and $\dot{q}''_{cr}$ could be considered material properties to predict flame spread.

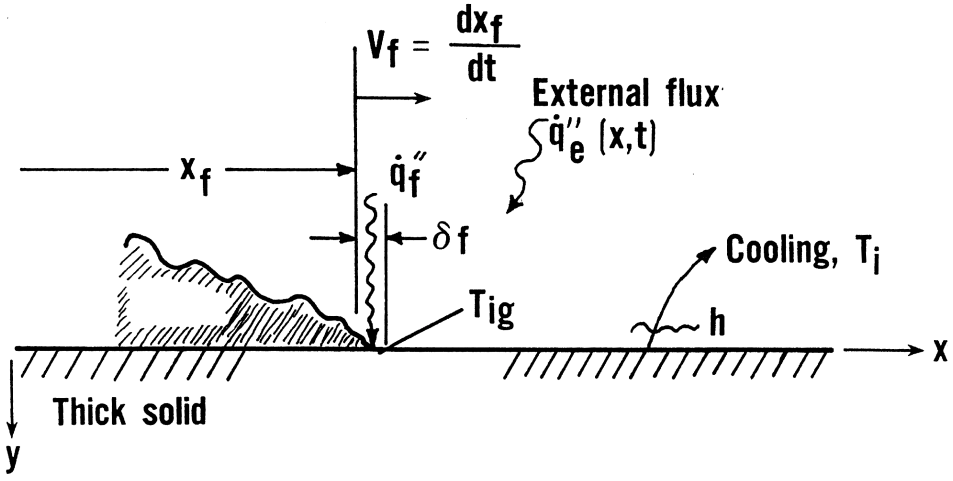


Figure 2.6: Lateral flame spread.

Standardized testing can then provide the necessary parameters, $C$ and $\dot{q}''_{cr}$, to predict the actual material flame spread [63, 64]. The experimental procedure for the LIFT apparatus is outlined in [65]. Analysis of the data produced allows the

determination of the thermal inertia, $k\rho c$, and the ignition temperature, $T_{ign}$, for a material. Computational methods are available to predict LIFT test data using the cone calorimeter [2, 66].

Keeping in mind the goal of developing an engineering tool for flame spread, the foundation for predicting the growth of fire from ignition to burnout on furniture in an enclosure will now be introduced. Simple thermal models for flame spread that do not include gas phase reactions are available, but in general prove too limiting when one considers the number of simplifying assumptions. Many of the elements necessary to generate a rigorous mathematical treatment of flame spread have been known for years [34], but have not yet been brought together in a comprehensive model. Some of the reasons why this has not occurred include difficult solution of stiff coupled non-linear PDE's, computationally intensive submodels (radiation, combustion), and problems with specification of solid phase pyrolysis boundary conditions.

# Chapter 3

# Predicting Fire Growth

Predicting the rate of fire growth on a surface requires a coupled solution for both the turbulent gas and solid phase reactions. In the fluid, conservation statements for mass, momentum, and energy are written, along with the equation of state, to provide predictions of fluid flow, velocity, pressure and temperature. The fluid flow prediction should be carried out for an entire compartment with vents and not be restricted to a boundary layer solution. Real fires are highly turbulent, and a time or mass average form of the conservation equations should be applied. The range of time and length scales for turbulence combined with limitations in computer resources necessitates some approximation for closure of the averaged conservation equations. Mixing length (zero equation) models for turbulence are not sufficient [67], but considering computational demands, a full Reynolds stress solution is an expensive option or as an alternative, two additional transport equations for turbulent kinetic energy and its dissipation rate can be solved. Such a technique is the two equation $k - \epsilon$ turbulence model that has been successful for prediction of general fluid flows.

Fire growth prediction methods that use the information on flame spread in Chapter 2 to predict fire growth on compartment linings and furniture will now be discussed. Classification models are available that use simple empirical relations based on test data to predict full scale behavior for untested assemblies. Coupling a fire growth prediction method with the results from a zone or CFD model can generate a more accurate solution. The compartment model is able to provide the necessary fluid flow boundary conditions for calculation of flame spread. Since predictions of fire growth and surface pyrolysis based on first principles are not possible for complex solids, bench scale test data are often used to provide the fuel surface mass loss rate. The scaling of small scale data to full size fuel packages is an important issue that will also be discussed.

## 3.1 Classification Models

A number of fire growth models have been developed to fit specific scenarios such as room or wall lining tests. The models rely less on physics, but instead are designed to calculate either a composite heat release rate curve or establish some pass/fail

measurement for a sample material [47]. By observing the mechanics of fire growth, empirical relations applicable to specific scenarios can be formulated. It is easily seen that classification type models do not address the physics of the process directly, so are limited to the specific configuration(s) tested. Some of these models will be reviewed briefly for the excellent insight they give to the difficulty in modeling flame spread, especially on furniture.

Data from eleven materials tested both in small scale (cone calorimeter) and large scale (standard room) were correlated using trial and error by Östman and Nussbaum [68, 69]. To predict time for a room lining material to result in flashover, $t_{fo}$, the data supported

$$t_{fo} = a\frac{\tau\sqrt{\rho}}{Q_{tp}} + b \tag{3.1}$$

with constants $a$ and $b$, $\tau$ the ignition time constant for small scale cone calorimeter testing at 25 $\frac{kW}{m^2}$, $Q_{tp}$ the total heat released during the peak heat release rate period for small scale cone calorimeter testing at 50 $\frac{kW}{m^2}$, and $\rho$ the material density. The time to flashover should be a good predictor of material behavior for many different fire scenarios and can be used for material ranking or classification. The correlation coefficient for the 11 materials was 0.96 when the lining materials where applied on two walls (corner) and the ceiling [70]. Smoke production and ranking for lining materials have also been correlated to cone calorimeter results [71].

The method was improved so that only a single cone calorimeter test at 50 $\frac{kW}{m^2}$ is necessary, while at the same time increasing the number of tested materials to 28. A correlation coefficient of 0.97 resulted when the curve fit

$$t_{fo} = a\frac{\tau^{0.25}\rho^{1.72}}{Q_{300}^{1.3}} + b \tag{3.2}$$

is used with $a = 7.159X10^{-2}$, $b = 57.4$, and $Q_{300}$ the total heat released during the peak heat release rate period (first 300 seconds) for small scale cone calorimeter testing at 50 $\frac{kW}{m^2}$. Material mass loss rate and thickness did not improve the correlation coefficient for the above relation. Similarly, the ratio of time for ignition to peak heat release rate has been used to predict the tendency for flashover of linings and furniture [72]. As the ratio becomes smaller, flashover is more likely. Petrella includes the total heat released, such that an evaluation of both $\frac{\tau}{\dot{Q}''_{max}}$ and $Q_t$ will improve the prediction since the total heat released is relatively independent of the incident flux, ventilation and vitiation, unlike the peak heat release rate which is dependent on the environment.

Karlsson has been involved in additional efforts to predict material performance based on small scale testing [47, 73]. A correlation for time to flashover in the standard room includes measurement of the exponential HRR decay, $\lambda$,

$$t_{fo} = 0.326(\dot{Q}''_{max})^{-1.14}(\lambda)^{0.085}(k\rho c)^{1.07}(T_{ign})^{2.19} \tag{3.3}$$

Parker *et al.* report on large scale testing of ten sets of furniture in the Califor-

nia Technical Bulletin 133 (TB133) and ASTM room lined with ceramic fiberboard [74]. Included is bench scale testing of the fabric and foam combinations in the cone calorimeter at a constant 35 $\frac{kW}{m^2}$ external flux. The TB133 room test is similar to the ASTM room, although slightly different in the dimensions (3.0 m by 3.7 m). One of the requirements for furniture to pass the TB133 test is that a thermocouple located above the furniture and 25 mm below the ceiling should not exceed a temperature of 110 $^{\circ}C$ during testing.

When the results of the room tests are compared with furniture calorimeter data for the same samples, the HRR measured in both the rooms and the furniture calorimeter agree very well. When peak HRR values go above 600 $kW$, enhanced burning was noticed in the rooms due to the upper layer radiation to the sample, resulting in much higher peak HRR in the rooms and less agreement between experiment and model.

The ASTM room measured HRR was used as input to HAZARDI to allow calculation of the upper layer temperature during testing. It was found that given the experimental HRR, HAZARDI was successful at predicting the upper layer temperature close to the TB133 thermocouple temperature measurement as long as the HRR remained low (furniture items should pass TB 133). For higher HRR producing furniture, the upper layer temperature predicted by HAZARDI is too low, since combustion taking place outside the compartment, but still being measured by the room hood calorimeter, is not taken into account.

Based on a series of full and bench scale testing on various residential furniture samples and mockups, Babrauskas [75] was able to correlate the peak full scale heat release rate, $\dot{Q}_{fs}$, to the heat release rate measured in the cone calorimeter, $\dot{Q}_{bs}$,

$$\dot{Q}_{fs} = 0.63\dot{Q}_{bs}\,[\text{mass factor}]\,[\text{frame factor}]\,[\text{style factor}] \tag{3.4}$$

A similar factor based prediction tool for peak HRR, total heat release, time to peak HRR and smoke production was developed during the CBUF test program for ten different upholstered furniture styles [50]. Full scale peak heat release rate, $\dot{Q}_{fs,pk}$, based on the peak HRR measured in the cone, $\dot{Q}_{bs,pk}$, is correlated with two factors, $x_1$ and $x_2$:

$$x_1 = (m_{\text{soft}})^{1.25}(\text{style factor A})(\dot{Q}''_{bs,pk} + \dot{Q}''_{300})^{0.7}(15 + t_{ign})^{-0.7} \tag{3.5}$$

$$x_2 = 800 + 500(m_{\text{soft}})^{0.7}(\text{style factor A})\left(\frac{\Delta h_c}{Q_{tot}}\right)^{1.4} \tag{3.6}$$

which are a function of the mass of upholstery materials, $m_{\text{soft}}$, the total heat released, $Q_{tot}$, and the 300 second average HRR, $\dot{Q}''_{300}$. All cone calorimeter measurements are taken during a single test at 35 $\frac{kW}{m^2}$. Almost 90% of the predictions for propagating fires ($\dot{Q}''_{\text{cone}} > 65\ \frac{kW}{m^2}$) fell within 200 $kW$ of the measured peak HRR's with no significant outlying points. Different style factors and correlations were necessary for the total heat release, smoke and time relations. Insufficient testing on chairs without frames and mattresses was conducted to permit statistically significant correlations

for these fuels.

## 3.2 Thermal Models using Bench Scale HRRs

To improve on the thermal models just discussed, empirical mass loss and heat release rate data from calorimeter testing can be used as model input. The model of Smith and that of Saito, Quintiere and Williams (SQW) have been used as the starting point for several such analytical and numerical upward flame spread efforts [47, 76, 77, 78]. Theoretical results using the model of SQW or other versions compare very well to experimental data for many different fuels. This fact, along with the benefit of almost trivial numerical solution for the resulting integral equations, has resulted in a deserved popularity for this type of model.

In general, models that include empirical HRR or mass loss rates, whether as constant, time, or flux dependent, provide a route for additional fuel specific material properties in the formulation of the model. A constant value for $\dot{Q}''$ or $\dot{m}''$ at a given incident flux level is used for input to analytical solutions of the governing equations. Curves of mass loss or energy released as a function of time using bench scale test data usually necessitate a numerical solution, although approximations such as exponential decay have been used successfully for analytical formulations.

The models discussed in this section can still be considered thermal models because they consider only energy conservation within the solid using fluxes, ignition and flame temperatures given to the model. Preferably, these should be items for which the model solves, and not specified by the user. Additionally, while chemical kinetics are not considered in the formulation of the equations, they are included approximately in the test data used for HRR. The models, however, still do not properly treat the combustion reaction, vitiation or fluid flow (where the reaction is actually taking place), thus the need for a more detailed treatment, to be discussed later.

### 3.2.1 Model of Saito, Quintiere and Williams

Upward flame spread on both charring (particle board) and non-charring (PMMA) samples was measured experimentally by Saito, Quintiere and Williams (SQW) and compared to the analytical solution of their thermal model. Vertically mounted samples were ignited at the base with a small methane gas burner that was shut off once the solid ignited. Thermocouples mounted to the sample were used to determine the location of the pyrolysis front based on a 320 $^oC$ temperature rise. The pyrolysis front on the PMMA continued upward propagation after the ignition source was removed, while sustained spread did not result on the wood sample even with continued burner application. With larger burner heat release rates, however, the pyrolysis front on wood advanced further up the sample, mainly as a result of the higher burner output.

To model the upward flame spread measured during the experimental portion of the work, SQW developed the following model for thick materials. A Volterra integral results, with the advantage of straightforward solutions both analytically

and numerically. Heat release rates for the specific fuel are input to the model based on bench scale cone calorimeter testing at a single external flux level equal to the flux from the flame to the wall in the large scale testing. The model is presented in [46], with detailed derivations found also in [47], and [77], which includes burnout.

Ignition of the vertical sample is produced by a gas burner with a heat release rate per unit width, $\dot{Q}'_b(t)$, taken as a function of time if it is not removed upon ignition. Both the burner and wall fire are considered to have flame heights that follow a power law relation, $x_f = K[\dot{Q}']^n$ discussed in Section 2.4.1. From the burner, a flame of height $x_{po} = K[\dot{Q}'_b]^n$ is produced, where $x_{po}$ is the initial pyrolyzing region. Different values of $K$ and $n$ can be used as Karlsson [47] has done to capture the specific geometry for flames in corners, under ceilings and on walls. The burner flame is assumed to heat the sample from the base to a height $x_{po}$ with a wall flux of $\dot{q}''_f > 0$ for $0 < x < x_{po}$ and $\dot{q}''_f = 0$ for $x > x_{po}$. With sufficient heating, the region from the base of the sample to $x_{po}$ will begin to burn, at which time the model considers ignition to occur, time is set to 0 seconds, and the flame spread calculations begin.

Upon ignition, each element is assumed to follow the same mass loss or HRR history as tested in the cone calorimeter at an external flux approximating the flux from the flame to solid in the preheating region. During the cone calorimeter testing, the time period from start of exposure until ignition is recorded and defined as the ignition time constant, $\tau$, for that material. Chemical kinetics are not included, so extreme rates of spread such as during vitiated combustion would not be modeled well.

An energy balance at the surface of an inert solid gives $\tau = t_{ign}$ as show in Equation 2.4. The velocity can then be found from [49]

$$V_p = \frac{dx_p}{dt} = \frac{x_p(t+\tau) - x_p(t)}{\tau} \tag{3.7}$$

Because the pyrolysis front location at time $t + \tau$ is equal to the flame front location at time $t$, Equation 3.7 becomes

$$V_p = \frac{(x_f - x_p)}{\tau} \tag{3.8}$$

where $\tau$ is assumed to remain approximately constant throughout the test. The initially pyrolyzing region from $x = 0$ to $x = x_{po}$ is assumed to burn with resulting flame height

$$x_{fo}(t) = K\left[\dot{Q}'_b + x_{po}\dot{Q}''(0)\right]^n \tag{3.9}$$

where the heat release rate, $\dot{Q}''(t)$, is taken from the calorimeter testing. For an analytical solution, a constant value or some form of mathematical approximation such as an exponential decay, $\dot{Q}''(t) = \dot{Q}''_{\max} e^{-\lambda t}$, is necessary. A numerical solution of the model allows the full time dependent curve from the bench scale testing to be input directly into the model.

A uniform flux of $\dot{q}''_f$ heats the wall from the pyrolysis front, $x_p(t) = x_{po}$, to the flame tip, $x_f$, with the heat transfer to the wall neglected above the flame tip, i.e.

$\dot{q}''_f = 0$ for $x > x_f$. The pyrolysis front location at any time after ignition is given by

$$x_p(t) = x_{po} + \int_0^t V_p(t_p) dt_p \tag{3.10}$$

where $t_p$ is a dummy variable of integration.

The corresponding flame height at any time after ignition is given by an application of Equation 2.28

$$x_f(t) = K \left[ \dot{Q}'_b + x_{po} \dot{Q}''(t) + \int_o^t \dot{Q}''(t - t_p) V(t_p) dt_p \right]^n \tag{3.11}$$

Substituting Equations 3.10 and 3.11 into Equation 3.8 results in

$$V_p(t) = \frac{1}{\tau} \left\{ K \left[ \dot{Q}'_b + x_{po} \dot{Q}''(t) + \int_o^t \dot{Q}''(t - t_p) V(t_p) dt_p \right]^n - \left[ x_{po} + \int_0^t V_p(t_p) dt_p \right] \right\} \tag{3.12}$$

An analytical solution is possible for Equation 3.12 when $n = 1$ and a suitable form of the cone heat release rate is used. For most non-charring fuels, $K\dot{Q}'' > 1$, so accelerating spread will be predicted as $\frac{t}{\tau} \rightarrow \infty$. Both $K\dot{Q}''$ and $\dot{Q}'_b$ must be considered for $K\dot{Q}'' < 1$. In most cases, this will lead to a decelerating spread with $V_p(t) \rightarrow 0$ as $x_p \rightarrow x_f$. If a large enough burner is used (such as in the room corner test), $\dot{Q}'_b$ can be sufficient to force acceleration far from the burner. For values of $n < 1$, $V_p(t)$ should decelerate until the flame front stops advancing as $x_p$ approaches $x_f$, at which time the flame height and velocity equations begin to break down. Again, if the burner is strong enough, acceleration would be observed for very long times.

Particle board was later studied by Saito [79], but this time the upward flame spread occurred with an external radiant flux. This is a more realistic picture for compartment fires where an external flux is available from a hot upper layer or adjacent burning items. Continued upward spread results, as opposed to the deceleration predicted by the model and experiments with no external heating [79]. The preheating of the sample serves to decrease $\tau$, which in Equation 3.12 increases the flame velocity.

Quintiere [49] gives an equation similar to 3.7 that can be applied for the burnout front velocity

$$V_b = \frac{dx_b}{dt} = \frac{x_b(t + \tau_b) - x_b(t)}{\tau_b} \tag{3.13}$$

and because the burnout location at time $t + \tau_b$ is the same as the pyrolysis front location at time $t$

$$V_b = \frac{x_p(t) - x_b(t)}{\tau_b} \tag{3.14}$$

If $m''_v$ is the volatile mass per unit area available for pyrolysis, then

$$\int_0^{\tau_b} \dot{m}''_v dt = m''_v \tag{3.15}$$

can be used to determine the burnout time [77].

### 3.2.2 Model of Karlsson

As part of his dissertation work at Lund University, Karlsson modified the SQW model for the prediction of upward flame spread on lining materials in compartments, with a concentration on corner tests [47, 73, 80, 81]. For an analytical solution, the heat release rate was assumed to follow an exponential decay and the flame height power law coefficient, $n$, was taken to be unity. Values for $\dot{Q}''_{max}$ and $\lambda$, the decay coefficient, are given for both the Swedish and EUREFIC lining materials [82, 83]. A value of $K = 0.015\ \frac{m^2}{\text{kW}}$ was used in the flame height correlation (to account for upper layer heating of the wall located in a standard room) instead of $K = 0.010\ \frac{m^2}{\text{kW}}$ given by [46]. A Laplace transform was performed, and the results used to describe the limits of propagation and non-propagation.

More importantly, the numerical solution of the model for lining materials in a standard room (ISO 9705) investigated two different scenarios. Testing included both lining materials on three of the four walls and three walls and ceiling. Karlsson found, as did Kulkarni, that lateral and opposed flow flame spread did not become important until close to the onset of flashover; thus these two mechanisms are not considered in the current model.

Upon heating by the burner, the lining material in the corner rapidly ignites with flame spreading out along the corners of the ceiling in what is known as a T pattern [47]. Once the wall material behind the burner is ignited and the flames reach the ceiling, an upper layer forms in the room with products of combustion flowing out the opening. For materials with a short ignition time or high heat release rate, the continued growth of fire will result in flashover. Conversely, if ignition is more difficult, significant char may decrease the HRR, or the fire may grow away from the area influenced by the burner. Briefly, the major unique components of the model are [47]

- Upper layer gas temperatures are determined to allow preheating of the lining material not yet ignited. A regression formula generates an approximate solution for the upper layer temperature in a naturally ventilated compartment fire using the method of McCaffrey, Quintiere and Harkleroad [84]

$$\frac{\Delta T}{T_\infty} = C \left( \frac{\dot{Q}}{\sqrt{gH_o}c_p\rho_\infty T_\infty A_v} \right)^{\frac{2}{3}} \left( \frac{h_k A_{\text{wall}}}{\sqrt{gH_o}c_p\rho_\infty T_\infty A_v} \right)^{-\frac{1}{3}} \tag{3.16}$$

- The effective heat transfer coefficient is given by $h_k = \sqrt{\frac{k\rho c}{t}}$, $H_o$ is the height of the ventilation opening, $A_v$ is the area of the ventilation opening, and $A_{\text{wall}}$ is the surface area of the interior combustible wall lining. The pre-exponential factor, C, was calculated to be between 3.1 and 4.05.

- The upward flame spread is calculated based on the flux from the heated upper layer and the burning walls. Radiation heat transfer between the flames in the

corner is ignored. Emission coefficients for the surfaces and flame were assumed equal to 0.5.

- Heat conduction in one wall was calculated via a Laplace transformation solution of the one-dimensional heat conduction equation for areas not heated by the upper layer. The results for one wall were then used for the other two walls along with the calculated surface temperature at a given height.

- For the ceiling and walls immersed in the upper layer, heating was assumed to be provided by the upper layer only; thus a single temperature for all of these surfaces is calculated based on a temperature difference between the wall and gas layer along with a user defined heat transfer coefficient.

The upward spread rate given by Equation 3.12 was solved numerically with the time dependent heat release rate directly from the cone calorimeter. The value of the calculated ignition time constant was modified to include the effect of material preheating resulting from the hot upper layer

$$\tau = \frac{\pi k_s \rho_s c_s (T_{ign} - T_s)^2}{4(\dot{q}''_f)^2} \tag{3.17}$$

where $T_s$ is the surface temperature calculated with the one-dimensional conduction equation. A value of $\dot{q}''_f = 35\ \frac{kW}{m^2}$ was used for the wall heat flux. The total heat release rate at a given time step, $\dot{Q}_{\rm tot}(t)$, is found from the sum of the burner, $\dot{Q}_b$, wall, $\dot{Q}''_w$, initial ceiling area, $\dot{Q}''_{co}$, and spread area, $\dot{Q}''_c$, heat release rates

$$\dot{Q}_{\rm tot}(t) = \dot{Q}_b + A_w \dot{Q}''_w(t-\tau) + A_o \dot{Q}''_{co}(t) + \int_o^{t_1} \dot{Q}''_c(t-t_p) V_p(t_p) dt_p \tag{3.18}$$

Burnout is not considered directly in the model since the base of the flame remains at $x_{po}$ throughout the model run. For lower parts of the solid, burnout is treated only in that the heat release rate tends toward zero as time advances. The model agreed quite well with experiment for most of the 22 materials modeled by Karlsson.

### 3.2.3 Model of Grant

Grant and Drysdale have investigated flame spread on packaging materials as part of the STEP (Science and Technology for Environmental Protection) project titled Major Hazards Arising from Fires in Warehouses and Chemical Stores [85, 77]. The goal of the work was an improved understanding of flame spread in warehouses, not for the usual property protection, but for evaluation of impact on the environment both from the products of combustion and suppression water runoff.

The model basically uses the formulation of SQW [46] and Karlsson [47] to predict upward flame spread on corrugated fiberboard based on heat release rate data measured during cone calorimeter testing.

A constant time for burnout, $\tau_b$, determined visually during the cone calorimeter testing can be used to allow a prediction of burnout front location and velocity for

$t > \tau_b$. Without burnout, it is usually required that the base of the pyrolysis zone be fixed to the bottom of the sample at the location of the ignition source. Grant [77] includes a form of Equation 3.12 with burnout

$$V_p(t) = \frac{1}{\tau}\left\{K\left[x_{po}\dot{Q}''(t) + \int_{t-\tau_b}^{t} \dot{Q}''(t-t_p)V_p(t_p)dt_p\right]^n - x_{po} + \int_{t-\tau_b}^{t} V_p(t_p)dt_p\right\} \quad (3.19)$$

published earlier by Kulkarni [41].

Equations 3.12 and 3.19 are integral equations of the Volterra form (second kind), where the upper limit of integration is the independent variable for time, t. A summary of the history and solution of Volterra equations is provided by Grant [85], with complete details given in Press [86].

Application of a quadrature technique, such as the trapezoidal rule, for a uniform mesh will result in a lower triangular matrix that is trivially solved by forward substitution. A non-unity value of the flame height equation exponent, n, which is supported by experimental data [46, 47, 77], complicates solution slightly by requiring the combination of a non-linear root finding technique. Brent's Method is an option in this case [86] and a forward substitution method for the Volterra equation is appropriate. Complete details on the numerical solution of Volterra equations can be found in standard texts on numerical methods [86, 87].

The first calculations by Grant resulted in a negative initial velocity. Such a physical impossibility was addressed by increasing the ignition delay time a few seconds until a positive velocity resulted. Numerical instabilities in the form of non-physical waves in the velocity versus time curves occurred and were attributed to problems in the numerical formulation of the model, and not physical reality. A smaller integration time step was required to reduce, but was not eliminate, the oscillations. It is the opinion of this author that the oscillations are a result of the initial prescription of the problem. Volterra equations are similar to initial value problems, and thus are sensitive to the starting formulation of the model. The numerical solution of the SQW model by Grant begins with the first area ignited equal to the burner flame height, $x_{po}$ (a physically unrealistic situation) and then depending on the time step, subsequent elements much smaller than $x_{po}$ are ignited. It is this initial large first element entered in the model that results in numerical instability that leads to the oscillations. Solution of the same equations, but with a small initial burning area equal to only a fraction of the burner height, produces no such oscillations and after a few time steps the final solution is found not to depend on the initial value chosen.

After the oscillations smoothed out, a steady flame spread velocity was reached. Equation 3.12 with $n = 1$ will produce the physically unrealistic scenario of continuously increasing flame spread rate, while for $n = \frac{2}{3}$, extinction is always predicted. Including burnout in Equation 3.19 results in a positive flame spread velocity that reaches a steady state. Ignoring the oscillations during the first 100 seconds of the calculations, the predicted velocities and pyrolysis front locations were in good agreement with experimental results.

A FORTRAN model was developed by Pehrson [28] to solve Equations 3.12 and 3.19 using raw heat release rate data from the cone calorimeter and user specified

geometry, material property data, and time step (basically the same formulation as Grant). The model output includes the pyrolysis and burnout front locations and velocities. The model developed includes an improved treatment of ignition by specifying the initial conditions in a physically more realistic way. The resulting output does not suffer from the numerical instabilities and unrealistic oscillations found by Grant [77] since the model is not subjected to a large initially burning region equal to the flame height of the ignition source. Instead, the first area that begins to pyrolyze upon exposure to the ignition source is only a fraction of the ignition source flame height. A real time calculation of 800 seconds was completed on a DEC 5000 in under 10 seconds of CPU time.

Clearly this and the other models based on the work of SQW suffer from the requirement that several important variables, including $K$, $\dot{q}''_w$, $T_{ign}$ and $T_f$, must be specified with the added difficulty that many of these are geometry (location) and environment specific. An additional disadvantage is that by running the cone calorimeter testing at a single flux level, the model is dependent on testing at a flux level that may not be representative of the actual conditions in the room [47]. The model is not truly scenario independent since, for example, a different flux level reaching the surface will change $\tau$ from the constant value used in the model. The integral upward spread models have shown an ability to model corner and room lining tests with relatively low computational demands. The greater variation in geometry, increased radiation heat transfer and importance of horizontal and lateral flame spread would make application of these models to furniture fires exceedingly difficult.

## 3.3 Fire Growth Incorporated in Zone Models

Zone models have been used for some time to quantify compartment conditions during a fire involving lining materials or contents such as furniture [74, 88, 89]. These cases depend on user supplied rates of heat release, usually coming from calorimeter testing, correlations or experience. No interaction between the input heat release rate and the compartment environment is normally considered. Given the rate of heat release, zone models have been shown to predict the compartment environment well, although user input based on freeburn data can not be expected to apply for vitiated conditions when approaching flashover. Piloted ignition is typically assumed, although modeling the smoldering ignition of furniture has been investigated [90].

In this section however, zone models that do consider the potential increase in fire growth due to energy feedback mechanisms of the enclosure will be discussed. While not going into many of the specifics of the equation development and solution, it is constructive to review fire growth in the context of zone modeling as a precursor to a more detailed treatment allowed by CFD.

One of the first zone models to incorporate the growth of fire was the Harvard Fire Code [91], originally a single room model, but now able to include multiple compartments. The spread of fire on a horizontal PU foam slab with a central ignition can be simulated based on a user supplied ignition temperature. A fire spread rate

parameter relates the feedback energy reaching the surface from convection and radiation to the rate of spread. The length of time the surface pyrolyzes is a function of a burnout parameter. Prediction of fire growth on other fuels is possible through fitting of fire growth rate constants [92].

### 3.3.1 Model of Smith

The model of Smith [17, 78] was one of the first models to incorporate bench scale heat release rate measurements into a compartment lining model for the prediction of fire growth, gas layer temperatures, and the rate of smoke generation. Both ignition and the instantaneous location of the pyrolysis front are determined based on the flux time product (FTP), as described in Section 2.2.4 on Page 13. The minimum flux time product for ignition, $\mathrm{FTP}_{\mathrm{min}}$, is determined from heat release rate testing at several different incident flux levels. Once ignition occurs, the heat release rate for a given element of the discretized fuel surface is based on the applied flux level and the total heat released, allowing the dependence of the HRR on external flux to be modeled. The bench scale test results at each flux level are reported as rate of heat release versus total heat released, instead of the typical rate of heat release versus time [78]. The total heat released for each control surface is monitored and coupled with the flux from the flame and gas layer to provide the HRR as a function of applied flux.

To improve the typical zone model formulation, the upper layer is divided into an upper zone comprised of the ceiling jet and plume plus a lower zone containing the remainder of the heated gases in the upper layer. The plume formed in the space between the two walls is divided into horizontal slabs of thickness $\Delta z$, termed incremental plume volumes (IPV). A corner ignition is assumed following standard room testing.

Conservation of mass, energy and momentum equations are solved for each IPV in the form of a detailed wall plume model to give the local gas temperature, composition and flux level. These calculated fluxes are based on several assumptions about flame location so that view factors and emissivities (based on local smoke concentrations) can be determined. Conduction in the solid phase is determined by a finite difference solution to the one-dimensional heat conduction equation. Venting rates through the compartment opening are determined, but with the assumption that the opening is sufficient to prevent restriction of the mass flow out the opening.

Restrictions on the model's use for ventilation controlled and post-flashover fires were removed by Sauer [93], at the expense of requiring an implicit solution. An individual oxygen balance was added for the upper zone in the hot upper layer. As a compartment approaches flashover, heat transfer to the floor becomes important, so the model was updated to include heat transfer to the floor by radiation. The conduction equations for the compartment boundaries were also changed to an implicit finite difference formulation that allows transient effects to be considered. The flow from the final IPV was also addressed by assuming a constant fraction, $\beta$, of the flow exits the room while the remainder mixes into the lower zone of the up-

per layer. Finally, lateral wall spread is considered by allowing the IPV's to widen due to horizontal flame travel, with each individual element following an independent heat release history. Model predictions matched the temperature and oxygen concentration measurements of room testing, although these values were found to be sensitive to the plume entrainment coefficient selected. The use of constants such as $\beta$, which do not have a theoretical basis for their selection, ultimately leaves determination to the user with potential for misuse. Sauer tested the model sensitivity to these adjustable constants and found that the results were relatively unchanged by all parameters except the plume entrainment coefficient.

### 3.3.2 Model of Mitler

Recent work by Mitler has looked at upward flame spread on vertical walls with and without a ceiling [94, 95]. A numerical solution for upward flame spread on a slab is provided with mass loss rates determined either by a simple steady pyrolysis rate model for non-charring materials or based on bench scale data from the cone calorimeter [55]. Actual mass loss rates for the cone calorimeter data at flux levels different than those tested are determined via a simple technique that considers local heat flux levels.

The wall is first discretized in directions both parallel and perpendicular to the surface. Flame spread is determined based on the one-dimensional thermal diffusion equation solution for the surface reaching a user defined ignition temperature during exposure to a transient flux with no diffusion of energy parallel to the surface or in-depth radiation into the solid. The exact location of the front between nodes is based on a simple average of the nodal temperatures. The most satisfactory model results were produced when flame heights were based on a $x_f \propto (\dot{Q}')^{\frac{1}{2}}$ dependence instead of the usual $x_f \propto (\dot{Q}')^{\frac{2}{3}}$ reported in the literature. With the latter, spread rates were found to change as the ignition source was increased from 1kW to 8kW, which for this size igniter is not expected based on experimental evidence. Using the square root dependence instead, spread rates were independent of igniter strength after a short initial period.

The model has been implemented as the computer program SPREAD and compared to experimental data for PMMA and particle board [96]. Upward, lateral and downward spread rates are determined along with ignition, mass loss, heat release rate and burnout based on bench scale data from the LIFT and cone calorimeter. The upper layer formed by compartmentation influences the lateral flame spread by producing a higher wall temperature in the hot gas layer. In this version of the model, the trapping of the gas layer is the only result of the ceiling. When the flux to the surface is above a critical value, lateral spread is calculated for both layers based on Quintiere [62].

Two options are available to the user for pyrolysis. First, the model can be used for non-charring, non-melting materials that do not burn through [55]. The second option can be selected based on user supplied cone calorimeter data. Mass loss from the surface is summed for each time step to determine burnout based on

fuel consumption. The final set of equations is highly coupled, and thus solved most effectively with an iterative procedure. The model SPREAD as currently implemented in a version of CFAST allows the user only the option of an upward flame spread calculation based on cone calorimeter data [96]. The pyrolysis model developed by Mitler [55], surprisingly, is not an option, although the code remains in the model to allow possible future use.

Additional work has allowed Mitler to develop a simple algorithm in SPREAD model to predict wall fire spread with a ceiling [97]. The non-vitiated hot layer is included in the coupling between SPREAD and zone model (FIRST in this case). The wall flame spread model is first run to obtain a trial value of the heat release rate that is used as input to the zone model for calculation of the upper layer temperature. The convective and radiative flux from the hot gasses in the compartment as determined by the zone model are then input to SPREAD to determine a new heat release rate that includes the preheating and resultant increase in spread rate (thus HRR). This process is repeated as many times as necessary. *A priori* assumptions based on symmetry are made about flow locations for the plume and flame at the intersections between the wall and ceiling (such as width, length and shape). Flames are assumed to follow a primary flow direction that allows calculation of the necessary view factors to account for flame tilt and spread along the intersection between the wall and ceiling.

### 3.3.3 Dietenberger Furniture Fire Model

No discussion of furniture fire growth would be complete without touching on the extensive work by Dietenberger at the University of Dayton [21, 98, 99, 100, 101, 102, 103]. The furniture fire model (FFM) was developed to be portable into zone compartment fire models such as FAST and provide the physical submodels necessary to predict the spread of fire on furniture. The FFM interfaces with FAST to receive information on the conditions in the compartment and to supply the zone model with fire source boundary conditions, using the following submodels:

**Ignition and Flame Spread Module (IFSM)** calculates the surface temperature and ignition condition of each surface element face that results in determination of the pyrolysis front location. Ignition properties are derived from a curve fit to cone data for ignition time versus external radiant flux for thermally thick materials. Evaluating the surface temperature of a thick solid with

$$T_s = T_o + \int_0^t \frac{\dot{q}_r''(t-t_p)}{\sqrt{\pi k \rho c t_p}} dt_p \tag{3.20}$$

allows for an approximate analytic solution of the form

$$T_s - T_o = \frac{\dot{q}_r''}{h_l}\left[1 - \exp\left(\frac{h_l^2 t}{k\rho c}\right)\mathrm{erfc}\left(\frac{h_l^2 t}{k\rho c}\right)^{\frac{1}{2}}\right] \tag{3.21}$$

with $h_l$ a linearized heat transfer coefficient. Ignition time, $t_{ign}$ and ignition temperature, $T_{ign}$ are used to replace the time, $t$, and surface temperature, $T_s$ in Equation 3.21. The curve fitting allows determination of $T_{ign}$ and the thermal inertia, $k\rho c$, for the thick material. A similar analysis is possible for thermally thin materials to evaluate $T_{ign}$ and the effective thermal thickness, $\rho c\delta$. Using this technique, the foam fabric assemblies tested showed intermediate behavior between thermally thick and thin.

Pyrolysis front velocity is then calculated using the net heat flux distribution from the flame over a distance, $s_e$, to determine surface heating. How to determine $s_e$ in the model is, however, unclear. Once an element temperature reaches the piloted ignition temperature, $T_{ign}$, the element is considered ignited [100] and the velocity is given by:

$$\begin{aligned} thick \qquad & V_f = \left[ \frac{\sum_k q''_k \sqrt{\frac{4s_k}{\pi}}}{\sqrt{k_s \rho_s c_s}(T_{ign} - T_s)} \right]^2 \\ thin \qquad & V_f = \frac{\sum_k q''_k s_k}{\rho_s c_s \delta_s (T_{ign} - T_s)} \end{aligned} \tag{3.22}$$

where $q''_k$ and $s_k$ are determined from a trapezoidal approximation (integration) of the flame forward heat flux with $k$ elements. The movement of the front is monitored following the motion of sides of a polygon, as shown in Figure 3.1. Equation 3.22 is

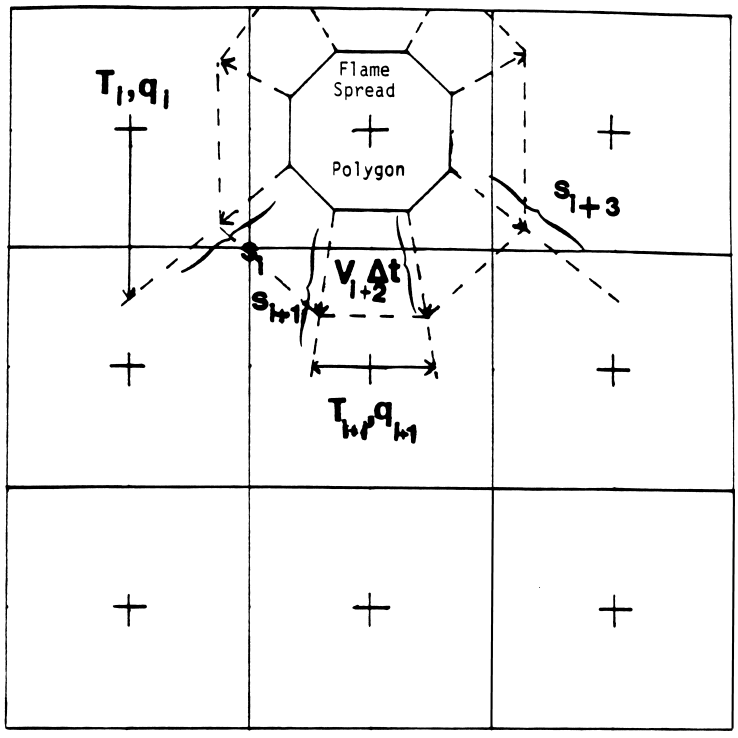


Figure 3.1: Polygon approximation to flame spread on chair [103] .

applied to all surface configurations with no consideration for lateral solid conduction heat transfer, which is instead treated with a calibration procedure that requires running the FFM first to calibrate itself. Each different surface configuration then has its own forward heat flux distribution. Opposed spread would have a different shape and strength compared to upward spread, for example.

**Flame Structure and Radiation Module (FSRM)** determines flame shape (area and height), plus calculates radiant heat transfer from surface to surface and from the flame to boundary elements. Figure 3.2 shows the surface elements generated for a representative chair. A mean beam length gray gas treatment with the Hottel

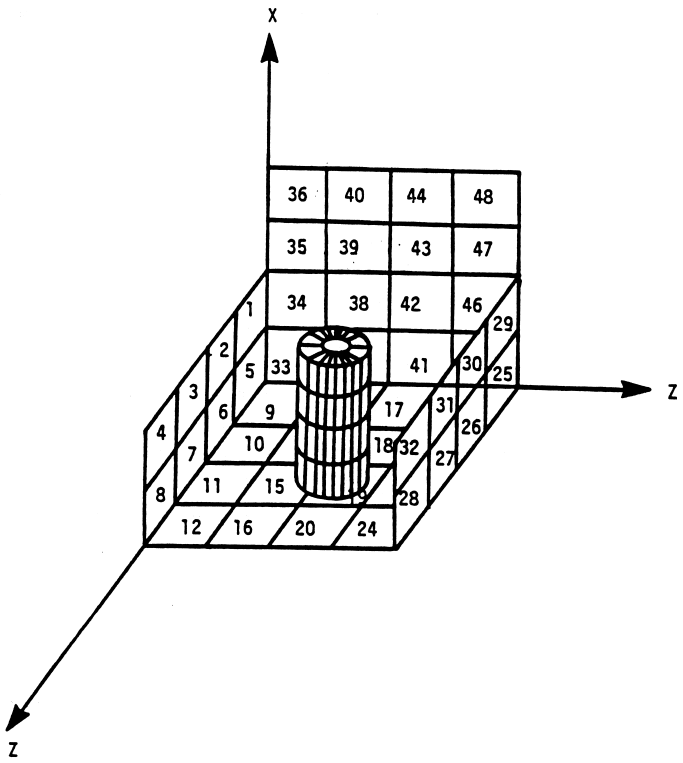


Figure 3.2: FFM Flame structure and chair elements [99] .

zonal model is used for radiation transfer with predetermined flame shapes assumed for horizontal, vertical and upside down orientations. A zonal radiation model treats radiation transfer through a non-isothermal gas volume by subdividing it into regions that can be considered isothermal (a flame-plume, upper layer, and lower layer for example). A significant amount of work has gone into determining the view factors between all of the surface elements and gases, with the flame treated as an isothermal volume. As isolated flames grow and approach each other, merging is considered approximately. Different convective heat transfer boundary conditions are specified depending on the orientation of the surface.

**Local Burning Rate Module (LBRM)** determines the local mass loss rate from the fuel surface given the pyrolysis front velocity and the net radiative flux reaching an element. Elaborate processing is necessary to adjust the ignitability and

flame spread data for non-tested flux levels and scale before they can be applied to the model. This scaling procedure is not straightforward since additional non-physically based scaling constants are introduced, which require closure. A technical review of the model is available from Beyler [104]; due to problems with the model, Beyler did not recommend inclusion of the method in the HAZARD zone model. The FFM was reviewed by CBUF, and determined not to be appropriate for inclusion in the modeling portion of the research project [50].

## 3.4 Fire Growth Incorporated in CFD Models

In the last few years, work has begun incorporating fire growth models similar to the ones used with the zone approach, but instead applying CFD to predict fire and smoke movement through the domain. The first work to be discussed involves the commercial code KAMELEON, which was used to study upward flame spread on compartment and tunnel linings. This will follow with additional work on predicting fire growth based on a non-commercial CFD code which also predicted upward spread on compartment linings. Both a full scale and $\frac{1}{3}$rd scale room corner test were modeled. A critical look at the differences between these two efforts and the current work will follow.

### 3.4.1 Model of Opstad

The first published use of bench scale tests to predict fire growth using CFD appears to be the work of Opstad [105, 106, 107]. Data used in the thermal fire growth prediction method were based on the 11 EUREFIC lining materials [82]. Additional supporting work was also carried out to obtain temperature dependent material properties from cone calorimeter testing and to develop a method of estimating cone calorimeter HRR values at untested flux levels.

The cone calorimeter was utilized first to obtain engineering values for the thermal modeling constants of the lining materials. Time to ignition measurements in the cone allowed Opstad to determine $k$ and $c$ from the one-dimensional heat conduction equation. Measurements at a minimum of two different flux levels were necessary, although more are recommended to improve accuracy.

During an exposure to the critical external flux, the incident energy at ignition is balanced by surface convection and re-radiation loss, plus conduction into the solid. Instead of treating conduction separately, it can be included in the convection term such that

$$\epsilon(\sigma T_{ign}^4 - \dot{q}_c'') + h(T_{ign} - T_\infty) = 0 \tag{3.23}$$

where values of $h$ equal to 12 and 15 $\frac{kW}{m^2\ ^\circ C}$ are used for the cone calorimeter and lift apparatus conditions respectively. To include conduction loss into the solid, a value of $h = 20\ \frac{kW}{m^2\ ^\circ C}$ was selected when using cone data. By assuming a constant emissivity, $\epsilon = 0.8$, Equation 3.23 can be solved for the experimental ignition temperature, $T_{ign}$.

A numerical solution of the 1-D conduction equation,

$$\frac{\partial^2 T}{\partial x^2} = \frac{1}{\alpha}\frac{\partial T}{\partial t} \tag{3.24}$$

was obtained with a fully implicit Crank-Nicolson scheme using boundary conditions

$$\dot{q}''_r - [\epsilon\sigma(T_s^4 - T_\infty^4) + h(T_s - T_\infty)] = -k\frac{dT}{dx} \tag{3.25}$$

at the exposed solid surface for time greater than zero, while for the back side, $-h_l(T_l - T_\infty) = -k\frac{dT}{dx}$. A heat transfer coefficient of $h_l = 10.0\ \frac{kW}{m^{2\circ}C}$ is assumed. The backside boundary condition is valid for thick materials and would need to be modified for thin materials or during long heating periods. One equation is then available to solve for the two unknowns, $k$ and the thermal inertia, $\alpha$. Studying the EURIFIC materials, Opstad found that in most cases when $0.05 < k < 1.0\ \frac{kW}{m^{2\circ}C}$, $k\rho c$ was independent of $k$, which allowed it to be specified as long as $k\rho c$ remained constant. $T_{ign}$ is then recalculated to improve the prediction.

The cone calorimeter data (HRR and burning time) can be adjusted to non-tested flux levels using an algorithm developed as part of the work based on Janssens' wood data that showed a linear relation between average HRR and burning time with irradiance level. This relation held up for all but two of the EURIFIC materials and was represented by curve fit constants (amplification factors). Opstad applied the amplification factors to the cone measured HRR curves and burning times directly, instead of just the average HRR values as done by Janssens.

The KAMELEON CFD code has been used in the past to predict fire and smoke transport on offshore oil drilling facilities. Opstad has extended its use to include lining corner fire growth in a compartment [108]. The $k - \epsilon$, discrete transfer and EDC models [109] are used for turbulence, radiation and combustion closure. Soot is modeled using the method of Magnussen [110] that has been developed for pure hydrocarbon fuels only. One equation is used to model the nucleus formation rate, while a second equation predicts the rate at which soot particles are then formed.

Gas phase and soot absorption are treated with the methods of Berge and Orloff respectively. One-dimensional heat conduction through solids is treated with temperature dependent thermal properties. The conservation equations are then solved with a finite volume formulation using a staggered grid for pressure-velocity coupling and the SIMPLE solver.

The boundary conditions on the wall lining materials are given by the flame spread algorithm using mass sources. Pyrolysis temperatures and thermal properties as a function of the heating history are determined from Equations 3.23 to 3.25 and used for input to the model. A correction factor, $\beta$, is used to account for additional flux resulting from flames above the sample surface in the cone calorimeter. This was done to make flame spread easier across the coarse mesh that was on the order of the same size as the cone calorimeter sample (.1m by .1m). In effect, this was to compensate for the coarse mesh and improve the prediction for low combustible

linings. When an element reaches the pyrolysis temperature ignition condition, fuel is allowed to flow from the surface. The rate of fuel production is based on converting the wall lining material pyrolysis products to a pure hydrocarbon (propane in this case). How the cone measured HRR is converted to a mass loss rate is not clear. The thermal flame spread model is still under development and has yet to have many of the submodels validated.

For the eleven materials tested, results were encouraging. The calculated HRR were generally overestimated for the more combustible linings, while underestimated for low combustible fuels. The strong influence on flame spread during the burner increase from 100 $kW$ to 300 $kW$ is evident in the results. Grid refinement resulted in a lower heat release rate for birch plywood. No study was done of the influence of treating soot formation as a pure hydrocarbon. The model was also used to predict combustible tunnel lining fire growth with control volumes on the order of .5 $m$ on a side. The calculated fire growth and duration of burning were greater than the experimental results.

### 3.4.2 Model of Yan

The similar corner configuration has also been modeled by Yan [111] using a code developed at Lund University. This time, the surface lining was limited to particle board, but additional modeling was conducted for a one-third scale compartment experiment. Radiation, turbulence and combustion closure were treated with the standard discrete transfer, $k-\epsilon$ and EDC models. Conduction in the fuel and walls was predicted with the 1-D diffusion equation using constant thermal properties from the literature. Constant soot yields from the literature were also used for soot generation, with absorption coefficients for $CO_2$, $H_2O$, and soot determined by the model of Modak [112] described in Section 4.4.4. A constant soot density of 1800 $\frac{kg}{m^3}$ was assumed to determine the soot volume fraction. How path lengths were determined was not discussed. Ignition was assumed for surface temperatures reaching 405 $^\circ C$.

Ignition of a given surface element releases heat using the cone data, which is converted to mass loss according to the heat of combustion. To account for the scale of the full size compartments, the cone HRR input to the model was increased by an arbitrary 20%. There was no increase for the one-third scale compartment. In addition to the use of cone calorimeter data, a solid thermal pyrolysis model that includes charring is also provided. The calorimeter data was used directly in the model, without accounting for variations in flux, while the solid pyrolysis model does have the ability to account for varied incident energy exposure.

A rather coarse grid (20X21X22) was used for the room fire experiments with elements skewed toward the corner containing the burner. Very small changes were noted by decreasing the time step from 2 seconds to 1 second. Convergence was based on residual decay and variables at monitor locations reaching asymptotic values.

Flame spread and fire growth was slower than measured experimentally with the difference growing as flashover was approached. This was determined as a possible result of downward flame spread, which was not reproduced well. Experimental tem-

peratures in the lower layer and at the interface between hot upper layer and the lower layer were underpredicted. This was thought to result from radiation effects on the value measured by the thermocouple. The measured solid surface temperatures were also higher than predicted, which was cited as another possible reason for the under prediction in fire growth. Additional problems with the radiant flux measurements were noted later in the fire. Errors in the soot treatment, temperature distribution or radiation properties were assumed possible causes. The full scale calculated HRR per unit area was well above that measured in the cone calorimeter. It appears that the calculated burning area is much smaller than expected, but when multiplied by an overpredicted HRR per unit area, the final result approximately agrees with experiment. Overall, general trends were predicted (temperature field and HRR for example), but many of the details differ and need additional study.

## 3.5 Furniture Reaction to Fire

### 3.5.1 Test Methods

The response of furniture and its components to fire can be measured with bench, full and real scale tests to quantify performance according to national and international standards. The goal of these tests is typically the generation of material fire properties that can be used for modeling, comparison and ranking.

**Bench scale** testing of furniture in the cone calorimeter involves a reduced sample size (100 $mm$ $X$ 100 $mm$) typically composed of foam and fabric covering and if included, an interliner Figure 3.3. Specimens can be tested in the vertical or more common horizontal orientation while exposed to an external radiant heat flux. Transient measurements are taken for mass loss, oxygen consumption (through which HRR can be determined), $CO$, $CO_2$, $H_2O$, specific extinction area, exhaust temperature and exhaust flow rate. Additional data can be collected in the form of gravimetric soot measurements that are useful for radiation predictions (see Section 4.4.5). Ignitability and time to ignition measurements can also be made for use in flame spread predictions. An example of data collected at three different flux levels for PU foam is shown in Figure 3.4. Accepted standards for cone calorimeter testing of materials have been generated as ASTM E 1354 [113], or ISO 5660 [114]. A review of fire testing and standards is given by Hirschler [115].

**Full scale** measurements go beyond bench scale since an entire piece of realistically constructed furniture can be burned under a large hood to gather the combustion products. Measurements similar to the cone are made using oxygen consumption calorimetry equipment located in the exhaust piping, Figure 3.5. Data gathered during testing in a furniture calorimeter can reasonably be expected to be universal, in that it will apply for fuel limited burning conditions when compartment effects are minimized. Once flashover occurs, however, changes in the burning rate due to increased radiant heating and vitiated conditions are not properly addressed. Testing is conducted under similar standardized methods such as UL 1056 [117], BS 5852 [118], ASTM E 1537 [119], or NT Fire 032 [116].

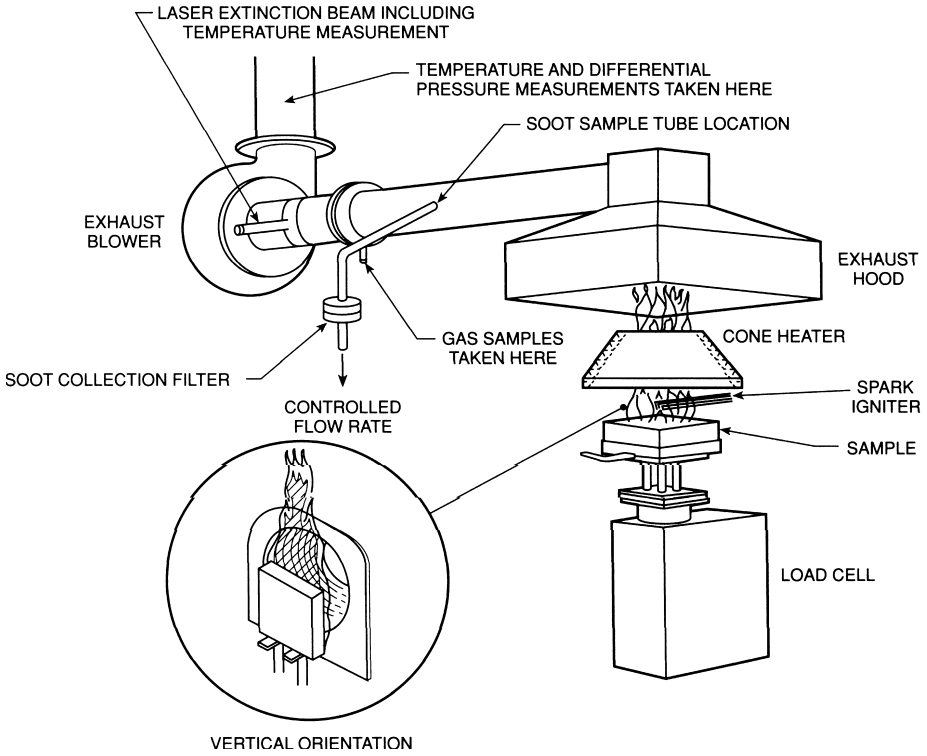


Figure 3.3: Cone calorimeter.

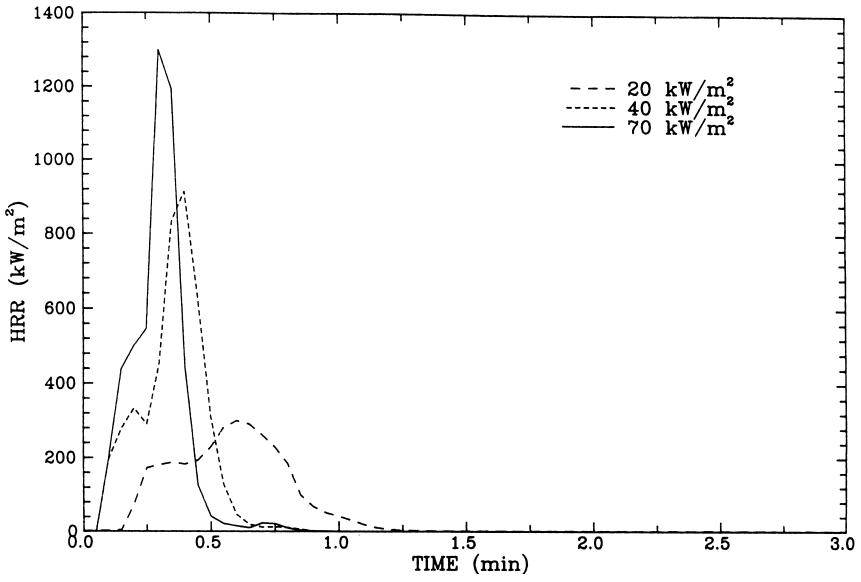


Figure 3.4: PU heat release rate as a function of external flux [2] .

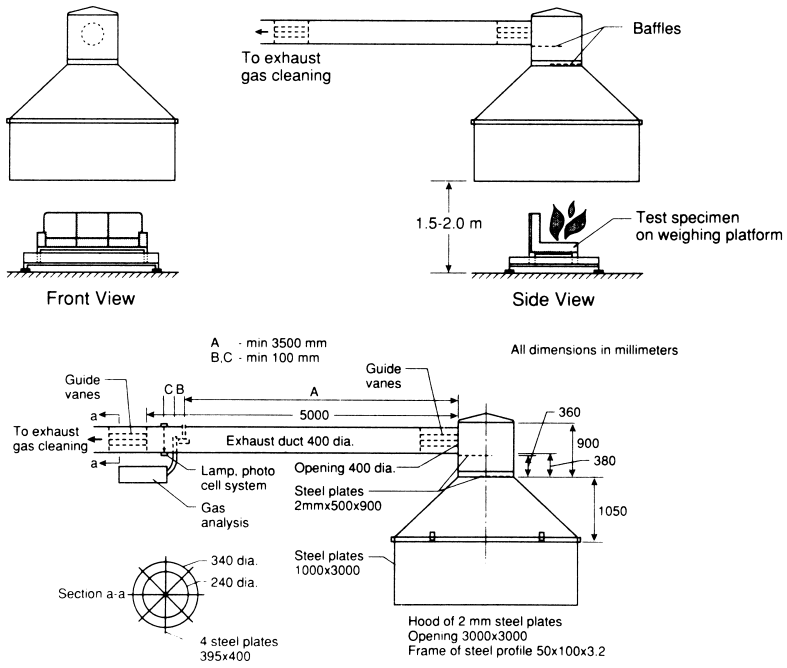


Figure 3.5: NT Fire 032 furniture calorimeter [116] .

**Real scale** tests involving furniture or mockups placed in a compartment with an opening allow for the most realistic appraisal of behavior during fire, Figure 3.6. By gathering the products of combustion with a hood above the opening, oxygen consumption methods can be applied that make the same measurements as in the cone and furniture calorimeters. Measurements made in a room calorimeter are no longer universal because specific geometry effects become important during the fire growth period.

## 3.6 Experimental Furniture Test Data

A significant amount of furniture fire test data has been gathered, but suitability for use in comparison to model predictions must be addressed. Some of the more complete and well documented test series available in the literature will be discussed here.

### 3.6.1 Furniture Component Testing

Characterization of 10 different cellular plastics exposed to a range of fire generated heat fluxes was the goal of a recent test series sponsored by the Society of the Plastics Industry [120]. A test protocol that would be an improvement over the Steiner Tunnel test for the measurement of foamed plastic fire performance was developed. The cone calorimeter and LIFT test were utilized to investigate ignition, flame spread and

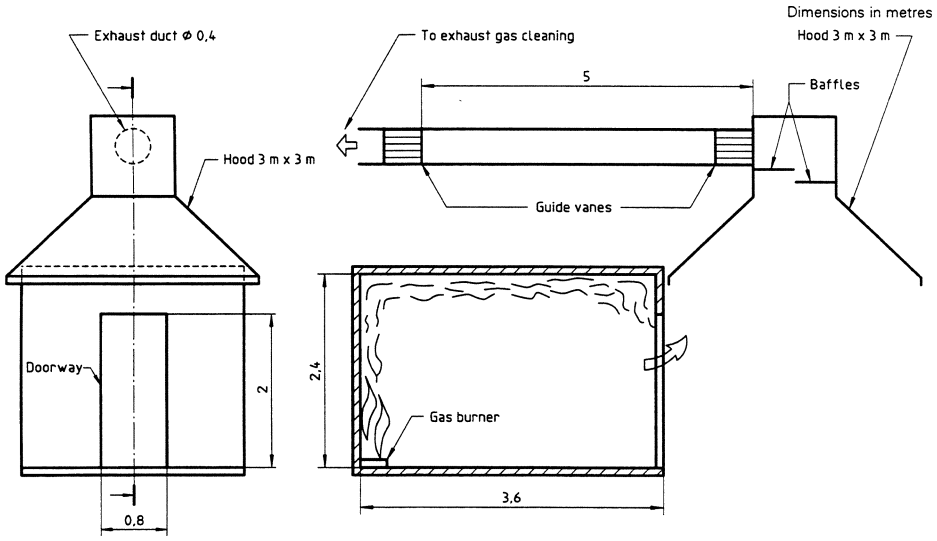


Figure 3.6: Room calorimeter [50] .

heat release rate parameters. Some of the conclusions important to the current work include:

- Ignition was found to be insensitive to apparatus (cone and LIFT) and orientation when the external flux and ambient conditions were held constant.
- Total heat released (THR) is nearly constant for a given PU foam thickness as external flux varies from 20 to 75 $\frac{kW}{m^2}$. The THR was not a strong function of external flux for non-charring fuels.
- The ignition temperature, external flux for ignition, effective thermal inertia, minimum flux for spread and minimum surface temperature for spread did not depend on PU foam slab thickness.
- When determined at the peak heat release, the heat of combustion and heat of vaporization are constants for a given material.
- Peak heat release rate was found to be nearly a linear function of irradiance.
- No recognized bench scale test is available to measure upward flame spread parameters similar to the LIFT test for lateral flame spread. The size of the sample necessary to obtain the data is well beyond bench scale since the growth rate depends on the size of the fire.
- The specific extinction area per unit mass pyrolyzed, $\sigma_m$, is not sensitive to local fire conditions. The average specific extinction area per unit mass pyrolyzed, $\bar{\sigma}_m$, varies only slightly with external flux.

Ohlemiller investigated fabric and barrier (interliner) effects tested to California Technical Bulletin 133 (TB133) for both bench scale samples in the cone and full scale mockups in a compartment [121]. Two different polyurethane foams covered with seven fabrics and four barriers were tested in a four cushion mockup arrangement. Geometry was fixed using a steel frame so that only the foam, interliner and fabric were varied. Several important conclusions can be drawn from this research:

- Thermoplastic fabrics showed a tendency to split open and expose either the foam or an interliner, if provided. Heavier polypropylene and cotton containing fabrics showed a greatly reduced rate of splitting.
- Cone calorimeter tests showed a tenting behavior of the fabric flames such that they tended to cover (merge above) both exposed and unexposed portions of the sample. Full scale cushions do not show a similar behavior since the flames are not able to cover the entire surface.
- Barrier performance can not be generalized without consideration of the specific fabric used since it appears to also be a factor of the cover fabric.
- Dimensional analysis was unsuccessful in predicting full scale peak HRR based on cone data for non-charring fabrics with an interliner.
- Foam melting in vertical cushions was a common barrier failure mechanism.

### 3.6.2 Full Scale Furniture Testing

A significant number of injuries and fatalities are the result of upholstered furniture fires occurring in residential settings [122]. During the 1970's and 1980's, fire research projects were carried out to quantify this fire risk, and have been reviewed by Babrauskas [123]. In general, most of the testing collected temperature, velocity and smoke production information for furniture packages located in compartments. Mass loss and heat release rate data were not collected, reducing the applicability for the current work and making it more difficult to use the results for other geometries. Of importance:

- Chairs with thermoplastic upholstery or foam padding tend to melt with the formation of a pool fire under the furniture.
- Chairs similar in construction, but not identical, often burned very differently. When the chairs were exactly identical, reproducibility was significantly improved.
- Burning behavior was influenced in large part by geometry.

A major early furniture flammability study was conducted at NIST (then NBS) to quantify furniture burning for the development of laboratory tests such as the furniture and cone calorimeters [123, 124, 125]. Various full size furniture mockups

and furnishings (such as wardrobes) were tested in the furniture calorimeter [126, 127, 128]. Some of the important results during the tests that varied fabric, ignition size, foam and number of cushions are:

- As the ignition source was made larger, the difference between flame retardant and non-flame retardant foams was reduced. The treated PU foam mockups burned slower, but would sometimes eventually reach maximum HRR's similar to the untreated PU foam. Olefin fabrics tend to shrink away from the ignition source and then burn at the edges, while cottons tend to char in advance of flame arrival. Cellulosic fabrics showed much better ignition resistance than the synthetics.

- The furniture frame construction did not influence surface flame spread, while the fabric covering the foam did and was a reliable indicator of overall hazard. Wood frames and related connections during fire have also been investigated [129].

- On vertical surfaces, the olefin and thermoplastic fabrics peeled away and burned on the edges with rapid involvement of the PU foam underneath. Cellulosic fabrics are slower to expose the foam padding they are covering. Large scale splitting would be an exception. Some coverings such as olefin increased the heat release over PU foam, while a heavy cotton covering reduced it.

- The fabrics that showed the strongest smoldering resistance generally showed lower open flame ignition resistance. The converse was also usually true.

- When air flowing into a room is not symmetric, a flaming fire on furniture tended to burn away from the ventilation source.

- Full scale heat release is a function of an upholstered item's combustible mass, a feature not considered by bench scale tests.

Room fire tests were completed with the same furniture fuel packages, and the furniture calorimeter reasonably predicted the flashover potential in a compartment [124]. The upholstered furniture flames appear to be of a sufficient radiative thickness to block most of the external flux generated from the compartment environment. When compartment opening conditions were changed to produce ventilation controlled burning, the room results showed a lower HRR compared to the furniture calorimeter. The furniture calorimeter, however, yields results that can be applied more generally since they do not originate in a compartment. Room fire test data, on the other hand, is much more difficult to apply to different geometries, even though the scenarios are much more like the real burning of furniture. Changing the opening size would, in effect, require a new full scale room test.

A significant amount of furniture fire research has been conducted in relation to California Technical Bulletin 133 [130]. Recent work has been reported as a series of three NIST technical reports looking at different subjects:

1. Characterization of measurements necessary to quantify furniture fire hazard that include rate of fire spread to other fuel packages, flashover potential, CO production and smoke obscuration [131].

2. Development of a reproducible ignition source to replace the crumpled newsprint that formerly was used in TB 133 [132] and showed a high degree of variability. The ring burner shown in Figure 3.7 represents a much more reproducible ignition source with a similar total energy released.

3. Testing of chairs to Technical Bulletin 133, the ASTM room and furniture calorimeter to determine the similarity in the three test methods [133]. Both the TB 133 and ASTM rooms provided similar test results. Additional quantification of the TB 133 failure criteria was also carried out.

Testing that has added to the growing TB 133 database is available from Grand [134], Forsten [135] and Damant [136]. It is hoped that these works will produce a method that will allow prediction of TB 133 results.

Many other furniture burn experiments have been reported. In general, these are less satisfactory for comparison with model results due to incomplete data, no measured HRR, and no corresponding cone calorimeter results. A review of the more significant furniture fire test programs through the years is given in Table 3.1.

A range of ignition sources (Table 3.2) have been applied to furniture items with varied strengths and locations. Ability to use large scale test data for modeling is an important consideration.

### 3.6.3 CBUF Test Series

By far, the most complete furniture fire test program is the Combustion Behaviour of Upholstered Furniture (CBUF) research effort conducted under the European Commission on Measurements and Testing. The goal was to develop standardized quantification methods to measure the fire behavior of furniture to support the harmonization of European regulations. A total of 71 room, 154 furniture and 63 lift tests were conducted. In addition, over 1200 cone calorimeter runs were carried out on both furniture composites and components. A significant number of the tests were devoted to quantify the reproducibility between labs and repeatability within the same lab. By following standardized test methods, excellent agreement was observed from the 11 laboratories involved.

The CBUF [50] test series results were obtained and evaluated for use in testing the furniture CFD fire growth routine discussed later in Chapters 5 and 6. The number and styles of furniture tested, plus the wide range of foam-fabric combinations, makes this data set ideal for model development and testing. Also possible are bench scale to furniture calorimeter to room calorimeter comparisons supported by the wide scope of the testing program. For modeling purposes though, the utility is somewhat limited by the use of a ring burner (Figure 3.7) for a majority of the full scale tests. Full scale tests were carried out on domestic residential chairs with smaller ignition

| Source | Furniture tested | Test standard | Cone data | Ignition source | Comments |
|---|---|---|---|---|---|
| Beck 1996 [137] | Chair mockup & PU slab | Room with door | No | Small igniter | Mass loss available |
| ACT-DFA 1995 [138] | Mockups | TB 133 room | Yes | TB 133 burner | 80 mockup tests |
| CBUF 1995 [50] | Commercial & mockup furn | Room, furn & cone | Yes | TB 133 burner | Large data set |
| Damant 1994 [136] | Commercial furniture | TB 133 room | No | TB 133 burner | Large data set |
| Forsten 1994 [135] | TB 133 mockups | TB 133 room | Yes | TB 133 burner | Two cushion chair |
| Grand 1994 [134] | Commercial & mockups | TB 133 room | No | TB 133 burner | |
| Hirschler 1994 [115] | Two cushion mockup | BS5852 | Yes | 8.5g wood crib | |
| Babrauskas 1993 [139] | Chairs & mattresses | TB 133 room | Yes | T head burner | |
| Parker 1991 [74, 133] | TB 133 mockups | TB 133 & furn calorimeter | Yes | TB 133 burner & newspaper | Simple geometries |
| Ohlemiller 1990 [132] | TB 133 mockups | TB 133 & furn cal | Yes | TB 133 burner | Simple geometries |
| Andersson 1985 [140] | Upholstered furniture | Room & furn cal | No | Small wood crib & pool | Spread rates smoke & flux |
| Krasny 1984 [125] | Upholstered mockups | Furniture calorimeter | Yes | Small flame | 1-6 cushions spread rate |
| Lawson 1984 [128] | Furnishings & chairs | Furniture calorimeter | Some | Square gas burner | Radiation & soot measured |
| Babrauskas 1983 [127] | Furniture mockups | Furniture calorimeter | Yes | Square gas burner | Burner flux map |
| Harkleroad 1983 [141] | PU slabs | Radiant panel | No | Pilot flame | Spread rate measured |
| Babrauskas 1982 [126] | Furnishings & chairs | Furniture calorimeter | Yes | Square gas burner | Radiation & soot measured |
| Herrington 1981 [142] | PU foam | OSU HRR apparatus | No | Gas burner | |
| Modak 1978 [143] | Square PU foam slabs | Hood with mass loss | no | Pill | Radiation & soot measured |
| Modak 1976 [144] | Mattress | Hood with mass loss | no | Pill | Radiation & soot measured |

Table 3.1: Published furniture tests.

| Igniter | Burn time (sec) | Heat output (kW) | Max heat flux $\left(\frac{\mathbf{kW}}{\mathbf{m^2}}\right)$ | Source |
|---|---|---|---|---|
| Methenamine pill | 90.0 | 0.045 | 4.0 | [145] |
| Wood match | 20.0-30.0 | 0.080 | 18.0-20.0 | [145] |
| 126g wood crib | 350.0 | 10.0 | 25.0 | [50] |
| TB 133 100g newspaper | <100.0 | 20.0-30.0 | 30.0 | [132] |
| TB 133 ring burner | 80.0 | 20.0 | $\leq$ 80.0 | [132] |
| CBUF ring burner | 120.0 | 30.0 | 30.0-40.0 (seat) 40.0-60.0 (back) | [50] |
| Polyethylene waste basket with 12 milk cartons | 200.0 | 50.0 | 35.0 | [145] |

Table 3.2: Furniture ignition sources.

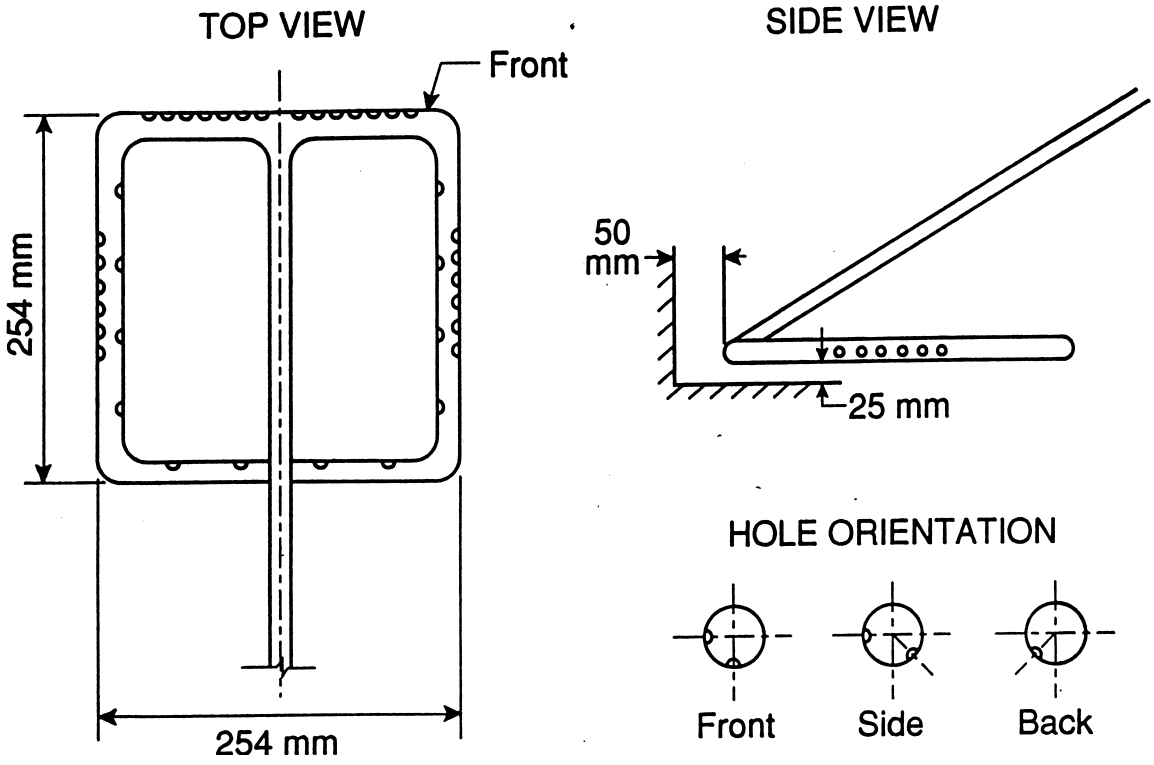


Figure 3.7: Ring burner ignition source [132] .

sources, although the complicated geometries for these fuel packages is beyond the scope of the current work. Additional small ignition sources (such as a match) were tested, but only for evaluation of full scale ignition resistance since not all tests were allowed to burn fully.

Furniture samples used for testing came from both the residential and commercial markets. To better characterize specific furniture configurations, a series of custom manufactured mockups were obtained to allow comparison of construction and material effects. This included both four cushion chairs with arms, as well as samples with only a seat and back, Figure 3.8.

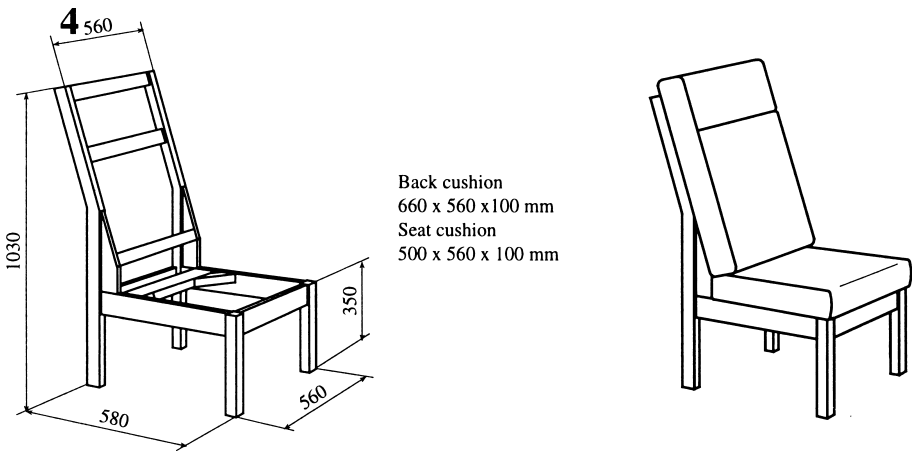


Figure 3.8: Two cushion CBUF furniture mockup [50] .

Testing and prediction procedures were developed that would allow furniture components (foam **or** fabric) to be individually tested in the cone calorimeter, and estimation made of behavior for untested composites (foam **and** fabric). With data in small scale from composite testing or a component model, real scale furniture predictions were developed for behavior in the furniture calorimeter. Open burning heat release rates measured in the furniture calorimeter, or determined from a prediction tool based on small scale test data, were used in a compartment fire model to predict real scale performance in different sized rooms.

Three different evaluation paths were developed for investigating the level of safety for the design of upholstered furniture, as depicted in Figure 3.9. When using cone calorimeter tests to evaluate real scale burning, a prediction tool was necessary to relate bench and full scale. Three such models were developed:

- **Model I** is as correlation based predictor of the peak HRR, time to peak HRR and smoke production as described in Section 3.1.
- **Model II** applies a convolution integral to estimate the burning area increase rate, $\dot{A}$, which when coupled with heat release rate from the cone calorime-

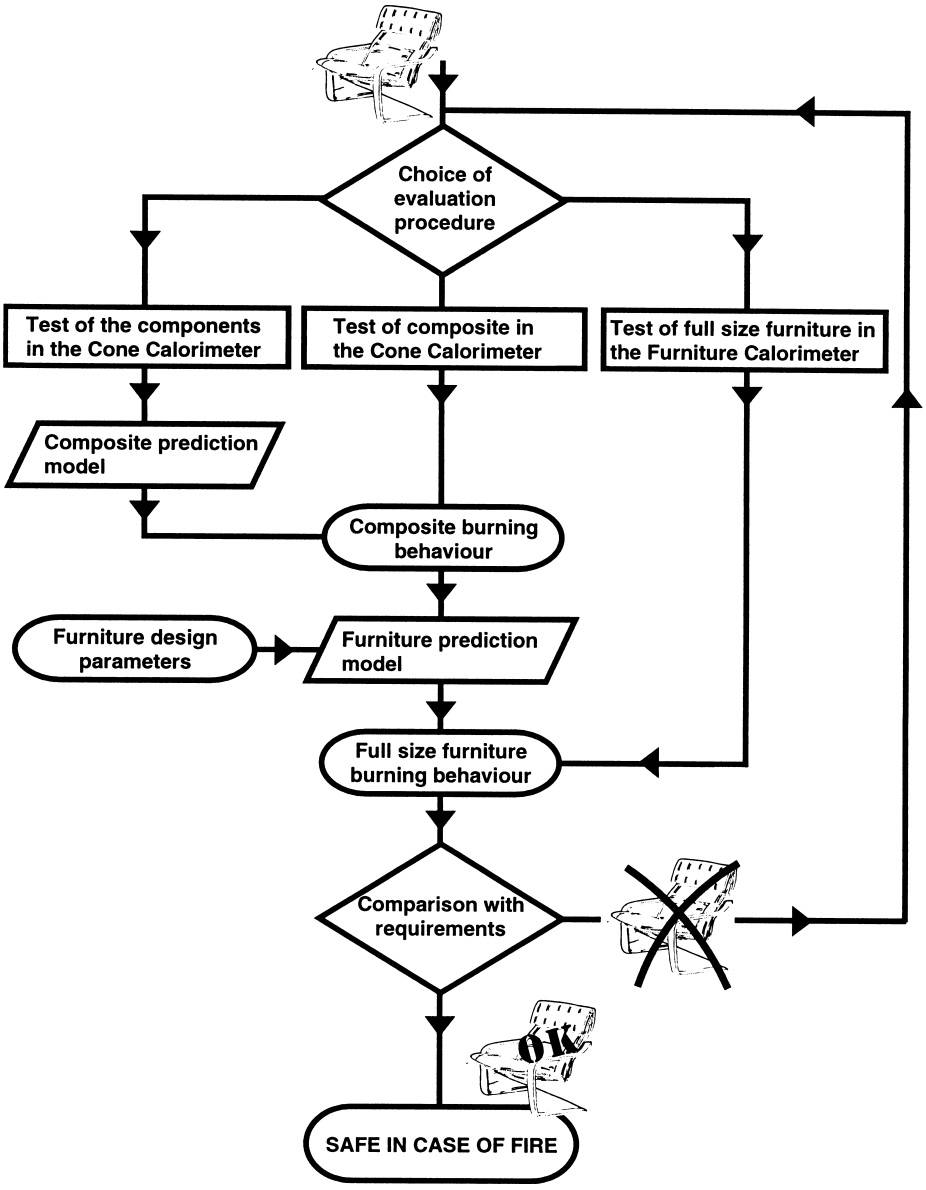


Figure 3.9: CBUF evaluation procedure [50] .

ter at a flux of 35 $\frac{kW}{m^2}$, $\dot{Q}''_{bs}(\vec{r};t)$, can predict full scale performance. Since the exact burning area is not known and exceedingly difficult to predict, $\dot{A}$ is instead an effective area that can take into consideration non-standard behavior such as pool formation, collapse, and fabric splitting. Given that the furniture calorimeter measured HRR, $\dot{Q}_{fs}$, can be described by the convolution integral of the form

$$\dot{Q}_{fs}(t) = \int_0^t \dot{Q}''_{bs}(\vec{r};t-\tau)\dot{A}(\tau)d\tau \tag{3.26}$$

$\dot{A}$ still occurs as an unknown quantity. For a specific furniture style, however, $\dot{A}(t)$, can be determined through deconvolution of Equation 3.26, since it is this increase in the burning area, when coupled with the cone calorimeter results that equals the full scale data from the furniture calorimeter. General trends were predicted, with agreement best for chairs with arms.

- **Model III** comprises the starting point in the evolution of a tool that will calculate the increase in burning area on furniture, but due to the difficulties in treating different geometries, is currently limited to mattresses. A cylindrical flame above the surface simplifies the calculation of the radiant heat flux from the flame as a function of distance, $\dot{q}''(r,t)$, and results in outward radial spread as shown in Figure 3.10. Although opposed flow flame spread is depicted,

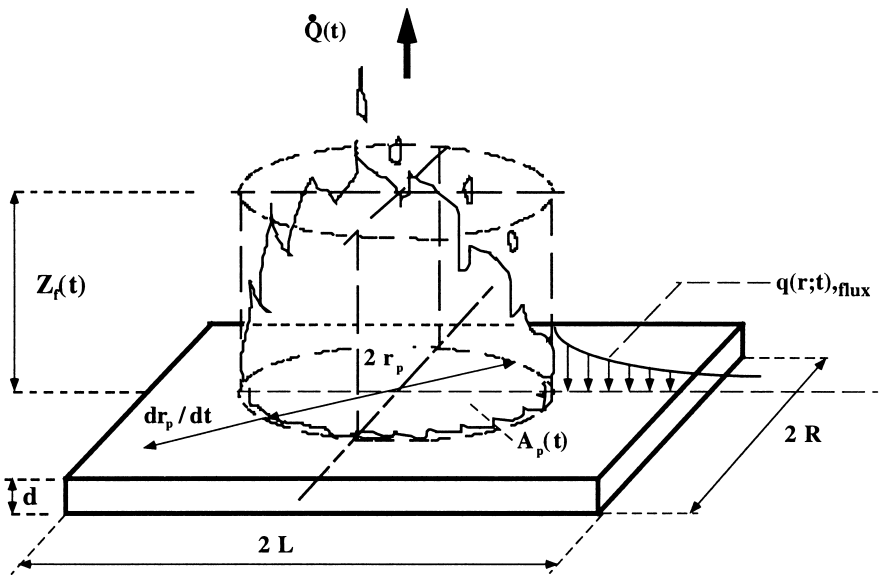


Figure 3.10: Model III geometry [50] .

the model instead treats the physical situation as upward spread with $\dot{q}''(r,t)$ constant from the flame foot, $r_p$, over the heating distance, $r_f$,

$$r_f = K(\dot{Q})^n \tag{3.27}$$

with constants $K$ and $n$ correlated to large scale data (Section 2.4.1). A heating distance divided by the ignition time determines the spread rate

$$\frac{dr_p(t)}{dt} = \frac{r_f(t) - r_p(t)}{t_{ign}} \tag{3.28}$$

The HRR from each area follows directly the cone calorimeter results at a flux of 35 $\frac{kW}{m^2}$ and allows integration over the entire surface to give the total HRR. A scaling procedure to account for materials of different thickness was developed and will be discussed in Section 3.7.

Work concentrated on evaluating performance once ignition occurs since this is when occupant safety becomes threatened. Results should be independent of the ignition source used, so the detectable fire size for the start of CBUF analysis was taken to be 50 $kW$. The HRR curves for the same furniture started with different igniters collapsed to a single curve starting at 50 $kW$, thereby removing the influence of an arbitrary ignition time on the analysis.

Tenability for occupants in the compartment of fire origin was evaluated based on upper layer location, temperature, toxic gas species concentration, visibility and radiant flux levels. A temperature difference of 100 $°C$ provided the definition for the layer height based on observations during room testing. In general, conditions in the upper layer were found to be untenable except for very short times, so it was determined that location of the interface was the principle factor to evaluate in determining survivability. Based on ISO room testing for small compartments with limited ventilation, untenable conditions could be generated before the detectable fire size of 50 $kW$ is reached. A fire safe design would require a furniture article that would not propagate fire once ignited.

## 3.7 Scaling

The use of bench scale test data requires the modeler to be able to relate the properties obtained in small scale to the real fire. To this end, a number of models that have already been described exist to predict transient burning rate from small scale data.

Babrauskas has been shown that furniture burns with approximately the same heat release rate both in the open (furniture calorimeter) and in a room calorimeter, as long the burning remains fuel limited (adequate ventilation) [124]. Furniture burns in such a way (optically thick flames with many surfaces viewing each other) that it minimizes compartment effects when compared to other combustibles, such as compartment linings. Should room fire burning become ventilation limited, measured heat release rates will be lower than found with open burning. Heat of combustion can be expected to remain relatively constant in going from the small to a full scale, as should material properties such as thermal conductivity [146].

Scale effects of the specific equipment on the measurement of ignition time and heat release rate have been studied for both horizontal and vertical solid fuel samples [2]. Ignition time was shown to decrease by 20% when sample area quadrupled from

100 $mm$ square to 200 $mm$ square. At the same time, the heat release increased by approximately 20%.

Predicting smoke production depends on the particular small scale procedure used. The NBS smoke chamber, a static smoke measurement test with collection in a box, has not been correlated to large scale smoke production [147]. The cone calorimeter, a dynamic test, has been more successful when including the amount of fuel burned in the assessment. This is embodied in the smoke parameter, SmkPar, which is the average specific extinction area multiplied by the peak heat release rate.

Values for smoke production in the furniture calorimeter were found to be half those measured in the cone calorimeter for both fire retardant and non-retardant materials [148]. A difference in $\dot{m}''$ due to flame spread effects is given as a possible reason for poor agreement. Measurements of specific extinction area show a very weak dependence on scale for smoke production when sample mass loss rates were equilibrated between bench and large scale through adjusting the bench scale irradiance [149].

As part of the EUREFIC lining studies, Heskestad looked at the ability to predict lining material smoke production in the ISO room with that from the cone calorimeter [71]. No single cone calorimeter variable was able to accurately predict full scale smoke production, although normalizing by the HRR improved the agreement. Very good agreement was possible based on a correlation including CO concentration and the time difference between the maximum HRR and $t_{ign}$.

In addition to smoke production, including the rate of mass loss through the heat release rate is necessary for an accurate assessment of the hazard from toxicity. Babrauskas has demonstrated that materials with high per gram toxic species production may, in fact, be much less hazardous than expected due to a low mass loss rate [150]. For upholstered furniture, the variation in mass loss between samples can be one or two orders of magnitude greater than the variation in toxic species yields.

Very early in a fire when plenty of oxygen is available, the CO yield depends on the specific fuel, and can be reasonably predicted with cone calorimeter results [151]. Scale may still be important since a difference is noted between CO yields measured in the cone and furniture calorimeters, with CO yields measured in the furniture calorimeter larger than the readings taken in the cone calorimeter [148]. As the fire continues to grow and oxygen falls below ambient levels, but still before flashover, there is less dependence on the specific fuel, and instead CO production can be related to the global equivalence ratio (GER), $\varphi$,

$$\varphi = \frac{\left(\frac{\text{kg fuel}}{\text{kg air}}\right)_{\text{actual}}}{\left(\frac{\text{kg fuel}}{\text{kg air}}\right)_{\text{stoich}}} \tag{3.29}$$

which represents a ratio between the mass of gas tracing its origin from the fuel in a region (upper layer for example), and the mass from the air. The ratio is then normalized by the stoichiometric ratio. Flashover can be expected by the time $\varphi = 0.3$.

For post flashover fires, it has been shown that for major toxic species except

CO, it is reasonable to assume that the species production rate in real scale is directly specified by that from the small scale test to within engineering acceptable levels [152]. The same can be said for $CO_2$, HCl, HBr, and HCN in real scale fires [148]. CO yield in the furniture calorimeter, however, did not agree with that from a full scale room, even though scale was similar between the two tests.

The rate of production of CO is directly tied to the local oxygen concentration. While CO production increases by an approximate factor of 2.5 when oxygen available for combustion goes from 21% to 14%, reducing the oxygen lower sends the CO yield up by an order of magnitude and more [152]. For predictions in vitiated atmospheres, the specific fuel is not as important, since there is significantly less variation in the CO yields between fuels when compared to the much wider difference in burning rates. The geometry and ventilation conditions important for CO during real scale testing are not addressed by the bench scale test method [153].

During the development of a furniture fire, well before flashover, species production including CO, can reasonably be expected to be scale independent. A check on the GER can provide a measure of the validity of such an assumption for CO. For engineering purposes involving conditions that are not vitiated, the rate of soot production should be weakly dependent on scale. With sufficient oxygen available, scale effects in the prediction of heat release rate will be minimized. The prediction of CO and soot production by direct application of bench scale data is admittedly tenuous, but the open burning in a furniture calorimeter will minimize the local reduction in oxygen concentrations and provide for reasonable agreement. Not taking scale into consideration when burning furniture in a compartment, however, is clearly unwarranted. Any results that depend on reduced oxygen concentrations (CO production and toxicity or soot production and flame spread) clearly must address scale. A starting point for more detailed soot and CO treatment involves including finite rate kinetics. Laminar flamelet combustion models are being developed to allow finite rate kinetics for simple hydrocarbon fuels where rudimentary combustion chemistry is understood [154, 155, 156]. For both premixed and diffusion flames, improved soot and CO production estimation can be expected.

For toxicity then, a prediction must incorporate both a measure of the production rate or mass loss and yield of species per unit mass of fuel burned. The bench scale test method used can then measure peak or transient mass loss and species yield for burning over the surface of the sample. In full scale, however, it is the increased involvement of fuel surface through flame spread that is more representative of the hazard, since it is directly related to the mass loss rate. It is this increase in pyrolyzing surface that bench scale methods, including the cone calorimeter, can not approximate because they do not account for the different flame travel speeds over materials with different compositions [150]. Geometry variations between bench and full scale complicate the picture. The current solution, according to Babrauskas, is through the use of fire modeling that can take the bench scale species production rates and couple it with flame spread predictions to provide a measure of the rate of mass loss. Problem specific geometry can also be addressed, along with detailed environmental conditions. When the cone calorimeter provides the bench scale data,

it is even possible to obtain the necessary parameters for the flame spread model prediction from the test used to gather the species production rates. The fire model then completes the loop by taking the bench scale data and incorporating details about the full scale geometry that are not addressed by the small scale test.

The use of bench scale results to predict full scale performance, either in the furniture or room calorimeter, is an important research topic. Most work involves the determination of correlations which will determine peak HRR in full scale using some form of averaging of cone results [139]. The importance of HRR is shown by the use of HAZARDI to model a single upholstered chair in a compartment [157]. A total of four scenarios were examined: a base case, doubling the HRR, doubling the toxicity of the chair materials and reducing the ignition delay time by a factor of two. Lethality was determined to be greater than 600 seconds for all cases except doubling the HRR for which death occurred in 180 seconds.

A final consideration for scaling comes from a limitation in the bench scale testing. The cone calorimeter can accept samples up to 50 $mm$ thick which is satisfactory for most compartment linings, but for foam-fabric composites, results in assemblies that are tested at a thickness different than in the real furniture. For a CMHR foam and polyester fabric, the effect of thickness on HRR is evident in Figure 3.11. The initial peak HRR due to fabric pyrolysis is generally not influenced by the sample thickness, while the later portions of the test, which represent the foam burning, show a longer period as the foam thickness increases with little change in amplitude.

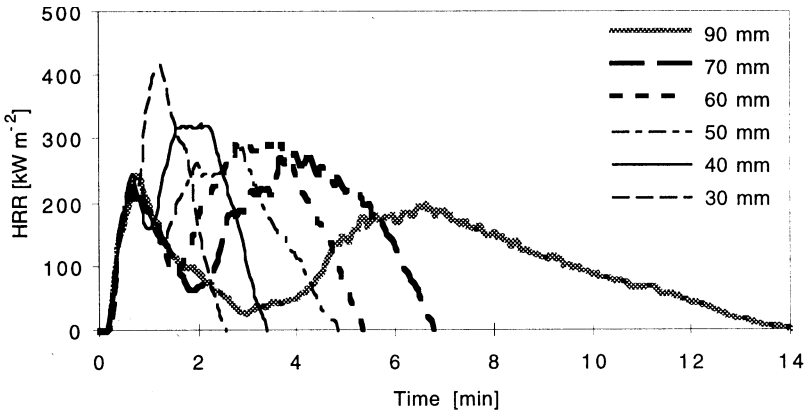


Figure 3.11: HRR as a function of composite thickness for CMHR foam and polyester fabric [50] .

A thickness scaling procedure was developed to support the CBUF furniture testing program that includes a time stretching technique to adjust cone calorimeter results to composite thickness values different than those tested. The initial portion of the curve that represents fabric burning, however, is not a function of the composite thickness and should not be scaled. For $t_o = t_{ign} + 60$ sec, if $t < t_o$, the HRR is not

scaled, while for $t > t_o$,

$$t_{scaled} - t_o = (t - t_o) \cdot \frac{\text{actual thickness in mm}}{50 \text{ mm}} \tag{3.30}$$

As shown in Figure 3.12, the approximate scaling procedure provides a reasonable adjustment to the HRR, although it fails to properly capture the trough between the fabric and foam burning portions of the test.

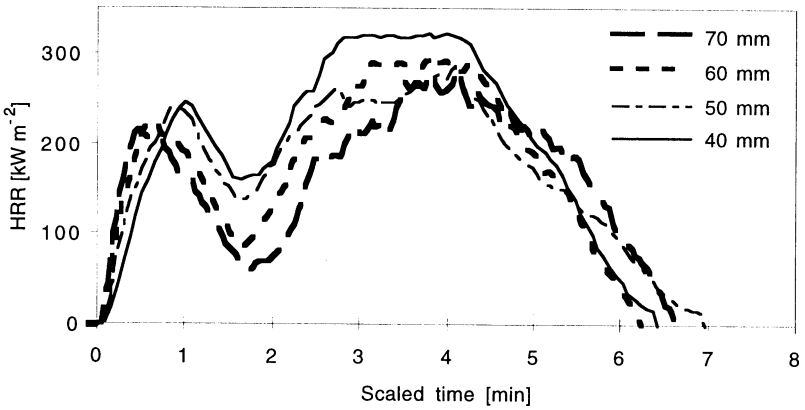


Figure 3.12: Scaled HRR as a function of composite thickness for CMHR foam and polyester fabric [50] .

A review of the tools available for predicting fluid flow, radiation transfer, combustion and multi-direction solid conduction will be presented next. This discussion will center upon the topic of computational fluid dynamics.

# Chapter 4

# Computational Fluid Dynamics

This section will highlight topics such as discretization, numerical methods, combustion and radiation heat transfer relating to computational fluid dynamics (CFD) and fire. This will not be a general review of CFD; for this the reader is directed to [23, 158, 159] for general aspects and to [4, 160] for specifics relating to fire. Instead, this section will focus on particular aspects of CFD that apply to the commercial package TASCflow [156]. The application of initial and boundary conditions will be discussed in the next section.

## 4.1 Governing Equations for Fluid Dynamics

The three basic conservation equations to be considered are

- Conservation of mass (continuity)
- Conservation of momentum (Newton's second law)
- Conservation of energy (first law of thermodynamics)

Adding equations of state will allow solution for the temperature, $T$, the pressure, $P$, the density, $\rho$, and the velocity vector, $u\boldsymbol{i} + v\boldsymbol{j} + w\boldsymbol{k}$. For the reacting flows involved with fire, equations for the conservation of species are necessary, as are relations for the transport properties such as viscosity, $\mu$, for momentum diffusion and thermal conductivity, $k$, for energy diffusion.

Index notation will be used for the presentation of many of the equations to follow. The basic rules are:

- A subscript that occurs only once in every term in an equation is a free index which represents a vector quantity.
- When a subscript appears twice in a term, this implies summation through the index range.

The governing equations will not be derived, but directly stated for completeness [156]. The differential (infinitesimally small control volume) formulation will be used and later integrated to give a finite volume formulation. The conservative form of the transport equations is particularly attractive in that global conservation can be maintained. As will be discussed in Section 4.2, it is necessary to assure that the discretized form of the conservation equations acquire a form that is also conservative.

### 4.1.1 Conservation of Mass

The continuity equation in conservation form for an infinitesimally small fluid element fixed in space is

$$\frac{\partial \rho}{\partial t} + \frac{\partial (\rho u)}{\partial x} + \frac{\partial (\rho v)}{\partial y} + \frac{\partial (\rho w)}{\partial z} = 0 \tag{4.1}$$

showing that the rate at which density in the element increases plus the mass flux through the surface of the element must equal zero (assuming no sources or sinks). With index notation, Equation (4.1) for cartesian coordinates is

$$\frac{\partial \rho}{\partial t} + \frac{\partial (\rho u_j)}{\partial x_j} = 0 \tag{4.2}$$

For compartment fires, fluid flows will be assumed incompressible ($\rho$ is constant), application of the chain rule for partial derivatives provides

$$\frac{\partial u_j}{\partial x_j} = \nabla \cdot \mathbf{V} = 0 \tag{4.3}$$

which is the simplified form of the continuity equation for incompressible flow (the divergence of velocity is zero).

### 4.1.2 Conservation of Momentum

The conservation of momentum, or momentum equation, is a statement of Newton's second Law, ($F = ma$), such that for a fixed infinitesimal fluid element, the equation of motion is

$$\frac{\partial (\rho u_i)}{\partial t} + \frac{\partial (\rho u_i u_j)}{\partial x_j} = \rho f_i + \frac{\partial \sigma_{ij}}{\partial x_j} + S_u \tag{4.4}$$

The first term on the left side is the rate of change (increase) of momentum with time in the control volume, and the second term represents the convective momentum loss per unit volume through the surface of the control volume. On the right side, the first term represents the body forces that act through the entire control volume. For our purposes, gravity will be the only body force. The next to the last term accounts for the surface forces (normal and shear forces resulting from the flow field) on a per unit volume basis and include the normal and shear stresses in the stress tensor, $\sigma_{ij}$. Momentum sources (sinks) conclude the equation.

Both normal and shear stresses make up the components of the stress tensor

$$\sigma_{ij} = \begin{pmatrix} \tau_{xx} & \tau_{xy} & \tau_{xz} \\ \tau_{yx} & \tau_{yy} & \tau_{yz} \\ \tau_{zx} & \tau_{zy} & \tau_{zz} \end{pmatrix} \tag{4.5}$$

where each stress term is located in a plane perpendicular to the direction specified by the first subscript and acts in a direction indicated by the second subscript. The diagonal terms with the repeated indices are thus normal stresses, while the six remaining off-diagonal terms represent the shear stresses. Since the stress tensor is symmetric, $\tau_{xy} = \tau_{yx}$, $\tau_{yz} = \tau_{zy}$, and $\tau_{xz} = \tau_{zx}$, only six independent terms result

$$\sigma_{ij} = \begin{pmatrix} \tau_{xx} & \tau_{xy} & \tau_{xz} \\ \tau_{xy} & \tau_{yy} & \tau_{yz} \\ \tau_{xz} & \tau_{yz} & \tau_{zz} \end{pmatrix} \tag{4.6}$$

Symmetry is required to prevent the angular acceleration for a fluid parcel from going to infinity as the volume approaches zero.

Pressure and stresses act upon the surface of the control volume resulting in a microscopic momentum flux across the surface. Assuming a linear dependence between stress and rate of strain provides a path for relating the stress terms in Equation 4.6 to the flow field for the molecular rate of transport of momentum

$$\sigma_{ij} = -p\delta_{ij} + \mu\left(\frac{\partial u_i}{\partial x_j} + \frac{\partial u_j}{\partial x_i}\right) + \delta_{ij}\mu'\frac{\partial u_k}{\partial x_k} \tag{4.7}$$

where $\mu$ is the coefficient of viscosity, $\mu'$ is the second coefficient of viscosity and $\delta_{ij}$ is the Kronecker delta which takes a value of 1 along the diagonal ($i = j$) and a value of 0 for off diagonal terms ($i \neq j$). A complete derivation with details can be found in Schlichting [161]. Equation 4.7 allows pressure and velocity terms to be related to the stress tensor for isotropic (properties do not depend on which direction they are measured) Newtonian fluids (stress is a linear function of the rate of strain or deformation).

Stoke's hypothesis can be used to reduce the number of constants from two to one. Define the coefficient of bulk viscosity, $\kappa$, as $\kappa = \frac{2}{3}\mu + \mu'$. For incompressible flows associated with compartment fires, $\kappa$ is assumed $\approx 0$, so that $\mu' = -\frac{2}{3}\mu$. Inserting this and Equation (4.7) into Equation 4.4 provides

$$\frac{\partial(\rho u_i)}{\partial t} + \frac{\partial(\rho u_i u_j)}{\partial x_j} = \rho f_i - \frac{\partial p}{\partial x_i} + \frac{\partial}{\partial x_j}\left[\mu\left(\frac{\partial u_i}{\partial x_j} + \frac{\partial u_j}{\partial x_i} - \frac{2}{3}\delta_{ij}\frac{\partial u_k}{\partial x_k}\right)\right] + S_u \tag{4.8}$$

which for incompressible flows allows the stress term to be simplified

$$\frac{\partial(\rho u_i)}{\partial t} + \frac{\partial(\rho u_i u_j)}{\partial x_j} = \rho f_i - \frac{\partial p}{\partial x_i} + \frac{\partial}{\partial x_j}\left[\mu\left(\frac{\partial u_i}{\partial x_j}\right)\right] + S_u \tag{4.9}$$

The advantage of using a momentum equation in conservation form is that global momentum conservation (no artificial sources or sinks created) can be satisfied.

With Equation 4.9, pressure does not exist as an absolute value, but instead as the gradient of pressure, $\frac{\partial p}{\partial x_i}$. Fire flows generally involve wide variations in temperature that lead to buoyancy induced flow resulting from differences in density, although the variations in density are still small compared to those expected with compressible flow. Taking the gravity term and splitting it results in

$$-\rho f_i = \rho g_i = \rho_o g_i + (\rho - \rho_o) g_i \tag{4.10}$$

with $\rho_o$ a reference density. The Boussinesq approximation then allows density variations to be neglected, except with respect to buoyancy (gravity terms). The gravity term is then taken as the second term on the right of Equation 4.10, while the first term is added to the pressure term to account for the mean density and with $\beta$ as the coefficient of volumetric expansion, $(\rho - \rho_o) g_i = -\rho_o g_i \beta (T - T_o)$.

### 4.1.3 Conservation of Energy

Applying the first law of thermodynamics representing the change in internal energy, $E$, and work, $W$, done by the addition of heat, $Q$, to a control volume

$$\frac{dQ}{dt} = \frac{dE}{dt} + \frac{dW}{dt} \tag{4.11}$$

to a fixed infinitesimal element provides the starting point for the energy equation based on enthalpy

$$\frac{\partial(\rho h)}{\partial t} + \frac{\partial(\rho u_j h)}{\partial x_j} = \frac{\partial p}{\partial t} - \frac{\partial q_j}{\partial x_j} + \rho u_j f_j + \frac{\partial(u_i \sigma_{ij})}{\partial x_j} + S_E \tag{4.12}$$

The two terms on the left hand side of Equation 4.12 represent the rate of increase in enthalpy per unit volume and the enthalpy per unit volume transferred by convection through the control surface. On the right hand side, this equals the sum of the rate of change of static pressure, heat transfer through the surface by temperature and concentration gradients, work done by body and surface forces and finally energy sources such as energy generation and radiation absorption-emission. Potential and kinetic energies for fires will be considered small (zero) when compared to the enthalpy of the fluid. The $\frac{\partial(u_i \sigma_{ij})}{\partial x_j}$ term is a dissipation function which represents the conversion of mechanical energy into heat as a result of viscous surface losses due to fluid motion. Since fire velocities are generally low, viscous dissipation can be dismissed as very small. Simplifying Equation 4.12 yields

$$\frac{\partial(\rho h)}{\partial t} + \frac{\partial(\rho u_j h)}{\partial x_j} = \frac{\partial p}{\partial t} - \frac{\partial q_j}{\partial x_j} + S_E \tag{4.13}$$

Turning to the gradient term, it represents the transfer of energy through the surface by conduction and molecular diffusion of species with different enthalpies

$$\frac{\partial q_j}{\partial x_j} = \frac{\partial q_{cond,j}}{\partial x_j} + \frac{\partial q_{diff,j}}{\partial x_j} \tag{4.14}$$

Fourier's law will be used for heat conduction,

$$q_{cond} = -k\frac{\partial T}{\partial x_j} \tag{4.15}$$

Energy exchange due to concentration gradients between n different species (Dufour effect), although small, is given for species $\alpha$ by

$$q_{diff} = -\sum_{\alpha}^{n} \Gamma_\alpha h_\alpha \frac{\partial Y_\alpha}{\partial x_j} \tag{4.16}$$

where $\Gamma_\alpha$ is the molecular diffusion coefficient, $Y_\alpha$ is the species mass fraction and $h_\alpha$ is the enthalpy of species $\alpha$. Substituting into Equation 4.13 yields

$$\frac{\partial(\rho h)}{\partial t} + \frac{\partial(\rho u_j h)}{\partial x_j} = \frac{\partial p}{\partial t} - \frac{\partial}{\partial x_j}\left[-k\frac{\partial T}{\partial x_j} - \sum_{\alpha}^{n} \Gamma_\alpha h_\alpha \frac{\partial Y_\alpha}{\partial x_j}\right] + S_E \tag{4.17}$$

The version of the energy conservation relation given by Equation 4.17 is coupled to the conservation of species through both the conduction and concentration gradient terms. Radiation can be included as a source, $S_E = -\frac{\partial \dot{q}_j^R}{\partial x_j}$, which will be discussed in more detail in Section 4.4.3.

### 4.1.4 Conservation of Species

Additional transport relations based on the continuity equation can be developed for each independent species, $\alpha$,

$$\frac{\partial(\rho Y_\alpha)}{\partial t} + \frac{\partial}{\partial x_j}\left(\rho u_j Y_\alpha\right) = -\frac{\partial J_{\alpha j}}{\partial x_j} + S_\alpha \tag{4.18}$$

with $J_{\alpha j}$ the species mass diffusion flux given by

$$J_{\alpha j} = -\Gamma_\alpha \frac{\partial Y_\alpha}{\partial x_j} \tag{4.19}$$

taking advantage of Fick's law for diffusion. Equation 4.18 is then

$$\frac{\partial(\rho Y_\alpha)}{\partial t} + \frac{\partial}{\partial x_j}\left(\rho u_j Y_\alpha\right) = -\frac{\partial}{\partial x_j}\left[-\Gamma_\alpha \frac{\partial Y_\alpha}{\partial x_j}\right] + S_\alpha \tag{4.20}$$

The diffusion coefficient can be related to the viscosity via the Schmidt number, $\sigma_\alpha$, the ratio of momentum to mass diffusion,

$$\sigma_\alpha = \frac{\mu}{\rho \Gamma_\alpha} \tag{4.21}$$

As a simplification, the Schmidt number is often assumed equal to the Prandtl number, Equation 4.26. The transport Equation 4.20 can be written for any scalar, $\phi$,

$$\frac{\partial(\rho\phi)}{\partial t} + \frac{\partial}{\partial x_j}\left(\rho u_j \phi\right) = -\frac{\partial}{\partial x_j}\left[-\Gamma_\phi \frac{\partial \phi}{\partial x_j}\right] + S_\phi \tag{4.22}$$

### 4.1.5 Equation of State

Through the conservation statements (4.3,4.8, 4.17), five equations are available to solve for the six independent primitive flow field variables, $\rho$, $p$, $u$, $v$, $w$, and $h$. If perfect gas behavior is assumed, the equation of state can be used as a sixth relation

$$p = \rho R T \tag{4.23}$$

but at the expense of introducing a seventh variable, the temperature, $T$. Using the thermodynamic relation for an ideal gas $\partial h = c_p \partial T$, temperature can be related to the enthalpy through the constant pressure specific heat $c_p$.

Additional state relationships are available to relate the thermodynamic variables to the transport constants. Sutherland's relation for viscosity as a function of temperature

$$\frac{\mu}{\mu_o} \approx \left(\frac{T}{T_o}\right)^{\frac{3}{2}} \frac{T_o + S_\mu}{T + S_\mu} \tag{4.24}$$

where $S_\mu$ is a specific constant. A similar relation can be used to approximate the gas thermal conductivity as a function of temperature

$$\frac{k}{k_o} \approx \left(\frac{T}{T_o}\right)^{\frac{3}{2}} \frac{T_o + S_k}{T + S_k} \tag{4.25}$$

Equation 4.24 provides values of $\mu \pm 2\%$ over temperature ranges found in compartment fires. With the specific heat and viscosity known, the Prandtl number relates momentum to thermal diffusivity

$$Pr = \frac{c_p \mu}{k} \tag{4.26}$$

## 4.2 Discretization

The conservation equations outlined above are formulated for a continuous domain. The first step in solving the set of non-linear PDE's is to replace the continuous formulations with algebraic approximations (differences) to the derivatives that are

evaluated at a finite (discrete) number of locations (nodes or grid points). Specifically, TASCflow uses a conservative finite volume formulation that integrates the transport equations over a volume element:

$$\frac{\partial}{\partial t}\left(\int_v \rho dv\right) + \int_s \rho u_j dn_j = 0 \tag{4.27}$$

$$\begin{aligned}\frac{\partial}{\partial t}\left(\int_v \rho u_i dv\right) + \int_s \rho u_i u_j dn_j &= \int_v \rho f_i dv - \int_s p dn_i \\ &+ \int_s \mu\left(\frac{\partial u_i}{\partial x_j} + \frac{\partial u_j}{\partial x_i} - \frac{2}{3}\delta_{ij}\frac{\partial u_k}{\partial x_k}\right) dn_j + \int_v S_{u_i} dv\end{aligned} \tag{4.28}$$

$$\begin{aligned}\frac{\partial}{\partial t}\left(\int_v \rho h dv\right) + \int_s \rho u_j h dn_j &= \frac{\partial}{\partial t}\left(\int_v p dv\right) - \int_s \left(-k\frac{\partial T}{\partial x_j} - \sum_\alpha^n \Gamma_\alpha h_\alpha \frac{\partial Y_\alpha}{\partial x_j}\right) dn_i \\ &+ \int_s \mu u_l \left(\frac{\partial u_l}{\partial x_j} + \frac{\partial u_j}{\partial x_l} - \frac{2}{3}\delta_{ij}\frac{\partial u_k}{\partial x_k}\right) dn_j + \int_v S_E dv\end{aligned} \tag{4.29}$$

$$\frac{\partial}{\partial t}\left(\int_v \rho\phi dv\right) + \int_s \rho u_j \phi dn_j = -\int_s -\Gamma_\phi \left(\frac{\partial \phi}{\partial x_j}\right) dn_j + \int_v S_\phi dv \tag{4.30}$$

For incompressible flow, Equations 4.27 to 4.30 simplify to

$$\int_s \rho u_j dn_j = 0 \tag{4.31}$$

$$\begin{aligned}\frac{\partial}{\partial t}\left(\int_v \rho u_i dv\right) + \int_s \rho u_i u_j dn_j &= \int_v \rho f_i dv \\ &- \int_s p dn_i + \int_s \mu\left(\frac{\partial u_i}{\partial x_j}\right) dn_j + \int_v S_{u_i} dv\end{aligned} \tag{4.32}$$

$$\begin{aligned}\frac{\partial}{\partial t}\left(\int_v \rho h dv\right) + \int_s \rho u_j h dn_j &= \frac{\partial}{\partial t}\left(\int_v p dv\right) \\ &- \int_s \left[-k\frac{\partial T}{\partial x_j} - \sum_\alpha^n \Gamma_\alpha h_\alpha \frac{\partial Y_\alpha}{\partial x_j}\right] dn_i + \int_v S_E dv\end{aligned} \tag{4.33}$$

$$\frac{\partial}{\partial t}\left(\int_v \rho\phi dv\right) + \int_s \rho u_j \phi dn_j = -\int_s -\Gamma_\phi \left(\frac{\partial \phi}{\partial x_j}\right) dn_j + \int_v S_\phi dv \tag{4.34}$$

### 4.2.1 Finite Element Geometry Specification

TASCflow uses a finite element based control volume method (CV-FEM) for discretization. The conservation equations are developed using the finite volume formulation shown above, but coupled with a finite element geometry specification that proves advantageous for complex geometries.

Nodes are specified throughout the computational domain using a structured format. As shown in Figure 4.1, a control volume forms the space around a node and is the region over which the integral equations described above are applied. The

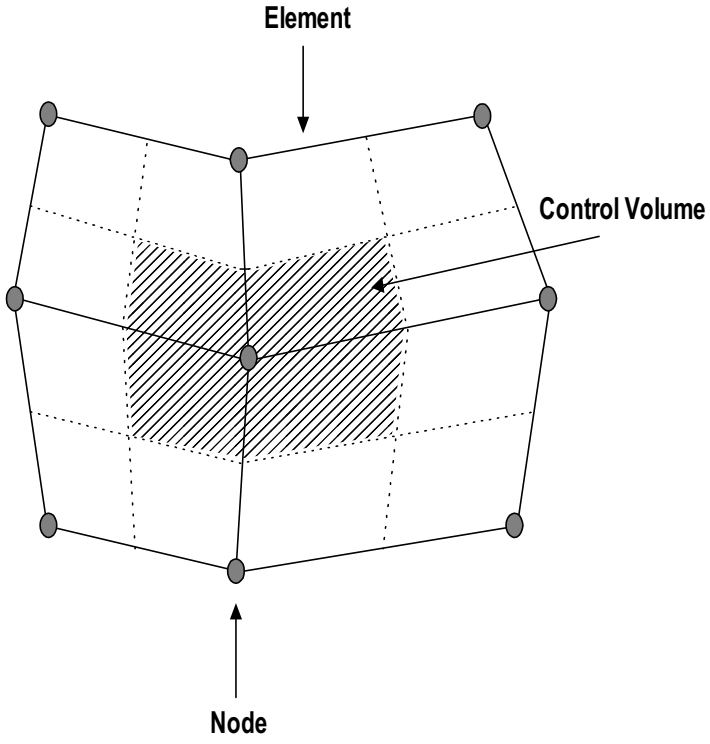


Figure 4.1: Control volume and flux element face description.

nodes are connected by line segments to form flux elements that are defined as a 3D linear hexahedral assembly of eight nodes as shown in Figure 4.2. A flux element face is then defined as the surface between four nodes and a flux element is thus the assembly of six such faces and the enclosed volume. The flux element interior can be further divided into 8 octants anchored by the 8 surrounding nodes as shown in Figure 4.3. The flux element edge midpoints and the centroid of the flux element specify the octants.

The surface of each control volume is composed of 6 control volume faces. Each control volume face is divided into 4 by the octants with which it is in contact (shaded area in Figure 4.1). The space contained within a control volume is thus formed by the composite of 24 quadrilateral surfaces defined at the midpoint of the flux element sides (six surfaces each with four quadrants). The surface of a node's control volume

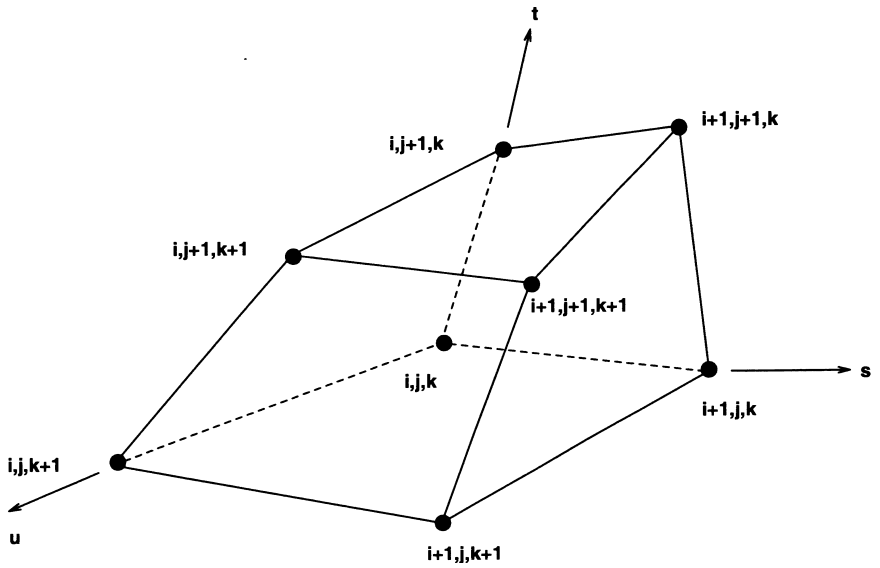


Figure 4.2: Eight nodes forming a flux element.

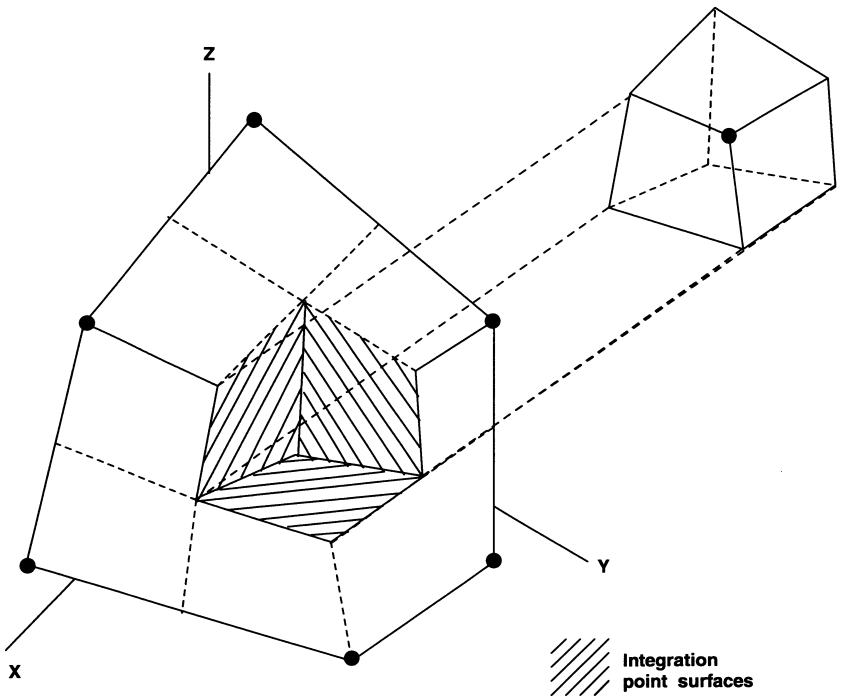


Figure 4.3: Flux element octants [156] .

is then assembled as the collection of these 24 quadrilateral surfaces.

Volume integrations and source application are carried out for each node using the enclosed control volume. Surface integrations to determine fluxes or sources through each control volume boundary use the idea of integration points (ip's). A single flux element face is shown in Figure 4.4 along with the four associated integration points where local fluxes are evaluated with discretized surface integrations. Numerical conservation is guaranteed since the flux leaving one octant integration point is the same flux entering the neighboring octant through the same integration point.

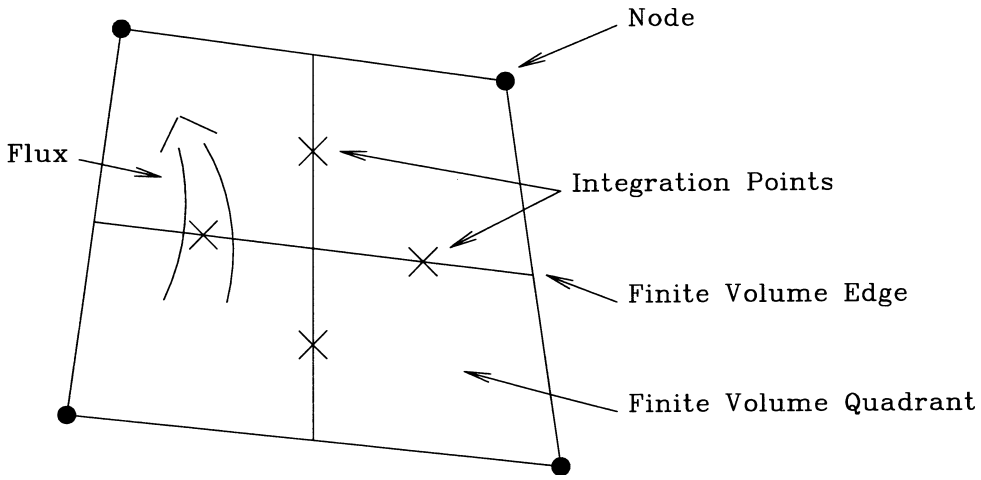


Figure 4.4: Flux element integration points [156] .

The eight octants shown in Figure 4.3 that form a flux element each have six surfaces. Three of these surfaces form the flux element sides (exterior), while the remaining three (interior) surfaces are defined as integration point surfaces since they compose the surfaces of the control volume where the discretized surface integrals are solved. A different eight octants then make up the control volume around each interior node. In this way, the volume integrals are calculated element wise using eight subvolumes (octants) and the surface integrations are carried out element wise with 24 subfaces. A significant advantage of such a formulation is increased accuracy in representing volume and surface integrals.

The structured grid used will define nodes from $i = 1 \rightarrow ID$, $j = 1 \rightarrow JD$, and $k = 1 \rightarrow KD$, or [1:ID,1:JD,1:KD], forming the computational domain. Nodes are thus located both on the interior and the surface of the computational domain. Interior control volumes are composed of eight octants. Control volumes around boundary nodes on the surface of the domain contain four octants, while the boundary

nodes on the edges of the domain contain two octants. Corner boundary nodes are composed of a single octant. Returning to the flux element definition, it is clear that this same computational domain is composed of $i = 1 \rightarrow ID-1$, $j = 1 \rightarrow JD-1$, and $k = 1 \rightarrow KD-1$ complete flux elements. Regions of the computational domain can be blocked off, given different values of porosity, specified as solid, involved in conjugate heat transfer, or have sources applied. This will be done using flux elements.

The finite element approach of using linear shape functions to represent values throughout a flux element based on the values at the surrounding nodes will be applied for evaluation of the pressure gradient and diffusion terms in the conservation relations. The region enclosed by the 8 nodes comprising the flux element in Figure 4.2 can be defined by the non-orthogonal local coordinates $s, t, u$ and can take values between -1 and 1

$$\begin{aligned} x(s,t,u) &= N_1 x_{i,j,k} + N_2 x_{i+1,j,k} + N_3 x_{i,j+1,k} + N_4 x_{i+1,j+1,k} + \\ &\quad N_5 x_{i,j,k+1} + N_6 x_{i+1,j,k+1} + N_7 x_{i,j+1,k+1} + N_8 x_{i+1,j+1,k+1} \\ y(s,t,u) &= N_1 y_{i,j,k} + N_2 y_{i+1,j,k} + N_3 y_{i,j+1,k} + N_4 y_{i+1,j+1,k} + \\ &\quad N_5 y_{i,j,k+1} + N_6 y_{i+1,j,k+1} + N_7 y_{i,j+1,k+1} + N_8 y_{i+1,j+1,k+1} \\ z(s,t,u) &= N_1 z_{i,j,k} + N_2 z_{i+1,j,k} + N_3 z_{i,j+1,k} + N_4 z_{i+1,j+1,k} + \\ &\quad N_5 z_{i,j,k+1} + N_6 z_{i+1,j,k+1} + N_7 z_{i,j+1,k+1} + N_8 z_{i+1,j+1,k+1} \end{aligned} \tag{4.35}$$

The $N_1 ... N_8$ shape functions provide a way to relate nodal values to other points within the flux element region

$$\begin{aligned} N_1 &= \frac{1}{8}(1-s)(1-t)(1-u) \\ N_2 &= \frac{1}{8}(1+s)(1-t)(1-u) \\ &\vdots \quad\quad \vdots \\ N_8 &= \frac{1}{8}(1+s)(1+t)(1+u) \end{aligned} \tag{4.36}$$

such that $N_1 = 1$ and $N_2 ... N_8 = 0$ at $x_{i,j,k}$ and $N_1 ... N_8 = \frac{1}{8}$ at the center of the element.

### 4.2.2 Physical Processes and Discretization

The conservation relations given by Equations 4.31 to 4.34 contain terms with a similar physical basis and simplifies the processes of discretization. For some terms, derivatives can be directly replaced by differences, but for others such a technique fails to properly capture the true physics, and can make a solution difficult, if not impossible, to obtain.

**Transient term**

Transient terms are approximated with a fully implicit backward difference formulation

$$\frac{\partial}{\partial t}\int_v \rho\phi dv \approx \rho \text{Vol}\left(\frac{\phi - \phi^o}{\Delta t}\right) \tag{4.37}$$

where an $^o$ represents values at the old (previous) time step. While not important for steady state solutions, such a form is only first order accurate for time in transient calculations. The fully implicit formulation has no restriction on the selection of a time step for stability, however, although a reduction in accuracy can occur as the time step increases.

**Diffusion Term**

The value of a scalar derivative of $\phi$ with respect to $x_j$ at an integration point, $\frac{\partial\phi}{\partial x_j}|_{ip}$, can be evaluated using the n shape functions, $N$,

$$\left.\frac{\partial\phi}{\partial x_j}\right|_{ip} = \sum_n \left.\frac{\partial N_n}{\partial x_j}\right|_{ip} \phi_n \tag{4.38}$$

where $n = 1...8$ in three dimensions. Local derivatives are used to evaluate the cartesian derivatives of the shape functions with the Jacobian transformation matrix (inverse Jacobian) relating the length scales between the orthogonal and local non-orthogonal coordinate systems

$$\begin{pmatrix} \frac{\partial N}{\partial x} \\ \\ \frac{\partial N}{\partial y} \\ \\ \frac{\partial N}{\partial z} \end{pmatrix} = \begin{pmatrix} \frac{\partial x}{\partial s} & \frac{\partial y}{\partial s} & \frac{\partial z}{\partial s} \\ \\ \frac{\partial x}{\partial t} & \frac{\partial y}{\partial t} & \frac{\partial z}{\partial t} \\ \\ \frac{\partial x}{\partial u} & \frac{\partial y}{\partial u} & \frac{\partial z}{\partial u} \end{pmatrix}^{-1} \begin{pmatrix} \frac{\partial N}{\partial s} \\ \\ \frac{\partial N}{\partial t} \\ \\ \frac{\partial N}{\partial u} \end{pmatrix} \tag{4.39}$$

The $\frac{\partial N}{\partial\{s,t,u\}}$ terms are evaluated at the intersection of the element edges and the $ip$ surface that is first order accurate, but unconditionally stable. Evaluation at the $ip$ itself (which is second order accurate) can produce oscillations and poor convergence behavior at large grid aspect ratio values. The integration point pressures for use in the pressure gradient terms given by Equation 4.38 are determined from the shape function

$$P_{ip} = \sum_n N_n(s,t,u)P_n \tag{4.40}$$

**Convective Term**

Discretization of the convective term, $\frac{\partial u}{\partial x}$, is not straight forward. An upwind difference,

$$\frac{\partial u}{\partial x} \approx \frac{u_i - u_{i-1}}{\Delta x} \tag{4.41}$$

is unconditionally stable, but is only first order accurate and highly diffusive. See Patankar [23] for a discussion of numerical diffusion (false diffusion) and its effect on the modeling of fire, especially for flows at an angle to the grid. Central differencing for the convection terms can lead to negative influence coefficients and unrealistic results (a node temperature drops, for example, even though all of its neighbors are increasing in temperature) and is limited to low Reynolds numbers.

The exponential, hybrid and power law schemes blend different amounts of upstream and downstream influence (upwind and central difference) depending on the cell Peclet number (ratio of cell convective to diffusive fluxes). This overcomes some of the problems with pure central differencing by improving the physical basis for the discretization. Central differencing gives an incorrect physical picture for advection dominated (high velocity) flows, but may still lead to negative influence coefficients.

Physical advection correction schemes are available that attempt to approximate as close as possible the actual physical process in the development of the algebraic equations. The Mass Weighted Skew Upstream Differencing scheme (MWS) show in Figure 4.5 is available in TASCflow [156]. The value of $\phi$ at the integration point $e$,

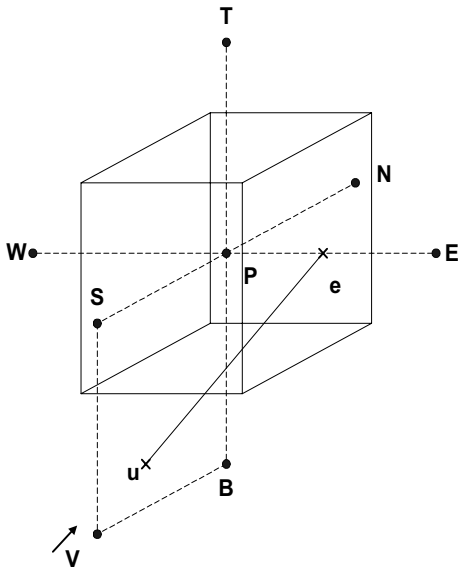


Figure 4.5: Mass weighted skew upstream differencing.

$\phi_e$, is approximated by

$$\phi_e \approx \phi_u + \Delta\phi_e \tag{4.42}$$

where $\phi_u$ is the value of $\phi$ at $u$, and $\Delta\phi_e$ accounts for the variation in $\phi$ between the value upstream at $\phi_u$ and the integration point $e$. The upstream value, $\phi_u$ is then determined from the surrounding $\phi$ values, but weighted based on the mass flows passing through the flux element faces around $\phi_u$. Predictions for $\Delta\phi_e$ can be improved by included Physical Advection Correction (PAC) terms that account for advection, diffusion and source terms in the determination of $\Delta\phi_e$.

**Pressure-Velocity Term**

Pressure-velocity coupling is not treated with the usual staggered grid, but instead an un-staggered collocated grid is applied. The continuity equation acts to constrain the pressure distribution since it requires the generation of a pressure field with velocities that are mass conserving. In effect, the *ip* velocities do not include the influence of the neighboring nodal pressure when a central difference formulation, $u_{i+1} - u_{i-1} = 0$, is used. To overcome the pressure-velocity decoupling (checker board) problem discussed by Patankar [23], the *ip* velocity must be determined with the effect of local pressures. This is accomplished through an algebraic momentum conservation relation written for the *ip* velocities that includes the pressure differences from the nodes surrounding the *ip* [156]. This leads to a fourth order pressure redistribution for direction $i$

$$\left(\frac{\partial u}{\partial x}\right)_i + \frac{\Delta x^3 A}{4\dot{m}} \left(\frac{\partial^4 p}{\partial x^4}\right)_i = 0 \tag{4.43}$$

which is used in place of the continuity equation. The second term on the left in Equation 4.43, which does not appear in the mass conservation relation, goes to zero rapidly as the grid is refined due to the $\Delta x^3$ term and serves to prevent the decoupling problem.

The discretized form of the integration point velocity, $u_{ip} \approx \frac{1}{2}(u_i + u_{i+1})$ is similarly modified to include the higher order pressure difference term:

$$u_{ip} \approx \frac{1}{2}(u_i + u_{i+1}) + \frac{1}{8\rho \mathrm{Vol}} \Delta x^3 \left(\frac{d^3 p}{dx^3}\right)_{ip} + O(\Delta x^4) \tag{4.44}$$

Physically, the *ip* velocity is thus the average of the surrounding nodal velocities, with an added pressure redistribution term to prevent pressure decoupling. Equation 4.44 then gives a way of relating velocity at a control volume face (which will be used to satisfy mass conservation), based on neighboring nodal values.

### 4.2.3 Discretized Form of the Conservation Equations

By summing over all of the integration points on the surface of the control volume and using a fully implicit formulation for the time step, the discretized form of the conservation equations for incompressible flow become:

$$\sum_{ip}(\rho u_j \Delta n_j)_{ip} = 0 \tag{4.45}$$

$$\begin{aligned}\rho \mathrm{Vol}\left(\frac{u_i - u_i^o}{\Delta t}\right) + \sum_{ip} \dot{m}_{ip}(u_i)_{ip} = \rho f_i \mathrm{Vol} \\ - \sum_{ip}(p\Delta n_i)_{ip} + \sum_{ip}\left(\mu\left(\frac{\partial u_i}{\partial x_j}\right)\Delta n_j\right)_{ip} + S_{u_i}\mathrm{Vol}\end{aligned} \tag{4.46}$$

$$\begin{aligned}\rho \mathrm{Vol}\left(\frac{h - h^o}{\Delta t}\right) + \sum_{ip} \dot{m}_{ip} h_{ip} = \\ \mathrm{Vol}\left(\frac{p - p^o}{\Delta t}\right) + \sum_{ip}\left(q_j \Delta n_i\right)_{ip} + S_E \mathrm{Vol}\end{aligned} \tag{4.47}$$

$$\rho \mathrm{Vol}\left(\frac{\phi - \phi^o}{\Delta t}\right) + \sum_{ip} \dot{m}_{ip}\phi_{ip} = \sum_{ip}\left(\Gamma\left(\frac{\partial \phi}{\partial x_j}\right)\Delta n_j\right)_{ip} + S_\phi \mathrm{Vol} \tag{4.48}$$

where the volume of the control volume is Vol, $\dot{m}_{ip} = (\rho u_j \Delta n_j)^o_{ip}$ and $\Delta n_j$ is the discrete outward surface vector.

## 4.3 Numerical Solution

Now that discretization has transformed the non-linear partial differential conservation equations into a set of linear algebraic equations, the focus shifts to the solution. A host of relaxation methods such as Gauss-Seidel (G-S) or alternating direction line Gauss-Seidel are available for reducing the residual (error) from solving the algebraic approximations. TASCflow uses an Algebraic Multigrid (AMG) with Additive Correction Multigrid (ACM) method that will be shown superior when compared to other relaxation techniques. The mass and momentum conservation equations are coupled and solved simultaneously, with the remaining scalar equations solved sequentially.

The solution error distribution throughout a domain occurs at different wavelengths. Using the 2D diffusion equation as an example [156],

$$\frac{\partial^2 \phi}{\partial x^2} + \frac{\partial^2 \phi}{\partial y^2} = 0 \tag{4.49}$$

the Gauss-Seidel approximation can be employed to iterate toward an approximate

solution

$$\phi_{i,j}^{n+1} = \frac{\Delta y^2(\phi_{i-1,j}^{n+1} + \phi_{i+1,j}^{n}) + \Delta x^2(\phi_{i,j-1}^{n+1} + \phi_{i,j+1}^{n})}{2\Delta y^2 + 2\Delta x^2} \tag{4.50}$$

The first thing to note about the G-S solution method is that a given node, $\phi_{i,j}$ receives influence from only a very local region of neighbors. Shorter wavelength errors on the order of the grid size should be reduced, but longer wavelength errors will hardly be affected. As a grid grows larger or is refined, the difference between the short and long wavelength errors increases, thus error reduction becomes more difficult.

A second serious error exists with the application of simple relaxation techniques. When a grid has a large aspect ratio (either $\Delta x \gg \Delta y$ or $\Delta y \gg \Delta x$ in this case), the i or j direction coefficients in Equation 4.50 will differ significantly with the large coefficient direction dominating. Thus $\phi_{i,j}^{n+1}$ will receive most of its influence from the large coefficient direction. A similar effect will be felt on error components that will be reduced preferentially in the large coefficient direction.

The final analysis of G-S methods is clear: it is best at reducing the small wavelength errors in the large coefficient direction and all but ignores the long wavelength errors in the small coefficient direction. The multigrid solution method provides a computationally efficient way of overcoming the two problems described above.

Whether a given wavelength error is short or long depends on the grid. If the grid is made more coarse, wavelengths that were long compared to the fine grid are now shorter in relation to a more coarse grid and will be reduced successfully by a simple relaxation method. A multigrid method uses this fact to its advantage, Figure 4.6. The fine grid is repeatedly made coarser until it may contain only a few nodes and then is again made finer. Each grid is then able to reduce errors with a wavelength on the order of the grid spacing, something a simple relaxation method can accomplish. The whole spectrum of errors is effectively reduced and the long wavelength problem addressed.

The method used to coarsen (or block) the grid, i.e. Algebraic Multigrid (AMG), can be effective in treating the different influence between the large and small coefficient directions. This is done by generating the coarse grid from the fine by making the fine grid more coarse in the large coefficient direction. This process is shown in Figure 4.7 for a 2-D grid.

The details of how the coarse grid equations are generated and how information flows between the fine and coarse grids are governed by the Additive Correction Multigrid (ACM) method [156]. The net flux across a grid of a conserved scalar should tend toward zero as convergence is approached. On a given grid then, the conservation equation residual before convergence represents the flux imbalance for the block. ACM generates corrections based on the coarse grid that adjust the fluxes in each block to satisfy the governing equation. With the coarse grid corrections made, the coarse equations are satisfied leaving only "pockets" of flux errors from the fine grid of each block. The correction forces the sum of the residuals for the fine grid members of each block to zero (no flux error) and in the process reduces the longer wavelength error. The solver then just needs to correct the local flux errors in the

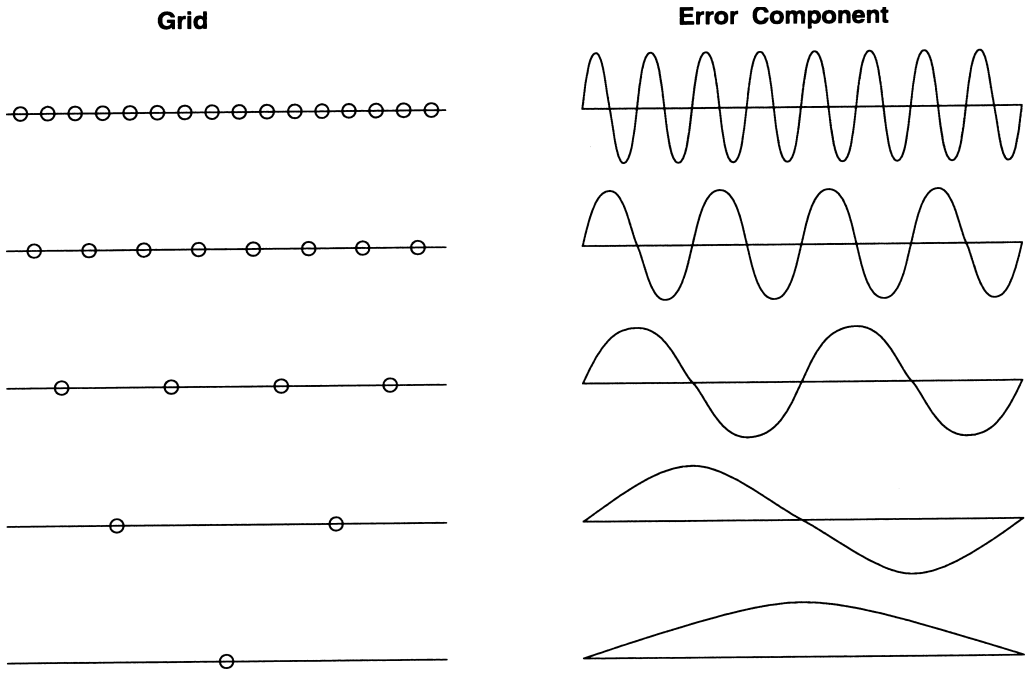


Figure 4.6: Grid and related error component most effectively reduced [156] .

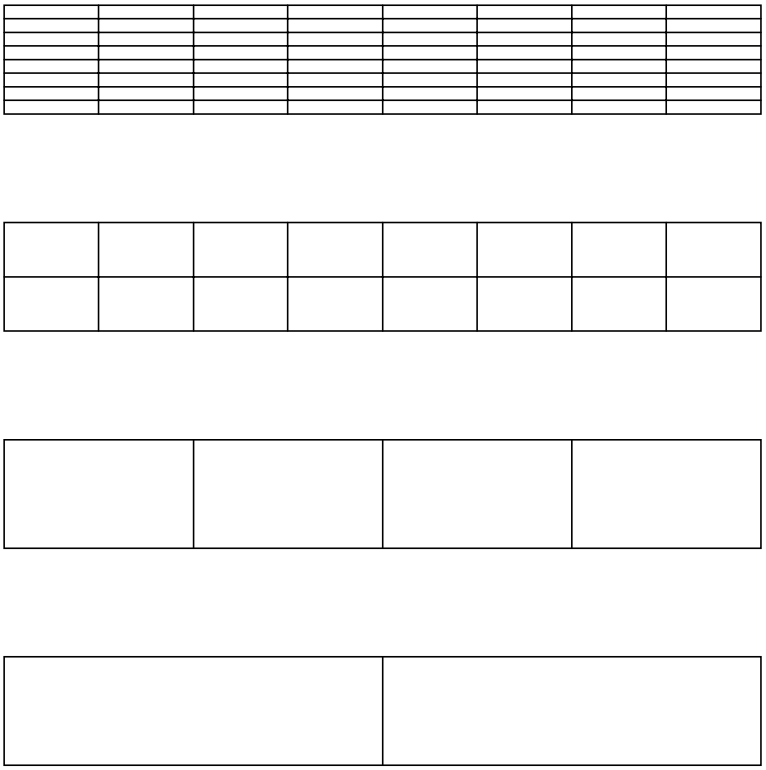

Figure 4.7: Grid coarsening by multigrid method.

fine grid members of each block.

The formulation of the coarse grid equations have been developed so that the influence coefficients are developed during solution of the fine grid equations and no separate equations need to be generated. A "W" cycle for visiting the grids from fine to coarse and back is shown in Figure 4.8. The matrix of linear algebraic

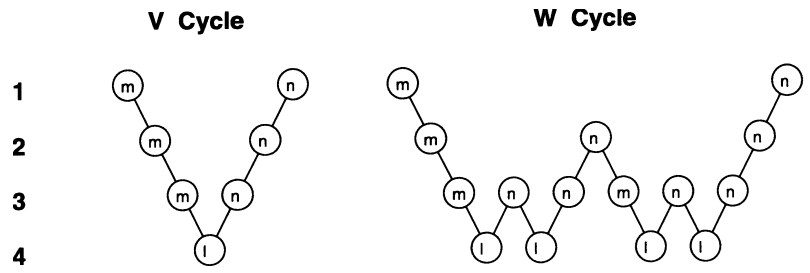


Figure 4.8: Multigrid using W cycle.

equations is solved using an Incomplete Lower Upper (ILU) solver that can be used on any non-singular (determinant is non-zero) matrix. The matrix is broken into a product of lower and upper triangular matrices that can be trivially solved by forward and backward substitutions. Although the matrix will be banded, additional band reduction is applied by TASCflow to reduce the memory requirements (a fraction of the 26 neighbors surrounding a node are lagged a time step). Once radiation is added to the model, every control volume no longer sees only its neighbors, but instead sees every other volume, so a banded matrix may not exist.

## 4.4 Closure Models Used in CFD Calculations

### 4.4.1 Time Averaging and Turbulence Modeling

The final set of conservation equations provide information about the flow at a given instant in time through the computational domain. This poses a problem for the numerical modeler of combustion phenomenon since the length and time scales in a typical compartment fire (and almost any turbulent flow) cover many orders of magnitude. For example, the height of a flame from a burning chair could be measured in terms of meters, while the fine scale mixing occurring in the flame that is important to entrainment and product of incomplete combustion formation would be on the order of a fraction of a millimeter. Proper numeric resolution of this reactive flow field would require the solution of the complete set of conservation equations on a grid fine enough to resolve a turbulent eddy. Up to $10^5$ control volumes would be necessary for each $cm^3$ of the flow field, clearly not possible with current or near future computer technology [4].

Instead, large-scale turbulent motion such as from a ceiling jet or plume will be determined from a solution of the conservation equations across the grid. Smaller scale motion such as fine turbulent eddies where mixing and momentum dissipation occur (molecular viscosity transferring kinetic energy into internal energy), can be approximated using a combination of empirical and theoretical models. It is at this point that the solution to the flow field is no longer exact since certain assumptions need to be introduced for closure of the system. The two equation $k-\epsilon$ model will be discussed exclusively, although other models are available for turbulent closure and are described elsewhere [162, 163]. This model should be considered an engineering approximation to an exceedingly complex system, since the final form involves a significant number of simplifications that are not based on first principles.

First, the conservation equations are given in their time averaged, or Reynolds form, by dividing each dependent variable, $\phi(x_i,t)$ into time mean $\bar{\phi}(x_i)$ and fluctuating $\phi'(x_i,t)$ components as shown in Figure 4.9,

$$\phi(x_i,t) = \bar{\phi}(x_i) + \phi'(x_i,t) \tag{4.51}$$

with the resulting equations then time averaged. The time averaging is carried out

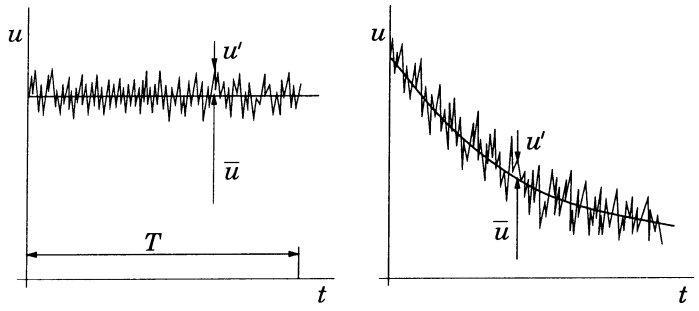


Figure 4.9: Fluctuating and mean velocity field [159] .

over an interval, $\tau$, which is larger than the time scale of the turbulent fluctuations

$$\bar{\phi}(x_i) = \lim_{\tau\to\infty} \frac{1}{\tau} \int_0^\tau \phi(x_i,t)dt \tag{4.52}$$

Although $\tau$ need not go to infinity, it must be sufficiently long so that $\bar{\phi}(x_i)$ is independent of the interval selected. Transport coefficients (viscosity, thermal conductivity) are not time averaged. By definition, the time average of a fluctuating quantity is zero, $\bar{\phi'} = 0$, but the time average of the product of two fluctuating quantities need not be zero, $\overline{\phi'\phi'} \neq 0$.

For compartment fire modeling where density can be considered constant, both the Reynolds (time) averaging and the Favre (mass) averaging methods will give the same final form of the conservation equations [164]. The Reynolds averaged form of the incompressible mass, momentum, energy, species and scalar conservation equations with negligible variation in density (except buoyancy), viscosity, and thermal conductivity are [4],

$$\frac{\partial}{\partial x_j}(\rho \bar{u}_j) = 0 \tag{4.53}$$

$$\frac{\partial}{\partial t}(\rho \bar{u}_i) + \frac{\partial}{\partial x_j}(\rho \bar{u}_i \bar{u}_j + \rho \overline{u_i' u_j'}) = \bar{g}_i - \frac{\partial \bar{p}}{\partial x_i} + \frac{\partial}{\partial x_j}(\bar{\sigma}_{ij}) + \bar{S}_u \tag{4.54}$$

$$\frac{\partial}{\partial t}(\rho \bar{h}) + \frac{\partial}{\partial x_j}(\rho \bar{u}_j \bar{h} + \rho \overline{u_j' h'}) = \frac{\partial \bar{p}}{\partial t} + \frac{\partial}{\partial x_j}\left(\frac{k}{c_p}\frac{\partial \bar{h}}{\partial x_j}\right) + \bar{S}_E \tag{4.55}$$

$$\frac{\partial}{\partial t}(\rho \bar{Y}_\alpha) + \frac{\partial}{\partial x_j}(\rho \bar{u}_j \bar{Y}_\alpha + \rho \overline{u_j' Y_\alpha'}) = \frac{\partial}{\partial x_j}\left(\rho \Gamma_\alpha \frac{\partial \bar{Y}_\alpha}{\partial x_j}\right) + \bar{S}_\alpha \tag{4.56}$$

$$\frac{\partial}{\partial t}(\rho \bar{\phi}) + \frac{\partial}{\partial x_j}\left(\rho \bar{u}_j \bar{\phi} + \rho \overline{u_j' \phi'}\right) = \frac{\partial}{\partial x_j}\left(\rho \Gamma_\phi \frac{\partial \bar{\phi}}{\partial x_j}\right) + \bar{S}_\phi \tag{4.57}$$

The mean viscous stress tensor is simply

$$\bar{\sigma}_{ij} = \mu\left(\frac{\partial \bar{u}_i}{\partial x_j} + \frac{\partial \bar{u}_j}{\partial x_i}\right) \tag{4.58}$$

The third term on the right of Equation 4.54 contains the same stress terms as in Equation 4.32 for laminar flow and can be replaced by mean velocities via the stress tensor, Equation 4.7. The last term on the left hand side, however, is new and can be thought of as the apparent stress gradient resulting from turbulent fluctuation induced momentum transport [164], just as the $-\rho\overline{u_j' h'}$ term in the Equation 4.55, can be viewed as a turbulent heat flux.

The $-\rho\overline{u_i' u_j'}$ term, called the Reynolds or turbulent stress, in Equation 4.54 represents the transport of momentum due to turbulence induced fluctuations. Moving the turbulent stress term in Equation 4.54 to the right hand side yields

$$\frac{\partial}{\partial t}(\rho \bar{u}_i) + \frac{\partial}{\partial x_j}(\rho \bar{u}_i \bar{u}_j) = \bar{g}_i - \frac{\partial \bar{p}}{\partial x_i} + \frac{\partial}{\partial x_j}(\bar{\sigma}_{ij} - \rho \overline{u_i' u_j'}) + \bar{S}_u \tag{4.59}$$

which shows that the additional term, which is actually a momentum flux, can also be viewed as acting as an apparent turbulent stress. It is the job of the turbulence model to relate these turbulent quantities (stresses and heat fluxes) to time mean flow variables for turbulent closure.

Taking an engineering approach, turbulence acts to increase diffusion of mass, momentum, energy and species, along with dissipation of energy, due to enhanced mixing resulting from turbulent eddies. Such a viewpoint is similar to relating viscous stresses in laminar flow and heat or mass transfer by molecular diffusion to velocity

gradients (rate of strain) through a transport coefficient (viscosity). Based on such molecular gradient-diffusion processes, Boussinesq showed the possibility of relating these apparent turbulent shearing stresses, $-\rho\overline{u_i u_j}$, to the mean rate of strain through a scalar eddy viscosity, $\mu_T$, of a form similar to Equation 4.7,

$$-\rho\overline{u_i' u_j'} = \mu_T \left( \frac{\partial \bar{u}_i}{\partial x_j} + \frac{\partial \bar{u}_j}{\partial x_i} \right) - \frac{2}{3}\rho\delta_{ij}\bar{k}_{tke} \tag{4.60}$$

The turbulent kinetic energy is defined as $\bar{k}_{tke} = \frac{1}{2}\overline{u_i' u_i'}$, where a $tke$ subscript has been applied to prevent confusion with the thermal conductivity [164]. The turbulent or eddy viscosity is a property of the flow, and not the fluid as it is for the fluid or laminar viscosity, $\mu$. The eddy viscosity thus accounts for momentum transfer resulting from subgrid turbulent fluctuations and can be treated as an increase in viscosity. A similar eddy diffusion coefficient, $\Gamma_\phi$, can be used to approximate other turbulent terms and is also a property of the flow field

$$-\rho\overline{u_j' \phi'} = \Gamma_T \frac{\partial \bar{\phi}}{\partial x_j} \tag{4.61}$$

For combustion, the gradient diffusion approximation may not be appropriate for premixed flames where diffusion is not necessarily in the direction of the $\phi$ gradient, although the same has not been shown to apply to diffusion flames [4]. Since the eddy viscosity is treated as a scalar, isotropic turbulence (principal axes for the mean strain rate tensor and the Reynolds stress tensor coincident) is assumed. This is not an entirely satisfactory assumption for fires due to buoyant driven flows that are acted upon in a principle direction based on the orientation of the gravity vector.

If one accepts the Boussinesq approximation, predicting the effect of turbulence has moved now to determining $\mu_T$. Dimensional analysis shows that

$$\frac{\mu_T}{\rho} \propto (velocity)(length) \tag{4.62}$$

Prandtl's mixing length hypothesis relates $\mu_T$ to a turbulent mixing velocity, $v_{mix}$ and the mixing length, $l_{mix}$

$$\mu_T \propto C\rho l_{mix} v_{mix} \tag{4.63}$$

The mixing length can be thought of as the distance over which a parcel of fluid travels while retaining its original momentum. An additional leap of faith is required to quantify the mixing velocity based on work with thin shear flows by Prandtl

$$v_{mix} = C l_{mix} \left| \frac{\partial u}{\partial y} \right| \tag{4.64}$$

The velocity gradient term involves the velocity in the primary flow direction, $u$, in relation to a transverse coordinate direction $y$ [164]. With the mixing velocity defined,

Equations 4.63 and 4.64 become Prandtl's mixing length hypothesis

$$\mu_T = \rho l_{mix}^2 \left| \frac{\partial u}{\partial y} \right| \tag{4.65}$$

Since it is not a fluid property, $l_{mix}$ can incorporate the constant, $C$. The problem at this point is that $l_{mix}$ is a function of the flow field and requires prior specification for different problems. Such a model would also lead to the non-physical prediction of $\mu_T = 0$ at the center of a pipe when $\left|\frac{\partial u}{\partial y}\right| \Rightarrow 0$. In addition, turbulence must be in a state of local equilibrium with a balance between production and dissipation [164]. There is no way to capture the physical process of turbulent transport or its history since only local flow conditions are included.

Twenty years after the mixing length hypothesis was proposed, Prandtl recommended that the mixing velocity be given by the square root of the kinetic energy of turbulence

$$v_T = \sqrt{\bar{k}_{tke}} = \left[\frac{1}{2}\overline{u_i' u_i'}\right]^{\frac{1}{2}} = \left[\frac{1}{2}(\bar{u}'^2 + \bar{v}'^2 + \bar{w}'^2)\right]^{\frac{1}{2}} \tag{4.66}$$

which includes fluctuations of intensity in the three coordinate directions. Eddy viscosity is then described by

$$\mu_T = C_\mu \rho \sqrt{\bar{k}_{tke}} L \tag{4.67}$$

were L is a turbulent length scale and represents the characteristic size of the large energy containing eddies. A transport equation for $\bar{k}_{tke}$ can be written

$$\frac{\partial \rho \bar{k}_{tke}}{\partial t} + \frac{\partial \bar{u}_j \bar{k}_{tke}}{\partial x_j} = \frac{\partial}{\partial x_j}\left(\mu \frac{\partial \bar{k}_{tke}}{\partial x_j}\right) - \frac{\partial}{\partial x_j}\left(\frac{\rho}{2}\overline{u_j' u_i' u_i'} + \overline{p' u_j'}\right) - \rho \overline{u_i' u_j'} \frac{\partial \bar{u}_i}{\partial x_j} - \mu \overline{\frac{\partial u_i'}{\partial x_j}\frac{\partial u_i'}{\partial x_j}} \tag{4.68}$$

The two terms on the left hand side represent the rate of change and convective transfer of turbulent kinetic energy. On the right, the first term involves movement of $\bar{k}_{tke}$ by molecular diffusion. A gradient diffusion approximation is used for the transport of $\bar{k}_{tke}$ by turbulent fluctuations [162]

$$-\left(\frac{\rho}{2}\overline{u_j' u_i' u_i'} + \overline{p' u_j'}\right) \approx \frac{\mu_T}{\mathrm{Pr}_k} \frac{\partial \bar{k}_{tke}}{\partial x_j} \tag{4.69}$$

$\mathrm{Pr}_k$ is a closure coefficient, the turbulent Prandtl number. Included with the turbulent transport is pressure induced diffusion due to pressure fluctuations. A value of unity is usually assumed for $Pr_k$ (momentum and mass transfer rates are equal). Turbulent kinetic energy is produced by the shear with the mean flow and transferred to the turbulence at a rate given by the second to last term in Equation 4.68

$$-\rho \overline{u_i' u_j'} \frac{\partial \bar{u}_i}{\partial x_j} \approx \mu_T \left(\frac{\partial \bar{u}_i}{\partial x_j} + \frac{\partial \bar{u}_j}{\partial x_i}\right) \frac{\partial \bar{u}_i}{\partial x_j} \tag{4.70}$$

which is approximated with the eddy viscosity for the $\rho\overline{u_i'u_j'}$ term. The last term in Equation 4.68 represents the rate at which turbulent kinetic energy is converted into internal energy

$$\mu\overline{\frac{\partial u_i'}{\partial x_j}\frac{\partial u_i'}{\partial x_j}} = \rho\epsilon \tag{4.71}$$

where $\epsilon$ is the dissipation rate of $\bar{k}_{tke}$ per unit mass and

$$\epsilon = C_D\frac{\left(\bar{k}_{tke}^{\frac{3}{2}}\right)}{L} \tag{4.72}$$

Here again equilibrium is assumed for turbulence (balanced production and destruction) which is not a physically correct picture for flows involving combustion.

The final form of Equation 4.68 is then

$$\frac{\partial\rho\bar{k}_{tke}}{\partial t} + \frac{\partial\bar{u}_j\bar{k}_{tke}}{\partial x_j} = \frac{\partial}{\partial x_j}\left[\left(\mu + \frac{\mu_T}{\mathrm{Pr}_k}\right)\frac{\partial\bar{k}_{tke}}{\partial x_j}\right] + \mu_T\left(\frac{\partial\bar{u}_i}{\partial x_j} + \frac{\partial\bar{u}_j}{\partial x_i}\right)\frac{\partial\bar{u}_i}{\partial x_j} - \rho\epsilon \tag{4.73}$$

with the molecular turbulent diffusion of $\bar{k}_{tke}$ combined in the first term on the right hand side. A buoyancy term, $\beta\rho g\overline{u_i'T'}$ can be added that accounts for transfer of $\bar{k}_{tke}$ to potential energy of the fluid [4]. In a hot gas layer with a stable, stratified flow, the term is negative, which acts to reduce turbulent mixing. A positive value in regions that are not stably stratified, such as in a plume or door flow, increases mixing. The buoyancy term can be modeled as [156]

$$\beta\rho g\overline{u_i'T'} \approx \beta\rho g\frac{\mu_T}{\mathrm{Pr}_T}\frac{\partial T}{\partial x_j} \tag{4.74}$$

Equation 4.73 still contains the length scale, L, through Equation 4.72. It seems reasonable that $L$ should also depend on history and upstream conditions, as does $\bar{k}_{tke}$. A transport equation can be developed for the length scale by taking the trace of the Reynolds stress equation, but only with the inclusion of difficult to model terms [164]. Instead, a transport equation for the dissipation rate, $\epsilon$ is usually employed

$$\frac{\partial(\rho\epsilon)}{\partial t} + \frac{\partial(\rho u_j\epsilon)}{\partial x_j} = \frac{\partial}{\partial x_j}\left[\left(\mu + \frac{\mu_T}{\sigma_\epsilon}\right)\frac{\partial\epsilon}{\partial x_j}\right] + C_{\epsilon 1}\mu_T\left(\frac{\partial\bar{u}_i}{\partial x_j} + \frac{\partial\bar{u}_j}{\partial x_i}\right)\frac{\partial\bar{u}_i}{\partial x_j}\frac{\epsilon}{\bar{k}_{tke}} - \rho C_{\epsilon 2}\frac{\epsilon^2}{\bar{k}_{tke}} \tag{4.75}$$

with

$$\mu_T = C_\mu\rho\sqrt{\bar{k}_{tke}}L = C_\mu\rho\frac{(\bar{k}_{tke})^2}{\epsilon} \tag{4.76}$$

to relate $k$, $\epsilon$ and $L$. The right hand side of Equation 4.75 represents dissipation transfer by molecular diffusion and turbulence, generation of dissipation, and dissipation of dissipation. Equation 4.75 is built on an even less stable foundation than Equation 4.68 and has required significant approximations to reach its current state [162]. Since it is important for fires, a buoyancy term of the form, $-\beta g\frac{\mu_T}{\mathrm{Pr}_\epsilon}\frac{\partial\bar{T}}{\partial x_j}$ can also

be included.

In combination, Equations 4.73 and 4.75 compose the widely used $k-\epsilon$ turbulence model. Discretization is relatively straight forward and follows the discussion of Section 4.2. The time and length scales for Equations 4.73 and 4.75 are much smaller than those for mean flow, resulting in a stiff equation set [159]. Typical closure constants based on experiment are shown in Table 4.1.

| **Constant** | **Value** |
|---|---|
| $C_\mu$ | 0.09 |
| $C_{\epsilon 1}$ | 1.44 |
| $C_{\epsilon 2}$ | 1.92 |
| $Pr_k$ | 1.0 |
| $Pr_\epsilon$ | 1.3 |

Table 4.1: $k-\epsilon$ turbulence model closure constants.

Caution is warranted in the use of the $k-\epsilon$ model with adverse pressure gradients, rotation, stratification and flows around curved surfaces. Problems can be shown to result from the Boussinesq eddy viscosity hypothesis [162]. In general, the $k-\epsilon$ model has done very well when used in the prediction of compartment fires, with one main exception [165, 166]. This closure model has experienced problems by overpredicting the centerline temperatures and velocities for turbulent buoyant plumes, as a result of underpredicting the plume width. To improve the results, three changes can be made to the standard $k-\epsilon$ model following the work of Nam and Bill based on pool fire experiments and modeling work done with PHOENICS [167]. First an additional buoyancy source is added to the production term for turbulence in the TKE transport equation

$$S_b = \mu_T g \frac{1}{\rho}\frac{\partial \rho}{\partial z} \tag{4.77}$$

TASCflow already includes such a buoyancy source term in the TKE transport relation of Equation 4.74. In effect, the source term helps to account for the anisotropic turbulence that occurs with strongly buoyant flows. The turbulent, or eddy, viscosity $\mu_T$ is approximated in the standard form for the two equation $k-\epsilon$ model by Equation 4.76. where $C_\mu$ is usually given the value of 0.09. Nam and Bill found that plume velocities were better predicted with a $C_\mu$ value of 0.18, which increases the diffusion of velocity. A combustion model, however, was not used during generation of the new turbulence model constants.

The temperature distribution in the plume is also poorly predicted by the standard $k-\epsilon$ model where a value of 1.0 is typically used for the thermal Prandtl number $\mathrm{Pr}_T$, representing heat diffusion (ratio of momentum to thermal diffusion). Instead, a revised value of 0.85 tends to fit the plume temperature profile more closely. Ceiling jet temperatures were also found to be well correlated using these revised constants.

### 4.4.2 Wall Functions

Near a solid boundary, the Reynolds numbers in a compartment fire are sufficiently high to produce a thin turbulent boundary layer with large gradients between the wall and the free stream. However, a significant number of nodes would be required to resolve the layer profile, leading to a severe computational penalty. Instead, empirically based relations can be applied to predict the shape of the boundary layer between a solid wall and the near node to determine the boundary conditions at the wall based on the near node. Looking at the boundary layer, three zones can be identified [162]. A **log-layer** is considered to exist in the boundary layer close enough to the surface that inertial terms are small and molecular viscosity dominates. It extends away from the wall as long as molecular (viscous) stresses are small compared to Reynolds stresses. The **viscous sublayer** is located between the log-layer and the wall and it is within this region that velocity goes to zero at the wall. Finally, the **defect layer** stretches from the log-layer to the outer edge of the boundary layer where it meets the bulk fluid flow. The log-layer in effect forms the attachment between the viscous sublayer and the defect layer, where the assumed shape of the boundary layer is shown in Figure 4.10

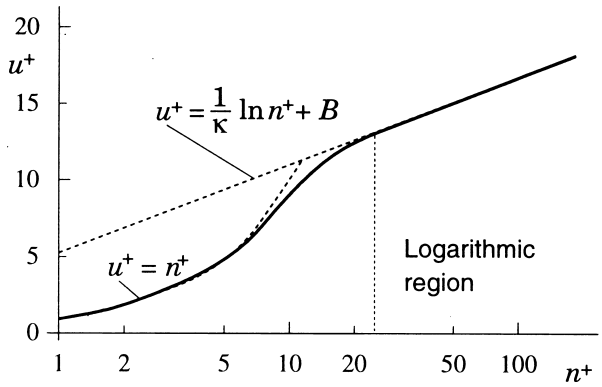


Figure 4.10: Turbulent boundary layer profile [159] .

At a stationary solid wall, the no slip boundary condition requires zero velocity at the wall, although the shear stress at the wall, $\tau_w$, still requires evaluation. Define the shear, or friction velocity, $u_\tau$, as $u_\tau \equiv \sqrt{\frac{\tau_w}{\rho}}$ and a non-dimensional velocity as $u^+ \equiv \frac{\bar{u}_t}{u_\tau}$, where $\bar{u}_t$ is the mean velocity tangent to the wall measured at a distance $\Delta n$ away from the wall. A non-dimensional distance from the wall is defined by $n^+ \equiv \frac{\rho u_\tau \Delta n}{\mu}$. Based on experimental data, the non-dimensional velocity is predicted to have a logarithmic profile

$$u^+ = \frac{1}{\kappa} \ln(n^+) + C \tag{4.78}$$

where $C$ is a measure of the viscous sublayer thickness and $\kappa$ is the von Karman constant [159]. Returning to Figure 4.10, it appears that Equation 4.78 fits well in

the log-layer but is less satisfactory in the viscous sublayer. If Couette flow and local equilibrium exist near the wall, then the shear velocity can be given by [159]

$$u_\tau = (C_\mu)^{\frac{1}{4}}\sqrt{k_{tke}} \tag{4.79}$$

From the definition of shear velocity and Equations 4.78 & 4.79, a relation for the wall shear stress based on the tangent velocity at the node above the wall is given by

$$\tau_w = \rho u_\tau^2 = \rho C_\mu^{\frac{1}{4}}\sqrt{k_{tke}}\frac{\bar{u}_t}{\frac{1}{\kappa}\ln(n^+)} \tag{4.80}$$

This is a necessary boundary condition for closure of the momentum equations.

Through the viscous sublayer, $u^+$ is best predicted instead with $u^+ \propto n^+$ for $n^+ \leq 5$. For the log-law region ($n^+ \geq 30$), Equation 4.79 applies, and a polynomial fit used to form a smooth transition between the two regions.

$$\begin{array}{lcll} u^+ & = & n^+ & n^+ \leq 5 \\ u^+ & = & d_1(n^+)^3 + d_2(n^+)^2 + d_3 n^+ + d_4 & 5 \leq n^+ \leq 30 \\ u^+ & = & \frac{1}{\kappa}\ln(n^+) + C & n^+ \geq 30 \end{array} \tag{4.81}$$

The typical fitting constants used with the log-law wall model are shown in Table 4.2 [156] For a reasonable estimation of the wall shear stress, the first node away

| **Constant** | **Value** |
|---|---|
| $C$ | 5.2 |
| $\kappa$ | 0.41 |
| $d_1$ | 6.426E-04 |
| $d_2$ | -5.2113E-02 |
| $d_3$ | 1.4729 |
| $d_4$ | -1.1422 |

Table 4.2: Turbulent wall function closure constants.

from the wall must be located in the log-law region at a distance, $\Delta n$, such that $30 \leq n^+ \leq 500$.

The thermal boundary layer is similarly approximated with a different log-law function for predicting the wall heat flux, $q''_w$, not including radiation, for use in closure of Equation [156]

$$q''_w = \frac{\rho c_p u^+}{T^+}(T_w - T_f) \tag{4.82}$$

where $T_w$ is the wall temperature, and

$$T^+ = \mathrm{Pr}_T n^+ \exp(-\Gamma) + [2.12\ln(n^+) + \beta]\exp\left(-\frac{1}{\Gamma}\right) \tag{4.83}$$

The resistance to enthalpy flow through the laminar sublayer is [4]

$$\beta = (3.85(\mathrm{Pr}_T)^{\frac{1}{3}} - 1.3)^2 + 2.12\ln(\mathrm{Pr}_T) \tag{4.84}$$

$$\Gamma = \frac{0.01((\mathrm{Pr}_T)n^+)^4}{1 + 5(\mathrm{Pr}_T)^3 n^+} \tag{4.85}$$

The wall heat flux is then multiplied by the flux element face surface area to obtain the total energy transferred to the flux element.

Kumar has presented a sensitivity study investigating temperature differences predicted in a tunnel fire scenario with different values of wall roughness. A lack of information on selecting $\beta$ for construction materials typical in compartment fires was reported [168]. The greatest differences between predicted and experimental temperature were found as distance down the tunnel from the fire increased due to heat loss over the large surface area of the tunnel. Cox reports that the use of wall functions for fire applications involving natural convection, surface mass loss and heated surfaces have not been sufficiently investigated [4].

### 4.4.3 Radiation Transfer

The problem of calculating radiation transfer in a fire can be divided into two parts. First, the local temperatures and soot concentrations must be determined. Second, a model must be employed to calculate the emission, absorption and scatter of incident radiation through the domain. This part of the problem is addressed with the introduction of the fundamental equation of radiation transfer. For our purposes, solids are assumed to be gray with all incident radiation absorbed at the surface. Numerical solutions for radiation transfer can be found in [169].

The spectral emissivity as a function of temperature for a gas mixture can be found from Hottel [170], or with band models that divide the thermal spectrum into a number of small intervals [171]. deRis discusses when it is appropriate to treat flames and smoke as gray [56]. The effective absorption coefficient for a polystyrene flame is relatively independent of path length, and thus can be treated as gray, as can polypropylene and PMMA. For fuels that burn cleaner with less soot, (methane and polyoxymethylene), the gray gas assumption is clearly not appropriate. An additional problem with determining grayness is that the chemical composition of the flame depends on the scale of fire; determining if a gas mixture is gray requires evaluation of more than just the fuel [171]. In general, for engineering work a homogeneous gray volume described by an average temperature and gray absorption-emission coefficient can approximate most flames.

The effects of turbulence on flame radiation have been investigated [172]. In addition to fuel and chemical reaction parameters, radiant energy transport also depends on the localized flow field. The straining rate of small (Kolmogorov microscale) eddies is important for soot formation, since it is at this scale that most of the burning in a turbulent diffusion flame takes place [171]. Data correlation supports the conclusion that soot concentrations in thin turbulent diffusion flames are controlled

not by macroscopic residence times, but by the Kolmogorov time scale.

For a beam of radiant energy of intensity $i'$, and wavelength, $\lambda$, passing through an absorbing, emitting and scattering volume, the change in intensity in the solid angle, $d\omega$, over a path S is given as [173]

$$\frac{di'_\lambda}{dS} = -K_\lambda i'_\lambda(S) + a_\lambda i'_{\lambda b}(S) + \frac{\sigma_{s\lambda}}{4\pi}\int_0^{4\pi} i'_\lambda(S,\omega_i)\phi(\lambda,\omega,\omega_i)d\omega_i \tag{4.86}$$

where $K = a_\lambda + \sigma_\lambda$ is the extinction coefficient and accounts for absorption and scattering. The intensity associated with blackbody emission at a temperature, $T_w$, is $i'_{\lambda b}$, and $\phi(\lambda,\omega,\omega_i)$ is the probability that radiation will be scattered in the $\omega$ direction along the solid angle $\omega_i$. Define the last two terms as the source function, $I'_\lambda$, representing the increase in intensity along the path S from emission and inscattering

$$I'_\lambda(\kappa_\lambda,\omega) \equiv (1-\Omega_{0\lambda})i'_{\lambda b}(\kappa_\lambda) + \frac{\Omega_{0\lambda}}{4\pi}\int_0^{4\pi} i'_\lambda(\kappa_\lambda,\omega_i)\phi(\lambda,\omega,\omega_i)d\omega_i \tag{4.87}$$

with the optical depth defined as

$$\kappa_\lambda(S) = \int_0^S K_\lambda(S^*)dS^* \tag{4.88}$$

and the albedo for scattering

$$\Omega_\lambda = \frac{\sigma_\lambda}{K_\lambda} = \frac{\sigma_\lambda}{a_\lambda + \sigma_\lambda} \tag{4.89}$$

The radiation transfer equation (RTE) is then

$$\frac{di'_\lambda}{d\kappa_\lambda} + i'_\lambda(\kappa_\lambda) = I'_\lambda(\kappa_\lambda,\omega) \tag{4.90}$$

The terms that go into altering the intensity of the beam are attenuation due to absorption and scattering during travel along $dS$, emission and finally the radiation in-scattered along $\omega$ from all directions. This integrates to

$$i'_\lambda(\kappa_\lambda) = i'_\lambda(0)\exp(-\kappa_\lambda) + \int_0^{\kappa_\lambda} I'_\lambda(\kappa^*_\lambda,\omega)\exp[-(\kappa_\lambda-\kappa^*_\lambda)]d\kappa^*_\lambda \tag{4.91}$$

with application of $\exp(\kappa)$ as an integrating factor.

Throughout the discretized fluid domain, a statement of conservation of energy is applied at every node location. While solving the energy equation to eventually obtain the temperature distribution, the divergence of the radiant flux, $\nabla\cdot q''_r$, appears in the energy equation as a source term. The divergence at a node is then found from the local intensity

$$\nabla\cdot q''_r = \int_{\lambda=0}^{\lambda=\infty} a_\lambda\left(4\pi i'_{\lambda b} - \int_{\omega=0}^{\omega=4\pi} i'_\lambda(\omega,\kappa_\lambda)d\omega\right)d\lambda \tag{4.92}$$

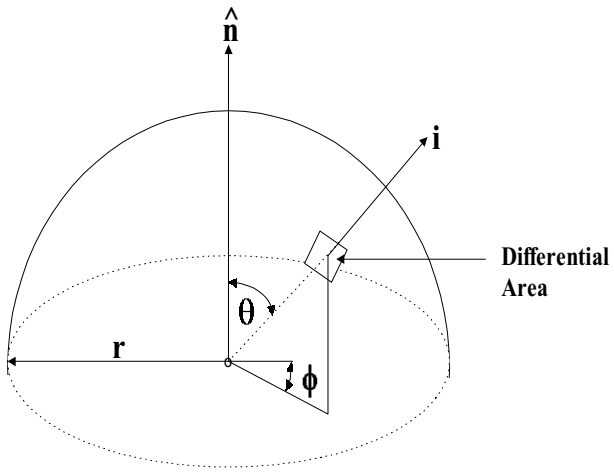


Figure 4.11: Intensity through differential area on hemisphere.

Closure necessitates integration of Equation 4.90 for $di'_\lambda$, then integration of Equation 4.92 over $4\pi$ steradians and finally integration over all wavelengths. For a finite difference grid with thousands of control volumes, performing this triple integration for every iteration is not realistically possible with current computer resources.

The radiation models to be discussed are all simplifications that provide relief from performing a triple integration for every control volume at each time step. For CFD modeling of fires, the temperature and species concentration distribution necessary to calculate the radiant transfer will be determined by a solution of the discretized conservation equations that include a number of approximations based on simplified models or experimental data.

Some form of finite quadrature will still be necessary to reduce the computational demands necessary for determining the radiation source term. Not only is the spatial calculation of the radiation intensity a problem, but it is the radiation source term going into the energy equation that ultimately yields the temperature. This coupling makes solving for both much more difficult.

A mean beam approximation would be satisfactory for a well-mixed enclosure, such as a furnace, but more general analysis of radiation is required when the bounding surfaces are not all at the same temperature and the fluid volume is non-isothermal. The discrete transfer model is currently the most popular among fire modelers, although the finite volume transfer method holds promise of increased accuracy, especially for non-orthogonal grids.

### Diffusion and surface to surface models

Both the optically thick and optically thin extremes of radiation transfer permit simplifications to be made to the solution of the radiation transfer equation. When a nonparticipating fluid occupies the space between surfaces at different temperatures (the classic oven problem), a surface to surface model is appropriate. An example of this type of environment where the fluid is transparent to radiation at the principle emitting wavelengths is the heating of room walls and floor due to solar radiation through a window. Such an environment would not, however, be representative of a fire since a significant portion of the fluid volume actively participates at wavelengths where a majority of the heat transfer occurs.

At the other end of environments, the fluid is optically thick enough such that each control volume is only able to transfer radiation energy between its six neighbors with intensity independent of direction. Radiation transfer to boundaries only results from control volumes in direct contact with the boundary. In this case, the diffusion model treats radiation transfer analogous to conduction. The region directly surrounding a sooty diffusion flame such as in a coal combustion furnace is a typical application of the diffusion model. Although very computationally efficient, the model can not be expected to provide accurate surface flux predictions over a fuel due to an optically intermediate gas volume above the surface. In actual testing with TASCflow, this was found to be the case.

### Flux models

The flux model is particularly well suited for use in the rectilinear grids commonly found during CFD modeling of fire in compartments. Differential equations are formulated for the radiant energy transfer only along the coordinate axes [174]. A six flux model then tracks radiation transfer only along the x, y and z axis, although formulating the model becomes very complex for non-rectilinear coordinate systems. For heat transfer from a hot upper layer to the floor, the flux model is expected to give much better results than when used to determine the forward heat transfer during flame spread, which occurs at an angle to the axis.

### Discrete transfer models

This model retains the basic ideas of the flux model, but without the restriction of transfer only along the axis [175]. Radiation transfer is solved along rays selected *a priori*, as opposed to a Monte Carlo method where the rays would be selected at random. As with the flux model, if the discretization is fine enough, the discrete transfer method will approach an exact solution.

Taking the length, $dS$, that a ray travels through a differential control volume, Lockwood defines the elemental optical depth as $dS^* = k_e dS$ plus a modified emissive power,

$$E^* = \frac{1}{k_e}\left(k_a \sigma T_g^4 + \frac{k_s}{4}\int_{4\pi} i'(S,\omega_i)\phi(\lambda,\omega,\omega_i)d\omega_i\right) \tag{4.93}$$

and then rewrites the equation of radiation transfer 4.90 as

$$\frac{di'}{dS^*} = -i' + \frac{E^*}{\pi} \tag{4.94}$$

Rays are traced from points $Q_1, Q_2...$ on a hemisphere around point $P_i$ that is located at the center of a control volume face on one of the boundaries. Equation 4.94 is used to calculate the intensity of radiation from $Q_1 \rightarrow P_1$, $Q_2 \rightarrow P_1$ etc. for all of the locations selected by the user. Figure 4.12 shows the general layout of the discrete transfer method. As the rays pass through control volumes that are assumed isothermal, the source-sink contributions are calculated using the intensity determined above. The total source-sink for a cell, $\nabla \cdot q_r$, in the conservation of energy equation is then the sum of the contributions from all of the rays that pass through it [175]. Taking $E^*$ as also being constant within a control volume (not unreasonable since most variables are assumed constant through the control volume), integration of Equation 4.94 gives

$$i' e^{S^*} = \frac{E^*}{\pi} e^{S^*} + \text{constant} \tag{4.95}$$

This can be discretized to give the intensity leaving, $i'_{n+1}$, based on the intensity entering, $i'_n$, a control volume

$$i'_{n+1} = i'_n e^{-\delta S^*} + \frac{E^*}{\pi}(1 - e^{-\delta S^*}) \tag{4.96}$$

where $\delta S^*$ is the optical length for control volume $n$ (the length of ray traversing the control volume). This equation is then applied repeatedly as the ray is traced from $Q_1$ to $P_1$. For control volume j, the net quantity of energy lost by the cell from a given ray i is [176]

$$S_{j,i} = (i'_{j+1} - i'_j) cos\theta A_i d\omega_i \tag{4.97}$$

where $A_i$ the area of the control volume face. The net source-sink is the summation of the number of rays, $k_j$ which pass through the control volume $j$ that has volume $\Delta V_j$

$$\int_{\Delta V_j} \nabla \cdot \vec{q_r} dV = \int_{A_j} \vec{q_r} \cdot d\vec{A_j} = \sum_{i=1}^{k_j} S_{j,i} \tag{4.98}$$

In an effort to conserve computing resources, it maybe necessary to solve for radiation transfer on a grid coarser than that used for the fluid problem.

### Finite Volume

The Finite Volume radiation transfer model of Raithby [177] uses the same mesh developed by the user for the fluid flow prediction to produce a fully conservative set of relations for radiant heat transfer in non-isothermal participating media. Non-orthogonal grids that are difficult to use with most transfer methods are easily treated.

Starting from the RTE written for the change in intensity of a pencil of radiation with cross sectional area $dA^n$ as it passes through a hexahedral control volume, the

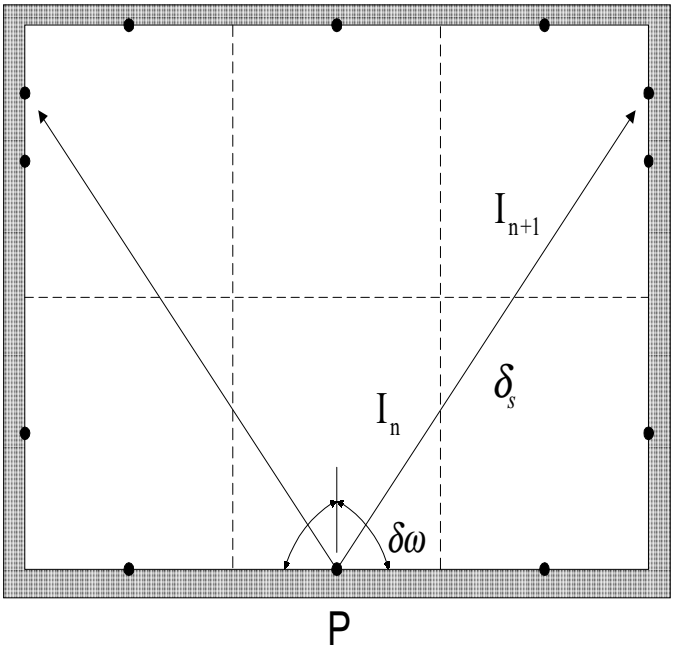


Figure 4.12: Discrete transfer method.

intensity at node P from integrating the RTE over a discrete solid angle $\omega$ is

$$\int_{\omega}\int_{A_{S,P}} i'_S(\mathbf{s}\cdot\mathbf{n})dA_s d\omega = \int_{\omega}\int_{dV}\left[-(a+\sigma_s)i' + ai'_b + \sigma_s\bar{i}'\right]dV\,d\omega \tag{4.99}$$

$A_{s,p}$ and V are the surface area and volume of control volume P. Quadrature is performed by dividing $A_{s,p}$ into a finite number of surface panels each containing a centered integration point, f, as shown in Figure 4.13. The ray passing through f is then traced back to a location, uf, where the intensity can be found by interpolation between nodal values. For simple two-dimensional enclosure problems containing a participating medium, very good agreement was observed with exact analytical solutions for course grids, producing between linear and quadratic improvement in the prediction as the grid was refined.

### 4.4.4 Radiation Properties

Now that the equations to treat radiation transfer are in place, it is necessary to consider how properties such as the coefficients for absorption, emission and scattering will be determined throughout the domain. Radiation properties are a complex function of temperature, composition, pressure and wavelength. It is this complex character of the absorption coefficient as a function of wavelength that produces difficulty in determining the value to be used for solution of the RTE.

The ABSORB model of Modak is available to compute the absorptivity and emissivity of homogeneous isothermal mixtures of $CO_2$, $H_2O$ and soot based on total

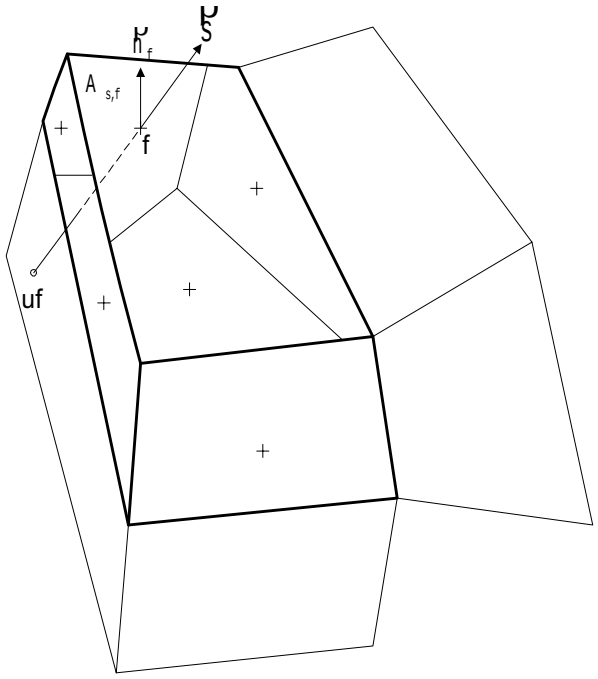


Figure 4.13: Finite volume transfer method.

emissivity curve fits of exponential wide band model results [112]. Approximations are completed using three parameter (temperature, partial pressure and pressure-pathlength) Chebyshev polynomials

$$\ln \epsilon_g = \sum_{i=0}^{2} T_i(x) \sum_{j=0}^{3} T_j(y) \sum_{k=0}^{3} c_{ijk} T_k(z) \tag{4.100}$$

with $x = 1 + \frac{\ln p}{3.45}$, $y = \frac{2.555 + \ln pl}{4.345}$, $z = \frac{T - 1150}{850}$, $T_o(x) = 1$, $T_1(x) = x$, and $T_{n+1}(x) = 2xT_n(x) - T_{n-1}(x)$. The absorptivity is then calculated from the emissivity using the approximation suggested by Hottel by taking into account the fraction of water vapor, $\zeta = \frac{p_w}{p_w + p_c}$,

$$a_g = \epsilon_g \left( \frac{T}{T_s} \right)^{0.65 - 0.2\zeta} \tag{4.101}$$

The curve fit relations are valid for temperatures of 300 $K$ to 2000 $K$ and pressure pathlengths of 0.0011 to 1.0 atm meter. Soot absorptivity is approximated using the soot concentration, $k_o$, measured at wavelength, $\lambda_o$, the path length, $l$, and a blackbody source temperature, $T_s$:

$$a_s = 1 - \frac{15}{\pi^4} \psi^3 \left( 1 + \frac{\lambda_o k_o T_s l}{c_2} \right) \tag{4.102}$$

along with $c_2$, Planck's second constant, and $\psi^3$, the pentagamma function. The

absorptivity of the mixture is then approximated as

$$a = a_s + a_g - a_s a_g \tag{4.103}$$

The agreement between the approximate absorption coefficient calculated by ABSORB and a full spectral integration for a mixture of $CO_2$, $H_2O$ and soot is shown in Figure 4.14. The non-spectral calculations of ABSORB produce results in two orders of magnitude less time than the full spectral calculation.

If the accumulated hot upper layer of gases in a compartment are considered homogeneous, ABSORB is expected to give very good results. Pathlengths will be on the order of the room dimension, about 1 to 3 meters, and pressure pathlengths close to .3 atm-meter are well in the region of close agreement between the exponential wide band model and ABSORB.

ABSORB has been used to predict the local absorption coefficient for each node throughout a discretized CFD domain based on local node fluid temperature, a blackbody source temperature, and concentrations of soot, $CO_2$, and $H_2O$ [111, 168]. The conditions throughout each control volume were considered homogeneous with representative path lengths on the order of .05 meters. Pressure path lengths as low as .005 atm-meter result, which for temperatures expected in compartment fires, approach the lower limit of applicability. This is a region where the disagreement between the approximate calculation and the curve fit in ABSORB can be as great as 25%. For pressure pathlengths less than .0011 atm meter, ABSORB assumes the absorptivity is zero; this is not an option when grid refinement is used. Also, the radiation source temperature, $T_s$, is required to determine the absorption coefficient from the emission coefficient in Equation 4.101. This too is a problem for CFD modeling of fire.

In terms of resolution, one step below line by line models and above wide band models are the narrow band models. Instead of carrying out the spectral integration over each line (wavelength), the spectrum for each species is divided into intervals on the order of 25 $cm^{-1}$ in which the spectral lines are assumed to have a random distribution. With the strength of the band following an exponential probability distribution, the emissivity for the interval, $\Delta\nu$, is [171]

$$\epsilon_{\Delta\nu} = 1 - \exp\left[-\frac{\left(\frac{S}{d}\right)X}{\sqrt{1+\left(\frac{S}{d}\right)\left(\frac{X}{B_d P_e}\right)}}\right] \tag{4.104}$$

when the path is homogeneous with a pressure pathlength $X$. $P_e$ is the line broadening pressure correction and $B_d$ is the mean line-width to spacing ratio times $\pi$. Averages for the mean line intensity to spacing ratio, $\frac{S}{d}$, taken along a path provide the Curtis-Godson approximation (equivalent length of isothermal absorbing gas used to replace a non-isothermal volume) for non-homogeneous mixtures. Grosshandler [178] has assembled a narrow band model called RADCAL using both theoretical approximations and tabulated spectral properties. The results of this model have been used

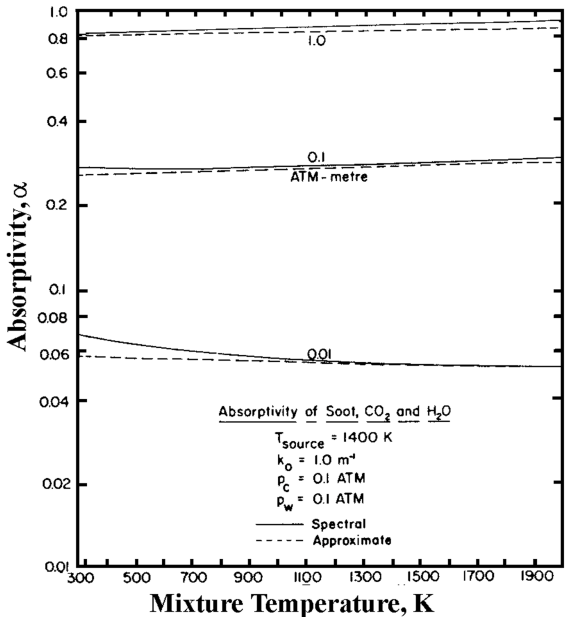


Figure 4.14: Modak ABSORB wide band model curve fit results versus spectral calculations [112] .

to generate input data for simpler models, and also serve as a benchmark to models for non-homogeneous gas volumes [179]. Soot absorptivity is treated as in ABSORB.

The range of path lengths accepted by RADCAL to assure the model stays close to experimental data is $10^{-4}$ to $10^{3}$ meters. Characteristic lengths associated with discretization of compartments for fire prediction are well within this range. While RADCAL could predict accurately the radiation properties in each control volume, the drawback is increased computer time demands. The Curtis-Godson approximation along with the Goody statistical narrow band model have been shown to have calculation times approaching two orders of magnitude longer than a simplified method such as the total transmittance non-homogeneous model [180], and approximately one order of magnitude over ABSORB.

### 4.4.5 Soot Production

Soot concentrations account for 70% or more of the total emitted radiation from solid fuel flames, showing the importance of properly predicting soot created as a result of incomplete combustion. Source terms representing the formation and consumption of soot can be modeled with an Arrhenius equation where $p_f$ is the fuel partial pressure [181],

$$S = C_f p_f \phi^n \exp\left(-\frac{E}{RT}\right) \tag{4.105}$$

The problem is, however, what values to use for the fuel specific constant, $C_f$, and the local equivalence ratio, $\phi$. This is not difficult for well-characterized fuels like

methane; however, complex solid fuels such as furniture do not admit themselves to such basic treatment.

The modeler can look toward flamelet modeling to provide soot production rates by relating soot source terms to mixture fraction based on kinetic rate equations [182]. The problem is determining the required multi-step rate equations necessary for the prediction. While the necessary flamelet libraries exist for simple gaseous fuels, the process is more difficult for determining the steps with solid combustion.

Product yield rates, $\psi$, for common gas, liquid and solid fuels have been published and offer a simple way for determining the generation rate of combustion products using relations of the form $\dot{m}_{\text{soot}} = \psi_{\text{soot}} \dot{m}_{\text{fuel}}$ [183]. The problem with such a simplified approach is that the smoke yield is highly dependent on the local burning conditions, especially the availability of oxygen, radiant flux, etc. Until a point is reached where smoke and soot production from solid fuels other than PMMA can be reasonably well predicted, the fire modeler will continue to depend upon experimental data for assistance. Babrauskas discusses many of the difficulties associated with using yield values to predict soot production [1].

The issue of taking small scale HRR and production data from a test under well ventilated conditions and using it to predict large scale behavior under different orientations and environments needs to be addressed [184]. The early stages of fire growth should be better predicted than times closer to flashover where combustion becomes ventilation controlled. Mulholland found that the smoke production rate in large scale for solids and liquids followed small scale cone calorimeter results when the mass loss rates per unit area were equal for both large and small scale [149]. Increasing the irradiance level during cone testing allows a higher mass loss rate to be achieved. In general, smoke production has been shown to be correlated between the cone calorimeter and full scale testing and the furniture calorimeter and standard room test [124, 145, 149].

Smoke produced by a sample burning in the cone calorimeter is measured dynamically with a monochromatic laser that provides results as the extinction coefficient, $k_e$,

$$k_e = -\frac{1}{l} \ln \left( \frac{I}{I_o} \right) \tag{4.106}$$

where $l$ is the path and the difference between the incident intensity emitted by the laser $I_o$ and that passing through the smoke flow that reaches the detector, $I$, is recorded. Since fuel mass loss, $\dot{m}_f$, and volumetric flow rate in the exhaust, $\dot{V}$, are recorded, a measure of the extinction area (cross section) of the smoke per unit mass of fuel burned can be derived

$$\sigma_f = k_e \frac{\dot{V}}{\dot{m}_f} \tag{4.107}$$

The specific extinction area, $\sigma_f$, is a measure of smoke generated by the combustion of a unit mass fuel. Mulholland found that the variation in specific extinction area with scale was small [149], which is important since no other variable used to characterize smoke shares this feature [185]. In addition, $\sigma_f$ is independent of $l$, $\dot{V}$, total fuel mass lost, and the surface area undergoing pyrolysis [2].

The specific extinction area can also be reported based per unit mass of soot,

$$\sigma_s = \frac{k_e}{C_s} \tag{4.108}$$

and using the definition of the mass concentration of soot, $C_s$, from [186],

$$C_s = \frac{\rho_s k_e \lambda}{\bar{c}} \tag{4.109}$$

gives

$$\sigma_s = \frac{\bar{c}}{\rho_s \lambda} \tag{4.110}$$

The average coefficient of particulate extinction, $\bar{c}$, has been found to be approximately 7.0 for many common fuels [186]. The same study also showed that a linear relation exists between $C_s$ and the soot volume fraction, $f_v$ for a variety of solid, liquid and gaseous fuels. The constant coefficient relating the two is the particulate (soot) density, which was found to be $1.1 \pm 0.1 \frac{g}{cm^3}$ over a range of almost three orders of magnitude for $C_s$. The specific extinction area per unit mass soot, $\sigma_s$, should then be close to 6400 $\frac{m^2}{kg \text{ soot}}$, which is near the value of 7600 $\frac{m^2}{kg \text{ soot}}$ recommended by Seader and Einhorn for flaming fires based on small scale tests [187]. Beyler shows, however, that $\sigma_s$ is in fact not constant, but instead was found to be a function of the soot yield, $\psi_{\text{soot}}$ [188]. For the fuels tabulated by Tewarson, Beyler shows that $\sigma_s$ is actually fit well by [183]

$$\sigma_s = 10,750 \exp(-4.95 \psi_{\text{soot}}) \tag{4.111}$$

The two specific extinction areas can be related by $\sigma_f = Y_{\text{soot}} \sigma_s$. Using the value of $\sigma_f$ derived from the experimental cone calorimeter results, plus the soot yield dependent value of $\sigma_s$ given above, provides a way of deriving a time dependent soot yield for modeling based on experimental results

$$\sigma_f = \psi_{\text{soot}} \left(10,750 \exp(-4.95 \psi_{\text{soot}})\right) \tag{4.112}$$

and can be solved for the soot yield given the measured value of $\sigma_f$. Figure 4.15 shows the value of the soot yield during cone testing of a PU foam sample with a flame retardant cover. Values for both a constant value of $\sigma_s$ and one that varies as a function of $\psi_{\text{soot}}$ from Equation 4.112 are shown.

### 4.4.6 Combustion

A one step Eddy Breakup (EBU) model for combustion takes advantage of the flame sheet approximation by assuming that the rate of reaction is much faster than the rate of mixing for fuel and oxidizer [189]. The characteristic chemical time for reaction in a diffusion flame, $\tau_c$, is expected to be on the order of micro seconds ($10^{-5}$ or $10^{-6}$ seconds) versus a physical mixing time, $\tau_g$, that would be measured in seconds [4].

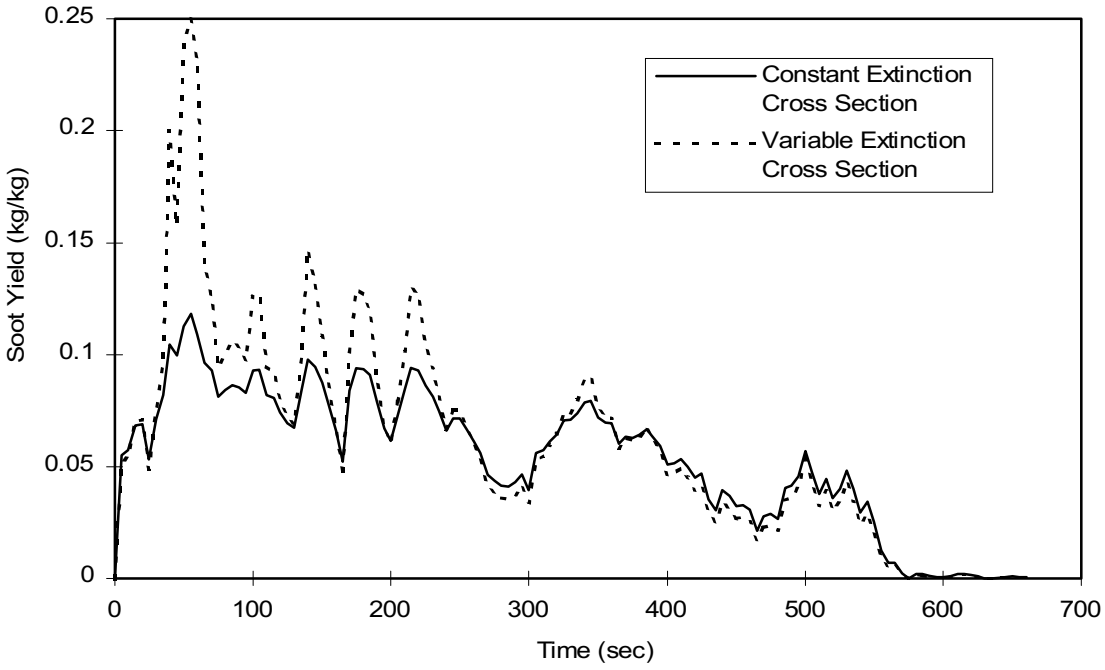


Figure 4.15: Particle extinction cross section.

When controlled by the small scale subgrid rate of mixing, the reaction for premixed flames can be approximated as:

$$S_f = -\rho C \left(\frac{\epsilon}{k}\right) (\bar{Y}_f')^2 \tag{4.113}$$

where $(\bar{Y}_f')^2$ is the mean square fuel mass fraction fluctuation. When diffusion flames are modeled, a slightly different form is used that depends on only mean quantities:

$$S_f = -C\rho \frac{\epsilon}{k} \min\left[Y_f, \frac{1}{s}Y_o, AY_fY_o \exp\left(-\frac{E}{RT}\right)\right] \tag{4.114}$$

with dimensionless constant $C$ usually close to 4.0, but actually $C = 23.6\left(\frac{\mu\epsilon}{\rho k^2}\right)^{\frac{1}{4}}$. The rate of small scale turbulent mixing between fuel and oxidizer and the smaller of the fuel, oxygen or product time mean fraction controls the rate of reaction. To obtain the most accurate estimate of the generation of products of incomplete combustion, finite rate kinetics could be applied. When the reaction rate is much slower (approaching the mixing time), products of incomplete combustion so important to fire safety engineering are generated.

Combustion adds a source term to the energy equation when both fuel and oxidizer exist in a control volume under conditions that allow burning. No attempt is made to solve the complete array of kinetic equations for combustion of a complex fuel. In most cases the appropriate rate equations are not even known.

When opposed flow flame spread occurs at or near the extinction limit [27], such

a combustion model can not be expected to capture all of the necessary details to insure accurate results. The gas phase reaction rate, and to a lesser degree the fuel and oxidizer mixing rate, control the forward progress of the reaction. When looking at upward or concurrent flame spread, kinetics are important for locating the flame since it is the heating of the fuel ahead of the pyrolysis front that produces rapid spread. Detailed chemical kinetic information is much less important in this case since the rate of fuel preheating drives the rate of spread.

The laminar flamelet model [154] holds promise, even for fuels encountered in fire safety engineering, although some form of simplified reaction mechanism will probably be necessary for some time [155]. It would be desirable to use such a PDF method for combustion, but after a thorough literature search, it was determined that although the laminar flamelet model may work for the solid fuels of interest to fire safety, it still has not received enough attention. If a series of simplified reaction steps for PU foam could be identified along with the necessary reaction rate information, it would allow more realistic modeling of combustion. Improvements in the prediction of toxic gas and soot production could be expected.

### 4.4.7 Conjugate Heat Transfer

Fire in a compartment causes energy transfer both in the fluid filling the enclosure and through solids such as the lining materials or fuels. In TASCflow, diffusion of heat between the solid and fluid is treated with the specification of Conjugate Heat Transfer (CHT) boundary conditions. The energy transport relation (Equation 4.17) is applied to the fluid, while diffusion is responsible for energy transfer in the solid

$$\frac{\partial(\rho_s c_s T)}{\partial t} = \frac{\partial}{\partial x_j}\left(k_s \frac{\partial T}{\partial x_j}\right) + S_T \tag{4.115}$$

or in discretized form

$$\rho_s c_s \mathrm{Vol}\left(\frac{T - T^o}{\Delta t}\right) = \sum_{ip}\left(k_s \frac{\partial T}{\partial x_j}\vec{n_j}\right)_{ip} + \bar{S}_T \mathrm{Vol} \tag{4.116}$$

where $\vec{n_j}$ is the outward normal surface vector [156]. A grid is created through the solid regions just as is done in the fluid, and boundary conditions must be specified on all faces separating the fluid and solid. The temperature and energy fluxes at the interface are determined as an implicit part of the calculations. Boundary conditions must also be given to all solid surfaces that are exposed to the exterior (outside of the computational domain), rather than the fluid. A full discussion of CHT boundary conditions will be given in the next chapter on the Numerical Simulation of Furniture Fires.

## 4.5 CFD Modeling of Fire

It is important to outline the current status of CFD modeling of fire and smoke transport, to put the current work in historical prospective. Excellent reviews on the subject of CFD and fire can be found in [4, 163, 190, 191].

### 4.5.1 Comparison with Experiment

Aspects of fire phenomenon have been successfully modeled using CFD. Some of the first work on the modeling of fire with CFD was carried out by Spalding [189] at Imperial College, and as part of this effort, the Eddy-Break-up model used for diffusion flame combustion was developed. Some of the first CFD modeling of fire also involved investigation into buoyant driven flow in enclosures [163, 166]

Railway tunnel fires have been predicted using FLUENT with results compared to the Zwenberg tunnel fire tests [192]. Unfortunately, HRR measurements were not made for the 2.6 $m$ square petroleum pool fire used during testing and were assumed to equal between 20.3 $MW$ and 25 $MW$ for 2 $\frac{m}{sec}$ and 4 $\frac{m}{sec}$ forced airflow, based on similar tunnel modeling by Kumar and Cox [193]. A uniform gas absorption coefficient of 1 $m^{-1}$ was used throughout the domain. The 390 meter tunnel was modeled with 30 to 60 nodes in the length direction, where results were found to agree qualitatively with experiment and improved further from the fire and as the grid was refined. Upward of 50,000 nodes are recommended for modeling the tunnel tests, instead of the 5,000 used for the study. Differences between test and model, especially for temperature, show that the current approach to the problem would be inappropriate for design work without large factors of safety. Improved combustion, radiation and heat transfer would be required along with more accurate boundary condition specification and a significantly refined grid.

High heat release rate (100 $MW$) fires have been modeled as a heat and mass source in tunnels with forced ventilation [194]. Although experimental data was available, insufficient information was known about the tests to allow complete specification of the boundary conditions. Transportation vehicles such as planes and trains have been modeled [195], as have large jet fires during the analysis of passive fire protection for offshore oil drilling facilities [196].

A decommissioned nuclear containment vessel in Germany has been used for both forced and naturally ventilated fire tests [197]. Fuel oil in pans was used as the fire source with mass loss rates, but not heat release rates, measured. Input to the model for the heat and mass source was based on the output of a zone model. Combustion was not treated, the gas was considered non-participating and turbulence was addressed with a simple algebraic mixing length model. Temperature values were reasonable, but consistently overpredicted, while vent velocities were overpredicted by up to 40%.

By far, the CFD code that has been compared to the greatest number of experiments is JASMINE. This has included standard rooms with a vent [198, 199], hospital wards [200, 201], rack storage [202], tunnels [168, 201], and a forced ven-

tilation fire test cell [165, 201]. Smoke movement in large structures has also been modeled with general success [203, 204]. What is important about this work with JASMINE is that there is an effort to find the reasons why CFD model results differ from experiment. What is still lacking, though, is some type of sensitivity study that evaluates the change in results to different input variables. In general, results agree with experiment, with the greatest differences noted closer to the fire source.

Ceiling jets formed by fire in a compartment are important for determining the activation of detection and suppression equipment, plus the prediction of rapid fire growth across combustible ceiling linings. Kumar has studied fluid flow and heat transfer under confined and unconfined ceilings [205]. JASMINE was able to match the results of Motevalli and Marks to within 20% in the turning region with results improving as the distance from the plume centerline increased. Differences were attributed to numerical diffusion. Also, the $k - \epsilon$ turbulence model was possibly in error at the point of impingement.

Plumes have proven difficult for modeling with CFD due to problems with the $k - \epsilon$ turbulence model; this subject has already been discussed in Section 4.4.1. Turbulent diffusion flames have also been treated with two equation turbulence models [206].

It is the coupled interaction of fluid flow, combustion and heat transfer that controls the quality of simulation results. Kumar has shown that an accurate representation of radiation is necessary for correct fluid flow predictions [199]. As an example, doorway mass flow rate predictions significantly improved when more detailed (6-flux) radiation transfer calculations were included in the simulations. The radiation transfer model also requires a realistic estimation of the absorption and emission characteristics of the fluid; this evaluation is non-trivial. Steady state predictions show, in general, much better agreement with experiment than transient data.

Compartment fire generated smoke movement has been one of the more frequently attempted CFD modeling problems [190, 191, 207, 208, 209, 210]. Again, general agreement between model results and experiment were noted for temperatures and velocities. Some of the cases were modeled with no combustion or radiation, which makes the agreement curious. Very little has been done to compare the results of different CFD models on the same problem. Pehrson [211] compared five commercial CFD codes used to model the Steckler room fire experiments [212], and found that door centerline velocities agreed extremely well between codes, while the door centerline and room corner temperatures differed by about 30%. Differences in the shape of the horizontal door velocity profile were noted. Since the grids were similar, other effects such as advection term discretization could be important. The mass weighted skewed upstream advection scheme was found to improve door velocity profile predictions compared to the upwind and hybrid differencing methods.

### 4.5.2 Fire Reconstruction and Design

One area in which CFD models are seeing more use is in the calculation of smoke generation and movement for atrium and smoke control applications. Atrium smoke control standards may include requirements for the size of the design fire [213] for which specification of the source terms in the CFD code is somewhat easier. Smoke control strategies were investigated by Cox [214] for an atrium planned in a large leisure center. A significant issue of traditional atrium smoke control design method of a steady 5 $MW$ fire was additional entrainment predicted to result from mixing caused by galleries located on the sides of the space. This resulted in smoke removal fans becoming overwhelmed. Also predicted, but not considered by traditional atrium design standards, is plume deflection caused by differential entrainment resulting from doors open in the base of the atrium.

In addition to tunnel design, CFD has been used to predict tunnel ventilation shaft conditions during a fire [215]. Several constant heat sources were used for 2-D simulations with FLUENT and compared to results from the Subway Environment Simulation, a 1-D model for natural and forced tunnel ventilation. Velocities were found to be in agreement, but temperatures were significantly different.

Fire in power generation spaces is a serious concern, especially when it involves nuclear energy. Huhtanen has used PHOENICS to predict pool fire conditions in a turbine hall [216]. Control volume sizes on the order of a meter were used to model the complicated space with a total of 8,000 nodes. The calculated heat release rate from the 100 $m^2$ pool was 180 $MW$. Very low temperatures in the area of the flame were attributed to numerical diffusion resulting from the coarse grid.

### 4.5.3 Suppression

One of the ultimate goals anticipated for the union of CFD and fire modeling is the prediction of suppression within a compartment. Modeling the discharge from a sprinkler and its interaction with the enclosure environment until the water reaches the fuel surface is one of the more difficult tasks currently envisioned. Sprinkler spray interaction with a compartment environment has been attempted from both the Lagrangian and Eulerian approaches [217, 218, 219]. The effect of venting on sprinkler spray has been investigated [220], as have other suppression systems such as water mist [221]. Also of importance is the interaction of sprinkler spray with hot gas upper layers found, for example, in atria spaces [222].

In general, current computer resources preclude the modeling of suppression for engineering work since computation times for even a relatively coarse grid can be measured in weeks. Without substantial improvements in solver technology, much faster hardware or the use of parallel computers would be necessary.

# Chapter 5

# Numerical Simulation of Furniture Fires

Based on the discussion in Chapters 2 and 3, the spread of flame on a solid surface is an exceedingly complicated problem involving many reactions and processes that have yet to be fully quantified. While flame spread has received considerable research, it is still not amenable to a solution based completely on first principles and is not expected to change in the near future. Empirical tools have been successful in ranking material performance, while other thermal models provide HRR and transient mass loss predictions acceptable for some engineering work. Physical and chemical reactions involved in the process such as radiation transport, species production and fluid flow are difficult to quantify and are often addressed in limited ways by simplified models. This chapter focuses on how the furniture CFD model addresses these issues.

## 5.1 Numerical Model Treatment of Physics

Solution of the conservation equations throughout the computational domain determines the rate of fuel combustion and resulting fluid motion and heat transfer. The most important result produced for flame spread is the heat flux to the wall, $\dot{q}''_{wall}$, providing the driving force for evaluating the rate of fire growth. Coupled with the fluid flow is a simultaneous solution for energy transfer in the solid fuel as part of the process for determining the heat flux to the wall.

To allow for modification of the core code, TASCflow includes a number of user source routines that provide access to nearly all portions of the code. These user source routines were modified to incorporate fire growth physics permitting physical treatment of flame spread. The current section discusses general aspects of TASCflow involved in the fluid flow and heat transfer predictions, along with numerical approximations for the processes important to flame spread.

### 5.1.1 Fluid Flow

Discretization of the fluid domain with a finite volume formulation naturally leads to a control volume around each node. Given that the properties within each control volume are considered homogeneous, it is reasonable to treat each as an independent parcel of fluid. With the Eulerian view, the control volumes are fixed in space, so the CFD code tracks the movement of mass, momentum, species and energy from volume to volume through control surfaces at the boundaries.

The fluid above the solid fuel provides a region where the combustion reaction can take place. Once the pyrolysis products are released from the surface, they are in a position to mix with air while being heated from the nearby flame. Initially the fuel occupies a region that is too rich to burn, but the action of mixing and diffusion reduce the concentration of fuel to a point where it can burn.

A complex mixture of pyrolysis products is produced by the heating of foam and fabric during a furniture fire, with the actual rate of consumption of fuel depending on both the reaction rate and the speed at which fuel and oxidizer are mixed. Once heated to ignition, oxidation of the gaseous fuel leads to the generation of products of combustion. The intermediates and products of combustion are a complex function of the rate of reaction and local conditions.

The conservation equations for mass, momentum, energy and species are derived in a conservative finite volume formulation for incompressible flow, Equations 4.31 to 4.34 as discussed in Section 4.2. A multi-component fluid is modeled, such that a scalar equation is solved for each mass fraction $Y_{\text{fuel}}, Y_{O_2}, Y_{CO_2}, Y_{H_2O}, Y_{\text{soot}}$, and $Y_{N_2}$, for application in the combustion reaction predictions. Discretization for the diffusion terms uses a shape function formulation and the Mass Weighted Skewed Upstream (MWS) scheme for advection term differencing as discussed in Section 4.2.2. The numerical solver used in TASCflow sequentially solves all scalar equations as individual segregated units. At the start of each iteration, however, the mass and momentum equations are solved first in a coupled fashion. In a compartment with a furniture fuel package, the range of velocities expected lead to only infinitesimal changes in fluid volume. For an ideal incompressible fluid (which is assumed in all cases considered here), the thermodynamic state of the fluid is specified uniquely by temperature since pressure is no longer an independent thermodynamic property.

Subgrid fluid motion and turbulence are modeled with the $k_{tke} - \epsilon$ model. Turbulence model closure constants usually employed for general engineering work have been modified to improve agreement for plumes and ceiling jets using the results of Nam and Bill described in Section 4.4.1. While these results can not be considered general for all fire modeling, they still serve as the best guide until more research is conducted. The log-law wall function approximation is applied to estimate the shear stress and temperature at the wall, both necessary boundary conditions at the solid-fluid interface as discussed in Section 4.4.2.

### 5.1.2 Solid Heat Transfer

Regions in the computational domain specified as solid are discretized in the same way as the fluid domain; however transport equations for mass, momentum, and species are not solved. This leaves a modified form of the energy equation for heat diffusion in a solid. Radiant energy will reach the surface from the flame, and for furniture testing, a gas burner or other ignition source. Especially for upward spread, the orientation of the flame increases heat transfer to solid fuel that has not yet ignited. Conduction and convection through the gas phase will also heat the solid close to the flame front. Surface emission will be present during preheating, which can delay the onset of ignition.

The spread of flame across a surface is a transient process represented by a continuous advancement of the flame front. Upon reaching a sufficient temperature, the solid will begin to lose mass through pyrolysis. The greater the heating through the action of an external flux or solid conduction, the larger the value of mass loss. During heating, the more volatile fractions of the fuel are released first with lower volatile fractions requiring additional heating for vaporization. Left behind, in some cases, is char and other residuals. Especially for furniture materials, the surface may undergo structural changes. Fabric materials can melt or break open exposing the foam, which may be consumed at a much faster rate than other solids.

A conjugate heat transfer (coupled fluid and solid heat diffusion) problem is required to predict the temperature distribution at the surface of the solid fuel. A discretized form of the heat diffusion equation given by Equation 4.116 is solved in three dimensions.

Thermal properties for the fabric and foam materials come from different sources as show in Section A.1 of Appendix A. Temperature dependent values are used in the solid conduction calculations for $c_s$, and $k_s$, while constant values are used for $\rho_s$. A subroutine called propt.f has been written to carry out such calculations as shown in Section B.11 of Appendix B. It is visited at the start of every iteration to update both fluid and solid node thermal property values.

Just as it is too computationally expensive to completely resolve a solid-fluid boundary layer with nodes, the same applies to fabrics with a thickness of a millimeter or two resting on top of the foam. Full scale testing shows that fabric may not always be the first component ignited. Fabrics that split, such as cotton, or melt and pool like synthetics, may expose the foam. This real behavior is outside the scope of a numerical solution at the current time. Ideal fabric reaction to fire will be assumed, such that the covering remains completely on top of the foam. For modeling, the fabric was divided with several nodes to capture the temperature gradient through the material, and allow determination of the surface temperature. The foam below was discretized with a much coarser grid on the order of a centimeter to estimate heat loss into the solid.

### 5.1.3 Transport Processes

#### Radiation Transfer

The finite volume radiation model, Section 4.4.3, has been implemented in TASCflow to determine the radiation source term, $\nabla \cdot q_r$, for the energy equation. Rays are traced through the domain, with changes due to absorption and emission (scattering is ignored) evaluated as the ray passes through each control volume.

#### Radiation Properties

The products of combustion above a burning fuel are non-homogeneous when evaluated at length scales on the order of the problem geometry. Based on the definition of a control volume, the fluid that occupies each control volume is considered homogeneous for the calculation of radiation transfer and properties as discussed in Section 4.4.4. To allow radiation properties to vary as a function of local species concentration throughout the computational domain, two different property models have been implemented.

The most computationally efficient of the two models is the exponential wide band curve fit model of Modak [112]. Included are contributions from soot, $CO_2$ and $H_2O$ as a function of temperature and pressure path length. When the grid is refined, shorter path lengths result, reducing the accuracy of the model and giving estimates that are outside the range of the original curve fits.

The RADCAL model of Grosshandler has also been implemented in TASCflow, although it places a significantly greater demand on computer resources [178]. In some cases, RADCAL may have calculation times approaching half the fluid solution, a completely unsatisfactory situation. Species included in the calculation are soot, $CO_2$, $H_2O$, CO, and $CH_4$. The model has been optimized, however, to improve performance when calculating properties for problems of interest to fire safety. Because most of the frequent changes in absorption coefficient occur in only a limited region, namely the fire and plume, much of the problem domain has properties that are close to ambient or contain slowly changing species concentrations. For engineering purposes, neither situation requires a recalculation of the absorptivity for each iteration. In addition, the concentration of emitting species in a control volume may be so small that they are not a significant participant in the absorptivity calculations. Changes made to RADCAL to improve performance include:

- The user can specify the minimum concentration for each species that is necessary for the program to calculate the contribution by that species. This prevents using computer resources to determine the absorptivity for minor participants.
- Additional computer resources can be saved by not recalculating the absorptivity in parts of the domain where species concentrations are changing very slowly, if at all. A user defined percent change in concentration is available that requires a fractional change in concentration before recalculation.

- The frequency of recalculating absorptivity based on a user supplied number of iterations is available.
- Absorptivity values are also updated only at the start of a time step. There is no need to continually recalculate the absorptivity with every inner loop calculation, when the code may only be working to improve the hydrodynamic solution.

With these changes in place, calculation time for RADCAL can be reduced by an order of magnitude, resulting in computational demands no larger than ABSORB. Generally, less than 10 to 20% of the nodes receive an updated absorption coefficient at any given time step using the controls shown in Table 5.1. Test runs have been completed and shown to change the absorption coefficient and overall results by less than 5% with increased iterations.

| Item | Value used |
|---|---|
| Minimum mass fraction of species $CO_2$, $H_2O$, CO, and $CH_4$ | $1E10^{-5}$ |
| Minimum mass fraction of soot | $1E10^{-10}$ |
| Percent change in species concentrations before recalculation of absorptivity | 5-7.5% |
| Iteration frequency for RADCAL | 5 |

Table 5.1: RADCAL controls used to decrease computation time.

#### Species, Momentum and Energy Diffusion

The viscosity of gaseous species is only moderately temperature dependent and can be evaluated through Sutherland's relation for viscosity, Equation 4.24. The calculations are included in the user source code propf.f as shown in Section B.8 of Appendix B. The thermal conductivity for each fluid species is also calculated in propt.f using Sutherland's equation, although with different constants.

Gas dependent mass diffusion coefficients are calculated in propq.f, to account for mass transfers due to concentration gradients in the multi-component fluid. Soot and fuel species are given values for methane. The transport properties for mass, momentum and heat diffusion in the fluid are updated at the start of each iteration for all non-solid nodes.

### 5.1.4 Source Terms

The transport equation for scalar $\phi$ takes the following form as covered in Section 4.1.

$$\frac{\partial}{\partial t}(\rho\phi) + \frac{\partial}{\partial x_j}(\rho u_j \phi) = \frac{\partial}{\partial x_j}\left(\Gamma \frac{\partial \phi}{\partial x_j}\right) + S_\phi \tag{5.1}$$

The volumetric source term, $S_\phi$, accounts for changes in $\phi$ through the control volume due to effects other than transient, convective and diffusive transfers. It is through the source terms that the user is able to access all of the governing equations to incorporate physics that are not included in the general purpose CFD code TASCflow.

To allow for blockages within the domain, TASCflow applies boundary conditions, CHT solids, and user source terms over flux elements, and not control volumes. This allows specification from one node to the next, and prevents the difficulties associated with the creation of boundary conditions applied over partial control volumes. As discussed in Section 4.2.1, a flux element face is comprised of the area enclosed by 4 nodes and a collection of 6 such faces with 8 nodes encloses the flux element volume. Boundary conditions are specified over flux element faces, while blockages and user source terms are applied on a volumetric basis using whole flux element volumes. The source terms to be discussed below are therefore all defined in a volumetric fashion, Figure 5.1.

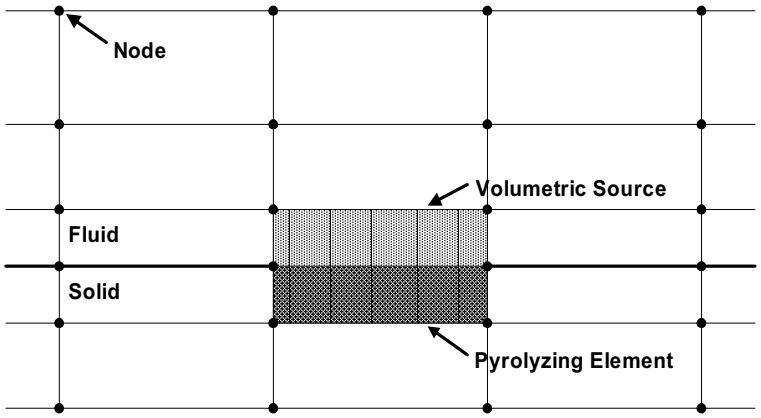


Figure 5.1: Cross sectional view of volumetric source application.

### 5.1.5 General Boundary Conditions

Interior control volumes do not contact edges of the domain, thus do not require any special boundary condition treatment. The conservation equations are assembled for each control volume surrounding a node, with fluxes through the control surfaces determined at the integration points as shown in Figure 5.2. The corresponding control volume and integration points for a boundary are shown in Figure 5.3, where the flow of a given conserved quantity through a flux element is evaluated at four interior integration points based on conditions at the neighboring nodes. Calculated fluxes at each integration point are inserted into the surrounding octants for assembly of the control volume equations.

Standard CFD boundary conditions available in TASCflow have been specified throughout the domain and are discussed in detail elsewhere [4, 156, 159]. Basically, five different boundary conditions have been applied to flux element faces:

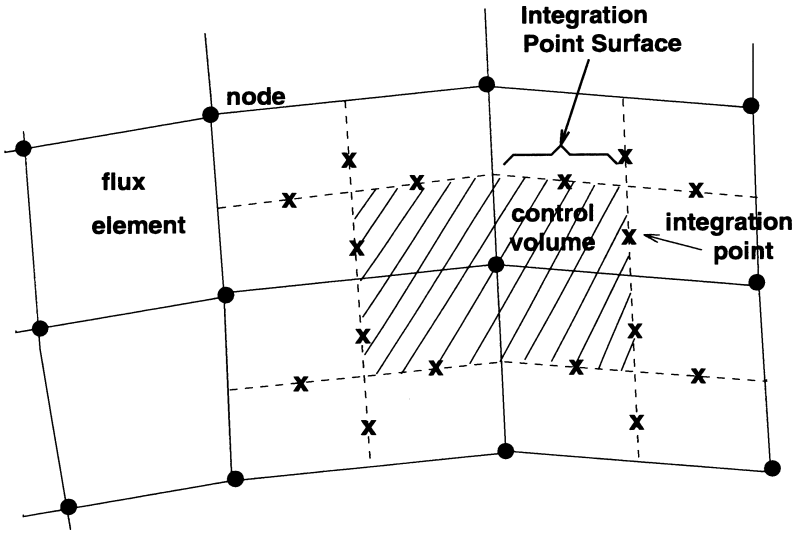


Figure 5.2: Interior control volume [156] .

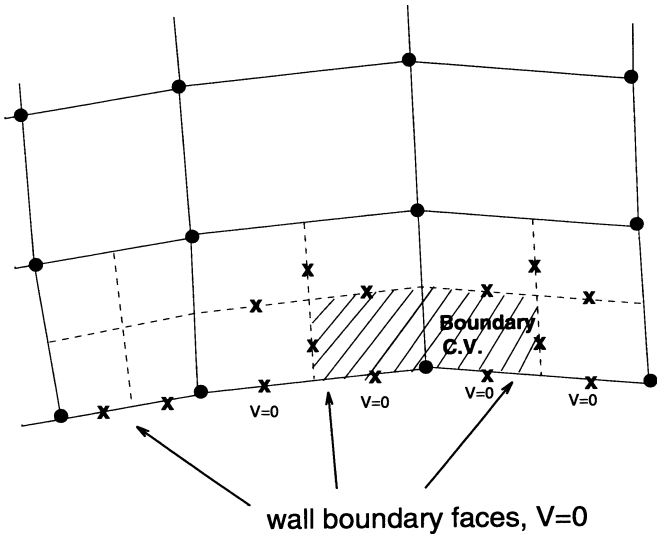


Figure 5.3: Boundary control volume [156] .

- An **opening** boundary allows bi-directional fluid flow based on conditions near the domain interface that are an implicit part of the calculation. Boundary conditions (temperature, species concentration, turbulence intensity and length scale, etc.) are specified by the user for flow into the domain, while properties for fluid leaving are based on fully developed local conditions as determined by the model.

- **Outlets** are openings to the computational domain that allow fluid to leave, but not enter. An example is the top of the hood in the furniture calorimeter where the fan produces a reduced pressure that induces a mass flow from the test apparatus. In this case, the mass flow is not known in advance, but instead the outlet boundary condition is defined with an average or total pressure less than ambient over the region. The specific pressure difference selected determines the total mass flow through the hood to match that outlined in the test method or measured during the testing for the furniture calorimeter discussed in Section 3.6.2.

- **Inlet** boundaries allow flow with user specified properties to enter the computational domain. The fuel flow rate from the burner in terms of $\dot{m}$, $T$, $Y_i$, and $u, v, w$ are specified over the region.

- Stationary **walls** prevent mass transfer since the surface is considered impermeable to fluid flow. A no-slip stipulation constrains the fluid velocity and normal viscous force to zero on the surface. Tangent to the wall, the viscous force (momentum flux) is evaluated based on the wall shear stress computed by the log-law boundary layer velocity profile (Section 4.4.2). Surface pressure forces are based on interpolated control volume values. Also at walls, the flux of species, $\phi_i$, and $k_{tke} - \epsilon$ is zero, while energy can be transported into the solid wall through diffusion. A wall can be adiabatic, $\frac{\partial T}{\partial n} = 0$, have $T_w$ or $\dot{q}''_w$ specified, or include a solid phase energy solution (CHT) for which $T_w$ and $\dot{q}''_w$ are an implicit part of the calculation.

- **Symmetry** along a plane in the problem domain can be put to use in reducing the computational demands of the problem. A chair with central ignition source burning in the furniture calorimeter may have mid-plane symmetry running down the center between the armrests. In this case, the fluid velocity normal to the symmetry plane goes to zero, $u_i n_i = 0$, such that $\dot{m} = 0$. Similarly, the viscous stresses tangent to the symmetry boundary are also zero, $\tau_t = 0$, as are normal gradients $\frac{\partial \phi}{\partial n} = 0$.

A summary of the boundary conditions applied is given in Table 5.2. The solution of the solid and fluid boundary conditions at the interface above a fuel surface warrants additional discussion as follows.

| BC Type | Mass and momentum | Energy | Turb-ulence | Scalar | Where applied |
|---|---|---|---|---|---|
| Opening | $P_{total}$ (inlet)<br>$P_{stat}$ (outlet)<br>$u_i = f(u_n, \frac{\partial p}{\partial x})$ | $T_{user}$ (inlet)<br>$T_{fluid}$ (outlet) | $T_u$ & $L_\epsilon$ specified for inlet | $\phi_{user}$ (inlet) | Openings below hood skirt |
| Outlet | $P_{static}$ (ave) | $T_{fluid}$ | $T_u$ & $L_\epsilon$ of fluid | $\phi_{fluid}$ | Fan outlet |
| Inlet | $u_i$ normal to surface | $T_{inlet}$ specified | $T_u$ & $L_\epsilon$ specified | $\phi_{user}$ | Burner |
| Wall CHT | log-law | CHT, $\dot{q}''_{wall}$ by code | log-law | $\frac{\partial \phi}{\partial x} = 0$ | Hood & fuel |
| Wall Adiabatic | log-law | $\dot{q}''_{wall} = 0$ | log-law | $\frac{\partial \phi}{\partial x} = 0$ | Floor |
| Symmetry | $u$,$v$,$w$ & $p$ symmetry | $\frac{\partial t}{\partial n} = 0$ | $k_{tke}$ & $\epsilon$ symmetry | $\frac{\partial \phi}{\partial n} = 0$ | Mid-plane |
| CHT Exterior | No fluid flow on exterior | $\dot{q}'' = h(T - T_\infty)$ $h$ specified | N.A. | N.A. | CHT solid exterior |

Table 5.2: Boundary condition application.

### 5.1.6 Coupling of Gas and Solid Energy Boundary Conditions

The coupling of energy equations for fluid and solid is critical since this produces the forward wall heat flux driving the rate of fire growth. The fluid control volume solution will be covered first, followed by that for the solid, and then coupling between fluid and solid.

#### Fluid Control Volumes

Repeating the time averaged energy relation, Equation 4.55,

$$\frac{\partial}{\partial t}(\rho \bar{h}) + \frac{\partial}{\partial x_j}(\rho \bar{u}_j \bar{h} + \rho \overline{u'_j h'}) = \frac{\partial \bar{p}}{\partial t} + \frac{\partial}{\partial x_j}\left(\frac{k_g}{c_p}\frac{\partial \bar{h}}{\partial x_j}\right) + \bar{S}_E \tag{5.2}$$

the turbulent convective energy flux term, $\rho \overline{u'_j h'}$, represents the additional heat transfer due to turbulence. In the momentum equation, the turbulent momentum flux term, $-\rho \overline{u'_i u'_j}$, that is formed by time averaging can be treated as an apparent turbulent stress, $(\bar{\tau}_{ij})_{turb} = -\rho \overline{u'_i u'_j}$ as shown in Equation 4.59. The same can be done with the energy equation by combining the turbulent convection term with conduction

$$\frac{\partial}{\partial t}(\rho \bar{h}) + \frac{\partial}{\partial x_j}(\rho \bar{u}_j \bar{h}) = \frac{\partial \bar{p}}{\partial t} + \frac{\partial}{\partial x_j}\left(\frac{k_g}{c_p}\frac{\partial \bar{h}}{\partial x_j} - \rho \overline{u'_j h'}\right) + \bar{S}_E \tag{5.3}$$

The addition of the turbulent convective flux term requires modeling to provide closure of the energy equation. No additional transport equations will be written to evaluate $\rho\overline{u_j'h'}$ (unlike the two written for $-\rho\overline{u_i'u_j'}$). Instead an algebraic model will be employed that uses the gradient diffusion assumption [4]

$$\overline{u_i'\phi'} = -\Gamma_\phi \frac{\partial \bar{\phi}}{\partial x_i} \tag{5.4}$$

were the turbulent, or eddy, diffusivity, $\Gamma_\phi$, is a function of the flow, and not the fluid. The effects of turbulence on the transport of momentum can be approximated as an increased viscosity, namely the turbulent viscosity, $\mu_T$. Implicit in Equation 5.4 is the assumption of isotropic turbulence with both $\mu_t$ and $\Gamma_\phi$ independent of direction (a poor assumption for buoyancy driven flows). A similar gradient diffusion assumption can be made to treat the heat transfer resulting from turbulence by an increased conductivity; the apparent (eddy) turbulent conductivity, $k_T$

$$\rho\overline{u_j'h'} = -\frac{k_T}{c_p}\frac{\partial \bar{h}}{\partial x_j} \tag{5.5}$$

Define the turbulent Prandtl number as

$$\mathrm{Pr}_T \equiv \frac{\mu_T c_p}{k_T} \tag{5.6}$$

to relate the turbulent diffusivities for momentum and heat transport. $k_T$ is still unknown, but can be related to the momentum diffusivity, $\mu_T$, through Equation 5.6

$$\rho\overline{u_j'h'} = -\frac{\mu_T}{\mathrm{Pr}_T}\frac{\partial \bar{h}}{\partial x_j} \tag{5.7}$$

This is not a completely satisfactory situation since $\mathrm{Pr}_T$ is generally unknown and is usually (arbitrarily) set equal to some constant value. A total energy flux vector can be defined as

$$\dot{q}_j'' \equiv \frac{k_g}{c_p}\frac{\partial \bar{h}}{\partial x_j} - \frac{\mu_T}{\mathrm{Pr}_T}\frac{\partial \bar{h}}{\partial x_j} \tag{5.8}$$

which includes both conduction and turbulent heat transfer and will be of assistance later when specifying boundary conditions.

A similar approximation is made in relating the scalar species diffusivity, $\Gamma_\phi$, to viscosity, $\mu_T$, through the turbulent Schmidt number (which relates viscous transport to mass diffusion)

$$\Gamma_\phi = \frac{\mu_T}{\mathrm{Sc}_T} \tag{5.9}$$

where

$$\mathrm{Sc}_T = \frac{\mu_T}{D_T} \tag{5.10}$$

and $D_T$ is the species turbulent diffusion coefficient.

Constant $\mathrm{Pr}_T$ values of 0.9 to 1.0 are often assumed for the bulk flow based on similarities between viscous and heat transport. A small amount of support in selecting values is available from experimental data. $\mathrm{Pr}_T \approx 0.7$ may be more appropriate for plumes and mixing layers since smaller $\mathrm{Pr}_T$ are observed when stronger adverse pressure gradients are experienced, although $Pr_T$ is known to increase through the boundary layer near a wall. If the Lewis number is defined to relate mass to thermal diffusion,

$$\mathrm{Le}_T = \frac{c_p D_T}{k_T} \tag{5.11}$$

then $\mathrm{Pr}_T = \mathrm{Sc}_T \mathrm{Le}_T$. A value for $\mathrm{Le}_T$ of unit is usually assumed, for which $\mathrm{Sc}_T = \mathrm{Pr}_T$. Energy and species conservation equations are now closed for bulk flow, but not on boundaries since $\dot{q}''_j$ in Equation 5.8 has yet to be specified.

Determination of the total heat flux to the wall, $\dot{q}''_w$, is necessary as the thermal boundary condition between fluid and solid CHT regions. For non-adiabatic walls, evaluation of the heat flux through the fluid-solid interface is complicated by the existence of the boundary layer. Just as the wall shear stresses were determined by approximating the shape of the velocity boundary layer between the wall and nearest node, the wall heat flux is similarly evaluated with assumptions about the corresponding turbulent thermal boundary layer temperature profile.

The wall heat flux not including radiation from Equation 4.82 is approximated as

$$q''_w = \frac{\rho c_p u^+}{T^+}(T_w - T_f) \tag{5.12}$$

with $T^+$ given by Equation 4.83. The value of $T_w$ results from evaluation of heat diffusion in the solid.

### Solid Control Volumes

The solid control volume energy relation given by Equation 4.115

$$\frac{\partial(\rho_s c_s T)}{\partial t} = \frac{\partial}{\partial x_j}\left(k_s \frac{\partial T}{\partial x_j}\right) + S_T \tag{5.13}$$

is applied through the discretized solid domain. At fluid boundaries the node temperature, $T$, is replaced by the wall temperature, $T_w$, which now couples Equation 5.13 to Equation 5.12 as part of the wall heat flux calculations. At the fluid-solid interface, radiation heat transfer also results in energy exchange as a wall flux, $\dot{q}''_{w,rad}$, as calculated by the radiation transfer model, and similarly coupled through $T_w$.

### Coupled Solution

The wall heat flow (from fluid to solid) at a given integration point is evaluated as

$$Q_{w,ip} = A_{ip}\left(\dot{q}''_w + \dot{q}''_{w,rad}\right) \tag{5.14}$$

with $A_{ip}$ the area surrounding the integration point. Employing Equation 5.12, the total heat flow is

$$Q_{w,ip} = A_{ip}\left(\frac{\rho c_p u^+}{T^+}(T_w - T_f) + \overline{\frac{\partial \dot{q}_j^R}{\partial x_j}}\right) \tag{5.15}$$

The divergence of the flux terms can be approximated at the integration points on the fluid-solid interface

$$\frac{\partial}{\partial x_j}\left(\dot{q}''_w + \dot{q}''_{w,rad}\right) \approx \sum_{ip}\left(\frac{\rho c_p u^+}{T^+}(T_w - T_f)\Delta n_j\right)_{ip} + \sum_{ip}\left(q_{w,rad}\Delta n_j\right) \tag{5.16}$$

with application of the divergence theorem to convert the volume integrations into surface integrals that can be evaluated at each face.

A coupled fluid-solid boundary calculation is carried out with $T_w$, $\dot{q}''_w$, and $\dot{q}''_{w,rad}$ determined as an implicit part of the calculation. The CHT interface boundary condition allows heat transfer between the fluid and solid, since the $\dot{q}''_w$ lost by the fluid node next to the surface is the same as $\dot{q}''_w$ gained by the solid node, and vise versa. The assembled system of equations is solved for every node during each iteration.

### Boundary Condition with Pyrolysis

Two criteria are used to predict ignition of a control surface (flux element face):

1. Based on the solid heat conduction calculations, a surface temperature on the solid at the fluid interface is calculated. When this temperature exceeds the ignition temperature for the fabric, ignition is assumed.

2. The radiation heat transfer model calculates the flux incident upon each flux element face, a second option for specification of ignition. When the external flux level reaching the surface exceeds the experimental flux, ignition results. A table of ignition time versus flux data is, however, necessary.

Values for the critical ignition temperature and flux for foam-fabric materials are given in Section A.1 of Appendix A. The solver in TASCflow allows the solid phase conduction solution to be coupled with the fluid flow prediction for treatment of boundary conditions and calculation of the wall heat flux.

With the inclusion of pyrolysis from a surface, the coupled CHT energy solution described by Equation 5.16 is used to compute the energy flux at the interface. The energy lost due to pyrolysis can be considered with addition of a source term in the solid energy equation that depends on the latent heat of pyrolysis, $\Delta H_p$:

$$S_E = -\Delta H_p \frac{\partial \rho_s}{\partial t} \tag{5.17}$$

The mass loss rate from the surface can be approximated by a zeroith order Arrhenius rate, Equation [4]

$$\frac{\partial \rho_s}{\partial t} \approx -A\rho_s \exp\left(-\frac{E_s}{RT_s}\right) \tag{5.18}$$

requiring knowledge of $A$ and $E_s$. Data for all but simple fuels is scarce, and will not be included as a source term in TASCflow. Instead, mass loss rate data based on cone calorimeter testing provides the pyrolysis closure as described in the next Section.

### 5.1.7 Source Term Calculation

#### Mass

Mass can be neither created nor destroyed, appearing to negate the necessity for a mass source term. However, it can be used to address a solid pyrolyzing surface that is introducing mass to the fluid phase. Directly above the surface, mass is not created, but instead transferred from the solid into the fluid boundary layer. With fire growth over a surface, the flame front movement results in each element face experiencing a different mass loss history depending on when ignition occurs. Unfortunately, for a surface containing 1000 element faces, this would require the specification of 1000 boundary conditions, not an efficient process. Instead, a mass source term can be utilized that allows the flame spread process to be coded into a single routine, usrsrc.f, which will be fully discussed shortly.

When ignition occurs at a given flux element, the surface begins to pyrolyze following the mass loss rate curve measured in the cone calorimeter, $\dot{m}''_{bs}(x, y, z, t)$. The $(x, y, z, t)$ is included to emphasize the fact that the transient value of $\dot{m}''_{bs}$ depends on location and is different for each flux element face.

In reality, fuel is released within the solid and travels through any char (not modeled) until it enters the fluid boundary layer above the surface. Numerically this is approximated by adding the fuel to the flux element directly above the surface with a volumetric source term, $S_{\text{fuel}}(x, y, z, t)$. A different source term can be applied over each flux element face $(x, y, z)$, which allows for the consideration of a growing fire. $S_{\text{fuel}}(x, y, z, t)$ is applied through a volume,

$$S_{\text{fuel}}(x, y, z, t) = \dot{m}''_{bs}(x, y, z, t) \left( \frac{A_{FE}}{\text{Vol}_{FE}} \right) \tag{5.19}$$

where $A_{\text{FE}}$ is the flux element face area at the solid-fluid interface and $\text{Vol}_{FE}$ is the volume of the flux element directly above the interface. As the solid pyrolyzes, a char layer may form due to the release of volatiles. Such a moving boundary problem is not considered by the calculations.

Mass loss rate data from the cone calorimeter is only gathered at a finite number of fluxes, such as 25, 35, and 50 $\frac{kW}{m^2}$. The model, however, is not limited to a few discrete levels, but instead predicts a continuous range of flux values. When mass loss rates at untested flux levels are necessary, linear interpolation is used for evaluation of $\dot{m}''_{bs}(x, y, z, t)$ between curves. For predicted fluxes below the lowest cone value, the cone data for the smallest flux is used. Should the model predict fluxes greater than tested, the cone data at the peak flux is applied.

Scaling of the cone data to account for differences in tested sample thickness adds to the difficulty in relating bench and full scale times. For example, the mass

loss rate at 100 seconds measured by the cone does not directly relate to the mass loss from a given part of the surface of the furniture at 100 seconds. Time as measured in the cone calorimeter does not relate directly to time in the model. When compared to the time variable fluxes in full scale, the difference is due to the constant flux imposed by the cone.

If time does not directly relate bench and full scale, what does? Either total mass or total energy lost appear to be possible alternatives since they could represent how far along combustion has proceeded. The greater the mass or energy lost, the longer the fuel has been pyrolyzing since ignition. Maintaining uniformity with other assumptions made in the model, total mass lost will be used as a substitute for time to determine position on a cone calorimeter curve.

An example is necessary to clarify how the model will carry out these calculations. Assume the mass loss rates measured in the cone calorimeter as shown in Table 5.3. Consider a single surface element on the furniture in the model. If during the

| **Time** (sec) | **Mass loss rate at 25** $\frac{\mathbf{kW}}{\mathbf{m^2}}$ $\left(\frac{\mathbf{kg}}{\mathbf{m^2 s}}\right)$ | **Total mass lost at 25** $\frac{\mathbf{kW}}{\mathbf{m^2}}$ $\left(\frac{\mathbf{kg}}{\mathbf{m^2}}\right)$ | **Mass loss rate at 35** $\frac{\mathbf{kW}}{\mathbf{m^2}}$ $\left(\frac{\mathbf{kg}}{\mathbf{m^2 s}}\right)$ | **Total mass lost at 35** $\frac{\mathbf{kW}}{\mathbf{m^2}}$ $\left(\frac{\mathbf{kg}}{\mathbf{m^2}}\right)$ |
|---|---|---|---|---|
| 0 | 0 | 0 | 0 | 0 |
| 1 | .1 | .1 | .2 | .2 |
| 2 | .1 | .2 | .4 | .6 |
| 3 | .2 | .4 | .6 | 1.2 |
| 4 | .2 | .6 | .8 | 2.0 |
| 5 | .2 | .8 | 1.0 | 3.0 |

Table 5.3: Sample cone calorimeter mass loss data

first 4 seconds after ignition the element is exposed to a flux of 25 $\frac{kW}{m^2}$, it will have a mass loss rate of .1 $\frac{kg}{m^2 s}$ over the first two seconds and a mass loss rate of .2 $\frac{kg}{m^2 s}$ from 3 seconds to 4 seconds. Summing, the total mass lost during these 4 seconds is thus .6 $\frac{kg}{m^2}$. Now say the flux increases to 35 $\frac{kW}{m^2}$. What is the mass loss rate for the next second? If the value is taken from the 35 $\frac{kW}{m^2}$ cone results at 4 seconds, the mass loss rate is .8 $\frac{kg}{m^2 s}$. But at this point the 35 $\frac{kW}{m^2}$ cone curve has already lost 2.0 $\frac{kg}{m^2}$. Thus it is not physically realistic to simply move between cone curves based on time since a discontinuity in total mass lost from the sample would result. Instead the model locates the same total mass lost on the 35 $\frac{kW}{m^2}$ curve and occurs at 2 seconds. The mass loss rate would then be .4 $\frac{kg}{m^2 s}$. Irrespective of the flux history of an element, the mass loss rate instead depends on the total mass lost. The total mass lost is considered the "history" of the element.

The data input file for the model also requires a heat of combustion and soot yield associated with the mass loss rate at each time step. An example of the full data input file for the model is shown in Appendix B.3 on Page 268. Once the correct mass loss rate is found as explained in the example above, the soot yield and heat of

combustion associated with the mass loss rate are used for that time step.

How the model uses the heat of combustion and soot yield data warrants additional discussion. Once ignited, each fuel surface element releases mass at the above described rate. All of these elements have different ignition times and mass loss rate histories, yet they all release pyrolysis products to be burned in the region above the fuel surface. The combustion model determines the rate at which this fuel is consumed. Distributed combustion results since the model, and not the user, determines where fuel is consumed. Fuel that is burned in a given control volume, however, has been derived from any number of control surfaces and over a wide range of times. At issue is what heat of combustion and soot yield should be used at this point since it would be fruitless to try and track the point of origin of all fuel. Instead an average value is calculated and applied throughout the domain.

After the model has calculated the mass loss rate at the start of a time step, the corresponding heat of combustion and soot yield for each surface is determined as the value corresponding to the mass loss rate. All of the heat of combustion values are averaged based on weighting that takes into account the mass loss rate from the surface. A similar procedure is use for soot yields. For example, based on the values in Table 5.4, the heat of combustion and soot yield throughout the domain for this time step would be 17.5 $\frac{MJ}{kg}$ and .313 $\frac{kg}{kg}$ respectively.

| **Element number** | **Mass loss rate** $\left(\frac{\mathbf{kg}}{\mathbf{m^2 s}}\right)$ | $\mathbf{\Delta H_c}$ $\left(\frac{\mathbf{MJ}}{\mathbf{kg}}\right)$ | $\mathbf{Y_{soot}}$ $\left(\frac{\mathbf{kg}}{\mathbf{kg}}\right)$ |
|---|---|---|---|
| 1 | .1 | 10. | .1 |
| 2 | .2 | 15. | .2 |
| 3 | .5 | 20. | .4 |
| **Average** | | 17.5 | .313 |

Table 5.4: Heat of combustion and soot yield averaging procedure used throughout the domain.

### Momentum

Pyrolysis of a fuel surface imparts an outward normal velocity on the mass leaving the surface. Since the real processes is much too difficult to address with a first principles approach, the initial fuel velocity can be approximated with an appropriate momentum source term, $S_u$

$$S_u(x,y,z,t) = \frac{[\dot{m}''_{bs}(x,y,z,t)]^2}{\rho_{\text{fuel}} A_{FE} \text{Vol}_{FE}} \tag{5.20}$$

where $S_u$ is applied to the $u$, $v$, or $w$ momentum conservation equation depending on the orientation and direction of the surface. Momentum per unit volume is imparted upon the mass of the flux element above the surface of the burning flux element face

such that a mass flux of $\dot{m}''_{bs}(x,y,z,t)$ is able to pass through an area $A_{FE}$ in time $t$. Since each flux element face has a different $\dot{m}''_{bs}(x,y,z,t)$ and $A_{FE}$, each will also have a different momentum source, $S_u(x,y,z,t)$.

**Energy**

The enthalpy of the fuel added to the flux element volume above the pyrolyzing surface can be included with a source term applied to the energy equation, $S_E$,

$$S_E(x,y,z,t) = \frac{\dot{m}''_{bs}(x,y,z,t)c_p(T_g - T_s)}{\mathrm{Vol}_{FE}} \tag{5.21}$$

where $T_g$ is the temperature of the gaseous fuel, usually assumed equal to the pyrolysis temperature. It is also necessary to include a similar enthalpy per unit volume term in the solid to account for energy loss due to pyrolysis and phase change. A user supplied $\Delta H_c$ is provided based on the code data to allow calculation of the solid energy source term.

**Species**

The distributed release of energy as a function of fuel and oxidizer reaction is predicted through the use of a combustion model. When a unit mass of fuel reacts with oxygen in a control volume, it is converted into products of combustion, with associated release of energy. For the one step irreversible reaction mechanism assumed (Equation 5.26), the scalar species considered are limited to $CO_2$, $H_2O$ and soot. The mass of species added per unit volume to a flux element where fuel is burned is

$$S(x,y,z,t) = \psi(t)\frac{\dot{m}''_{bs}(x,y,z,t)}{\mathrm{Vol}_{FE}} \tag{5.22}$$

for which the yield of each species, $\psi(t)$, is taken from the bench scale testing. Table 5.5 summarizes the source terms applied in usrsrc.f.

### 5.1.8 Combustion and Species Production

The average composition by weight of PU foam mattresses based on elemental analysis was determined by Bard [223]

$$(\mathrm{CH_{1.68}O_{0.31}N_{0.071}Cl_{0.002}})_n \tag{5.23}$$

and by Gross [224]

$$(\mathrm{CH_{1.74}O_{0.323}N_{0.0697}})_n \tag{5.24}$$

For GM21 flexible PU foam, a slightly different composition was found [225]

$$(\mathrm{CH_{1.78}O_{0.295}N_{0.0536}})_n \tag{5.25}$$

| Source | Equation where applied | Physics addressed |
|---|---|---|
| $S_m$ | Conservation of Mass | Accounts for mass lost from solid that enters fluid due to pyrolysis |
| $S_{u,v,w}$ | Conservation of Momentum | Accounts for initial velocity given to pyrolysis products leaving solid |
| $S_E$ | Conservation of Energy | Accounts for enthalpy of pyrolysis products leaving solid |
| $S_{\text{fuel}}$ | Conservation of Species | Accounts for fuel produced from solid that enters fluid due to pyrolysis |
| $S_{prod}$ | Conservation of Species | Accounts for products produced from combustion of fuel |
| $S_{\text{soot}}$ | Conservation of Species | Accounts for soot produced from combustion of fuel |

Table 5.5: Source terms added to conservation equations.

Stoichiometric reaction of GM21 foam with air and no intermediate reactions would then follow

$$\mathrm{CH_{1.78}O_{0.295}N_{0.0536}} + 1.2975\mathrm{O_2} + 4.87\mathrm{N_2} \rightarrow \mathrm{CO_2} + 0.89\mathrm{H_2O} + 4.8968\mathrm{N_2} \quad (5.26)$$

A similar one-step irreversible reaction was used by Kumar to model PU foam mattress fires in hospital wards with JASMINE [200]

$$\mathrm{CH_{1.9}O_{.26}} + 1.35\mathrm{O_2} \rightarrow \mathrm{CO_2} + 0.95\mathrm{H_2O} \quad (5.27)$$

The heat of formation for PU, $\Delta H_f(\mathrm{PU})$, following Equation 5.26 can be determined with knowledge of the heat of combustion. Application of Hess' law shows that the energy change for a system is a function of the initial and final states, and not the particular path taken [7]. Given the measured net heat of combustion for GM21, $\Delta H_c(\mathrm{PU}) = 26.15\ \frac{MJ}{kg}$, the heat of formation can be determined by

$$\begin{aligned}\Delta H_c(\mathrm{PU}) = {} & \Delta H_f(\mathrm{CO_2}) + 0.89\Delta H_f(\mathrm{H_2O})_g + 4.8968\Delta H_f(\mathrm{N_2}) \\ & -\Delta H_f(\mathrm{CH_{1.78}O_{0.295}N_{0.0536}}) - 1.2975\Delta H_f(\mathrm{O_2}) - 4.87\Delta H_f(\mathrm{N_2}) \end{aligned} \quad (5.28)$$

where standard heat of formation values are used for the right hand side. The resulting $\Delta H_f(\mathrm{PU})$ is $-5.47\ \frac{MJ}{kg}$. This compares with $\Delta H_f(\mathrm{PU}) = -5.6\ \frac{MJ}{kg}$ from [224] for a slightly different foam.

The stoichiometric mass oxygen to fuel ratio calculated based on Equation 5.26 is 2.16, while the stoichiometric mass air to fuel ratio is 9.25 (versus 9.79 from Gross [224]). The stoichiometric yields of carbon containing species during pyrolysis and combustion of GM21 are available, although very little data has been reported in the literature on similar properties for fabric materials, Table 5.6. On a per mass basis, foam dominates fabric for upholstered furniture, so for all combustion calculations,

| Species | Pyrolysis of GM21 % by mass | Combustion of GM21 % by mass |
|---|---|---|
| $CH_4$ | 0.374 | 0.374 |
| $CO_2$ | 0.337 | 2.284 |
| CO | 0.429 | 1.453 |

Table 5.6: Stoichiometric yields of carbon containing species [225] .

properties for foam will be used exclusively.

To track the different components participating in the reaction, scalar transport equations are solved for fuel, $O_2$, products, and soot. A fifth equation is not necessary for $N_2$ since $\sum Y_i = 1$. Similarly, separate equations for $CO_2$ and $H_2O$ need not be applied since the assumption of stoichiometric combustion constrains the ratio between $Y_{CO_2}$ and $Y_{H_2O}$.

The speed at which Equation 5.26 proceeds depends on the turbulent mixing time at a rate $\propto \frac{\epsilon}{k}$ as given by the Eddy Dissipation Combustion Model

$$S_f = -C\rho\frac{\epsilon}{k}\min\left[Y_f, \frac{1}{s}Y_o, AY_fY_o\exp\left(-\frac{E}{RT}\right)\right] \tag{5.29}$$

Similar source terms are applied to the remaining scalars to account for the combustion reaction.

### 5.1.9 Convergence Criteria

To improve the flow field prediction, a number of inner loop iterations can be performed between time steps, or outer loop iterations. Irregardless of the quality of the convergence, an absolute limit to the number of inner loop iterations, or maximum number of CPU work units can be implemented to stop processing the current iteration when the solution stalls.

For general CFD fluid flow predictions, normalized RMS residuals (dimensionless) can be expected to drop to the range of $10^{-4}$ to $10^{-7}$, values that will be difficult to reach with reacting combustion flows with radiation transfer. The maximum residual for a particular scalar is generally one order of magnitude larger than the RMS residual. If larger, local regions of poor convergence can be expected. Maximum residuals should also be less that 1% of average values, with spot changes in monitor values under .1%.

### 5.1.10 Summary of Physics Treatment

Table 5.7 outlines the processes that comprise the fluid node solution. Coupled with the fluid flow is a simultaneous solution for energy transfer in the solid fuel as part of the process in determining $\dot{q}''_w$. The thermal theory of flame spread is employed by treating the fuel as an inert solid, Table 5.8. Treatment of the physics unique to

the furniture calorimeter are summarized in Table 5.9. Consideration also needs to be given to how TASCflow implements the above numerical approximations. Most of the items in Table 5.10 were discussed in detail in Chapter 4. Finally, to assure a closed system of equations, Table 5.11 provides the equation used for the solution of each variable. Since the number of equations equals the number of unknowns, the system is considered closed.

| **Physical process** | **Treatment by model** | **Reference** |
|---|---|---|
| Radiation transfer between gas and solid phases | Finite volume model traces rays and follows absorption and emission from each volume with no scattering | Equation 4.99 in Section 4.4.3 |
| Convection from flameto fuel | Gas phase convection through $\frac{\partial(\rho u_j h)}{\partial x_j}$ term in energy equation | Equation 4.12 in Section 4.1.3 |
| Conduction from flame to fuel | Gas phase conduction through $\frac{\partial}{\partial x_j}\left(k_g \frac{\partial T}{\partial x_j}\right)$ term in energy equation | Equation 4.12 in Section 4.1.3 |
| Heat transfer from flame to fuel due to turbulence | Gradient diffusion assumption with apparent turbulent conductivity, $k_T$, evaluated through $\mathrm{Pr}_T = \frac{\mu_T c_p}{k_T}$ | Equation 5.8 in Section 5.1.6 |
| Absorption coefficient | Narrow band model that includes $Y_{\mathrm{fuel}}$, $Y_{\mathrm{CO_2}}$, $Y_{\mathrm{H_2O}}$, and $Y_{\mathrm{soot}}$ | Section 4.4.4 |
| Gas thermal props | Sutherland's relation or power law | Section 4.1.5 |
| Mixing of fuel and oxidizer | Large scale by bulk fluid motion with subgrid motions approximated using eddy diffusion coefficient, $\Gamma_\phi$ | Equation 4.61 in Section 4.4.1 |
| Rate and location of fuel combustion | Minimum of fuel, oxidizer or product through Eddy Breakup Model | Equation 4.114 in Section 4.4.6 |
| Production rate of $CO_2$ and $H_2O$ | Specified stoichiometric coefficient giving a constant production rate per unit mass fuel consumed | Equation 5.26 in Section 5.1.8 |
| Production rate of soot | Direct application of volumetric soot data from cone test at a particular flux level | Section 4.4.5 |
| Distributed soot production | Soot is released where fuel burns | Section 4.4.5 |
| Energy released per unit mass fuel burned | Average $\Delta H_c$ based on cone calorimeter data | Section 5.1.8 |
| Rate of plume entrainment | Large scale by bulk fluid motion with subgrid motions approximated using eddy diffusion coefficient, $\Gamma_\phi$ | Equation 4.61 in Section 4.4.1 |

Table 5.7: Flame spread **GAS** phase physical process treatment.

| Physical process | Treatment by model | Reference |
|---|---|---|
| Radiation transfer from fuel surface back to gas phase | Surface is diffuse gray emitter with user supplied constant surface emissivity, $\epsilon$. | Equation 4.92 in Section 4.4.3 |
| Conduction within fuel | Energy diffusion equation in 3-D | Equation 4.115 in Section 4.4.7 |
| Thermal properties of fabric and foam | Temperature dependent to extent data is available | Appendix A.1 |
| Change in energy | Conservation of energy eqn. | Equation 4.17 |
| Discretization of fuel surface | Source terms specified over flux element assembly | Section 4.2.1 |
| Coupling of gas and solid phase boundary conditions | Coupled fluid-solid calculation is carried out with $T_w$ and $\dot{q}''_w$ an implicit part of calculation | Section 5.1.6 |
| Ignition condition at fuel surface | User specified $T_{ign}$ or $\dot{q}''_w$ for ignition | Section 2.1 |
| Chemical composition of fuel | Single step stoichiometric reaction for foam | Equation 5.26 in Section 5.1.8 |
| Mass, momentum and energy source terms | $S_{\text{fuel}}$, $S_u$, $S_E$ and $S_\phi$ calculated by flame spread routine | Table 5.5 and Section 5.1.4 |
| Velocity of fuel leaving surface | $V = \frac{\dot{m}\rho}{A_{FE}}$ with direction assumed normal to surface | Section 5.1.7 |
| Location fuel is released | In flux element above surface | Figure 5.1 |
| Rate of fuel pyrolysis as a function of flux | Linear interpolation used between curves | Section 5.1.4 |
| Surface deformation and fabric separation | Not directly considered. Addressed through small scale test results | |
| Char formation and fuel burnout | Not directly considered. Addressed through small scale test results | |
| Energy lost by unexposed solid | $\dot{q}''_w = h(T_w - T_\infty)$ with $h$ and $T_\infty$ specified by user | |
| Energy absorbed during fuel vaporization | User supplied $\Delta H_v$ | Section 2.4.1 |

Table 5.8: Flame spread **SOLID** phase physical process treatment.

| Physical process | Treatment by model | Reference |
|---|---|---|
| Radiation transfer from hood surface to gas phase and fuel | Surface is diffuse gray emitter with user supplied constant surface emissivity, $\epsilon$. | Equation 4.92 in Section 4.4.3 |
| Radiation transfer from exhaust gases back to fuel surface | Finite volume model traces rays and follows absorption and emission from each volume | Equation 4.99 in Section 4.4.3 |
| Surface temperature of steel hood and skirt | Coupled fluid-solid calculation is carried out with $T_w$ and $\dot{q}''_w$ an implicit part of calculation | Section 5.1.6 |
| Rate gases are exhausted from hood | $\dot{m}''$ specified by user through an average pressure distribution across hood opening to represent fan | Section 5.1.5 |
| Rate ambient air is introduced into furniture calorimeter | Domain extended beyond hood with ambient pressure boundary condition specified across opening | Section 5.1.5 |
| Simulation of ignition source | Mass flow specified fuel inlet boundary giving equal HRR. Yields are based on cone measurements | Table 3.2 |

Table 5.9: **Furniture calorimeter** physical process treatment.

## 5.2 Fire Growth Routine

A furniture CFD fire growth routine has been incorporated into TASCflow to generate transient boundary conditions for pyrolysis from a burning surface. Now that the model treatment for the physics of flame spread, heat transfer and fluid flow have been discussed, focus will move to specifically how TASCflow and the fire growth routine interact to predict increase in burning area with time. As with the physics discussion in the last section, it is easier to separate the solid and fluid node solutions and then show how they are coupled at the interface. Briefly, the process is as follows:

1. Before starting a model run, fuel surfaces are specified in the model, along with ignition criteria, thermal properties, $\dot{m}''_{bs}$, $\Delta H_c$, and $\psi_{soot}$, and the ignition source.

2. At the start of a run and at each new time step, all solid fuel surface nodes on the boundary interface with the fluid are visited to evaluate ignition status. This allows ignition on surfaces that were not involved in the initial ignition (spread from seat to chair back, for example).

3. Nodes that satisfy the ignition criteria, $T_w > T_{ign}$ or $\dot{q}''_w > \dot{q}''_{ign}(t)$, are considered to be pyrolyzing and the time of ignition saved.

| **Physical process** | **Treatment by model** | **Reference** |
|---|---|---|
| Fluid flow predictions | Coupled solution for mass & momentum followed by sequential solution of remaining equations during each iteration | Section 4.3 |
| Pressure velocity coupling | Continuity equation replaced with fourth order pressure redistribution to prevent P-velocity decoupling | Equation 4.43 in Section 4.2.2 |
| Upstream Differencing | Mass weighted skew upstream differencing with PAC terms | Section 4.2.2 |
| Subgrid mixing and turbulence | Large scale by bulk fluid motion & subgrid motions approximated by eddy diffusion coefficient, $\Gamma_\phi$ | Equation 4.61 in Section 4.4.1 |
| Subgrid wall boundary layers | Log-law approximation to shape of viscous and thermal boundary layer | Section 4.4.2 |
| Buoyancy | Added buoyancy term of the form $\beta\rho g\overline{u_i'T'} \approx \beta\rho g\frac{\mu_T}{\mathrm{Pr}_T}\frac{\partial T}{\partial x_j}$ | Equation 4.74 in Section 4.4.1 |
| Solution of conservation equations | Algebraic multigrid (AMG) solver with additive correction blocking and user specified "W" cycles | Section 4.3 |
| Relaxation of matrix of linear algebraic equations | Incomplete Lower Upper (ILU) decomposition with upper and lower matrices solved by forward and backward substitutions | Section 4.3 |
| Convergence criteria | Maximum number of innerloop iterations, RMS & MAX residuals sufficiently reduced | Section 5.1.9 |

Table 5.10: **CFD** modeling physical process treatment.

| **Primitive variable** | **Calculation method** | **Reference** |
|---|---|---|
| $p, u, v, w$ | Coupled mass and momentum with pressure redistribution | Equations 4.31, 4.32 and Equation of state |
| $h$ | Energy conservation | Equation 4.33 |
| $T$ | Equation of state, $h = c_p T$ | T is sufficient to specify state for an ideal incompressible fluid |
| $\rho$ | $\rho_i = \frac{m_i}{Volume}$ | |
| $Y_f$ | Conservation of species for $Y_f$ | Equation 4.34, $\phi = Y_f$ |
| $Y_{O_2}$ | Conservation of species for $Y_{O_2}$ | Equation 4.34, $\phi = Y_{O_2}$ |
| $Y_{CO_2}$ | Conservation of species for $Y_p$ | Equation 4.34, $\phi = Y_p$ |
| $Y_{H_2O}$ | Conservation of species for $Y_p$ | Equation 4.34, $\phi = Y_p$ |
| $Y_s$ | Conservation of species for $Y_s$ | Equation 4.34, $\phi = Y_s$ |
| $Y_{N_2}$ | $1 - \sum_i Y_i$ | Mass fractions must sum to 1 |
| $-\rho\overline{u_i' u_j'}$ | Boussinesq approximation | Equation 4.60 |
| $k_{tke}$ | $k_{tke}$ transport equation | Equation 4.73 |
| $\epsilon$ | $\epsilon$ transport equation | Equation 4.75 |
| $\mu$ | Sutherland's law for $\mu = \mu(T)$ | Equation 4.24 |
| $k_g$ | Sutherland's law for $k_g = k_g(T)$ | Equation 4.24 |
| $\nabla \cdot \dot{q}_r$ | Source term in energy equation | Equation 4.92 |
| $S_f$ | EBU combustion model | Equation 4.114 |
| $S_s$ | $S_s = \psi_s S_f$ | Equation 4.114 |

Table 5.11: Variable solution for fluid flow predictions.

4. For all ignited nodes, source terms for fuel, soot, momentum and energy are added to the fluid control volume above the burning node.

5. The value of $\dot{m}''_f$ depends on the radiant flux at the node and the time since ignition based on the user supplied cone calorimeter measured mass loss rates at different flux levels. Total mass lost is used to locate the current $\dot{m}''_f(t)$ on a curve, with linear interpolation used for flux levels between tested levels. Burnout is considered when a node has released total mass equal to that measured in the cone calorimeter (all solid fuel is gone).

6. Control is then returned to TASCflow. CFD calculations are carried out for fluid flow and heat transfer through the domain. This includes updating of solid-fluid surface boundary temperature and flux levels used to evaluate ignition conditions.

7. Inner loop iterations are repeated until satisfactory convergence is reached for the current time step. The time step is advanced bringing the process back to step 2.

A series of user source routines have been developed that interface with the TASCflow source code to allow the application of source terms, specification of thermo-fluid properties, generation of boundary conditions, post-processing, and creation of models that incorporate different physical processes. The user source routines listed in Table 5.12 are linked to the TASCflow source code and result in the creation of a problem specific local executable. Upon running the local executable, the flame spread data input files are read and TASCflow operates with the fire growth routines. Upon completion, TASCflow writes standard output files (.out and .rso) and also produces the file flame.out that contains transient results of the fire growth calculation.

Solid and fluid node solution algorithms are shown in Figures 5.4 and 5.5, with the loop repeated upon each advancement of the time step. When inner loop iterations (time step held constant) are specified to improve convergence, the furniture fire growth routine is implemented at the start of each time step, and all source terms that are generated held constant while inner loop iterations continue. The use of TASCflow in such areas as problem specification, run monitoring, and file handling will not be discussed here, but are covered fully in the technical documentation [156]. The focus of this section is on the details unique to the furniture CFD model.

### 5.2.1 Start of Run

Definition of boundary conditions, domain geometry, grid, solution parameters, embedding and blockages are carried out through the standard TASCflow routines TASCgrid, TASCtool and TASCbob. Few changes are necessary during problem specification to facilitate flame spread predictions. The principle addition is in the definition of fuel surfaces. During generation of the **b**oundary **c**ondition **f**ile (.bcf), solids are blocked off from the fluid regions by specification of zero porosity.

| **Routine** | **Purpose** | **Appendix location** |
|---|---|---|
| usrsrc.f | Applies source terms to conservation equations. Also contains main controlling routines for flame spread calculations | B.1 |
| propb.f | Calculates the bulk compressibility for natural convection fluid flows | B.7 |
| prpfvr.f | Contains Modak and Grosshandler absorption coefficient routines | B.12 |
| propf.f | Calculates dynamic viscosity, $\mu_i$, for species $i$ | B.8 |
| propq.f | Calculates mass diffusion coefficient, $\Gamma_i$, for species $i$ | B.9 |
| propr.f | Calculates density, $\rho$ | B.10 |
| propt.f | Calculates fluid and CHT solid thermal properties | B.11 |
| flame.com | Fortran common file that contains subroutine variable and array definitions | B.6 |
| flame.dat | Flame spread routine problem input data file | B.2 |
| flame.hrr | Bench scale $\dot{m}''_{bs}$, $Y_s$, and $\Delta H_c$ input file | B.3 |
| flame.out | Flame spread routine results output file | B.4 |

Table 5.12: User source code routines.

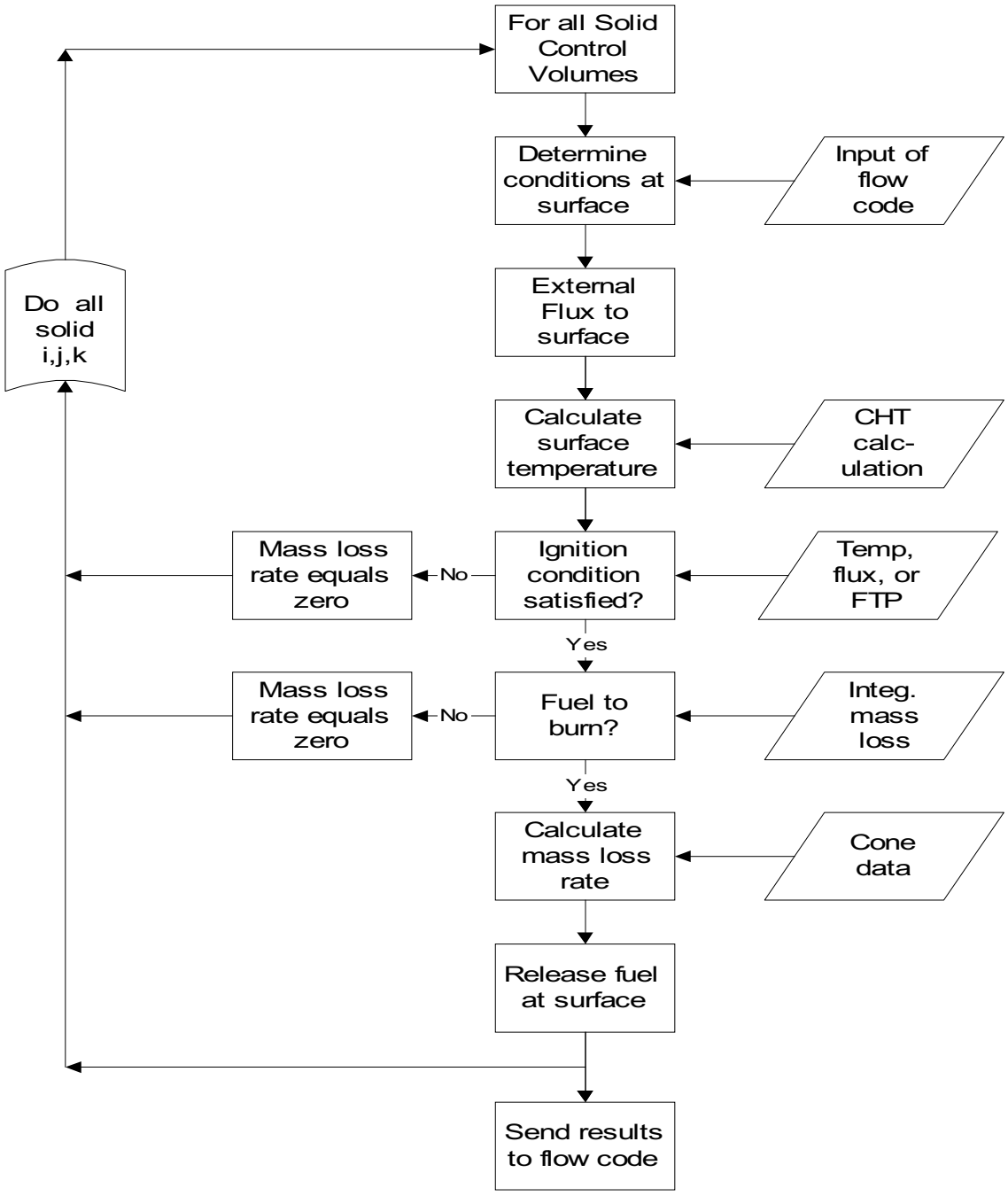


Figure 5.4: **Solid** control volume solution.

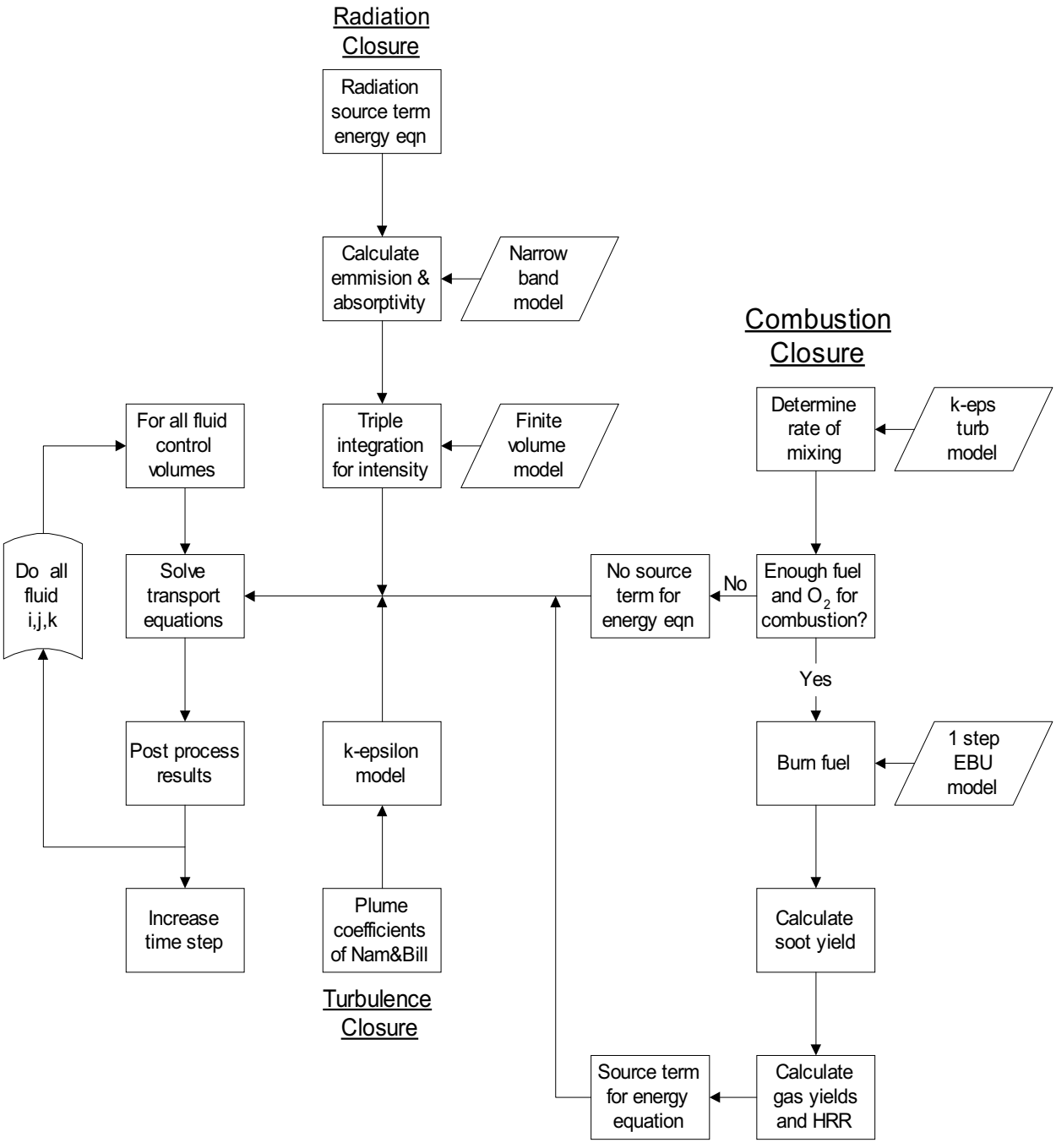


Figure 5.5: **Fluid** control volume solution.

Calculation of solid heat transfer requires an additional step for such regions by including definition as a CHT solid along with inclusion of appropriate thermal properties that are defined in propt.f. Any CHT solid can be a fuel and participate in fire growth calculations with selection of an appropriate region label. By simply naming the fuel surfaces at the solid fluid interface surf1, surf2, ..., surfL, were L is the number of fuel surfaces, a region is able to undergo pyrolysis.

Supporting the fire growth predictions are a number of auxiliary calculations conducted by usrsrc.f at the start of a run. Calls are made to the TASCflow source to obtain both the physical location of each node in the domain and also the volume of each flux element. The $\{x, y, z\}$ coordinate for each node on all fuel surfaces is used to calculate the flux element face area from which the total area of region surfL is evaluated as the sum of N faces

$$A(\text{surfL}) = \sum_{i}^{N} A_{i,FE} \tag{5.30}$$

Specification of fuel regions using the surfL convention follows naturally from the region definition method in TASCtool

```
TASCtool:> define region surf1=[1:NI,13:NJ,NK-5]:main
```

as an example is all that is necessary. In this case, a surface for flame spread has been defined on the grid main. It includes all nodes in the domain x direction, from node 13 to the end of the domain in the y direction, and incorporates the plane of nodes 5 from the end of the z domain extent. Taking the TASCtool region definition above, the usrsrc.f code then evaluates each fuel surface for orientation and alignment. This places each surfL definition on a particular CHT solid and also identifies the flux elements above the solid that will receive the pyrolysis products upon ignition. The particular orientation of a fuel surface must be established to allow the usrsrc.f routine to apply source terms in the proper location and direction. This assures that the pyrolysis products predicted as leaving a surface are released normal to the face of the fuel, irrespective of how the surface is oriented in computational space. Additional information about the direction or angle of a surface in the domain is not necessary since it is determined automatically by usrsrc.f based on the region definition.

The user supplies the measured bench scale mass loss rate per unit area, $\dot{m}''_{bs}(t)$, soot yield, $\psi_s(t)$, and heat of combustion, $\Delta H_c(t)$, through the flame.hrr input file show in Section B.3 of the Appendix. At the beginning of a run, the data is read in along with problem specific data from the other input file, flame.dat.

The total mass loss from a unit area, $m''_{bs,tot}$, based on the user data

$$m''_{bs} = \int_0^t \dot{m}''_{bs}(t_p - t_{ign})dt_p \tag{5.31}$$

is calculated by summing the mass loss rates over the $M$ data points in flame.hrr

$$m''_{bs,tot} = \sum_{j=0}^{j=M} \dot{m}''_{bs}(t_j)\Delta t \tag{5.32}$$

and will be used later to predict burnout. When needed, linear interpolation is applied for evaluating $\dot{m}''_{bs}(t)$, $\Delta H_c$, and $\psi_{\text{soot}}(t)$ at times falling between data values.

### 5.2.2 Nodal Solution Procedure

The solution procedure developed for solid control volumes is shown in Figure 5.4 on Page 134. At the start of a time step, all fuel surface nodes on the interface with the fluid are visited to evaluate ignition status. If the temperature of node $i$ at time $t$ is greater than the ignition temperature, $T_i(t) \geq T_{ign}$, or the external flux is greater than the ignition time versus flux data, ignition is assumed. Recalling the discussion of Section 4.2.1, both boundary conditions and user source terms are applied over flux element faces which represent the area enclosed by line segments connecting four nodes. Ignition for a given flux element is then based on the average of the four surrounding node temperatures.

At the instant of ignition, the flux element begins to release fuel following the user supplied cone calorimeter mass loss curve, $\dot{m}''_i(t_{ign}) = \dot{m}''_{bs}(0)$. At the next time step, $\dot{m}''_i(t_{ign} + \Delta t) = \dot{m}''_{bs}(\Delta t)$, followed by $\dot{m}''_i(t_{ign} + 2\Delta t) = \dot{m}''_{bs}(2\Delta t)$ and so on.

Pyrolysis will continue until burnout occurs when the fuel is depleted. This is approximated in the model to occur when the total mass lost from a flux element equals the total mass lost in bench scale, thus $\dot{m}''_i = 0$ when

$$m''_i = \int_0^t \dot{m}''_i(t_p - t_{ign})dt_p = m''_{bs,tot} \tag{5.33}$$

with $\dot{m}''_{bs,tot}$ from Equation 5.31. Each flux element, 1...N, can have a different mass loss rate depending on what time ignition occurred. Sources applied in usrsrc.f are done so per unit volume of the scalar, so for fuel

$$S_{\text{fuel}}(t) = \frac{\dot{m}''_{bs}(t - t_{ign})}{\text{Vol}_{FE}} \tag{5.34}$$

The total mass lost measured by the load cell in the furniture calorimeter

$$m_{fs}(t) = \int_0^t \dot{m}_i(t_p)dt_p = m_{start} - m_{end} \tag{5.35}$$

is available to compare to the composite predicted in the model

$$m_{model}(t) = \sum_{i=0}^{i=N} \dot{m}''_{bs}(t - t_{ign})A_i \tag{5.36}$$

Similar relations are possible for heat release rate

$$\dot{Q}(t) = \int_0^t \dot{A}_{FE}(t_p)\dot{q}''_{bs}(t - t_p)dt_p \tag{5.37}$$

which can be approximated numerically as

$$\dot{Q}(t) = \sum_i^n \dot{A}_i\dot{q}''_i(t - t_{ign}) \tag{5.38}$$

Equation 5.38 is in reality much more difficult to evaluate than expected.

It would appear easier to implement the measured HRR, $\dot{q}''_{bs}(t)$, rather than mass loss rate, $\dot{m}''_{bs}(t)$, since this is the driving force behind fire growth and the natural variable used to compare model versus experiment. Physically, a HRR boundary condition does not work since the location for the heat to be released is not known in advance. Local conditions, such as species concentration and fluid flow that influence when and where the combustion reaction take place, are not considered. Applying the bench scale cone calorimeter data instead with the measured mass loss rate is a more natural closure of the problem. In this case, mass (fuel) is introduced into the fluid domain at the solid surface, a much more reasonable assumption, but still does not address in-depth burning. The combustion model then determines where the energy is released based on the control volume in which the fuel is burned.

With the mass source term inserting fuel above the solid surface, the velocity is introduced through the momentum source term, $S_u$, calculated as

$$V = \frac{\dot{m}''_{bs}(t - t_{ign})}{\beta\rho_f A_{FE}} \tag{5.39}$$

where $\beta$ can account for the fraction of fuel surface available for pyrolysis. For some burning fuels such as wood, pyrolysis products may be released through the grain or non-charred regions of the surface, thus an approximation that uses the entire surface area to determine the velocity will be in error. The density for the pyrolysis products is specified by the user and is taken to be equal to the fuel density at the ignition temperature. Three momentum source terms are applied in usrsrc.f, one for each of the principle coordinate directions. The values of $S_u$, $S_v$ and $S_w$ are calculated to give the pyrolysis products an initial velocity normal to the fuel surface; a reasonable assumption given a lack of better treatment.

The pyrolysis products arrive in the fluid region at a temperature assumed equal to the pyrolysis temperature, $T_{ign}$. This energy addition is addressed through the energy source term, $S_E$

$$S_E(x, y, z, t) = c_p(T_{ign})\frac{\dot{m}''_{bs}(T_{ign} - T_s)}{\mathrm{Vol}_{FE}} \tag{5.40}$$

The flame spread velocity normal to the pyrolysis front is then

$$V_p = \frac{dr_p}{dt} = \frac{r(t+\Delta t) - r(t)}{\Delta t} \tag{5.41}$$

where the distance traveled during $\Delta t$ is $r(t) - r(t-\Delta t)$. When located between two nodes, the position of the flame front is determined with a linear interpolation of the node temperatures.

The pyrolyzing area on a cushion, for example, is evaluated by assessing the ignition condition of each flux element face

$$\dot{A}(t) = \sum_{i}^{N} A_i (T \geq T_{ign} \text{ or } \dot{q}'' \geq \dot{q}''(t)) \tag{5.42}$$

The fraction of the surface burning at a particular time, $\eta(t) = \frac{\dot{A}(t)}{A_{tot}}$, is also calculated and can be compared with estimates from video tape recordings of full scale testing.

### 5.2.3 Physics Not Addressed in the Model

While many of the processes involved in fire growth have been approximated to differing extents, there is still much left that has not been addressed. Based on the current state of the art, many of the processes in Table 5.13 have not been adequately studied, let alone researched to the point of providing tools for the numerical modeler. It will be left to the results of the next chapter to show how important these neglected items are to the process. It is hoped that the bench scale results address some of these issues, but they can not be expected to include them all.

| | |
|---|---|
| Solid pyrolysis | Energy absorbed by pyrolysis |
| | Solid char formation |
| | Non-constant ignition condition ($T_{ign}$ or $\dot{q}''_{ign}$) |
| | In-depth radiation absorption |
| | Heat transfer by pyrolysis products in the solid |
| Foam-fabric behavior | Surface deformation and fabric separation |
| | Effect of interliners |
| | Pooling |
| | Foam-fabric pulling away from ignition source |
| Combustion | Non-stoichiometric multi-step reactions |
| | Species generation under vitiated conditions |
| Soot | Aging and combustion |
| | Lagrangian tracking-solid soot |
| Radiation | Scattering |
| | Non-gray behavior |
| | Turbulence-radiation interaction |

Table 5.13: Physics not included in the model.

# Chapter 6

# Results of Numerical Experiments

A comparison between experiment and model prediction will be presented for five different scenarios that attempt to cover the range of mattress and furniture fire behavior measured during the CBUF test series [50]:

- Mattress 1:21 was constructed of a solid polyether foam core covered by cotton-viscose fabric for a total thickness of 120 $mm$. This fuel package resulted in a significant fire with flame spread over the complete sample. The burning rate was sufficient to cause smoke to spill from under the furniture calorimeter hood.

- Mattress 1:22 was constructed similar to Mattress 1:21, except latex foam was substituted resulting in a finished thickness of 100 $mm$. The change in foam produced much slower fire growth, along with a lower peak heat release rate that occurred later in the fire. A period of reduced intensity burning was observed for over 15 minutes after the peak HRR was reached.

- Mattress 1:23 incorporated 10 $mm$ of polyether foam and 10 $mm$ of polyester fabric on each side of an inner spring interior, for a total thickness of 150 $mm$. This fuel configuration produced an extremely rapid increase in HRR over a 30 second period, with peak burning completed before the burner was turned off at 120 seconds.

- Mattress 1:24, the final mattress investigated, also included an inner spring and polyester fabric, but instead utilized combustion modified high resilience (CMHR) foam. A very limited HRR, slowly propagating fire resulted.

- Chair 3:13 was selected for its simple design consisting of a single foam-fabric slab for both the seat and back. A solid wood frame without arms provided support. The back of the chair was not perfectly vertical, but instead sloped from vertical $10^o$. Components consisted of high resilience polyurethane (HRPU) foam covered by 100% polyester fabric with flame retardant. This chair configuration allowed for both horizontal and vertical fire development.

## 6.1 Problem Specification

### Geometry

Space, time and radiation discretization are based on the geometry and desired accuracy for the solution. TASCflow uses a structured code, which when coupled with the regular rectangular geometry of the furniture calorimeter, results in grids with skew angles very close or equal to orthogonal. An unstructured version of TASCflow is also available.

Calorimeter, fuel and opening geometries are specified throughout the extent of the computational domain, $[1:\texttt{NI}, 1:\texttt{NJ}, 1:\texttt{NK}]$, depending on the particular problem. TASCflow input routines have been coded to allow for the changing of only one variable in a global data file, with the results applied through all portions of the problem setup. The geometry wire frame, which outlines the extent of the computational domain developed for the furniture calorimeter, is presented in Figure 6.1. The hood defining the top of the calorimeter is shown without the usual piping for instrumentation (not modeled). A CHT solid representing the mattress is located on a steel support upon which the mattresses were placed for testing. Based on the fact that the mattress is elevated, the wire frame view shown in Figure 6.1 does not appear symmetric due to the orientation of the lines in the picture. The domain is extended out below the hood on both sides to provide a location to specify ambient pressure. Two grids are embedded above the fuel surface. The lower one contains two sides of the ring burner (only two of the four sides of the burner are shown due to symmetry).

The accompanying grid in Figure 6.2 provides an order of magnitude feel for the distance between nodes on the +y face. Embedding is used in the solid and through the fluid above to resolve areas of high gradients such as in the plume. Near wall nodes must still be located inside the log-law region to assure proper prediction of the boundary layer velocity and temperature profiles. Additional nodes are shown for the +x face in Figure 6.3. This view best displays the quarter mid-plane symmetry used to take advantage of computational savings resulting from the similarity across the domain. To improve the predictions in areas with high gradients, grid refinement (embedding) is used around fuel surfaces and extends from fluid regions into the solid. At their smallest, grid length scales on the order of 5 $mm$ to 2 $cm$ are used to resolve the region near the surface. This is still greater than the $\approx 1$ $mm$ length scale associated with flame foot gas phase conduction heating during horizontal opposed flow flame spread mentioned in Section 2.4.4. The corresponding grid in the solid mattress is shown from the +x direction in Figure 6.4, which clearly demonstrates the symmetry of the mattress in the corner. An isometric view is also given in Figure 6.5. The embedding in the mattress and around the burner is clearly shown. Approximately 600 nodes are used to refine the .5 $m$ by .25 $m$ portion of the mattress modeled.

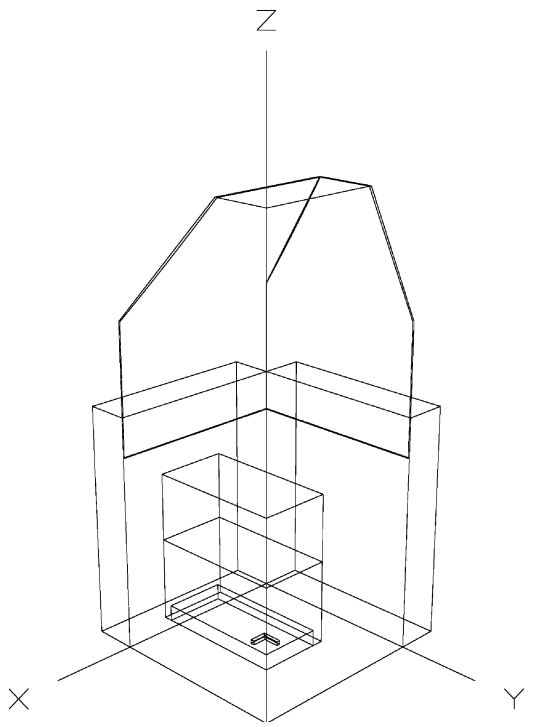


Figure 6.1: Wire frame of furniture calorimeter showing quarter symmetry.

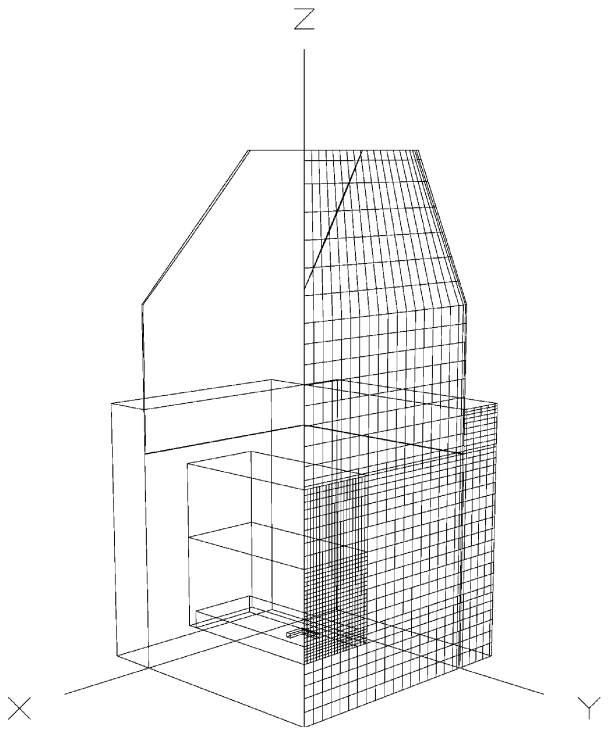


Figure 6.2: Grid shown on +y face.

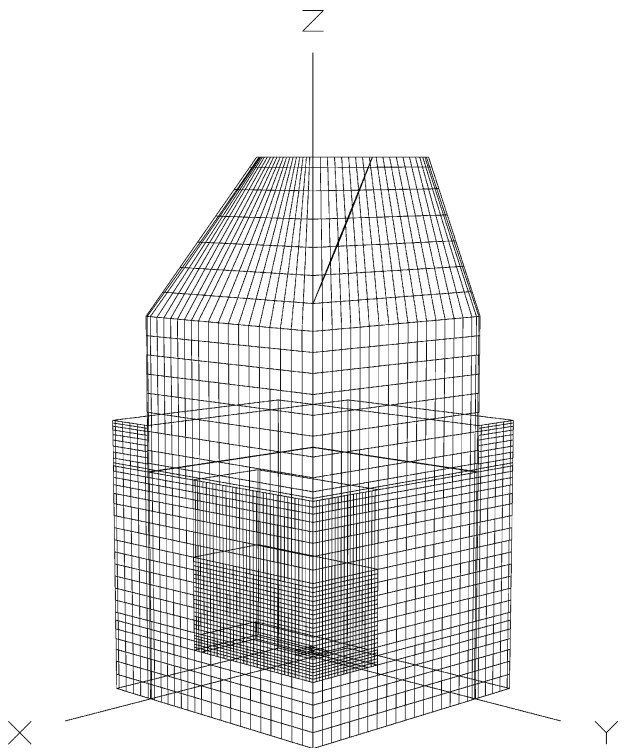


Figure 6.3: Grid shown on +x and +y faces.

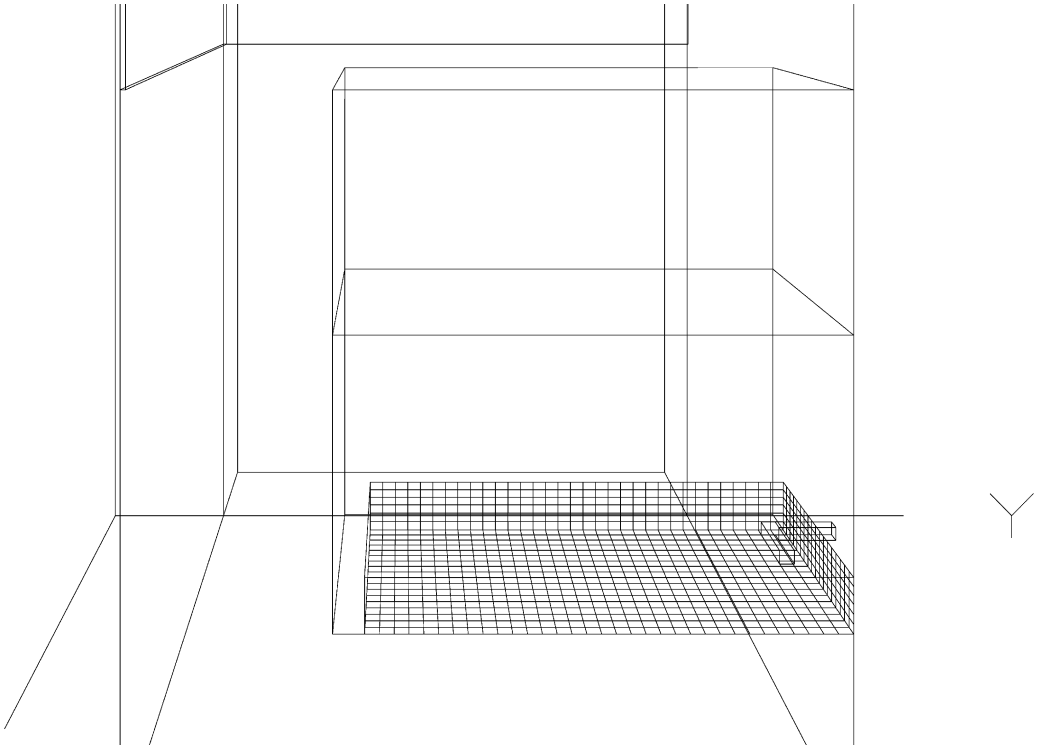


Figure 6.4: Embedding of solid fuel.

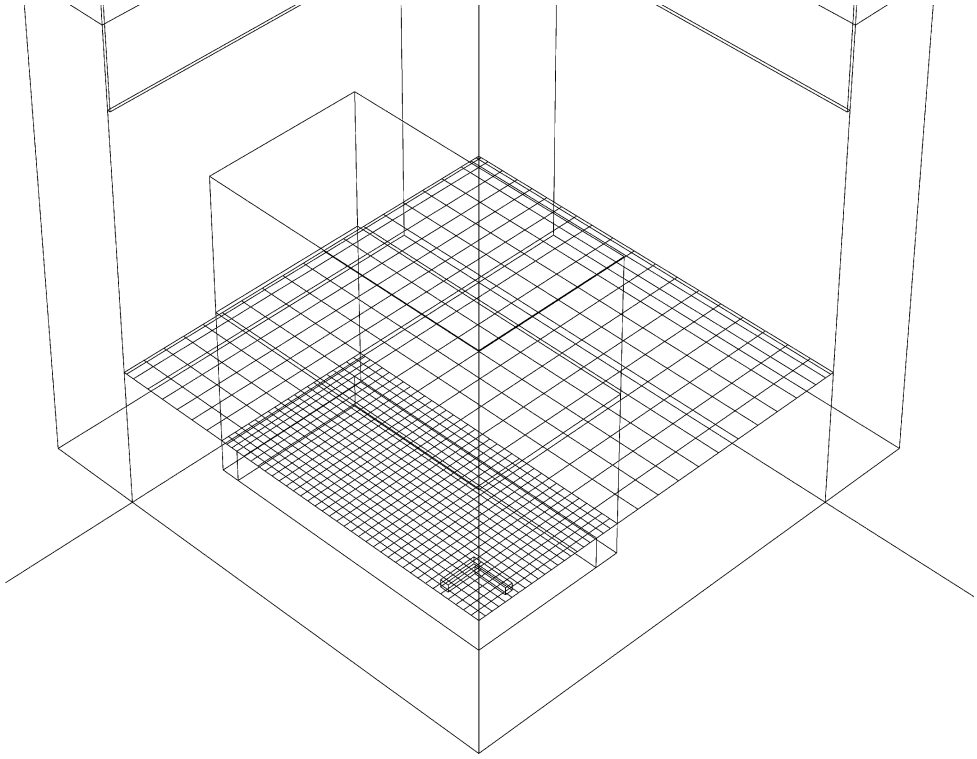

Figure 6.5: Isometric view of embedding over the fuel surface.

### Initial Conditions

Furniture calorimeter testing begins with the hood extraction fan operating at a level sufficient to remove the products of combustion, but not too great that accuracy is diminished due to overly diluted gases passing the analysis instrumentation. Both real and numerical experiments, therefore, were initiated with the fan at its steady state operating level before ignition. A fully developed flow field of uncontaminated ambient air was thus the starting point for fire spread predictions. The CFD code was run without combustion to generate this starting point for fire growth calculations. Using average outlet pressure of $101,310\ Pa$, the flow field represents the scalar $\texttt{SPEED} = \sqrt{u^2 + v^2 + w^2}$. Ambient conditions are included in Table 6.1 to complete specification of the initial values.

### Boundary Conditions

Boundary conditions must be specified over the entire computational domain, the implementation of which is by a flux element assembly as discussed in Section 4.2.1. During numerical experiments of a furniture calorimeter, standard conditions suffice for all boundaries except one, namely fire growth. That problem is addressed with the user source code, the topic of Section 5.2. Appropriate values associated with each boundary condition are shown in Table 6.2. The particular values given have been developed through repeated testing and form a numerically stable basis from

| Variable | Value | Units |
|---|---|---|
| $u, v, w, P_{fluid}$ | Determined by fan solution | - |
| Fan pressure | 101,310. | Pa |
| $T_{fluid}, T solid$ | 303. | $K$ |
| $Y_{fuel}, Y_{soot}, Y_{prod}$ | 0.0 | $\frac{kg}{kg}$ |
| $Y_{O_2}$ | 0.23 | $\frac{kg}{kg}$ |
| $Y_{N_2}$ | 0.77 | $\frac{kg}{kg}$ |
| Turbulence intensity, TKE | 0.05 | - |
| Eddy length scale, $\epsilon$ | 0.03 | - |

Table 6.1: Initial conditions.

| BC type | Where applied | Values |
|---|---|---|
| Average pressure opening (Total pressure specified for inflow, static for outflow) | Region extending beyond the base of the hood | $\overline{P} = 101,325\ Pa$<br>$(u, v, w)_{in}$ normal to surface<br>$T_{in} = 303\ K$<br>$(Y_{fuel}, Y_{prod}, Y_{soot})_{in} = 0$<br>$(Y_{O_2})_{in} = .23$; $(Y_{N_2})_{in} = .77$<br>$TKE = .05$, $\epsilon = .1$ |
| Average pressure outlet | Extraction fan | $\overline{P}_{static} = 101,310\ Pa$ |
| Inlet (mass specified) | Burner | $(\dot{m}''_{fuel})_{in} = 0.00125\ \frac{kg}{sec}$<br>$(u, v, w)_{in}$ normal to surface<br>$(Y_{fuel})_{in} = .988$; $(Y_{soot})_{in} = .002$<br>$(Y_{O_2}, Y_{N_2})_{in} = 0$; $(Y_{prod})_{in} = .01$<br>$T_{in} = 303\ K$<br>$TKE = .05$, $\epsilon = .01$ |
| Wall with heat transfer (CHT) | Mattress/chair and steel hood | $(u, v, w) = 0$<br>smooth wall |
| Exterior wall with heat transfer (CHT exterior) | Unexposed side of mattress and steel hood | $h = 10\ \frac{kW}{m^2\ K}$<br>$T_\infty = 303\ K$ |
| Adiabatic wall | Floor | $T_{surface} = 303\ K$ |
| Symmetry | Mid-plane | Not specified |

Table 6.2: Boundary condition values.

which to explore fire growth predictions.

As mentioned in Section 3.6.2, modeling the fuel distribution of the ring burner is not straight forward. An experimentally measured flux map can be input to the model as a boundary condition, but this still does not fully approximate the influence during the critical initial fire growth period. Another option is to assume some finite initial burning region that results from the igniter, thus bypassing the detailed ignition period.

Sufficient grid embedding is included to allow a reasonable representation of the ring burner. The sub-millimeter gas openings were not modeled, but instead fuel ($CH_4$) is assumed to be produced uniformly over the surface of the burner. A small amount of soot and products are added to the fuel inflow to seed the combustion reaction. This is necessary to numerically start a combustion reaction using the eddy dissipation model that predicts a reaction rate based on the minimum of the fuel concentration, oxygen concentration or existence of products. Even with a combustible concentration of fuel being produced, the model will not carry out the reaction unless a sufficient concentration of products exist to show that temperatures are sufficient for reaction.

Figures 6.6 and 6.7 show the measured and predicted fluxes produced by the ring burner located 25 $mm$ above a horizontal fuel surface. Fluxes are mapped over only one corner of the burner since symmetry exists. The measured values were taken for a seatback arrangement (back at X distance = 150 $mm$), while predictions are for a seat only. This may be the cause of the larger flux values measured for 100 $mm < X < 150$ $mm$.

Modeling environmental conditions within the furniture calorimeter necessitates careful selection of boundary conditions. Below the hood, flow conditions around the perimeter into the calorimeter are not known, making it difficult to specify a pressure distribution across this plane. Further from the calorimeter, the air in the laboratory should be reasonably quiescent, with ambient properties of pressure and temperature. Extending the computational domain away from the hood to a point where an ambient pressure opening can be applied properly specifies this boundary condition. The downside is that the boundary condition statement becomes very weak, especially in the far corners removed from the forced flow induced by the extraction fan. The robustness of the CFD code and solver are tested fully since convergence will suffer due to the formation of regions (pockets) of poorly reduced residuals that can stall out a transient run.

The flow rate of combustion products through the top of the hood induced by the extraction fan is also not known in advance. It is, however, measured during testing. A required flow rate of at least 4 $\frac{kg}{sec}$ for the furniture calorimeter is specified in the NORDTEST standard and can form the basis for a mass flow boundary condition, $\dot{m}_{user}$, to be applied at the top of the hood. Two potential problems result with such a treatment. First, if the vent is defined as an opening that allows both inflow and outflow, for large fires, $\dot{m}_{plume} > \dot{m}_{user}$ may result, which requires the code to numerically force ambient fluid into the domain at the rate $\dot{m}_{inflow} = \dot{m}_{plume} - \dot{m}_{user}$; a wholly unrealistic situation. Changing the opening to an outlet that prevents mass

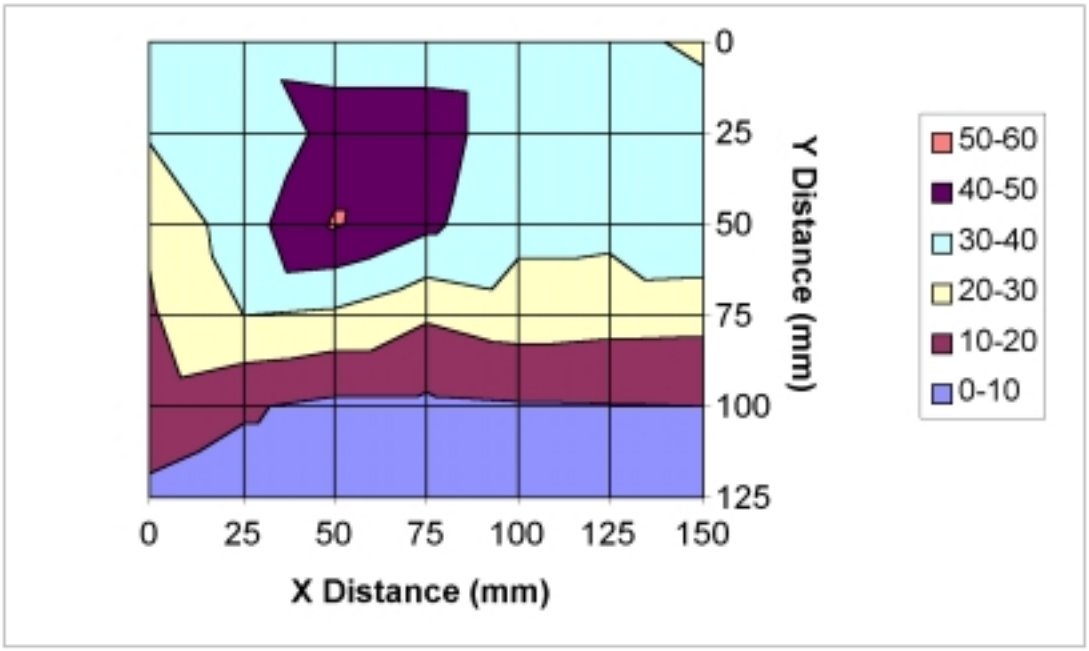


Figure 6.6: Measured flux map for CBUF burner with quarter symmetry (flux values are in $\frac{kW}{m^2}$).

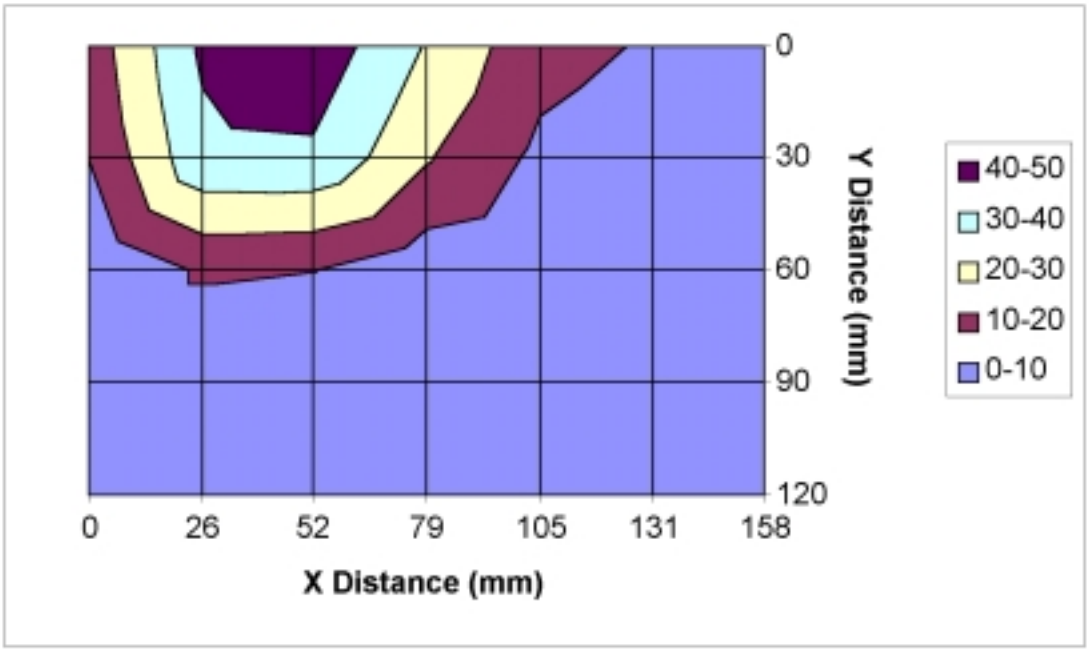


Figure 6.7: Predicted flux map for CBUF burner with quarter symmetry (flux values are in $\frac{kW}{m^2}$).

inflow introduces a second numerically induced problem. By constraining the mass flow out of the domain, the plume of large fires will transport more mass to the top of the hood than is removed. This forces the CFD code to turn the plume tangent to the outlet boundary with the eventual formation of a downward wall jet along the hood with flow possibly out the skirt. Such a radical reversal in the flow pattern is another strain on the solver, although in this case it is predicting the correct physical phenomenon. What is not considered, however, is the increase in fan flow rate caused by the upward motion of the fluid induced by the plume. The $\dot{m}_{user}$ boundary condition across the inlet thus predicts smoke spilling from under the hood in some cases where it was not actually experienced during testing. Solution stability then suffers.

The pressure drop induced by the fan can be estimated and is a better alternative than specifying a $\dot{m}_{user}$ opening condition. An average pressure distribution across the top of the hood on the order of $101,310\ Pa$ is sufficient to draw 4 $\frac{kg}{sec}$ of air at standard temperature and pressure though the fan; a more realistic situation since this is what the fan rating is actually based upon. Convergence difficulties are thus minimized. To prevent the loss of accuracy when subtracting large numbers, a pressure difference, and not the total pressure, is used for all calculations. An untested, but possibly more realistic measure of fan performance, would be the specification of a constant fan volume flowrate boundary condition. When exposed to heated fire gases, smoke removal fans provide constant volume (not mass) behavior, in reality reducing effectiveness and not usually included in the design.

### TASCflow Control Parameters

Other than flame spread, the final step in completing the problem specification involves selecting the parameters that control the operation and performance of TASCflow. This includes what equations to solve, the frequency of updating, discretization, solver controls, and values to be used in the submodels employed for closure of the problem. Table 6.3 lists many of the control parameters set in the .prm file.

### Fire Growth Model Parameters

A number of input files and routines have been developed to facilitate specification of the fire growth part of the problem. The files shown in Table 5.12 on Page 133 are available to the user, although only a few need to be modified for a given problem.

Values from flame.dat typical to all mattress experiments are shown in Table 6.4. Thermal properties applicable to PU foam were used in propr.f and propt.f. Insufficient information was available for other foams to permit using values other than those for PU.

| Parameter | Purpose | Value |
|---|---|---|
| cmu | $k-\epsilon$ constant for effective turbulent viscosity | 0.18 |
| prandt | Energy equation turbulent Prandtl number | 0.85 |
| iskew | Specifies mass weighted skew upstream (MWS) differencing scheme | 2 |
| kntlin | Maximum number of inner loop iterations per time step | 2 |
| kntrst | Frequency of writing to .rso file | 10 |
| multigrid | Specifies multigrid solver | t |
| lpac | Include physical advection correction (PAC) terms in transport equations | t |
| ertime | Target maximum residual for moving to next time step | 0.001 |
| gravz | Z direction acceleration due to gravity | $-9.81\ \frac{m}{sec^2}$ |
| poff | Pressure offset used to prevent round-off errors | $101,325\ Pa$ |
| tref | Reference temperature for natural convection | $303\ K$ |
| relex_ptotal | Relaxation for total pressure BC | .9 |
| max_solver_its_int | Solver work units per radiation iteration | 7.5 |
| max_loops_outer_rad | Radiation solver outer iterations | 1 |

Table 6.3: TASCflow control parameters.

| Variable | Value | Units |
|---|---|---|
| Density of pyrolysis products | 0.6454 | $\frac{kg}{m^3}$ |
| MW of fuel | 20. | $\frac{kg}{kmol}$ |
| MW of oxidizer | 32. | $\frac{kg}{kmol}$ |
| MW of products | 28.8 | $\frac{kg}{kmol}$ |
| MW of soot | 12. | $\frac{kg}{kmol}$ |
| Latent heat of vaporization | .605 | $\frac{MJ}{kg}$ |
| Maximum change in species concentration at a node before absorption coefficient is recalculated | 0.075 | (-) |
| Blackbody source temperature for absorption coefficient calculation | 303. | $K$ |
| Minimum mass fraction of gas species $i$ for absorption coefficient calculation | $1X10^{-5}$ | $\frac{kg}{kg}$ |
| Minimum mass fraction of soot species for absorption coefficient calculation | $1 \times 10^{-15}$ | $\frac{kg}{kg}$ |
| Iteration frequency for updating absorption coefficient calculation | 5 | (-) |
| Flux levels for data set in flame.hrr | 25, 35, 50 | $\frac{kW}{m^2}$ |

Table 6.4: Variables specified in flame.dat.

## 6.2 Results

### 6.2.1 CBUF Mattress 1:21

#### Model Input

Mattress 1:21 was constructed of a solid polyether foam core covered by cotton-viscose fabric giving a total thickness of 120 $mm$. As with all of the mattresses tested, item 1:21 was 2.0 $m$ long by 0.95 $m$ wide. As shown in Figure 6.8, this particular mattress was intended to represent domestic and contract products currently found in the marketplace.


Figure 6.8: CBUF mattress 1:21.

TASCflow and flame spread model parameters specific to this run are shown in Tables 6.5 and 6.6. Based on average product yields, the stoichiometric coefficient (mass of oxygen consumed per mass fuel burned) was determined to be 1.44. This agrees with, or is slightly lower than, values given in the literature for PU foam [183, 225]. Two cone calorimeter data sets are available at each flux level of 25, 35, and 50 $\frac{kW}{m^2}$ as shown in Figures 6.9 and 6.10. The two cone tests were averaged for each flux level, Figure 6.11.

Scaling of the cone results was necessary to account for differences between the thickness of the cone sample tested (50 $mm$) and the actual mattress thickness (120 $mm$). The same fabric thickness is used for cone testing, with sufficient foam to bring the overall sample to 50 $mm$. To account for the foam thickness difference, the time dimension for the cone calorimeter mass loss curve is strethched (lengthened) by a factor $\frac{120}{50} = 2.4$. Scaling started at 45 seconds, the apparent point of transition between fabric and foam burning. The flux averaged scaled values input directly to the model are shown in Figure 6.12.

| Parameter | Purpose | Value |
|---|---|---|
| znuf | Number of moles of fuel that react with znuo moles of oxidizer | 1 |
| znuo | Number of moles of oxidizer that react with znuf moles of fuel | 1.295 |
| stoich | Stoichiometric coefficient (oxygen) | 1.44 |
| dtime | Time step for fluid and CHT solution | 0.3 seconds |
| density_solid | Solid fuel density | 20 $\frac{kg}{m^3}$ |

Table 6.5: TASCflow control parameters for mattress 1:21.

| Variable | Value | Units |
|---|---|---|
| Number of fuel surfaces | 1 | (-) |
| Ignition temperature for fuel | 523 | $K$ |
| Minimum (critical) flux for piloted ignition | 12 | $\frac{kW}{m^2}$ |
| Number of moles of H2O formed per mole of CO2 | 0.89 | (-) |

Table 6.6: Variables specified in flame.dat for mattress 1:21.

The soot values shown in Figure 6.11 have been calculated based on the smoke production rate (SPR) values in $\frac{m^2}{s}$ as the product of the light extinction coefficient, $k$, and the duct flow rate, $V_f$, measured in the cone calorimeter. Using the specific extinction area on a fuel mass loss basis, $\sigma_f = \frac{\text{SPR}}{\dot{m}}$, the soot yield for input into the model can be calculated as $\psi_s = \frac{\sigma_f}{\sigma_m}$. The specific extinction coefficient per unit mass soot, $\sigma_m$, is taken equal to 7600 $\frac{m^2}{kg\ soot}$.

The model was started with a steady state fan solution and burner fuel inlet boundary condition ($\dot{m}_{CH_4} = 3.26X10^{-4}\ \frac{kg}{s}$), sufficient to give the 30 $kW$ from the burner used for testing. The fuel flow from the burner was "seeded" with 1% product ($CO_2$ & $H_2O$) and 0.2% soot to allow the combustion model to begin reaction of the fuel. All fluids and solids were given ambient temperature and properties.

Thermal and ignition properties for foam and fabric were not reported in the CBUF data set, although reasonable values for similar materials were found in the literature as shown in Appendix A.1. For solid phase heat transfer calculations, TASCflow requires separate values for $k$, $\rho$ and $c$, and not a composite $k\rho c$. Using these values and a user specified surface emissivity, TASCflow calculates a surface temperature at each node. Since four nodes surround each control surface, the flame spread routine uses these values to determine ignition. When the average temperature of the 4 nodes exceeds the user specified ignition temperature, a surface is considered to be burning. Since a flame is readily available from the burner, piloted ignition properties are reasonable. This is the primary way the flame spread routine determines flame spread.

Accurately determining $k\rho c$ values based on ignition data requires the use of

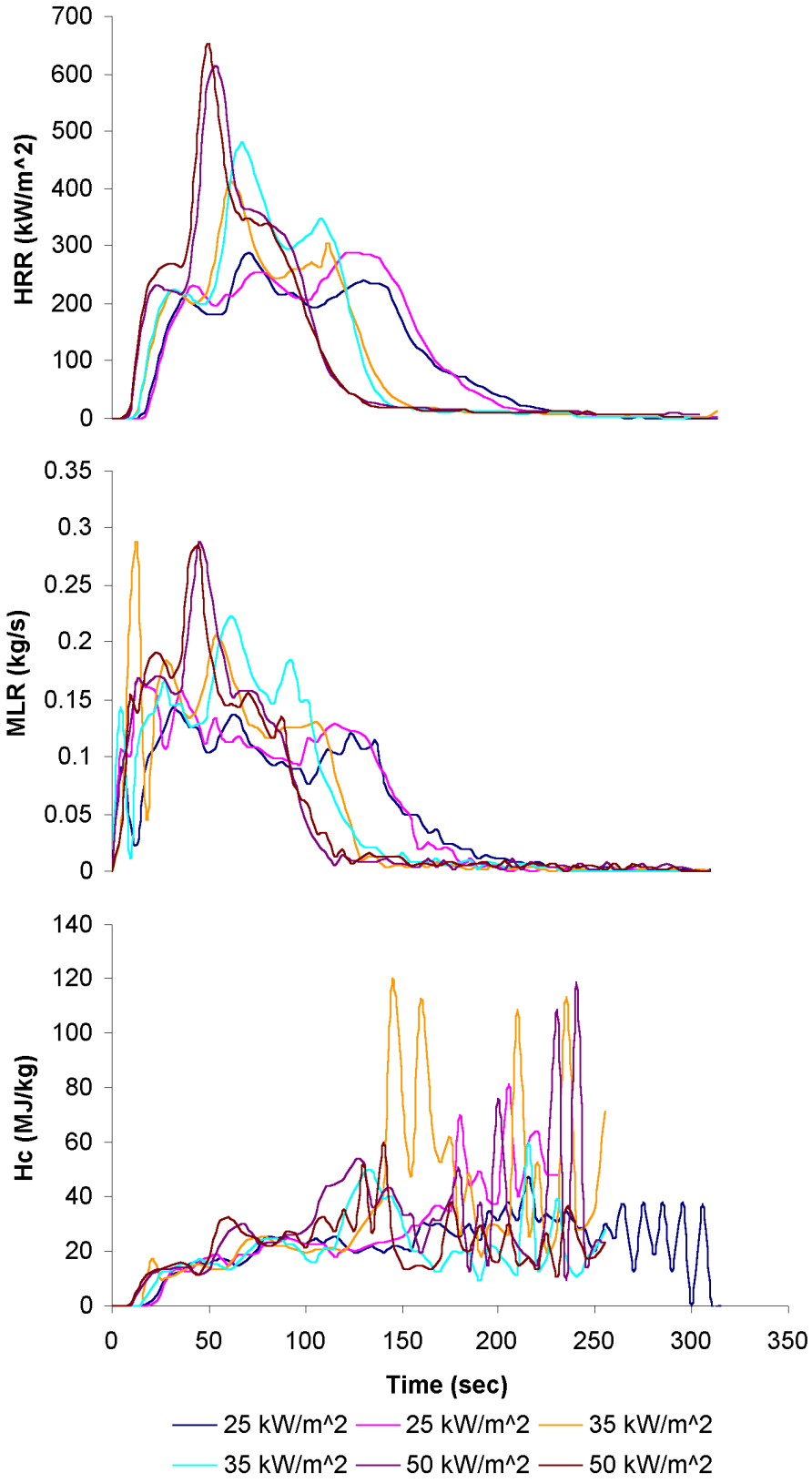


Figure 6.9: Raw cone calorimeter results for mattress 1:21.

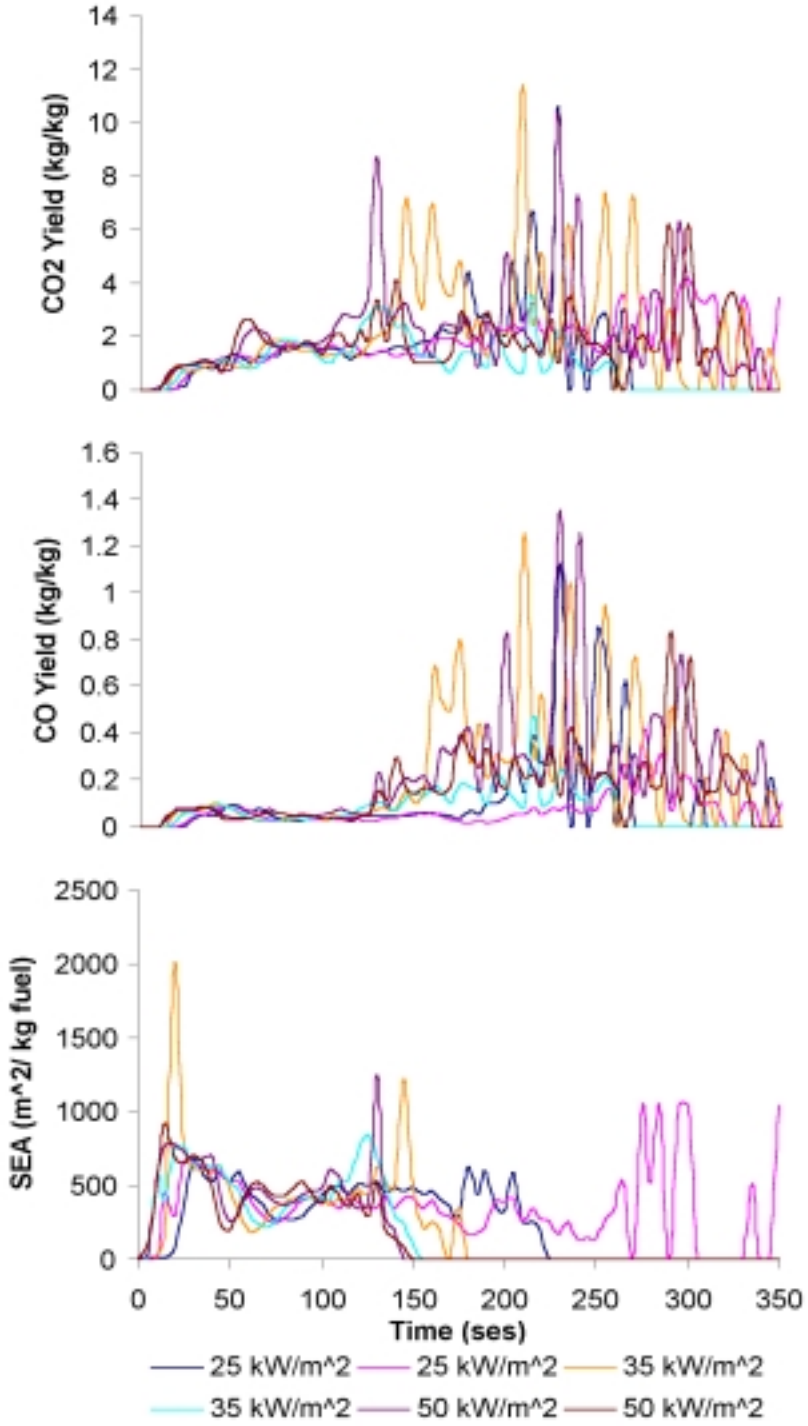


Figure 6.10: Raw cone calorimeter results for mattress 1:21.

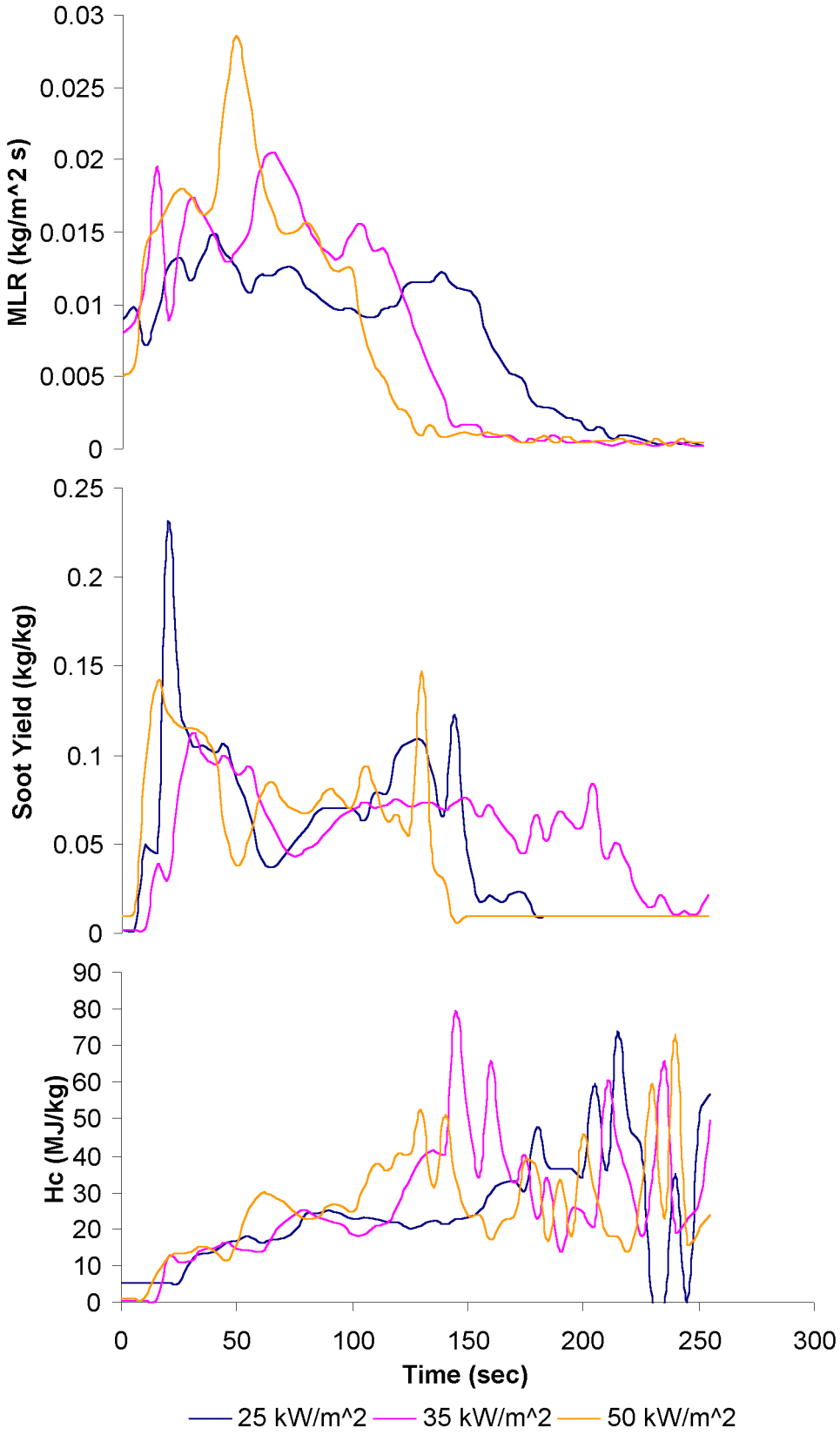


Figure 6.11: Flux averaged cone calorimeter results for mattress 1:21.

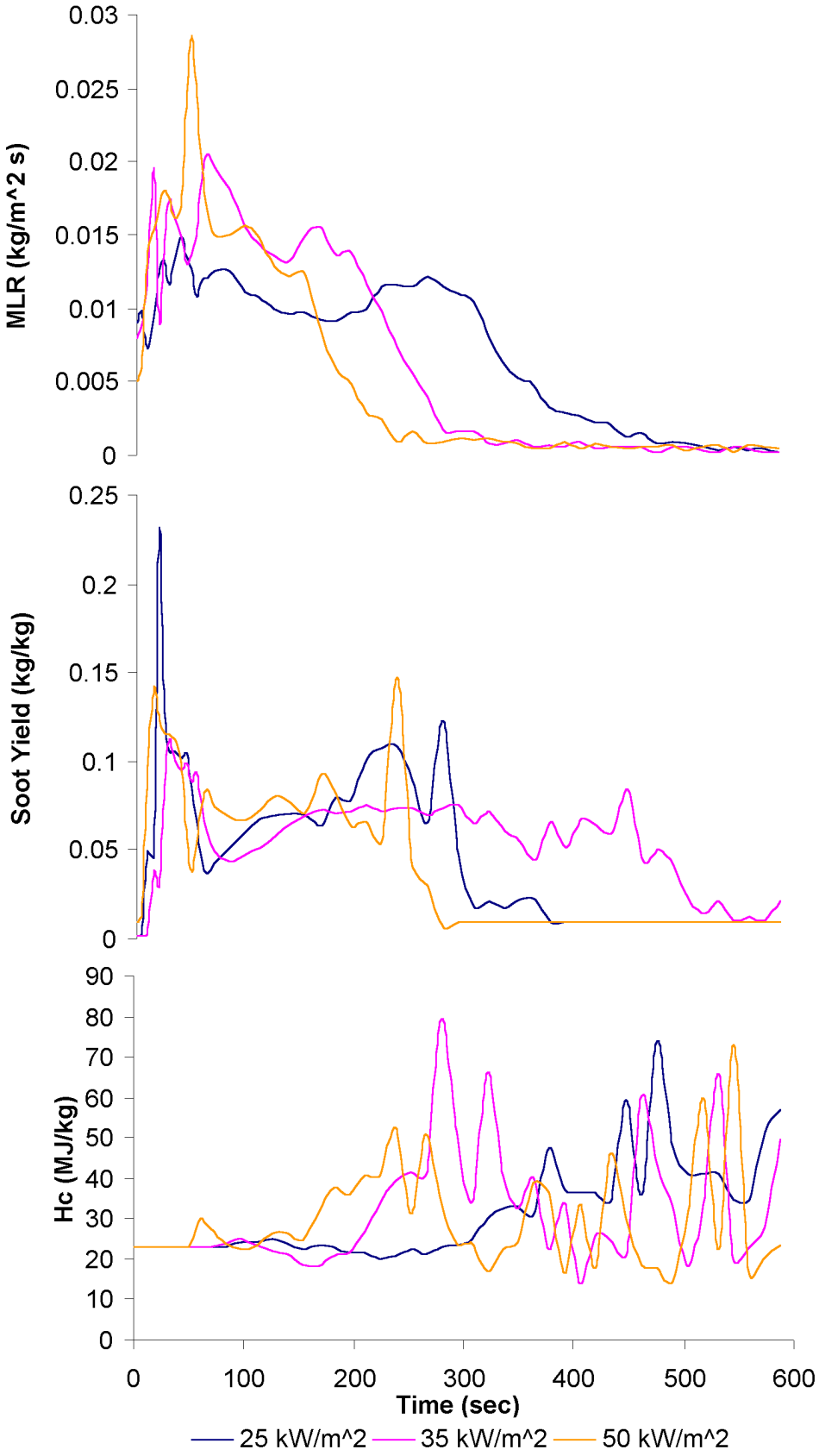


Figure 6.12: Scaled flux averaged cone calorimeter results for mattress 1:21.

some form of ignition model as described in Section 2.2. This, however, introduces a new level of uncertainty since a model must be selected that can add additional unknowns. An alternate route by which ignition of the solid can be addressed is through data on ignition time as a function of radiant flux. Above some minimum critical flux for piloted ignition, the time to ignition decreases as the flux level increases. For example, a surface element with an imposed flux of 50 $\frac{kW}{m^2}$ would ignite in 8 seconds. Values shown in Table 6.7 were also used in the flame spread model to supplement the surface temperature calculations. In effect, this ignition flux data

| **Flux** $\left(\frac{\mathbf{kW}}{\mathbf{m^2}}\right)$ | **Time for ignition (sec)** |
|---|---|
| 50 | 8 |
| 35 | 13 |
| 25 | 18 |
| 12 | $t \rightarrow \infty$ |

Table 6.7: Flux values as a function of time for ignition of mattress 1:21.

includes $T_{ign}$ and $k\rho c$ values implicitly and allows a more direct avenue for specifying ignition properties. Either the critical flux or the ignition temperature can determine the rate at which flame advances across the surface.

A transient heat of combustion value can be calculated from the cone calorimeter results for HRR and $\dot{m}$ as shown in Figures 6.9 and 6.11. When input directly into the flame spread model, the initial period of low $\Delta H_c$ values result in significantly reduced energy release rates. It is necessary to investigate the cause of this problem that appears to inhibit the model from calculating realistic flame spread rates.

The CBUF raw oxygen analyzer data from the cone calorimeter is time shifted to account for the delay in transport from the fuel to the instrumentation through an equation of the form

$$X_{O_2}(t) = X_{O_2}(t + t_d) \tag{6.1}$$

Thus, the oxygen analyzer mole fraction reading, $X_{O_2}$ is adjusted to account for the oxygen analyzer transport delay time, $t_d$. Additional time delays due to instrument response, however, must be considered. Oxygen analyzers used during the CBUF test series have response times on the order of 10 seconds [226]. The possibility of this measurement delay producing the initially low $\Delta H_c$ values was investigated. The heat release rate data used to calculate $\Delta H_c$ was shifted by 10 seconds as shown in Figure 6.13. The time shift appears to account for some, but not all, of the initial low $\Delta H_c$ values. Additionally, it is necessary to consider the delay between the start of exposure and ignition since significant mass loss, without combustion, can occur during this period. For the cone data shown in Table 6.7, the ignition times were 18, 13 and 8 seconds for fluxes of 25, 35 and 50 $\frac{kW}{m^2}$. This could approximately account for some of the additional delay, although it is still necessary to consider the delay from first ignition until flame establishes itself over the surface of the fuel. It may also be appropriate for input to the model to start the cone runs at the point of

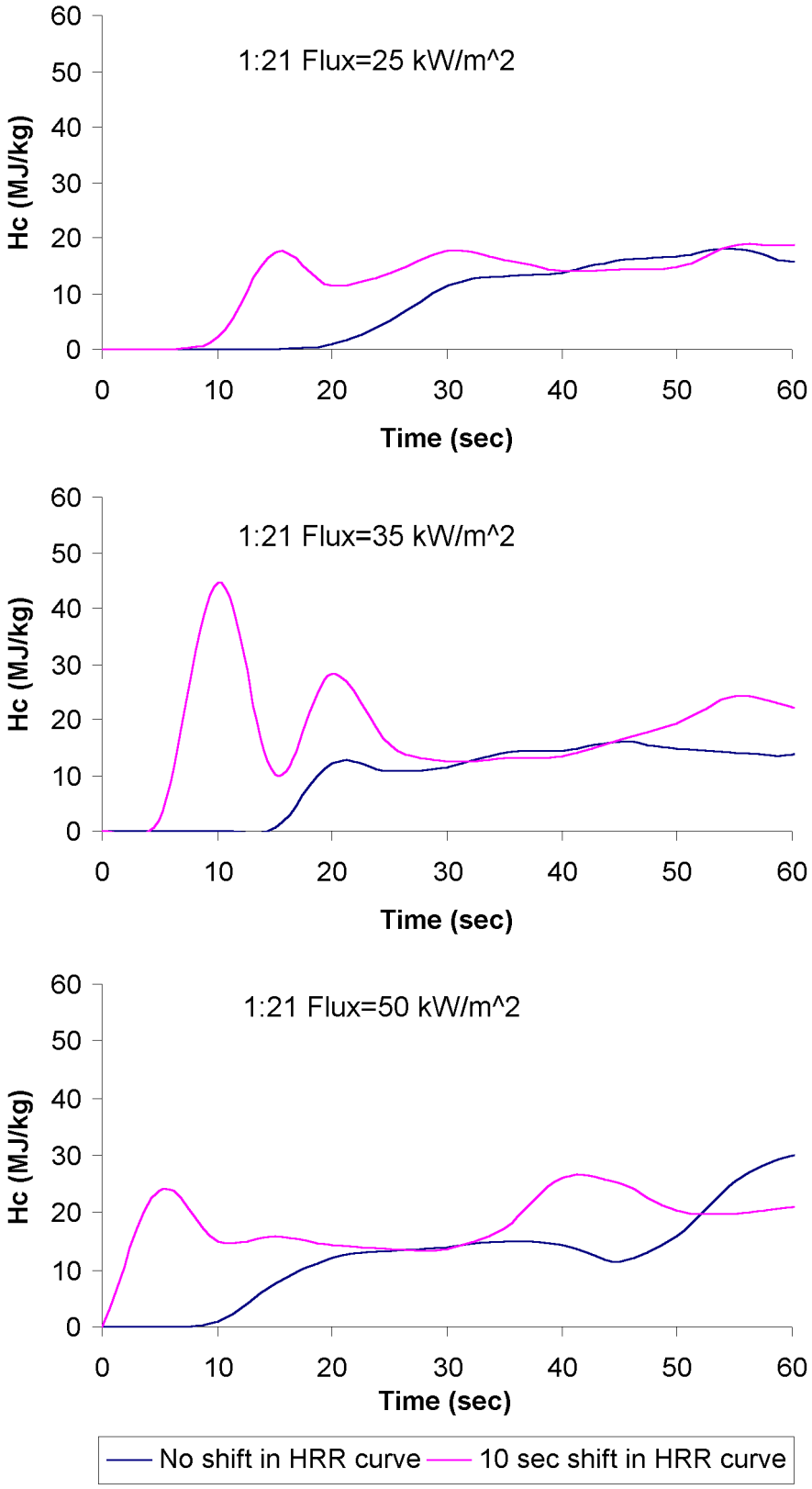


Figure 6.13: Time shifted cone calorimeter heat of combustion values based on FDMS data for mattress 1:21.

ignition, thus removing the delay from the start of each curve. This was not done for the current work, although it would appear to correct the remainder of the problem. If one has access to the raw cone data before it is reduced by the data collection software, deconvolution of the data may allow the original peaks to be captured. This would be the ideal situation permitting the best chance of a physically correct picture. Since the raw data from the CBUF data set was not available, this will not be discussed further.

To address this situation in the model, the heat of combustion value at 30 seconds was used for times less than 30 seconds, Figure 6.12. Although this is one solution, shifting the cone data at each flux level so that time=0 seconds occurs at ignition should be considered for future work.

As mass loss rates tend toward zero at the end of a cone run, calculated $\Delta H_c$ values become highly irregular. The composite $\Delta H_c$ value used during a given time step of the calculations is the mass loss rate weighted average of the values from all burning surfaces. Since mass loss rates at this point are very small, the effect of variations in $\Delta H_c$ are minimal.

Two additional modifications were made to the raw cone data given in Figures 6.9 and 6.10 to obtain the data for implementation in the model:

- Thickness scaling was applied to account for the difference between bench and full scale foam thickness during testing.
- Multiple cone calorimeter tests at a given flux level where combined into a single data set by simple averaging.

### Model Results

Model and experiment results for heat release rate (HRR), mass loss rate (MLR), heat of combustion ($\Delta H_c$), soot yield, total energy released, and total mass lost are given in Figures 6.14 and 6.15. Full scale testing of this fuel package resulted in a significant fire with flame spread over the complete sample. A peak heat release rate of 0.91 $MW$ was observed 256 seconds into the test. A total of 160 $MJ$ of energy was released by the 7.3 $kg$ of fuel generated (the mattress was completely consumed). From 144 to 220 seconds, the burning rate was sufficient to cause smoke to spill from under the furniture calorimeter hood and continued until the fan speed could be increased. This resulted in a reduction in the measured HRR during this period as shown in Figure 6.14. Mass loss measurements may be up to 10% off since .7 $kg$ more fuel was reported lost than the total starting mass of the mattress. Both experimental and model HRR results for all cases include the 30 $kW$ from the burner [226]. Flame was observed to go out 1124 seconds into the test.

### Discussion

Although the model is not able to simulate the complete range of furniture burning behavior, it has captured sufficient detail for prediction of the period during flame spread across the surface. Analysis of the results reveals the following:

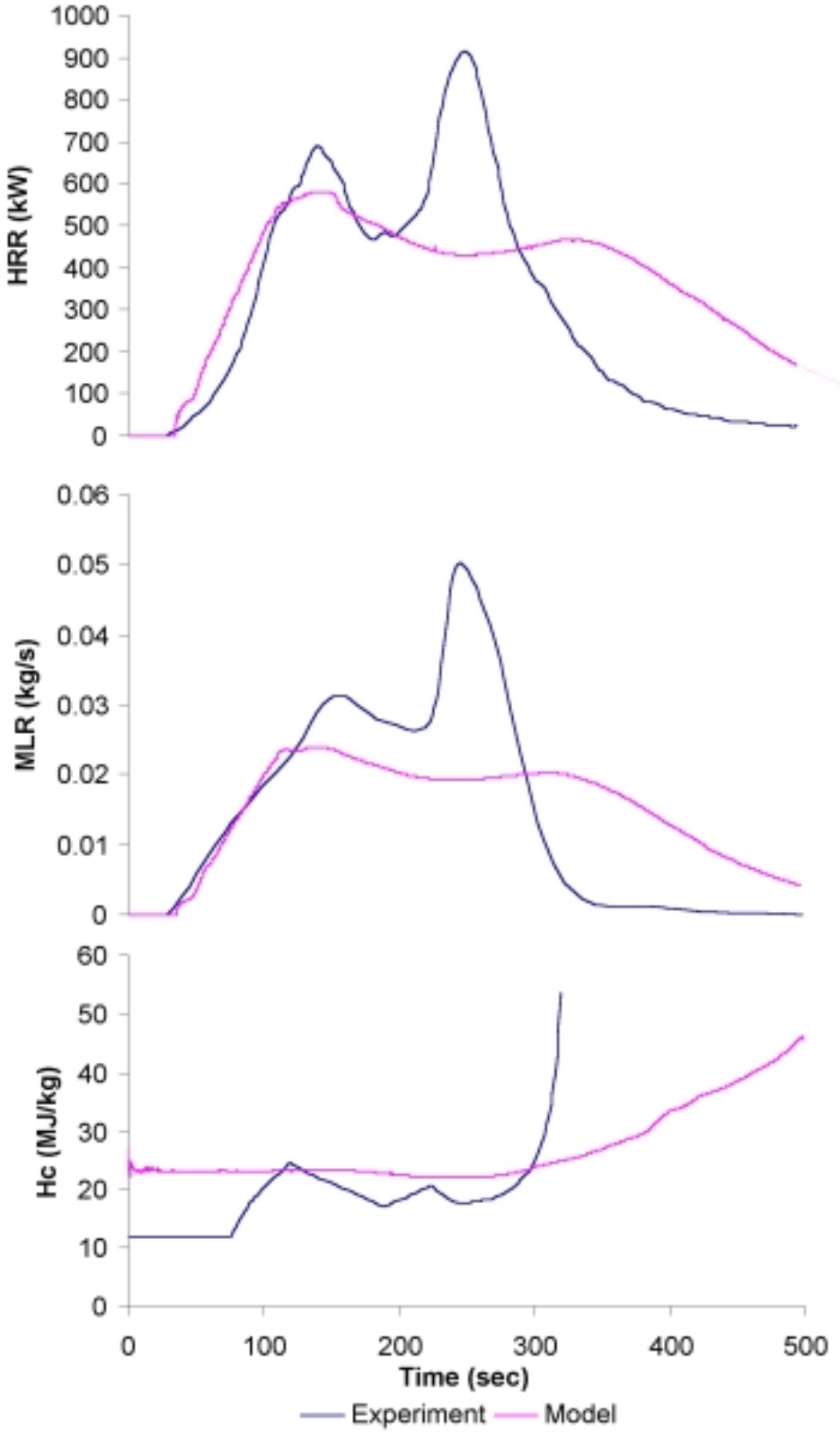


Figure 6.14: Furniture calorimeter and model results for mattress 1:21.

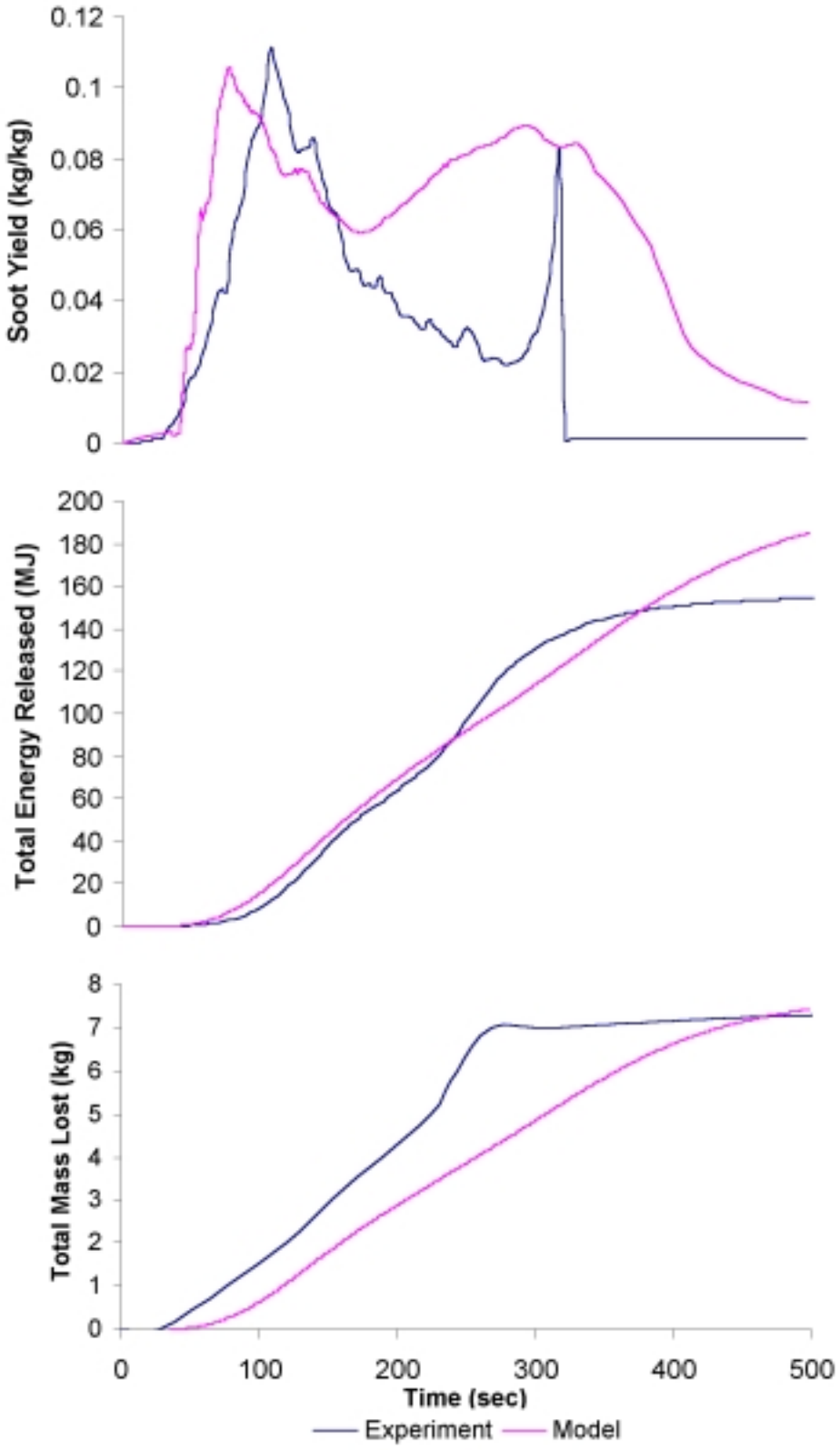


Figure 6.15: Furniture calorimeter and model results for mattress 1:21.

- The initial rapid fire spread across the fuel package appears to be well predicted. After the burner is turned off at 120 seconds, the model captures the decrease in HRR as shown in the experiment.

- The model, however, fails to capture the second later HRR peak measured for the mattress. By missing this peak, the model's lower mass loss rate takes approximately 200 seconds longer to consume the total mass of the mattress. For the mattresses, the top only, and not the sides or bottom, was modeled. This artificially constrains the area available for pyrolysis. The metal rack with slats used to support the mattresses off the floor during testing was also not modeled in detail. Difficult to predict behavior, such as the formation of a pool fire of burning liquid foam under the mattress, were not included. Such an increase in burning area could lead to the formation of a second peak in mass loss and resultant heat release rate.

- During the first 120 seconds, the mass loss rate predicted by the model agrees much better with experiment than the HRR. The discrepancy appears due to differences in the actual and predicted heats of combustion.

- The first model runs were attempted with a constant user supplied value for $\Delta H_c$. As expected, model results were highly sensitive to this one variable. Too low a $\Delta H_c$ allowed flame spread to languish, while fire would cover the mattress much too quickly when larger $\Delta H_c$ values were used. Analysis of furniture calorimeter data shows that heat of combustion values are, in fact, not constant. During the early periods of a fire, $\Delta H_c$ values match what is burning, namely the fabric. With time, the $\Delta H_c$ increases as the fire consumes more of the foam. Model results improved when input was modified to include the calculated $\Delta H_c$ based on transient cone calorimeter results.

- After 300 seconds, the experimentally derived $\Delta H_c$ rapidly increased as the mass loss rate approaches zero. Although the total mass lost values are in agreement, the model over-predicts the total energy lost.

- Peak soot values are in close agreement, although the model peak occurs slightly earlier than measured. In the model, soot yields are determined based on the mass of fuel burned and are calculated at the point of fuel combustion. The furniture calorimeter, however, measures soot in the instrumentation region of the apparatus, away from the point of combustion. Differences in timing for the two peaks can be attributed to transport time differences since the two curves represent the same measurement, although taken at different locations.

- Distributed soot production was found to be essential for correct flame spread calculations. An early version of the Furniture CFD model released the soot with fuel above the surface of the burning solid. A region of soot with mass fraction above .5 formed. This soot layer prevented flame radiation from reaching the fuel and slowed flame spread. In addition, numerical instabilities resulted

with the radiation model due to non-physically large absorption coefficients on the order of $10 - 100\ \frac{1}{m}$. When the flame spread code was modified so that soot was released at the point of combustion, realistic soot concentrations and radiation properties resulted.

- Use of the $k_{tke} - \epsilon$ model plume coefficients determined by Nam and Bill improved results of the Furniture CFD model. Without the corrections, the turbulence model predicted a very narrow plume with excessive centerline temperatures and a negligible view factor to the mattress. The low radiant flux levels to fuel ahead of the pyrolysis front delayed flame spread.

- Because they are minor radiating species, the exact composition of gas phase combustion products was not found to be critical to the radiation modeling.

- Flame spread velocities across the mattress were not recorded during the experiments, thus a direct comparison can not be made. Both model and experiment, however, show that the fire consumes the entire mattress. More importantly, the slopes of the experiment and model heat release rate curves can be used as a substitute for the missing spread rate data. Measured between 10% and 90% of the peak HRR, the slopes for the experiment and model are 6.6 $\frac{kW}{sec}$ and 7.4 $\frac{kW}{sec}$ respectively, for a difference of approximately 13%. The experimental slope was measured to the first peak shown in Figure 6.14, which represents the time during which flame is spreading over the mattress. A second larger peak was measured during the experiments, but this was due to the formation of a pool fire of burning polyurethane under the mattress, a behavior not addressed by the model. Although the HRR is an aggregate of the overall spread rate, pyrolysis, and fluid flow, it can serve as a measure of the global performance of the model.

- Because flame spreads rapidly across the fuel, the approximately 1 $cm$ grid size used for the mattress surface provides adequate resolution.

- Thickness scaling of the cone calorimeter data was critical to obtaining reasonable results considering the foam in the mattress was almost two and a half times thicker than that tested in the cone. Runs without thickness scaling greatly under-predicted the HRR and MLR since burnout resulted prematurely.

- The reasonable agreement between fluxes from the CBUF and model burners shown in Figures 6.6 and 6.7 was necessary to allow the model to predict the ignition and beginning stages of flame spread across the mattress. Without accurate initial ignition predictions, time shifting of the model results to match the experiment would have been necessary.

- Detailed modeling of the burner gas jets proved unimportant. More critical was the total burner heat release rate.

- The TASCflow solver proved to be very robust. Very few numerical difficulties were experienced during computation. At most, infrequent overflow or local convergence problems were observed.

- A numerically stable boundary condition specification at the interface between the hood opening and the area outside the hood (i.e. the laboratory) was difficult to obtain. Specification of an ambient pressure boundary condition directly under the hood produced numerical overflow and negative velocities as air would flow from outside at high speed directly below the bottom of the hood. Stability was possible by expanding the domain under the hoods and specifying the ambient pressure boundary conditions further from the opening. Since a weak boundary condition specification resulted, a small amount of total pressure relaxation (.9) was necessary. Overall results were not changed due to the relaxation.

Two weeks (slightly under 16 days) of computation time were required for the 500 seconds of model results. On average, 0.77 hours of CPU time were required for each second of real model time. The model was executed on an Alpha EV5 (21164) processor running at 300 $MHz$ and using 512 $Mb$ of RAM. When a converged initial guess can be used as a starting point, setting up additional scenarios can take much less time, although the computation time will generally remain the same.

Model results varied by less than 5% when the time step was reduced by one-half. Over 50 initial test runs were completed on a smaller scale to optimize the grid and time step used for the furniture calorimeter calculations. It was found that with discretization of the fuel surface greater than 5 $cm$, flame spread would stall as the front moved further away from the burner. Since the average of the temperature of the four nodes that define each control surface is used to indicate ignition, the two nodes furthest from the front hold down the average. Once ignited, heating starts on the next ring of nodes. Plots of the spread rate exhibited "leap frog" behavior that would also show up in the total heat release rate. Initial nodes were spaced too far apart in a direction perpendicular to the openings. Slight pressure differences resulted in large mass flow rates that inhibited convergence and frequently resulted in numerical overflow problems.

Time step size was controlled by both accuracy and numerical stability demands. Time steps under 5 seconds were found to be very stable, although additional iterations or solver work units were necessary to maintain acceptable residual levels. Flame spread calculations, were not accurate with a time step this large. Time steps of 3 seconds, 2.5 seconds and 1 second still resulted in changes in the rate of spread with each smaller time step. Runs with time steps less than 1 second (such as .5 seconds) provided results that were nearly independent (within 5%).

Net momentum, mass, species and energy values through the domain balanced within $1E-03$ to $1E-04$ of maximum values; reasonable levels for reacting multi-component fluid flows. Radiant heat transfer balanced globally on the order of $1E-02$ based on 24 work units per iteration. A significant increase in required solver time was necessary for improvement in the radiation solution. The greatest challenge for

the finite volume radiation model results both in the areas of large gradients near the fire and in evaluating the radiation lost to the large surrounding areas outside the furniture calorimeter that remain at ambient temperature. For the .3 second time step used to generate the model results presented, two inner loop iterations were used for each outer loop iteration. TASCflow computation time was divided approximately as shown in Table 6.8.

| **Component** | **Percent of CPU time** |
|---|---|
| Pre-process | 1 |
| U-V-W-P-T | 25 |
| $k_{tke} - \epsilon$ | 6 |
| Scalars | 12 |
| FV radiation | 54 |
| Post-process | 1 |
| Miscellaneous | 1 |

Table 6.8: Breakdown of CPU usage for mattress 1:21.

Clearly the fact that the FV radiation calculations were consuming more than half the CPU time shows the difficulty in performing computer modeling of problems incorporating intensive radiation calculations. Unfortunately, based on the physics involved, flame spread problems usually require detailed information on local radiant flux levels.

**Analysis of Radiation Results**

Used without radiation heat transfer calculations, the Furniture CFD Model greatly underpredicts flame spread rates. Driven by the burner, the flame front was found to move approximately 0.1 $m$ and then slow considerably, since only gas and solid phase conduction drives the spread. Without sufficient forward heating, conduction into the solid preventes the surface of the fuel from reaching the ignition temperature. The resulting bulk heating of the solid did not show the expected large gradient in temperature near the surface. Flame temperatures were also significantly overpredicted since the flame was only cooled through convection, conduction and entrainment of ambient air. Similar results have been demonstrated during the modeling of fires in large bay spaces with JASMINE [204]. The impact of radiation modeling on fluid flow predictions for the Steckler room fire experiments have also been shown [168, 211].

The region above a piece of burning furniture is far from homogeneous with respect to radiant heat transfer, so a mean beam approximation would not be appropriate. Because the surfaces are at different temperatures and the fluid volume is non-isothermal, a more detailed approach is necessary. Two different radiation models were used during initial testing of the flame spread routine. As discussed in Section 4.4.3, the diffusion and surface to surface models represent optically thick

and thin behavior respectively. Although both models were investigated, neither gave satisfactory results measured in terms of net radiative flux from the flame to the fuel surface.

The diffusion model approximates radiation transfer from each control volume to its six neighbors. This could be the correct physical situation when combustion is taking place in a narrow band surrounding a flame or with extremely high soot concentrations, but was found to provide peak radiation flux levels to the fuel surface of 5 $\frac{kW}{m^2}$. Comparing to experiment, these predictions are more than an order of magnitude less than the measured burner fluxes given in Figure 6.6. Although it is very computationally efficient, the model failed to simulate actual conditions.

At the other end of radiation model behavior, the surface to surface model did not even consider the existence of a participating medium between surfaces. This model predicted surface radiation energy loss from the fuel to the ambient temperature hood, openings and floor. Since the model produced a net loss of radiation, fuel surfaces were unable to reach the ignition temperature, so sustained spread was not predicted. Physically this appears incorrect because the environment is not transparent to radiation at emitting wavelengths important for heat transfer in fires.

For non-isothermal fluid domains with intermediate behavior, the finite volume radiation transfer model was found to provide more reasonable flux estimates. As a ray tracing method, it can become computationally intensive as the grid is refined. As a less demanding alternative, six-flux models only solve for participating radiation transfer along the coordinate axis. Since the model does not calculate radiant heat transfer at angles to the grid, it can not be expected to accurately predict some scenarios such as a flame above a horizontal fuel. Although it does not appear studied, the six-flux model may provide acceptable estimates for upward flame spread.

Selection of a solver must consider the numerical issues involved with radiation transfer in participating media. Multi-component fluid flow predictions using CFD result in a banded matrix since each node is receiving influence from only near neighbors. A solver such as Gauss-Seidel may be appropriate in this case.

The situation changes drastically when participating radiation is considered. Now each node can "see" every other node, destroying any matrix banding. Without excessive iterations, Gauss-Seidel will not transport radiation information across the grid due to its local behavior. As a grid is refined, error reduction becomes even more difficult since the solver barely reduces long wavelength errors in the small coefficient direction. The disastrous situation of grid refinement reducing solver performance appears, yet this situation has not received attention in the literature dealing with CFD modeling and fire. The majority of published results are based on convergence criteria looking at change in scalar values of less than 1%. By not considering how the solver treats radiation, the model may be transferring radiation information across the domain so slowly that the user mistakes the situation for convergence.

The multigrid solver employed by TASCflow is an ideal match for the numerical characteristics of participating radiation heat transport. During a given iteration, TASCflow moves between coarse and fine grids through the Algebraic Multigrid (AMG) method. Additive Correction Multigrid (ACM) governs the formation of

coarse grid equations to improve convergence through minimization of flux imbalances on the various grids. Additional benefits include a reduction in computation time since the solver is working coarse grids for a large part of a each iteration.

### 6.2.2 CBUF Mattress 1:22

#### Model Input

Mattress 1:22 was constructed of a solid latex foam core covered by cotton-viscose fabric giving a total thickness of 100 $mm$. As with all of the mattresses tested, item 1:22 was 2.0 $m$ long by 0.95 $m$ wide. This particular mattress was intended to represent domestic and contract products currently found in the marketplace as shown in Figure 6.16.


Figure 6.16: CBUF mattress 1:22.

TASCflow and flame spread model parameters specific to this run are given in Tables 6.9 and 6.10. Based on average product yields, the stoichiometric coefficient (mass of oxygen consumed per mass fuel burned) was determined to be 0.569. Two cone calorimeter data sets were available at each flux level of 25, 35, and 50 $\frac{kW}{m^2}$ as shown in Figures 6.17 and 6.18. The two cone tests were averaged for each flux level, Figure 6.19.

| Parameter | Purpose | Value |
|---|---|---|
| znuf | Number of moles of fuel that react with znuo moles of oxidizer | 1 |
| znuo | Number of moles of oxidizer that react with znuf moles of fuel | 0.356 |
| stoich | Stoichiometric coefficient (oxygen) | 0.569 |
| dtime | Time step for fluid and CHT solution | 0.3 seconds |
| density_solid | Solid fuel density | 61.7 $\frac{kg}{m^3}$ |

Table 6.9: TASCflow control parameters for mattress 1:22.

| Variable | Value | Units |
|---|---|---|
| Number of fuel surfaces | 1 | (-) |
| Ignition temperature for fuel | 664 | $K$ |
| Minimum (critical) flux for piloted ignition | 15 | $\frac{kW}{m^2}$ |
| Number of moles of H2O formed per mole of CO2 | 0.89 | (-) |

Table 6.10: Variables specified in flame.dat for mattress 1:22.

Scaling of the cone results was necessary to account for differences between the thickness of the cone sample tested (50 $mm$) and the actual mattress thickness (100 $mm$). The same fabric thickness is used for cone testing, with sufficient foam to bring the overall sample to 50 $mm$. To account for the foam thickness difference, the time dimension for the cone calorimeter mass loss curve is strethched (lengthened) by a factor $\frac{100}{50} = 2.0$. Scaling started at 35 seconds, the apparent point of transition between fabric and foam burning. The flux averaged scaled values input directly to the model are shown in Figure 6.19.

The transient heat of combustion value is calculated from the cone calorimeter results for HRR and $\dot{m}$ as shown in Figure 6.17 and 6.19. As discussed in Section 6.2.1, the average $\Delta H_c$ value is substituted for the first portion of the cone curve as shown in Figure 6.20. This was especially important for mattress 1:22 since a large mass loss rate occurs during the first 30 seconds of the cone data.

The soot values shown in Figure 6.19 have been calculated based on the smoke production rate (SPR) in $\frac{m^2}{s}$ as the product of the light extinction coefficient, $k$, and the duct flow rate, $V_f$, measured in the cone calorimeter. Using the specific extinction area on a fuel mass loss basis, $\sigma_f = \frac{\text{SPR}}{\dot{m}}$, the soot yield for input into the model can be calculated as $\psi_s = \frac{\sigma_f}{\sigma_m}$. The specific extinction coefficient per unit mass soot, $\sigma_m$, is taken equal to 7600 $\frac{m^2}{kg\ soot}$.

The model was started with a steady state fan solution and burner fuel inlet boundary condition ($\dot{m}_{CH_4} = 6.0X10^{-4}\ \frac{kg}{s}$), sufficient to give the 30 $kW$ from the burner used for testing. The fuel flow from the burner was "seeded" with 1% product ($CO_2$ & $H_2O$) and 0.2% soot to allow the combustion model to begin reaction of the fuel. All fluids and solids were given ambient temperature and properties.

The user specifies the critical radiant flux for piloted ignition. At fluxes above this value, the time to ignition decreases as flux increases. To model the time after the burner is ignited, but before the mattress starts burning, values shown in Table 6.11 were used.

The minimum flux level tested in the cone calorimeter was 25 $\frac{kW}{m^2}$. When an ignited surface element was exposed to a flux less than 25 $\frac{kW}{m^2}$, the cone results for 25 $\frac{kW}{m^2}$ were used. Linear interpolation was applied to evaluate properties between tested flux levels and cone data points. Three modifications were made to the raw cone given in Figures 6.17 and 6.18, to obtain the data for implementation in the model:

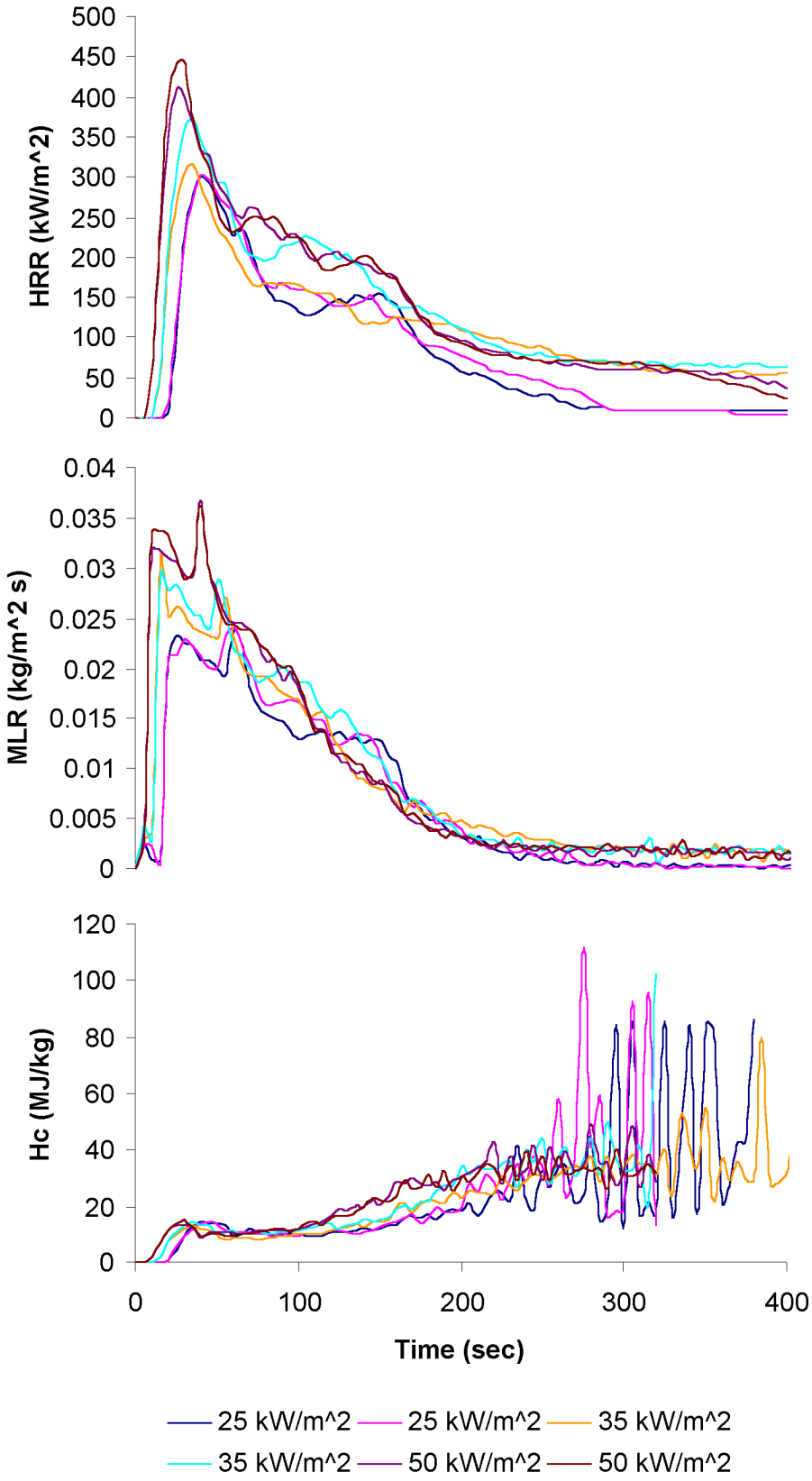


Figure 6.17: Raw cone calorimeter results for mattress 1:22.

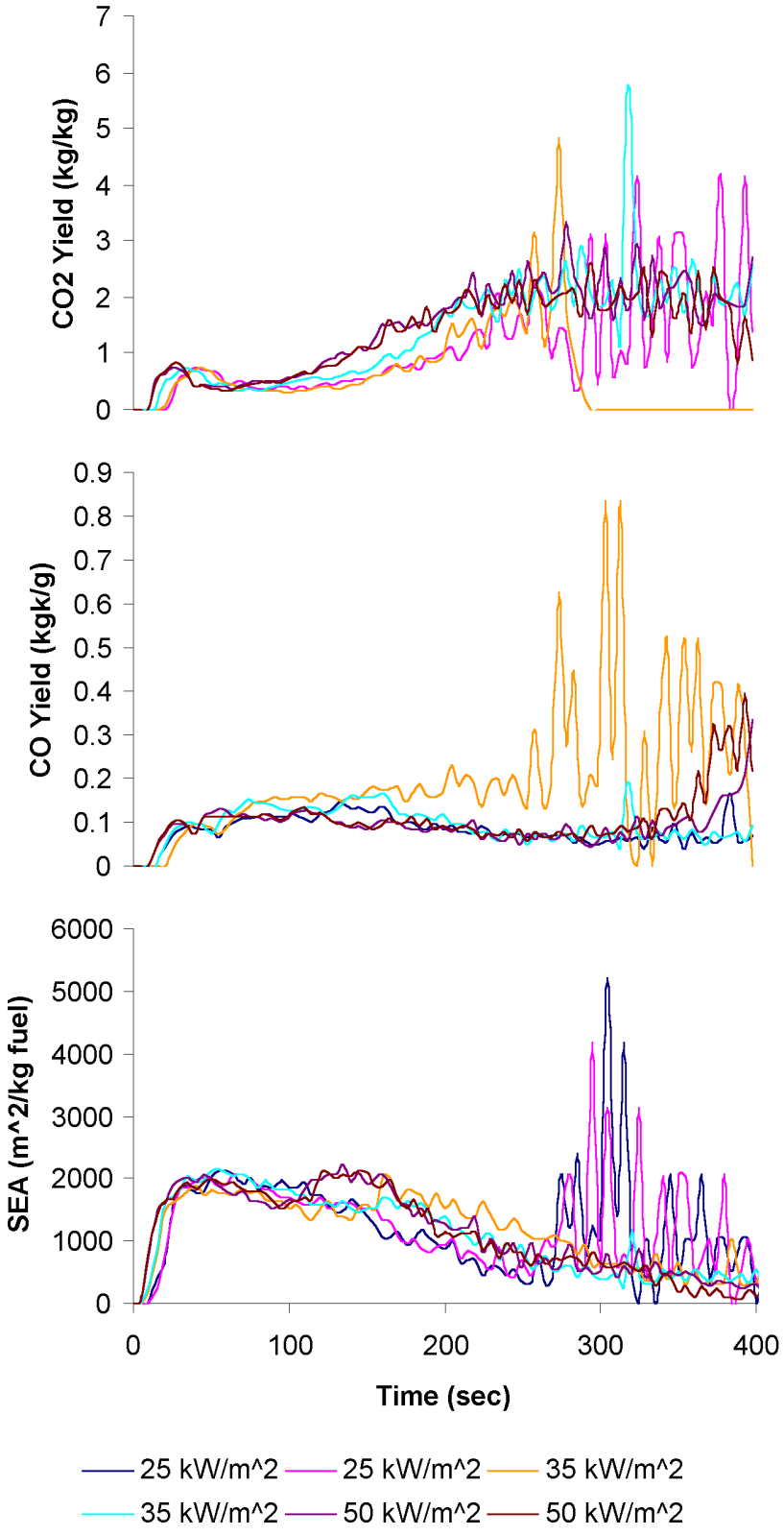


Figure 6.18: Raw cone calorimeter results for mattress 1:22.

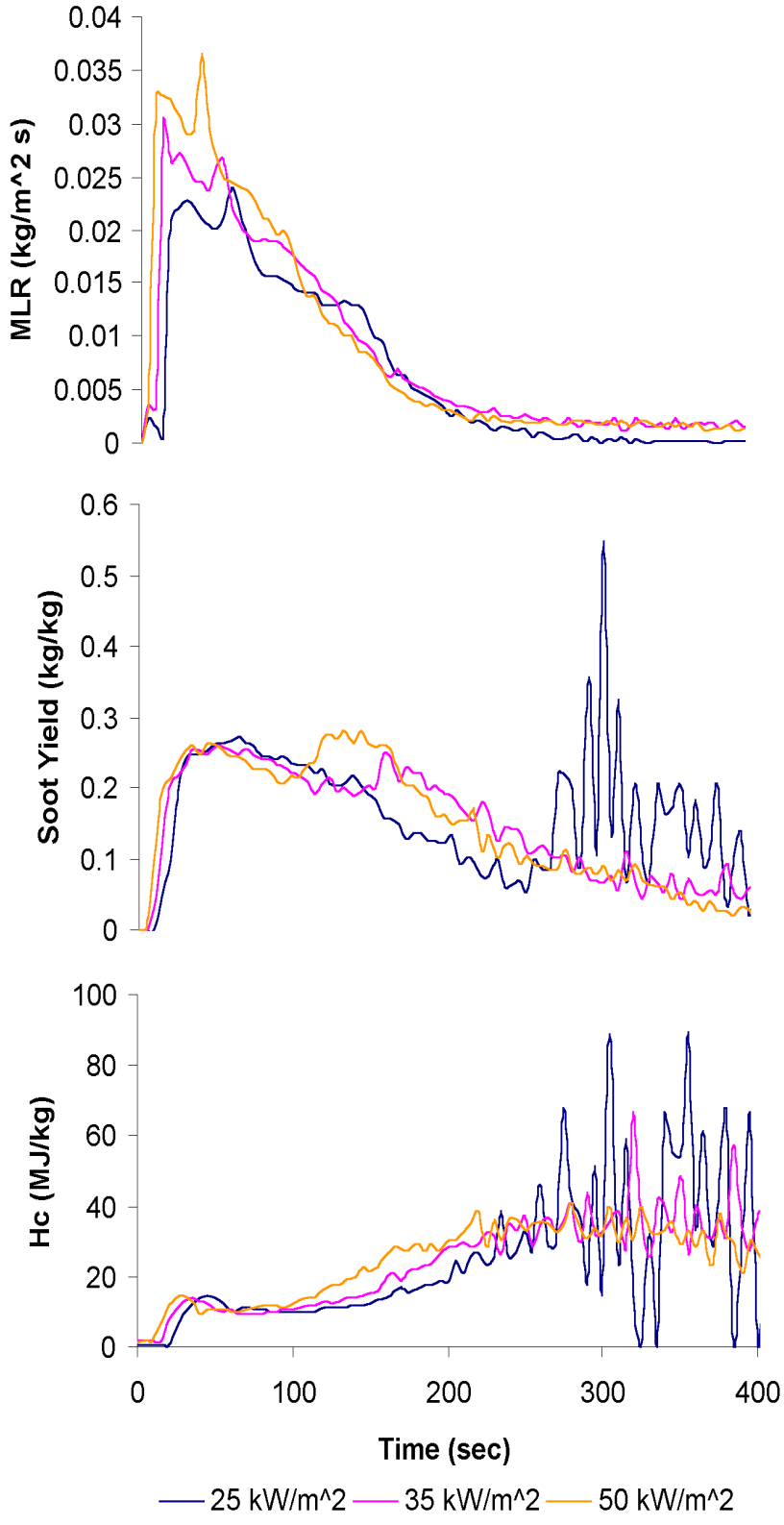


Figure 6.19: Flux averaged cone calorimeter results for mattress 1:22.

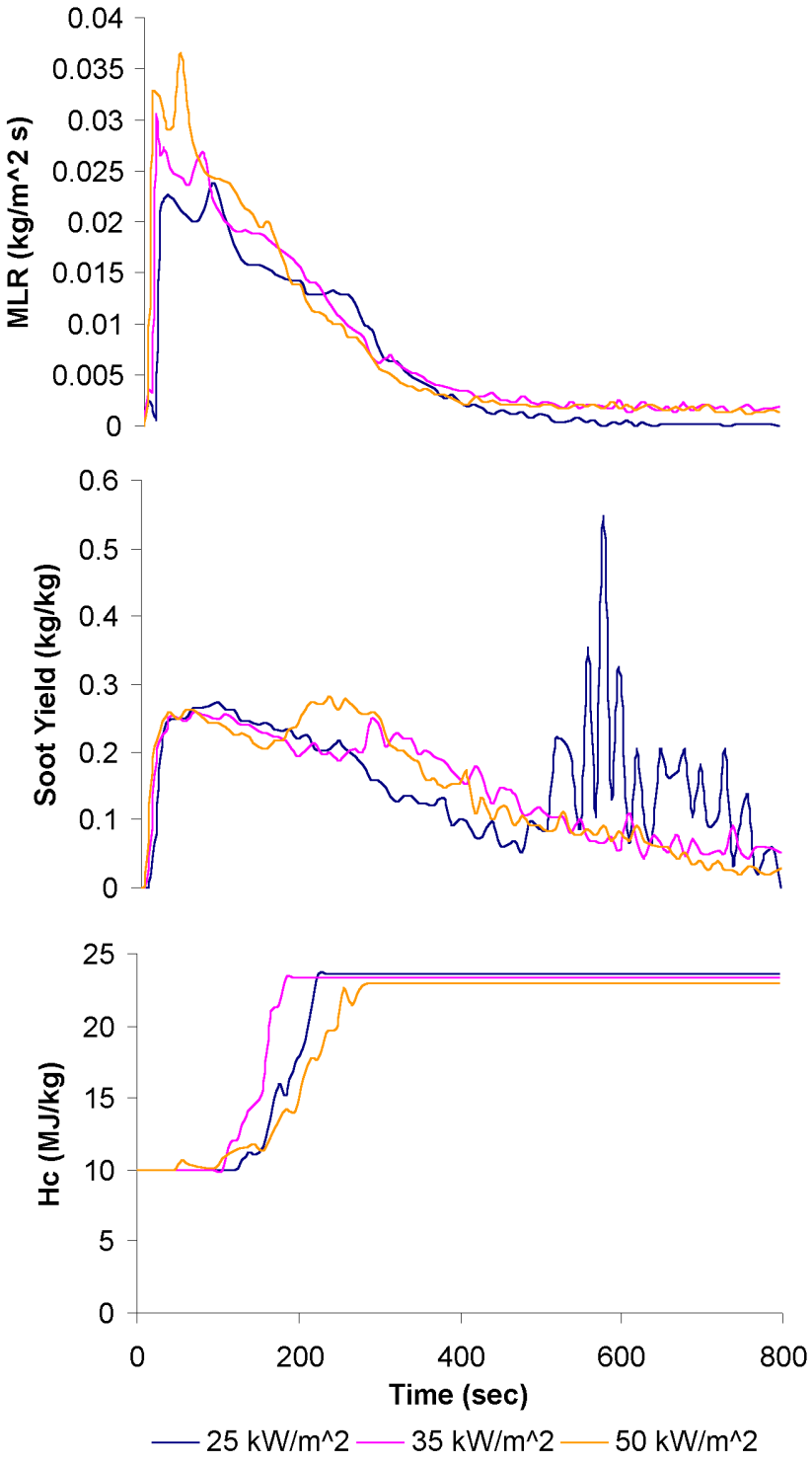


Figure 6.20: Scaled flux averaged cone calorimeter results for mattress 1:22.

| Flux $\left(\frac{\mathbf{kW}}{\mathbf{m^2}}\right)$ | Time for ignition (sec) |
|---|---|
| 50 | 8 |
| 35 | 13 |
| 20 | 19 |
| 12 | $t \rightarrow \infty$ |

Table 6.11: Flux values as a function of time for ignition of mattress 1:22.

- Thickness scaling was applied to account for the difference between bench and full scale foam thickness during testing.
- Multiple cone calorimeter tests at a given flux level where combined into a single data set by simple averaging.
- Very low (zero) initial heat of combustion values were reported during the first 10-20 seconds of the cone data. To prevent this physically unrealistic situation, the heat of combustion value at 30 seconds was used for times less than 30 seconds.

### Model Results

Full scale testing of this fuel package resulted in a delayed fire with a peak heat release rate of 310 $kW$ observed 360 seconds into the test. A total of 130 $MJ$ of energy was released by the 9.8 $kg$ of fuel liberated (100% of the mattress was consumed). The fan speed was increased at 5:30 into the test to prevent products of combustion from spilling under the hood. Flame was observed to go out 1796 seconds into the test.

Model and experimental results for heat release rate (HRR), mass loss rate (MLR), heat of combustion ($\Delta H_c$), soot yield, total energy released, and total mass lost are given in Figures 6.21 and 6.22. Model results varied by less than 5% when the time step was reduced by one half.

### Discussion

The model was able to capture the spread of flame over the surface, peak burning and eventual decay in heat release rate. Many of the same points discussed for mattress 1:21 would apply for mattress 1:22. Analysis of the results for mattress 1:22 reveals the following unique points:

- The initial rapid fire spread across the fuel package appears to be well predicted. After the burner is turned off at 120 seconds, the model captures the brief decrease in HRR shown in the experiment. The model reports the total HRR instantly upon combustion based on a summation of all control volumes, while the experimental HRR's are measured in the instrumentation section of the apparatus (not modeled). Although this is accounted for in the data collection

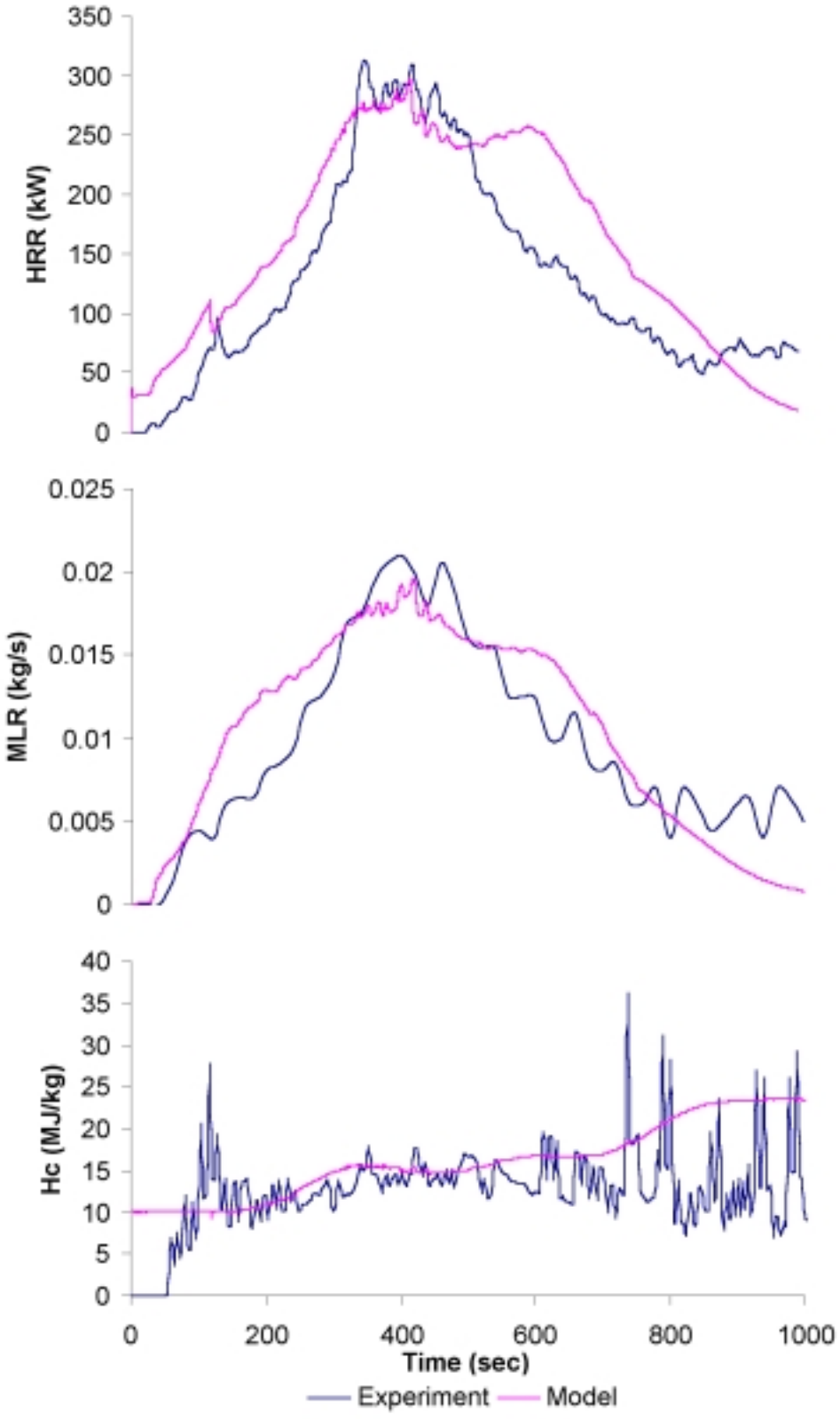


Figure 6.21: Furniture calorimeter and model results for mattress 1:22.

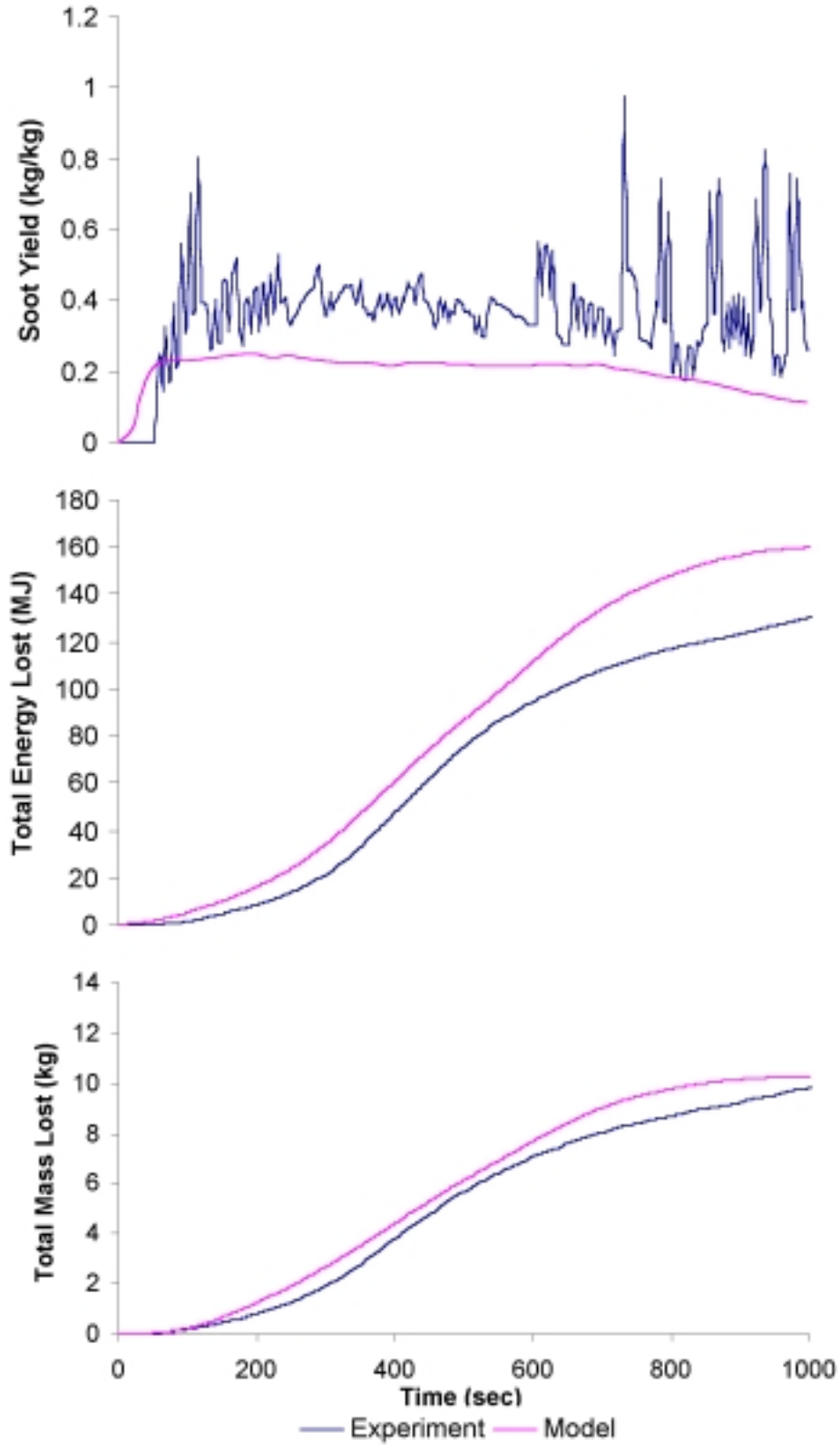


Figure 6.22: Furniture calorimeter and model results for mattress 1:22.

procedure for the furniture calorimeter, a slight time differences is shown when the burner is turned off in Figure 6.21.

- Around 200 seconds, the model over-predicts the mass loss rate, which when coupled with an under-prediction of the heat of combustion, produces the fortuitous agreement between experimental and model HRR's.

- Overall, the $\Delta H_c$ values calculated by the model are slightly above the measured results, producing an over-prediction of total energy lost. The total mass released, however, is in much closer agreement.

- During fire growth across the mattress before the peak HRR, mass loss rates are too large by at lease a factor of two in some cases. Rates of flame spread for the experimental work would benefit the comparison greatly since it is probable that the model is over-predicting the rate of flame spread across this mattress. Values of the ignition time versus flux from the literature were used for this material, which may in fact be too low for the actual foam-fabric composite.

- The cone data for soot production reveals a material that is relatively insensitive to flux level. In the full scale, the model is under-predicting soot production by a factor of 1.5 to 2, which is interesting because the latex foam in this mattress produced the highest soot yield of all furniture modeled. For all mattresses, the specific extinction coefficient per unit mass soot, $\sigma_m$, was taken equal to 7600 $\frac{m^2}{kg\ soot}$ as recommended by Seader and Einhorn [187]. Equation 4.111 of Beyler [188], however, would instead recommend $\sigma_m = 4000\ \frac{m^2}{kg\ soot}$ based on a soot yield of 0.2. This would account for the difference between model and experiment.

- Flame spread velocities across the mattress were not recorded during the experiments, thus a direct comparison can not be made. Both model and experiment, however, show that the fire consumes the entire mattress. More importantly, the slopes of the experiment and model heat release rate curves can be used as a substitute for the missing spread rate data. Measured between 10% and 90% of the peak HRR, the slopes for the experimental and model are .92 $\frac{kW}{sec}$ and .78 $\frac{kW}{sec}$ respectively, for a difference of approximately 15%. Although the HRR is an aggregate of the overall spread rate, pyrolysis, and fluid flow, it can serve as a measure of the global performance of the model.

- Thickness scaling of the cone calorimeter data was critical to obtaining reasonable results considering the foam in the mattress was two times thicker than that tested in the cone. Runs without thickness scaling greatly under-predicted the HRR and MLR since burnout resulted prematurely.

- Slight differences in the starting heat release rates shown in Figure 6.21 are due to how the initial guess is implemented in TASCflow. Model runs are started with the fan operating and a steady flame established on the burner.

Thus the model begins with a heat release rate of $30kW$ at time zero. Time shifting of the curves to a common zero would create problems with the length of time for burner application. Instead, both the experimental and model curves are matched at the point where the burner is turned off. If the model curve was shifted to a common starting HRR (such as 30 $kW$), then the time for burner application would be different for model and experiment. A less desirable alternative would be for the user to shut the burner off in the model at a HRR equal to that in the furniture calorimeter when the burner is removed at 120 seconds.

A total of 32 days computation time was required for the 1000 seconds of model results. The model was executed on an Alpha EV5 (21164) processor running at 300 $MHz$ and using 512 $Mb$ of RAM. An average of .67 hours of CPU time was used to model each second of the actual test. For the 0.3 second time step used in the model results presented, two inner loop iterations were used for each outer loop iteration. TASCflow computation time was divided approximately as shown in Figure 6.8 on Page 166. Net momentum, mass, species and energy values through the domain balanced within $1E-03$ to $1E-04$ of maximum values; reasonable levels for reacting multi-component fluid flows. Radiant heat transfer balanced globally on the order of $1E-02$ based on 36 work units per iteration. A significant increase in required solver time was necessary for improvement in the radiation solution residuals.

### 6.2.3 CBUF Mattress 1:23

#### Model Input

Mattress 1:23 was constructed of a interior spring core 150 $mm$ thick, covered by 10 $mm$ polyether fabric over 10 $mm$ of polyether foam. As with all of the mattresses tested, item 1:23 was 2.0 $m$ long by 0.95 $m$ wide. This particular mattress was intended to represent domestic products currently found in the marketplace, Figure 6.23.


Figure 6.23: CBUF mattress 1:23.

TASCflow and flame spread model parameters specific to this run are shown in Tables 6.12 and 6.13. Based on average product yields, the stoichiometric coefficient (mass of oxygen consumed per mass fuel burned) was determined to be 1.96. Two cone calorimeter data sets are available at each flux level of 25, 35, and 50 $\frac{kW}{m^2}$ as shown in Figures 6.24 and 6.25. The two cone tests were averaged for each flux level, Figure 6.26.

| Parameter | Purpose | Value |
|---|---|---|
| znuf | Number of moles of fuel that react with znuo moles of oxidizer | 1 |
| znuo | Number of moles of oxidizer that react with znuf moles of fuel | 1.225 |
| stoich | Stoichiometric coefficient (oxygen) | 1.96 |
| dtime | Time step for fluid and CHT solution | 0.3 seconds |
| density_solid | Solid fuel density | 20 $\frac{kg}{m^3}$ |

Table 6.12: TASCflow control parameters for mattress 1:23.

| Variable | Value | Units |
|---|---|---|
| Number of fuel surfaces | 1 | (-) |
| Ignition temperature for fuel | 543 | $K$ |
| Minimum (critical) flux for piloted ignition | 10 | $\frac{kW}{m^2}$ |
| Number of moles of H2O formed per mole of CO2 | 0.89 | (-) |

Table 6.13: Variables specified in flame.dat for mattress 1:23.

Scaling of the cone results was necessary to account for differences between the thickness of the cone sample tested (50 $mm$) and the actual combustible mattress thickness (20 $mm$). The same fabric thickness is used for cone testing, with sufficient foam to bring the overall sample to 50 $mm$. To account for the foam thickness difference, the time dimension for the cone calorimeter mass loss curve is strethched (shortened) by a factor $\frac{20}{50} = 0.4$. Scaling started at 30 seconds, the apparent point of transition between fabric and foam burning. The flux average scaled values input directly to the model are shown in Figure 6.27.

A transient heat of combustion value can be calculated from the cone calorimeter results for HRR and $\dot{m}$ as shown in Figures 6.24 and 6.26. When input directly into the flame spread model, the initial period of low $\Delta H_c$ values due to equipment startup, transport and measurement delay result in low energy release rates that are not physically realistic. The average $\Delta H_c$ value is substituted for the first portion of the cone curve to correct this problem, as shown in Figure 6.27. As mass loss rates tend toward zero at the end of a cone run, calculated $\Delta H_c$ values become highly irregular. The composite $\Delta H_c$ value used during a given time step of the calculations is the mass loss rate weighted average of the values from all burning surfaces. Since mass loss rates at this point are very small, the effect of variations in $\Delta H_c$ were minimal.

The soot values shown in Figure 6.26 have been calculated based on the smoke production rate (SPR) values in $\frac{m^2}{s}$, as the product of the light extinction coefficient, $k$, and the duct flow rate, $V_f$, measured in the cone calorimeter. Using the specific extinction area on a fuel mass loss basis, $\sigma_f = \frac{\text{SPR}}{\dot{m}}$, the soot yield for input into the model can be calculated as$\psi_s = \frac{\sigma_f}{\sigma_m}$. The specific extinction coefficient per unit mass soot, $\sigma_m$, is taken equal to 7600 $\frac{m^2}{kg\ soot}$.

The model was started with a steady state fan solution and burner fuel inlet boundary condition ($\dot{m}_{CH_4} = 3.75X10^{-4}\ \frac{kg}{s}$), sufficient to give the 30 $kW$ from the burner used for testing. The fuel flow from the burner was "seeded" with 1% product ($CO_2$ & $H_2O$) and 0.2% soot to allow the combustion model to begin reaction of the fuel. All fluids and solids were given ambient temperature and properties.

The user specifies the critical radiant flux for piloted ignition. At fluxes above this value, the time to ignition decreases as flux increases. To model the time after the burner is ignited, but before the mattress starts burning, the values shown in Table 6.14 were used. Once a flame was established on the mattress, piloted ignition was assumed.

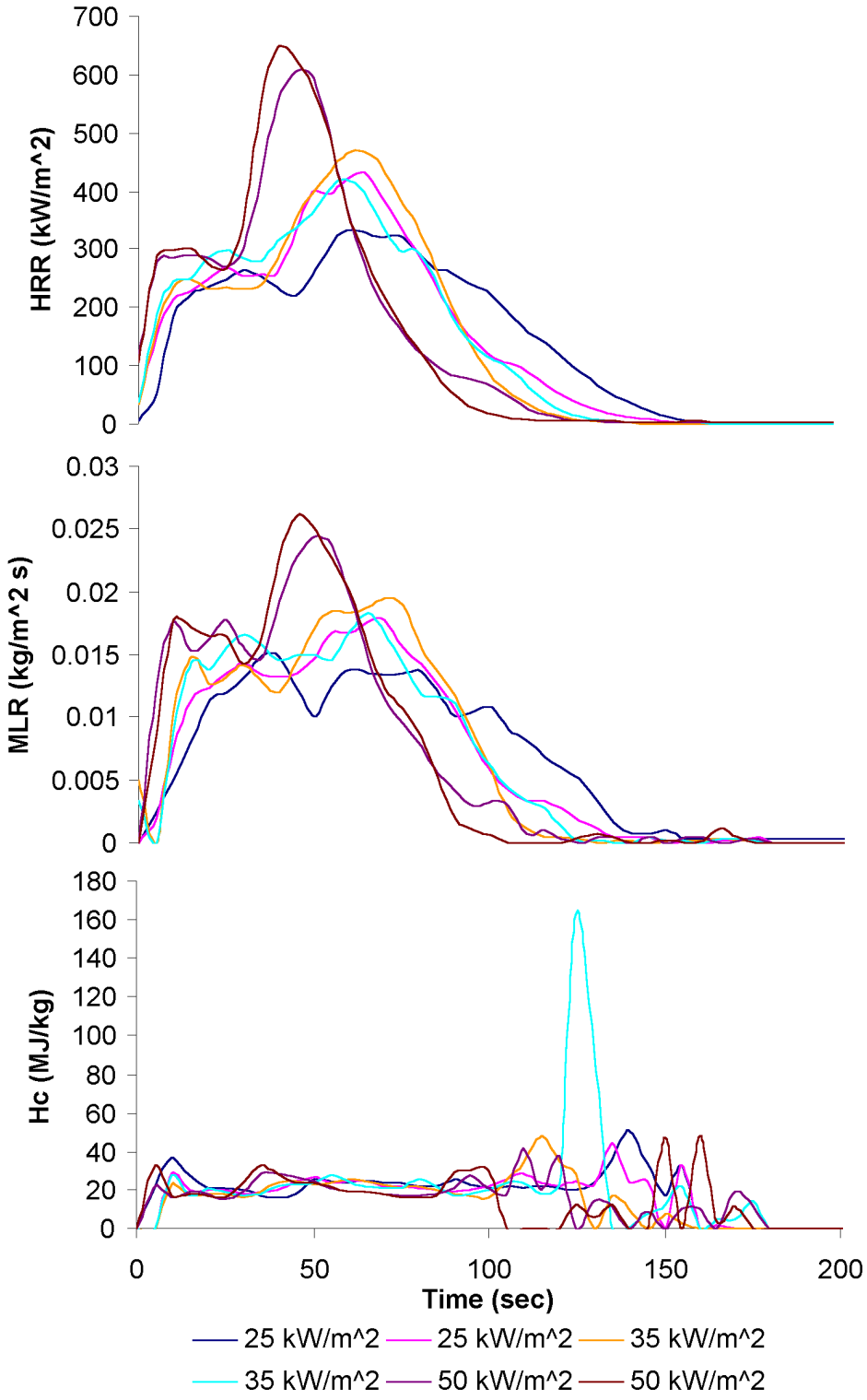


Figure 6.24: Raw cone calorimeter results for mattress 1:23.

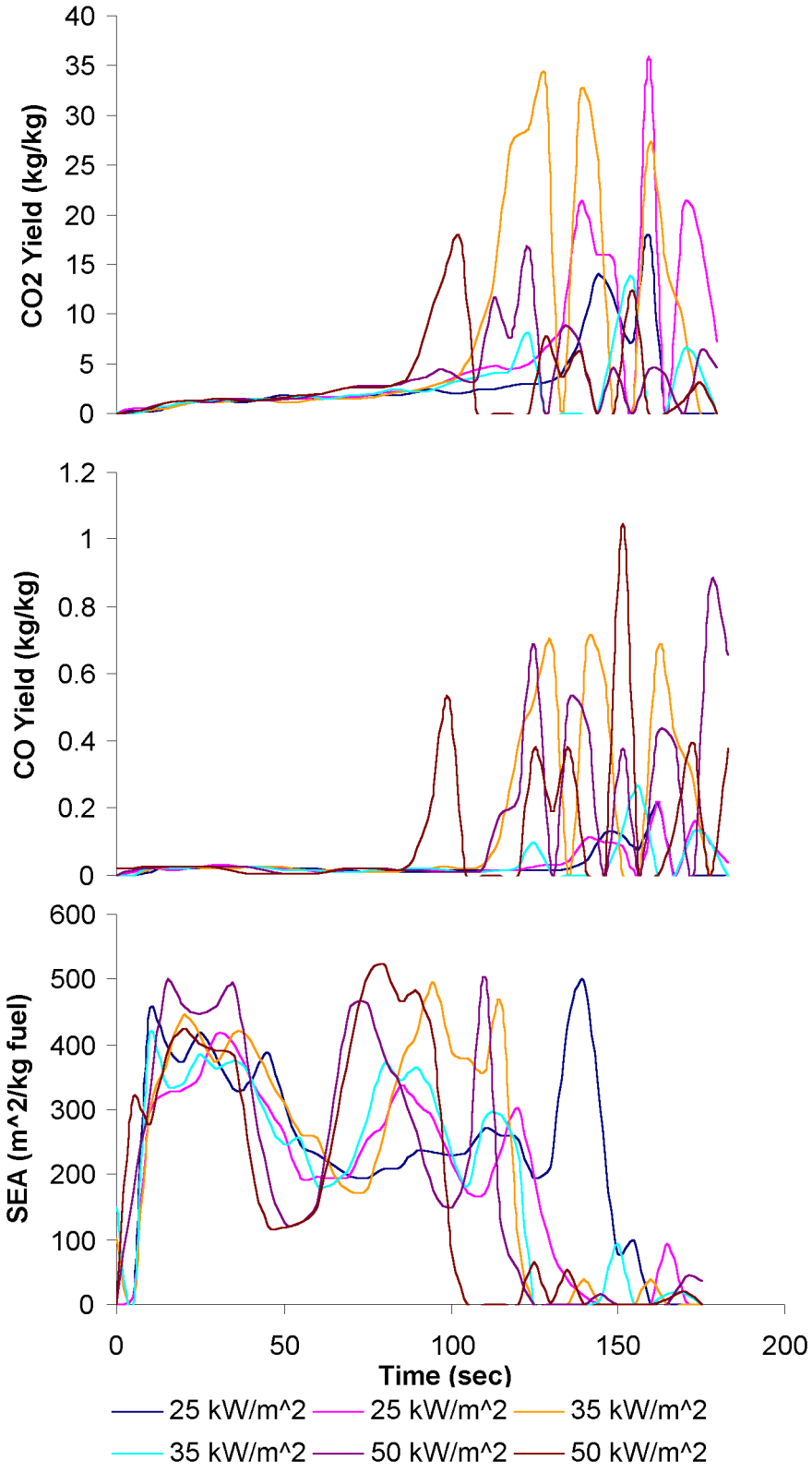


Figure 6.25: Raw cone calorimeter results for mattress 1:23.

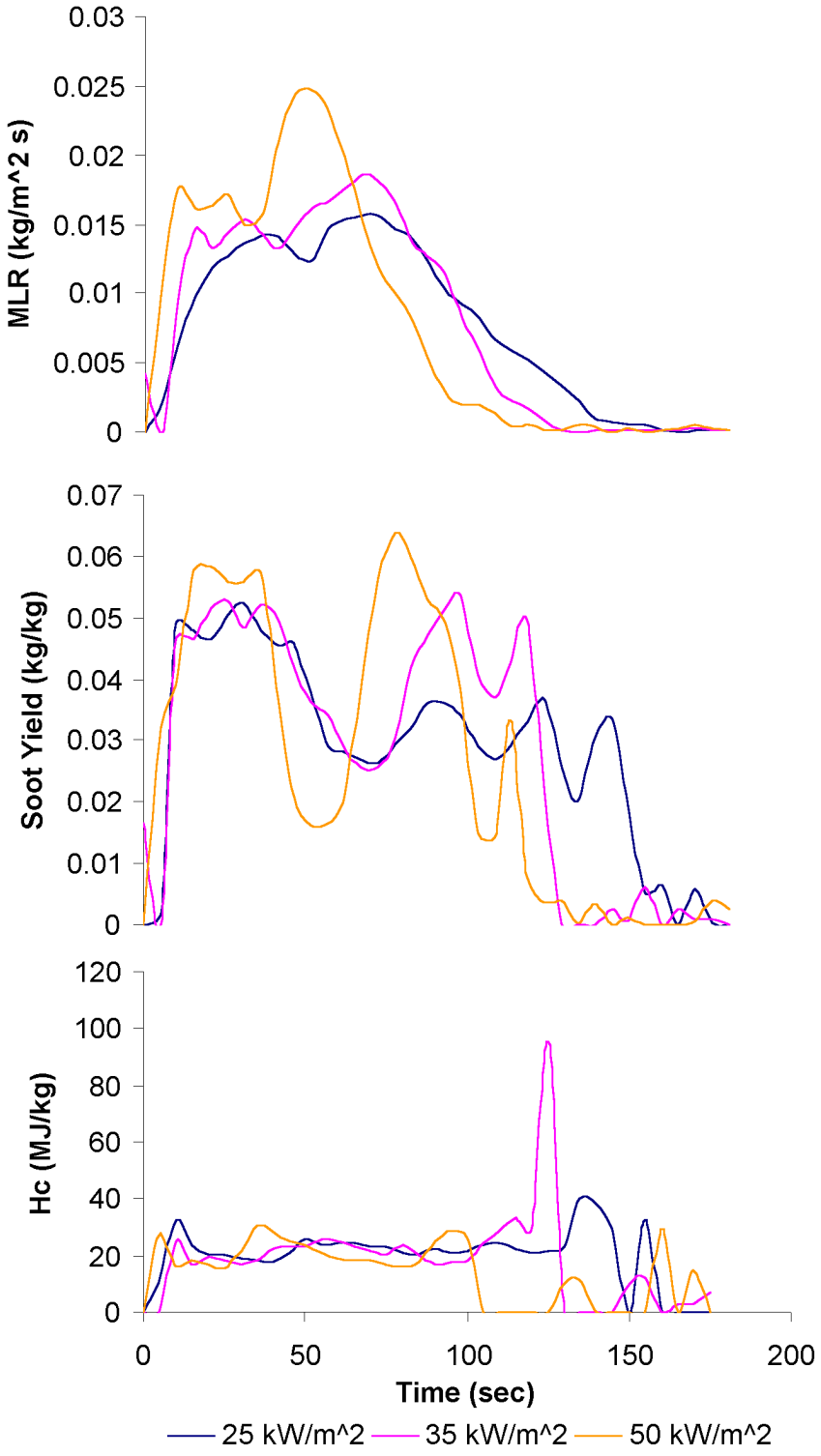


Figure 6.26: Flux averaged cone calorimeter results for mattress 1:23.

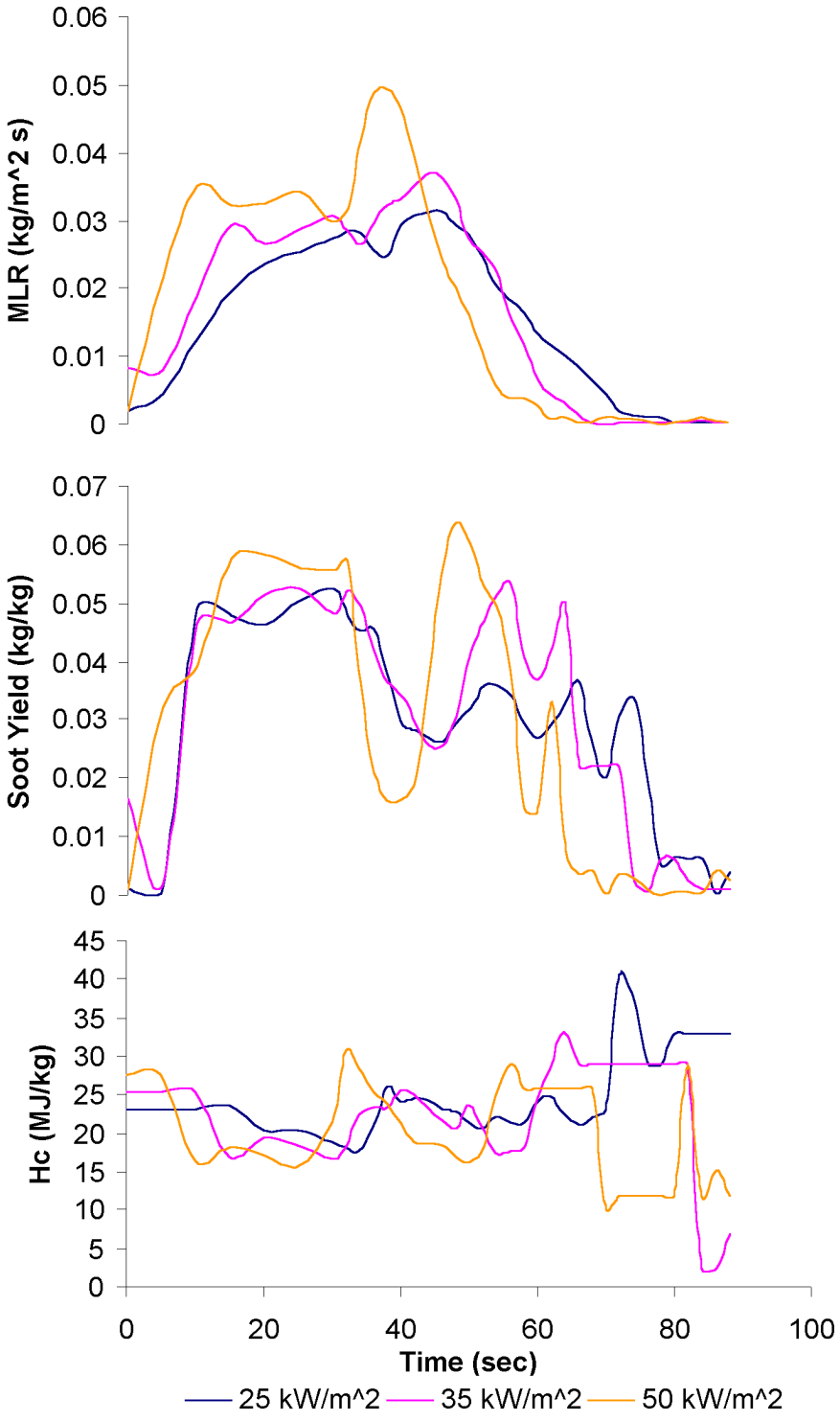


Figure 6.27: Scaled flux averaged cone calorimeter results for mattress 1:23.

| Flux $\left(\frac{\mathbf{kW}}{\mathbf{m^2}}\right)$ | Time for ignition (sec) |
|---|---|
| 50 | 5 |
| 35 | 6 |
| 20 | 8 |
| 10 | $t \rightarrow \infty$ |

Table 6.14: Flux values as a function of time for ignition for mattress 1:23.

The minimum flux level tested in the cone calorimeter for all mattresses was 25 $\frac{kW}{m^2}$. When an ignited surface element was exposed to a flux less than 25 $\frac{kW}{m^2}$, the cone results for 25 $\frac{kW}{m^2}$ were used. Linear interpolation was applied to evaluate properties between tested flux levels and cone data points.

To obtain the data for implementation in the model, three modifications were made to the raw cone data given in Figures 6.24 and 6.25:

- Thickness scaling was applied to account for the difference between bench and full scale foam thickness during testing.
- Multiple cone calorimeter tests at a given flux level where combined into a single data set by simple averaging.
- Very low (zero) initial heat of combustion values were reported during the first 10-20 seconds of the cone data. To prevent this physically unrealistic situation, the heat of combustion value at 30 seconds was used for times less than 30 seconds.

### Model Results

Full scale testing of this fuel package resulted in quickly developing flame spread over the complete sample. A peak heat release rate of 350 $kW$ was observed 80 seconds into the test. A total of 34.2 $MJ$ of energy was released by the 1.4 $kg$ of fuel generated. Approximately 75% of the mass lost during burning occurred in the first 80 seconds of burning. Slightly over 15% of the original mass of the mattress was consumed by the fire, including the metal innersprings. Flame was observed to go out 948 seconds into the test.

Model and experimental results for heat release rate (HRR), mass loss rate (MLR), heat of combustion ($\Delta H_c$), soot yield, total energy released and total mass lost are given in Figures 6.28 to 6.29. Model results varied by less than 5% when the time step was reduced by one half.

### Discussion

The model was able to capture the rate of spread of flame over the surface, peak burning and eventual decay in heat release rate. Many of the same points discussed

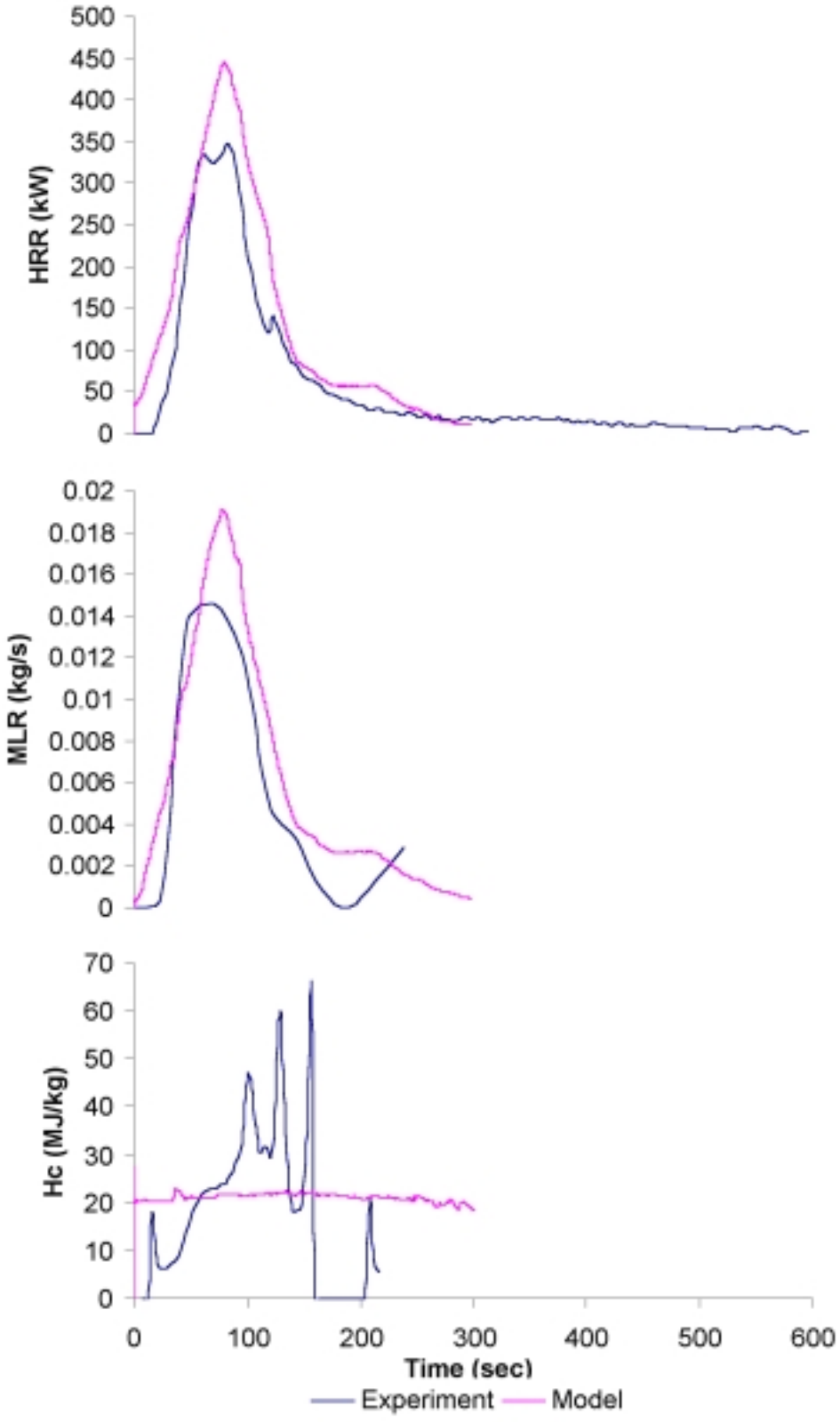


Figure 6.28: Furniture calorimeter and model results for mattress 1:23.

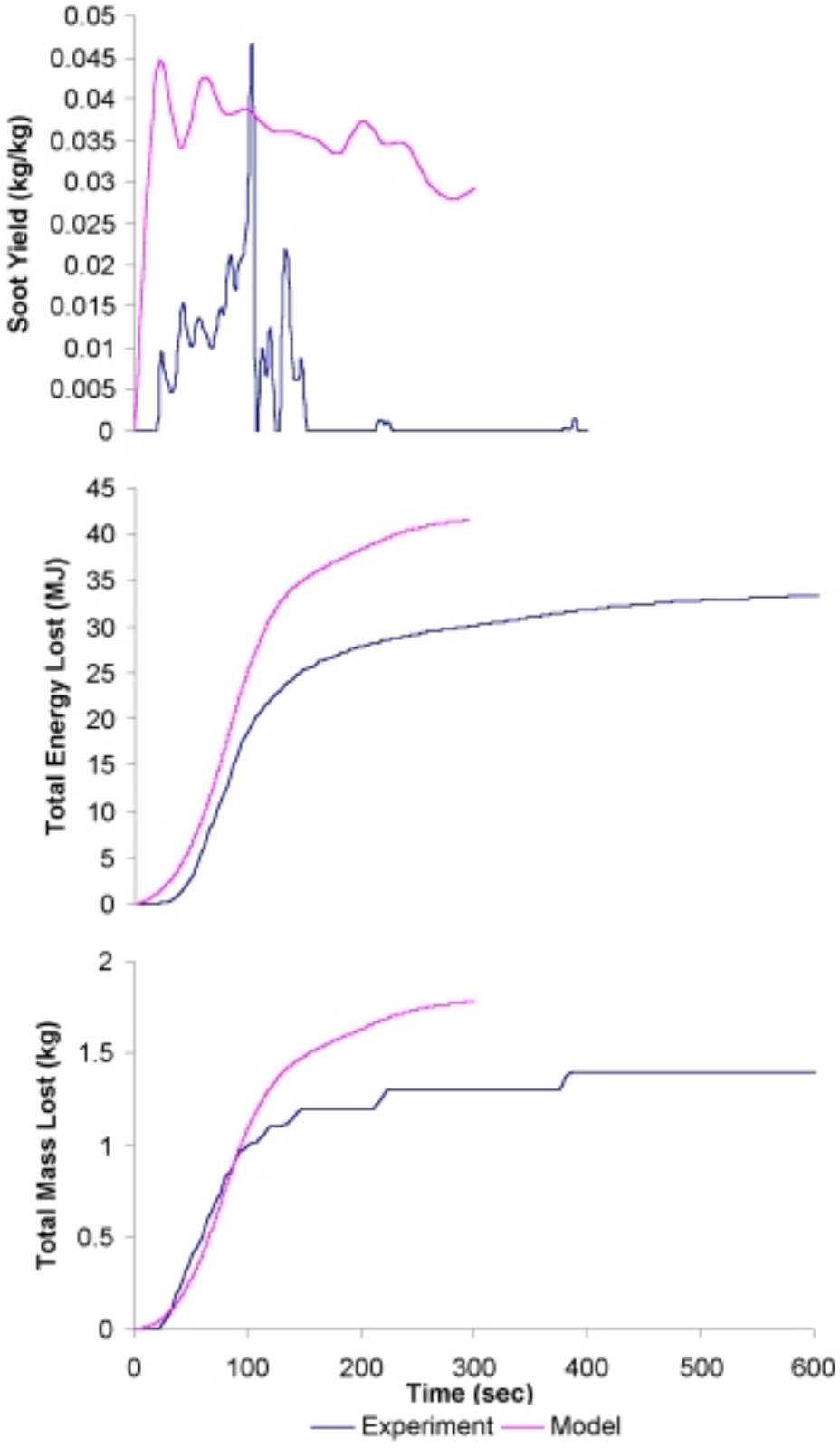


Figure 6.29: Furniture calorimeter and model results for mattress 1:23.

for mattress 1:21 and 1:22 would apply for mattress 1:23. Analysis of the results for mattress 1:23 reveals the following:

- Timing for the model peak HRR and MLR agree very well with experiment, although both are over-predicted. The rapid fire growth may have caused the actual peak to be missed due to smoothing by the instrumentation. Due to this over-prediction, the total energy and mass lost by the model is greater than measured.

- Peak soot yields produced by the model agree with experiment, although for much of the fire they are over-predicted. Differences may be due to the value of the specific extinction coefficient per unit mass soot, $\sigma_m$, which is assumed equal to 7600 $\frac{m^2}{kg\ soot}$.

- One of the first runs for mattress 1:23 only modeled the foam and fabric on the top side of the interior spring core. The results showed that the model was predicting only half of the total mass lost compared to the experiment, although most of the fuel available was consumed. Based on a review of the experimental results, it appeared that the foam and fabric on the bottom side of the mattress were also burning. To approximate this difficult to model situation, it was assumed that burning pieces of the top foam would drop down and ignite the lower foam. The result was that the predicted flame spread for the lower foam and fabric was assumed the same as for the upper foam and fabric. In effect, the mass loss rate for the upper foam and fabric was doubled.

- Thickness scaling of the cone calorimeter data was critical to obtaining reasonable results considering the foam in the mattress was only 20% as thick as that tested in the cone. Runs without thickness scaling greatly over-predicted the flame spread rate, HRR, MLR, total energy released and total mass lost.

- Flame spread velocities across the mattress were not recorded during the experiments, thus a direct comparison can not be made. Both model and experiment, however, show that the fire consumes the entire mattress. More importantly, the slopes of the experimental and model heat release rate curves can be used as a substitute for the missing spread rate data. Measured between 10% and 90% of the peak HRR, the slopes for the experimental and model are 6.3 $\frac{kW}{sec}$ and 5.6 $\frac{kW}{sec}$ respectively, for a difference of approximately 12%. Although the HRR is an aggregate of the overall spread rate, pyrolysis, and fluid flow, it can serve as a measure of the global performance of the model.

- Slight differences in the starting heat release rates shown in Figure 6.28 are due to how the initial guess is implemented in TASCflow. Model runs are started with the fan operating and a steady flame established on the burner. Thus the model starts out with a heat release rate of 30 $kW$ at time zero. Time shifting of the curves to a common zero would not be appropriate. Instead, both the experimental and model curves are matched at the point where the burner is

turned off. If the model curve was shifted to a common starting HRR (such as 30 $kW$), then the time for burner application would be different for model and experiment. A less desirable alternative would be for the user to shut the burner off in the model at a HRR equal to that in the furniture calorimeter when the burner is removed at 120 seconds.

A total of 11.5 days of computation time was required for the 300 seconds of model results. The model was executed on an Alpha EV5 (21164) processor running at 300 $MHz$ and using 512 $Mb$ of RAM. An average of .63 hours of CPU time was used to model each second of the actual test. For the 0.3 second time step used for the model results presented, two inner loop iterations were used for each outer loop iteration. TASCflow computation time was divided approximately as shown in Table 6.8 on Page 166. Net momentum, mass, species and energy values through the domain balanced within $1E-03$ to $1E-04$ of maximum values. Reasonable levels for reacting multi-component fluid flows. Radiant heat transfer balanced globally on the order of $1E-02$ based on 24 work units per iteration.

### 6.2.4 CBUF Mattress 1:24

#### Model Input

Mattress 1:24 was constructed of an interior spring core 150 $mm$ thick covered by combustion modified high resilience (CMHR) foam and polyester fabric giving a total thickness of 160 $mm$. As with all of the mattresses tested, item 1:24 was 2.0 $m$ long by 0.95 $m$ wide. This mattress was similar to that shown in Figure 6.23 and is intended to represent domestic products currently found in the marketplace.

TASCflow and flame spread model parameters specific to this run are shown in Tables 6.15 and 6.16. Based on average product yields, the stoichiometric coefficient (mass of oxygen consumed per mass fuel burned) was determined to be 1.229. Two cone calorimeter data sets are available at each flux level of 25, 35, and 50 $\frac{kW}{m^2}$ as shown in Figures 6.30 and 6.31. The two cone tests were averaged for each flux level, Figure 6.32.

| Parameter | Purpose | Value |
|---|---|---|
| znuf | Number of moles of fuel that react with znuo moles of oxidizer | 1 |
| znuo | Number of moles of oxidizer that react with znuf moles of fuel | 0.768 |
| stoich | Stoichiometric coefficient (oxygen) | 1.229 |
| dtime | Time step for fluid and CHT solution | 0.3 seconds |
| density_solid | Solid fuel density | 40 $\frac{kg}{m^3}$ |

Table 6.15: TASCflow control parameters for mattress 1:24.

| Variable | Value | Units |
|---|---|---|
| Number of fuel surfaces | 1 | (-) |
| Ignition temperature for fuel | 664 | $K$ |
| Minimum (critical) flux for piloted ignition | 13 | $\frac{kW}{m^2}$ |
| Number of moles of H2O formed per mole of CO2 | 0.89 | (-) |

Table 6.16: Variables specified in flame.dat for mattress 1:24.

Scaling of the cone results was necessary to account for differences between the thickness of the cone sample tested (50 $mm$) and the actual combustible mattress thickness (10 $mm$). The same fabric thickness is used for cone testing, with sufficient foam to bring the overall sample to 50 $mm$. To account for the foam thickness difference, the time dimension for the cone calorimeter mass loss curve is strethched (shortened) by a factor $\frac{5}{45} = .11$. Scaling started at 45 seconds, the apparent point of transition between fabric and foam burning. The flux average scaled values input directly to the model are shown in Figure 6.33.

A transient heat of combustion value can be calculated from the cone calorimeter results for HRR and $\dot{m}$ as shown in Figures 6.30 and 6.32. When input directly into the flame spread model, the initial period of low $\Delta H_c$ values due to equipment startup, transport and measurement delay result in low energy release rates that are not physically realistic. The average $\Delta H_c$ value is substituted for the first portion of the cone curve to correct this problem.

The soot values shown in Figure 6.32 have been calculated based on the smoke production rate (SPR) values in $\frac{m^2}{s}$, as the product of the light extinction coefficient, $k$, and the duct flow rate, $V_f$, measured in the cone calorimeter. Using the specific extinction area on a fuel mass loss basis, $\sigma_f = \frac{\text{SPR}}{\dot{m}}$, the soot yield for input into the model can be calculated as $\psi_s = \frac{\sigma_f}{\sigma_m}$. The specific extinction coefficient per unit mass soot, $\sigma_m$, is taken equal to 7600 $\frac{m^2}{kg\ soot}$.

The model was started with a steady state fan solution and burner fuel inlet boundary condition ($\dot{m}_{CH_4} = 4.27X10^{-4}\ \frac{kg}{s}$), sufficient to give the 30 $kW$ from the burner used for testing. The fuel flow from the burner was "seeded" with 1% product ($CO_2$ & $H_2O$) and 0.2% soot to allow the combustion model to begin reaction of the fuel. All fluids and solids were given ambient temperature and properties.

The user specifies the ignition time versus radiant flux for piloted ignition. At fluxes above the critical value, the time to ignition decreases as flux increases. To model the time after the burner is ignited, but before the mattress starts burning, values shown in Table 6.17 were used. Once a flame was established on the mattress,

| **Flux** $\left(\frac{\mathbf{kW}}{\mathbf{m^2}}\right)$ | **Time for ignition (sec)** |
|---|---|
| 50 | 4.5 |
| 35 | 6 |
| 20 | 11 |
| 13 | $t \rightarrow \infty$ |

Table 6.17: Flux values as a function of time for ignition of mattress 1:24.

piloted ignition was assumed through the ignition temperature.

The minimum flux level tested in the cone calorimeter for all mattresses was 25 $\frac{kW}{m^2}$. When an ignited surface element was exposed to a flux less than 25 $\frac{kW}{m^2}$, the cone results for 25 $\frac{kW}{m^2}$ were used. Linear interpolation was applied to evaluate properties between tested flux levels and cone data points.

Three modifications were made to the raw cone given in Figures 6.30 and 6.31, to obtain the data for implementation in the model:

- Thickness scaling was applied to account for the difference between bench and full scale foam thickness during testing.
- Multiple cone calorimeter tests at a given flux level where combined into a single data set by simple averaging.

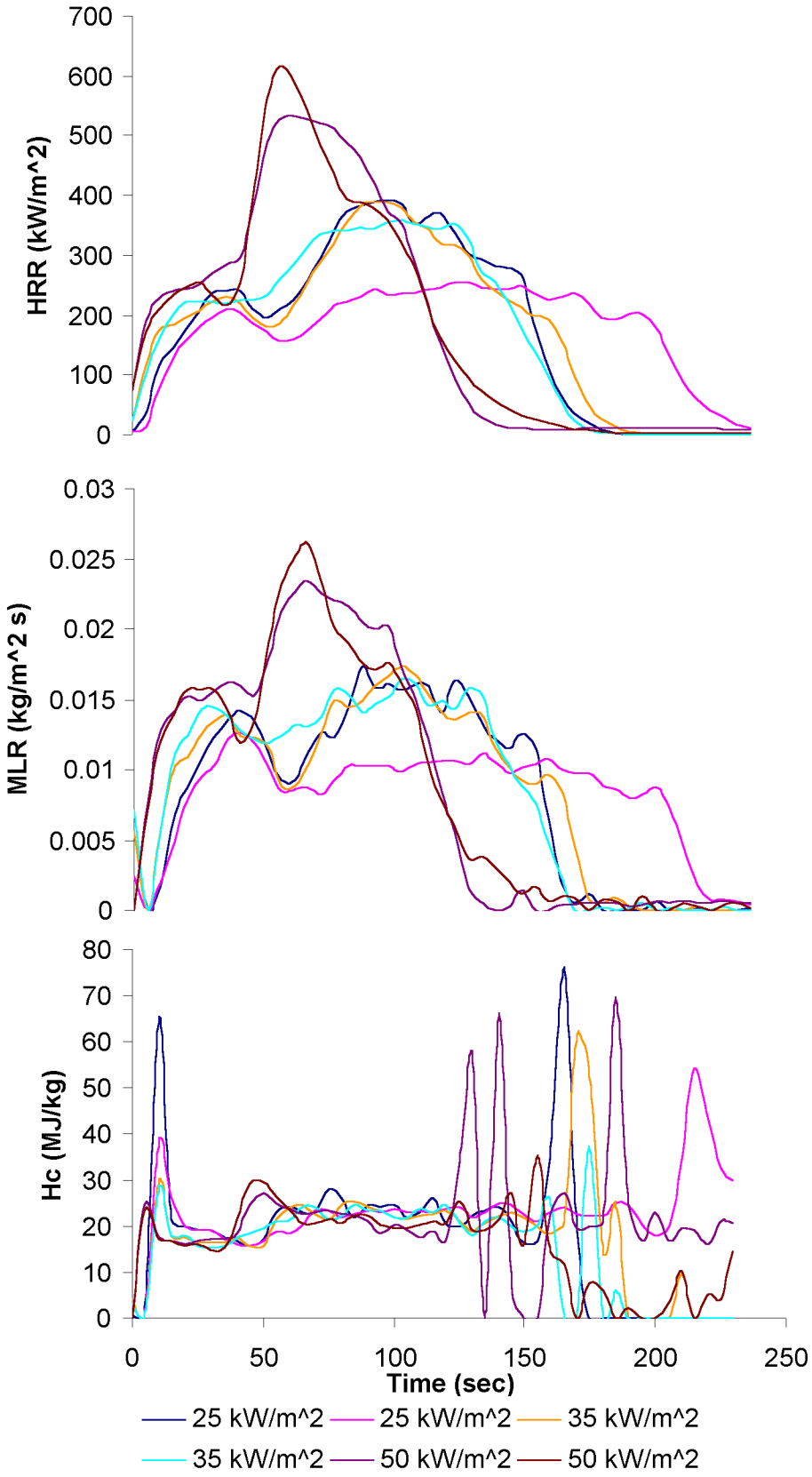


Figure 6.30: Raw cone calorimeter results for mattress 1:24.

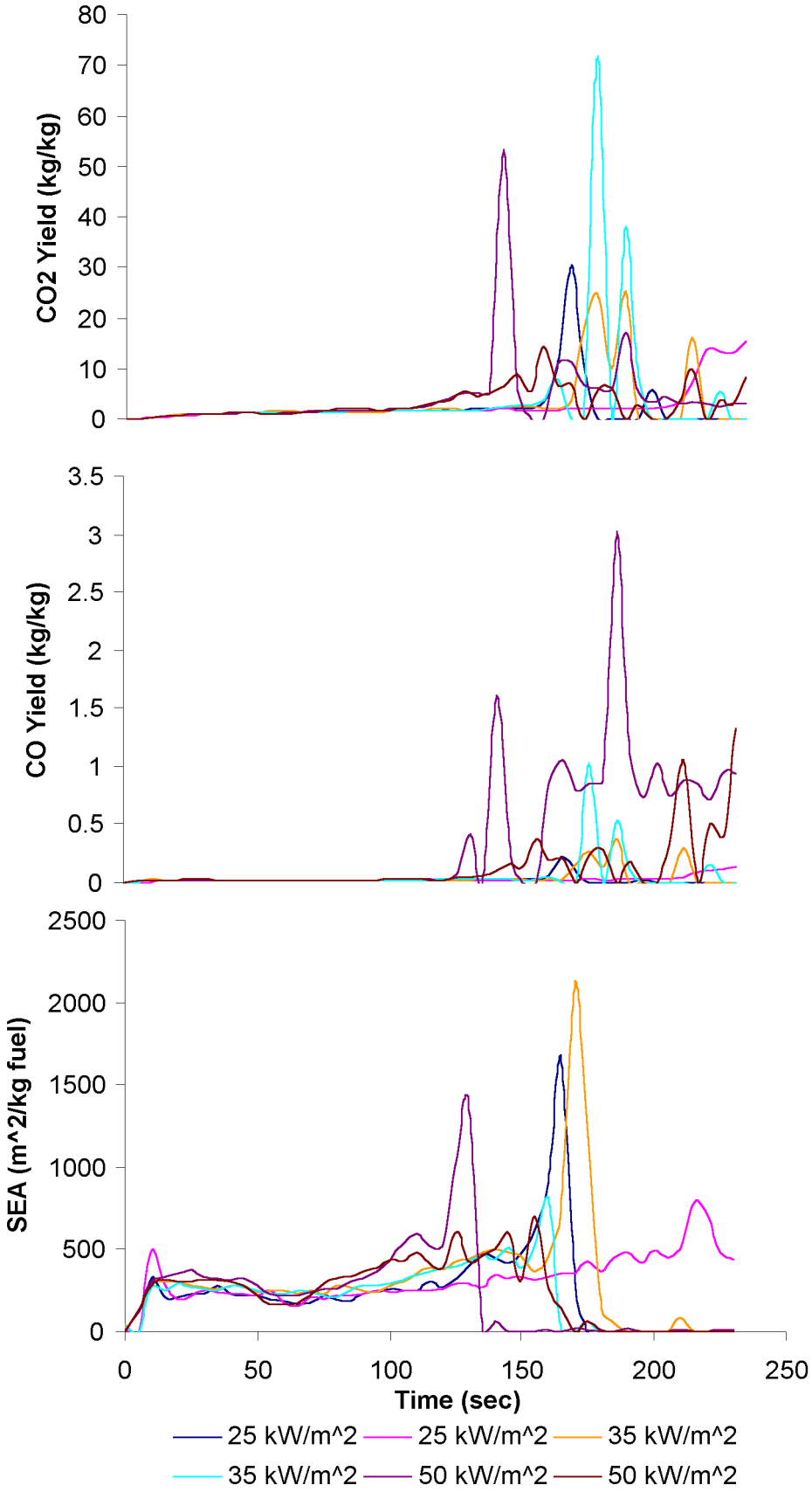


Figure 6.31: Raw cone calorimeter results for mattress 1:24.

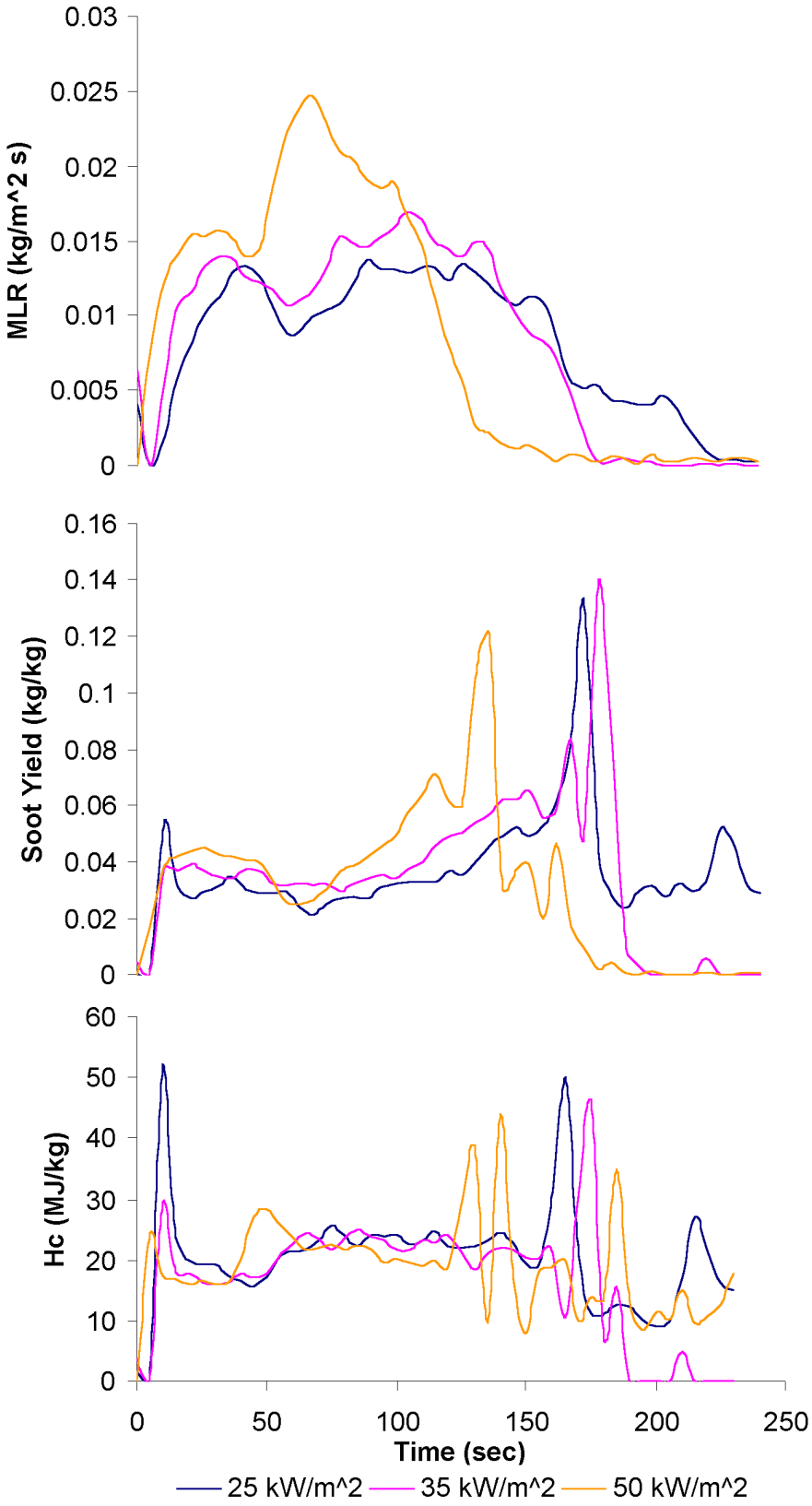


Figure 6.32: Flux averaged cone calorimeter results for mattress 1:24.

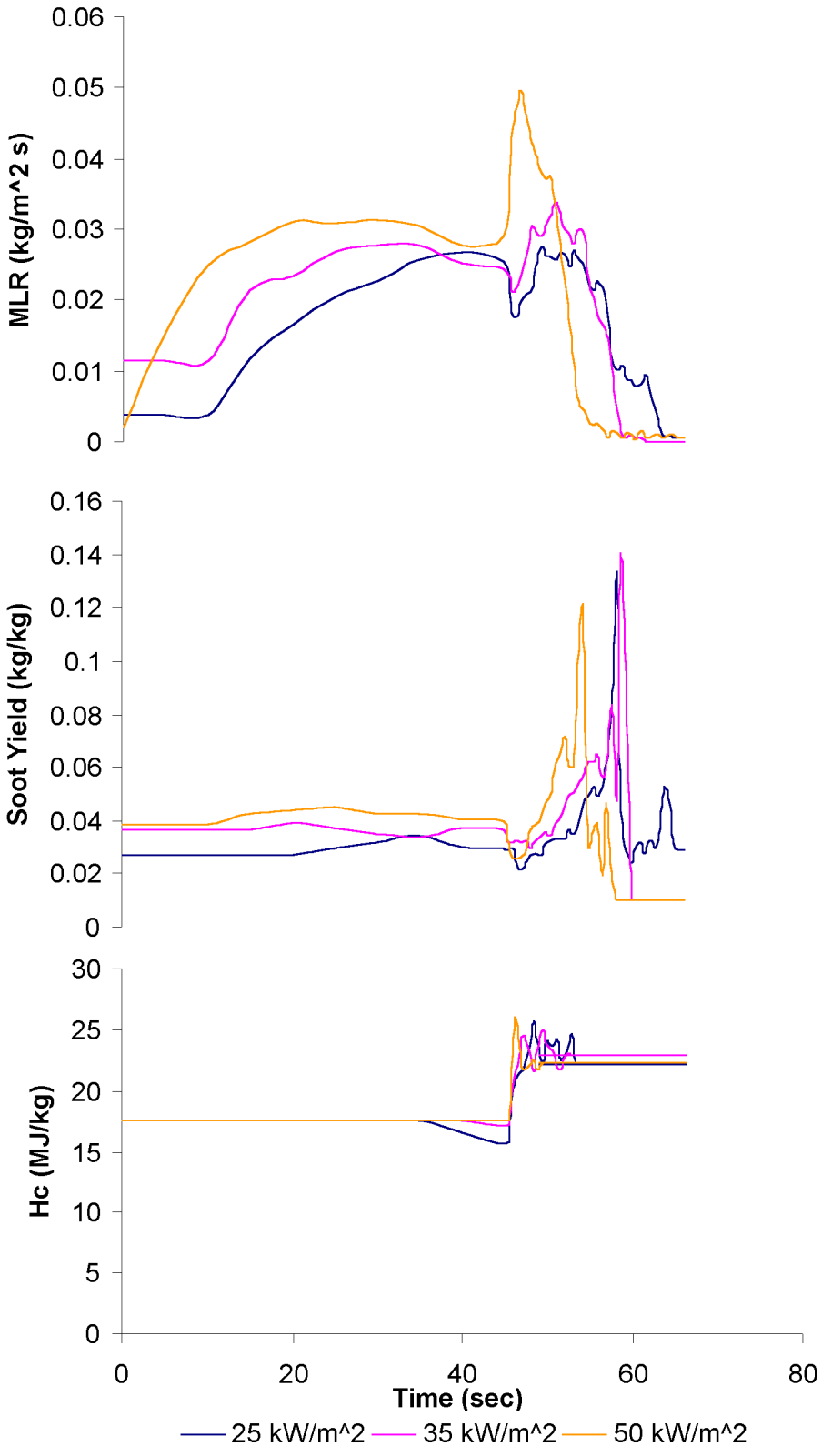


Figure 6.33: Scaled flux averaged cone calorimeter results for mattress 1:24.

- Very low (zero) initial heat of combustion values were reported during the first 10-20 seconds of the cone data. To prevent this physically unrealistic situation, the heat of combustion value at 30 seconds was used for times less than 30 seconds.

### Model Results

Full scale testing of this fuel package resulted in an extended period of very limited burning. A peak heat release rate of 47 $kW$ was observed 128 seconds into the test. A total of 17.1 $MJ$ of energy was released by the 1.3 $kg$ of fuel consumed. During much of the first 120 seconds of the test, measured heat release rates were below 30 $kW$, the energy produced by the burner. This shows the difficulty in measuring very small HRR's under the large hood. After the burner was turned off, flame continued to spread slowly over the sample for the next 800 seconds with an approximately constant heat release rate of 20 $kW$. Flame was observed to go out 1192 seconds into the test.

Model and experimental results for heat release rate (HRR), mass loss rate (MLR), heat of combustion ($\Delta H_c$), soot yield, total energy released, and total mass lost are given in Figures 6.34 to 6.35. Model results varied by less than 5% when the time step was reduced by one half.

### Discussion

Comparisons between model predictions and CBUF mattress 1:24 show that additional work is necessary before the model will be able to predict slowly spreading, limited burning furniture fires. The model was unable to capture the spread of flame over the surface. Many of the same points discussed for mattress 1:21, 1:22 and 1:23 would apply for mattress 1:24. Analysis of the results for mattress 1:24 reveals the following:

- Clearly the furniture CFD model did not produce a slow sustained period of burning as displayed by the experiment. Comparisons of the HRR measurements, however, should be viewed cautiously since the measured HRR during the first 120 seconds is only a fraction of that expected from the burner alone. The mattress was also burning during this period since the peak MLR occurs very early in the test. Since the duct flow rate of $3 - 4\ \frac{kg}{s}$ was the same as used for other tests, the furniture calorimeter should not be expected to have the same accuracy measuring a 30 $kW$ fire as compared to a 300 $kW$ or .9 $MW$ fire.

- The problem with obtaining accurate material property data applies to the current problem. Radiant flux and temperature values for ignition of the combustion modified high resilience (CMHR) foam and polyester fabric were taken from the literature. The range of properties for combustion modified foams varies greatly, but without additional information, determination of the exact ignition values to use in the model is not possible.

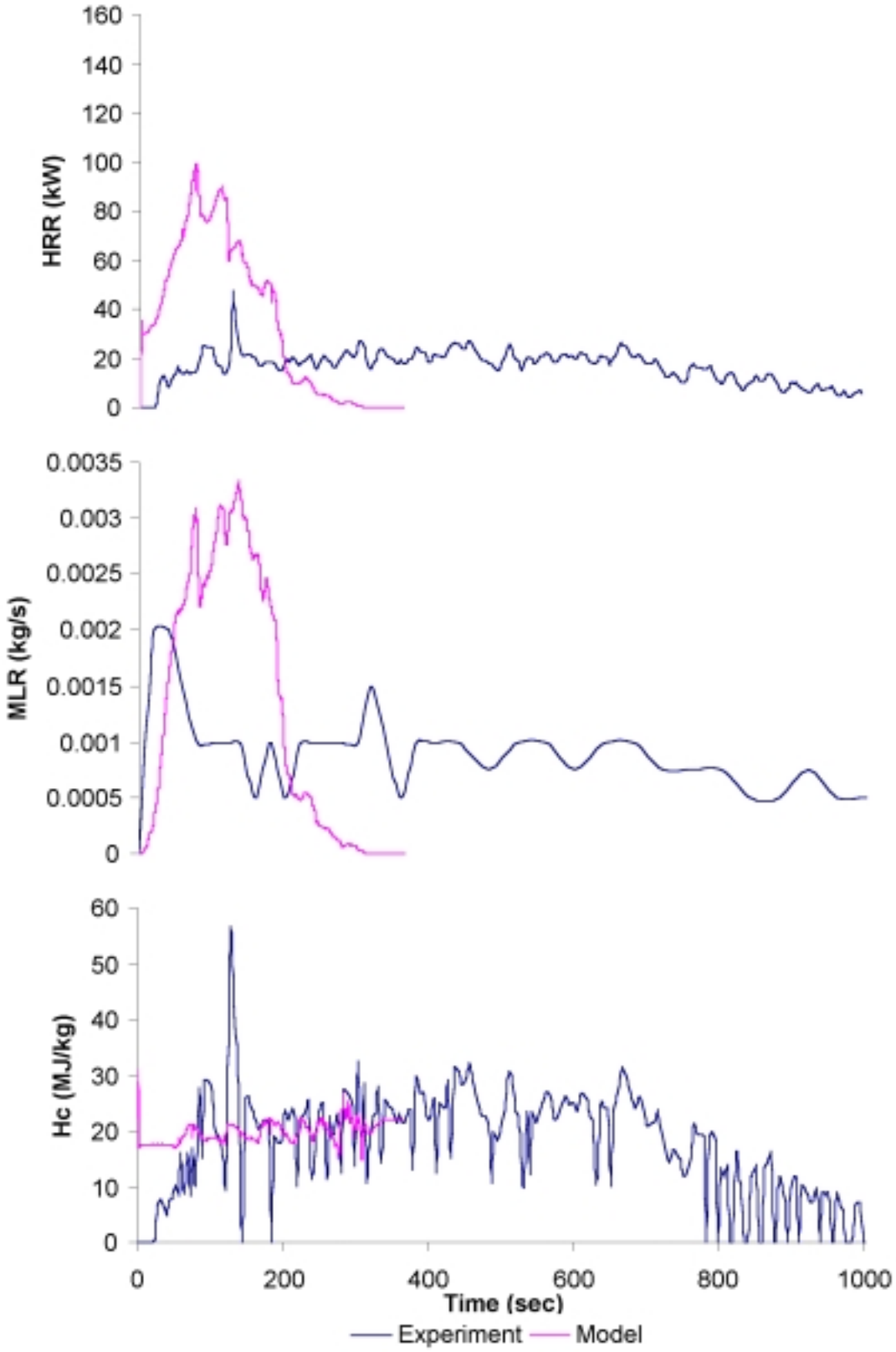


Figure 6.34: Furniture calorimeter and model results for mattress 1:24.

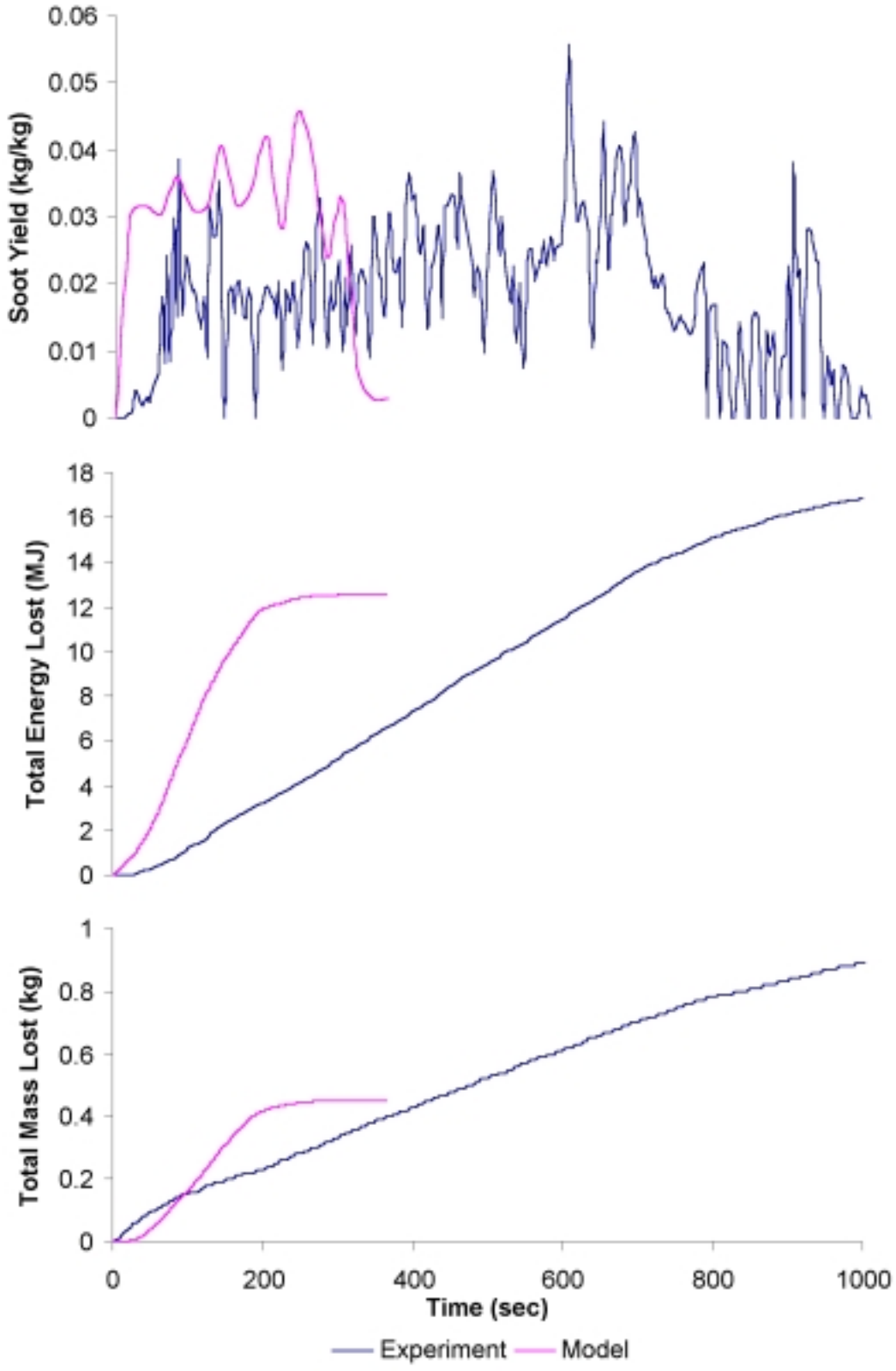


Figure 6.35: Furniture calorimeter and model results for mattress 1:24.

- To a greater extent than the three mattresses already discussed, test 1:24 involved slow creeping horizontal flame spread. Model results for this run show the increased importance of both solid phase conduction and conduction-convection in the gas phase above the fuel. Very low levels of radiant preheating of the mattress were calculated by the model that used the same approximately 1 $cm$ discretization of the pyrolysis region. Because the pyrolysis front region may not have been refined sufficiently, the resulting forward flame flux was probably insufficient to support the continued spread of flame across the fuel surface. Results for concurrent flame spread over horizontal surfaces discussed in Section 2.3.3 show that solid phase conduction at the flame foot is on the order of 1 $mm$ and dominates heat transfer to preheating fuel. Since the grid used for mattress 1:24 was significantly larger than this, a primary driving force for extended flame spreading was missed.

- A test run was attempted with 5 $mm$ grid spacing in both the solid and fluid regions of the combustion domain. Unfortunately, this resulted in a 5-10 fold increase in calculation time and rapidly approached the limits on memory available for the computer used. In addition, problems in the fluid regions were noted when absorption coefficients were calculated on such a small length scale. Improvements in the Furniture CFD code and TASCflow would be necessary before realistic flame spread calculations could be carried out on the $\approx 1$ $mm$ length scales necessary to capture solid phase conduction dominated horizontal flame spread.

- As with other model runs, the mass loss rate from a given control surface was taken to be a function of flux based on the 25, 35, and 50 $\frac{kW}{m^2}$ flux levels. For ignited surfaces receiving a flux below 25 $\frac{kW}{m^2}$, the MLR for 25 $\frac{kW}{m^2}$ was used, resulting in a possible over-prediction of the fuel generated.

- Approximately the same total energy and mass were released in the simulation, although they occurred over a period of 300 seconds instead of the 1000 seconds shown in the experiment. Except during the first 100 seconds, calculated $\Delta H_c$, and to a lesser extent soot yield values, compared well with experiment.

- Based on a review of the test results, it appears that the foam and fabric on the bottom side of the mattress were also burning. To approximate this difficult to model situation, it was assumed that burning pieces of the top foam would drop down and ignite the lower foam. The result was that the predicted flame spread for the lower foam and fabric was the same as for the upper foam and fabric. In effect, the mass loss rate for the upper foam and fabric was doubled to account for the lower layer burning.

- Thickness scaling of the cone calorimeter data was critical to obtaining reasonable results considering the foam in the mattress was less than 20% as thick as that tested in the cone. Runs without thickness scaling greatly over-predicted the flame spread rate, HRR, MLR, total energy released and total mass lost.

- Utilization of ignition times at the start of a run that depended on flux as shown in Table 6.17 were important. Without this, ignition resulted instantly across the fuel surface. Such a physically impossible situation significantly over-predicted flame spread rates.

A total of 7.5 days of computation time was required for the 380 seconds of model results. The model was executed on an Alpha EV5 (21164) processor running at 300 $MHz$ and using 512 $Mb$ of RAM. An average of .47 hours of CPU time was used to model each second of the actual test. For the 0.4 second time step used for the model results presented, two inner loop iterations were used for each outer loop iteration. TASCflow computation time was divided approximately as shown in Figure 6.8, on Page 166. Net momentum, mass, species and energy values through the domain balanced within $1E-03$ to $1E-04$ of maximum values. Reasonable levels for reacting multi-component fluid flows. Radiant heat transfer balanced globally on the order of $1E-02$ based on 24 work units per iteration.

### 6.2.5 CBUF Chair 3:13

#### Model Input

Chair 3:13 was constructed of a simple seat and back with no arms and supported by a beech wood frame. Each of the two cushions were composed of a high resilience urethane foam core covered by flame retardant cotton fabric giving a total thickness of 100 $mm$. The back of the chair was not perfectly vertical, but instead sloped back $10^o$. This chair configuration allows for both horizontal and vertical fire development. As shown in Figure 6.36, this particular chair was intended to represent domestic products currently found in the marketplace.


Figure 6.36: CBUF chair 3:13.

TASCflow and flame spread model parameters specific to this run are shown in Tables 6.18 and 6.19. Based on average product yields, the stoichiometric coefficient (mass of oxygen consumed per mass fuel burned) was determined to be 0.42. Three cone calorimeter data sets are available at each flux level of 25, 35, and 50 $\frac{kW}{m^2}$ as shown in Figures 6.37 to 6.38. The three cone tests were averaged for each flux level, Figure 6.39.

| Parameter | Purpose | Value |
|---|---|---|
| znuf | Number of moles of fuel that react with znuo moles of oxidizer | 1 |
| znuo | Number of moles of oxidizer that react with znuf moles of fuel | 1.295 |
| stoich | Stoichiometric coefficient (oxygen) | 0.42 |
| dtime | Time step for fluid and CHT solution | 0.3 seconds |
| density_solid | Solid fuel density | 20 $\frac{kg}{m^3}$ |

Table 6.18: TASCflow control parameters for chair 3:13.

| Variable | Value | Units |
|---|---|---|
| Number of fuel surfaces | 1 | (-) |
| Ignition temperature for fuel | 523 | $K$ |
| Minimum (critical) flux for piloted ignition | 12 | $\frac{kW}{m^2}$ |
| Number of moles of H2O formed per mole of CO2 | 0.89 | (-) |

Table 6.19: Variables specified in flame.dat for chair 3:13.

Scaling of the cone results was necessary to account for differences between the thickness of the cone sample tested (50 $mm$) and the actual chair cushion thickness (100 $mm$). The same fabric thickness is used for cone testing, with sufficient foam to bring the overall sample to 50 $mm$. To account for the foam thickness difference, the time dimension for the cone calorimeter mass loss curve is strethched (lengthened) by a factor $\frac{100}{50} = 2.0$. Scaling started at 50 seconds, the apparent point of transition between fabric and foam burning. The flux averaged scaled values input directly to the model are shown in Figure 6.40.

A transient heat of combustion value can be calculated from the cone calorimeter results for HRR and $\dot{m}$ as shown in Figures 6.37 and 6.39. When input directly into the flame spread model, the initial period of low $\Delta H_c$ values due to equipment startup, transport and measurement delay result in low energy release rates that are not physically realistic. The average $\Delta H_c$ value is substituted for the first portion of the cone curve to correct this problem as shown in Figure 6.40.

The soot values shown in Figure 6.39 have been calculated based on the smoke production rate (SPR) values in $\frac{m^2}{s}$ as product of the light extinction coefficient, $k$, and the duct flow rate, $V_f$, measured in the cone calorimeter. Using the specific extinction area on a fuel mass loss basis, $\sigma_f = \frac{\text{SPR}}{\dot{m}}$, the soot yield for input into the model can be calculated, $\psi_s = \frac{\sigma_f}{\sigma_m}$. The specific extinction coefficient per unit mass soot, $\sigma_m$, is taken equal to 7600 $\frac{m^2}{kg\ soot}$.

The model was started with a steady state fan solution and burner fuel inlet boundary condition ($\dot{m}_{CH_4} = 1.4X10^{-3}\ \frac{kg}{s}$), sufficient to give the 30 $kW$ from the burner used for testing. The fuel flow from the burner was "seeded" with 1% product ($CO_2$ & $H_2O$) and 0.2% soot to allow the combustion model to begin reaction of the fuel. All fluids and solids were given ambient temperature and properties.

The user specifies the critical radiant flux for piloted ignition. At fluxes above this value, the time to ignition decreases as flux increases. To model the time after the burner is ignited, but before the chair starts burning, values shown in Table 6.20 were used. Once a flame was established on the chair, piloted ignition was assumed.

The minimum flux level tested in the cone calorimeter for this chair was 25 $\frac{kW}{m^2}$. When an ignited surface element was exposed to a flux less than 25 $\frac{kW}{m^2}$, the cone results for 25 $\frac{kW}{m^2}$ were used. Linear interpolation was applied to evaluate properties between tested flux levels and cone data points.

To obtain the data for implementation in the model, three modifications were made to the raw cone given in Figures 6.37 and 6.38:

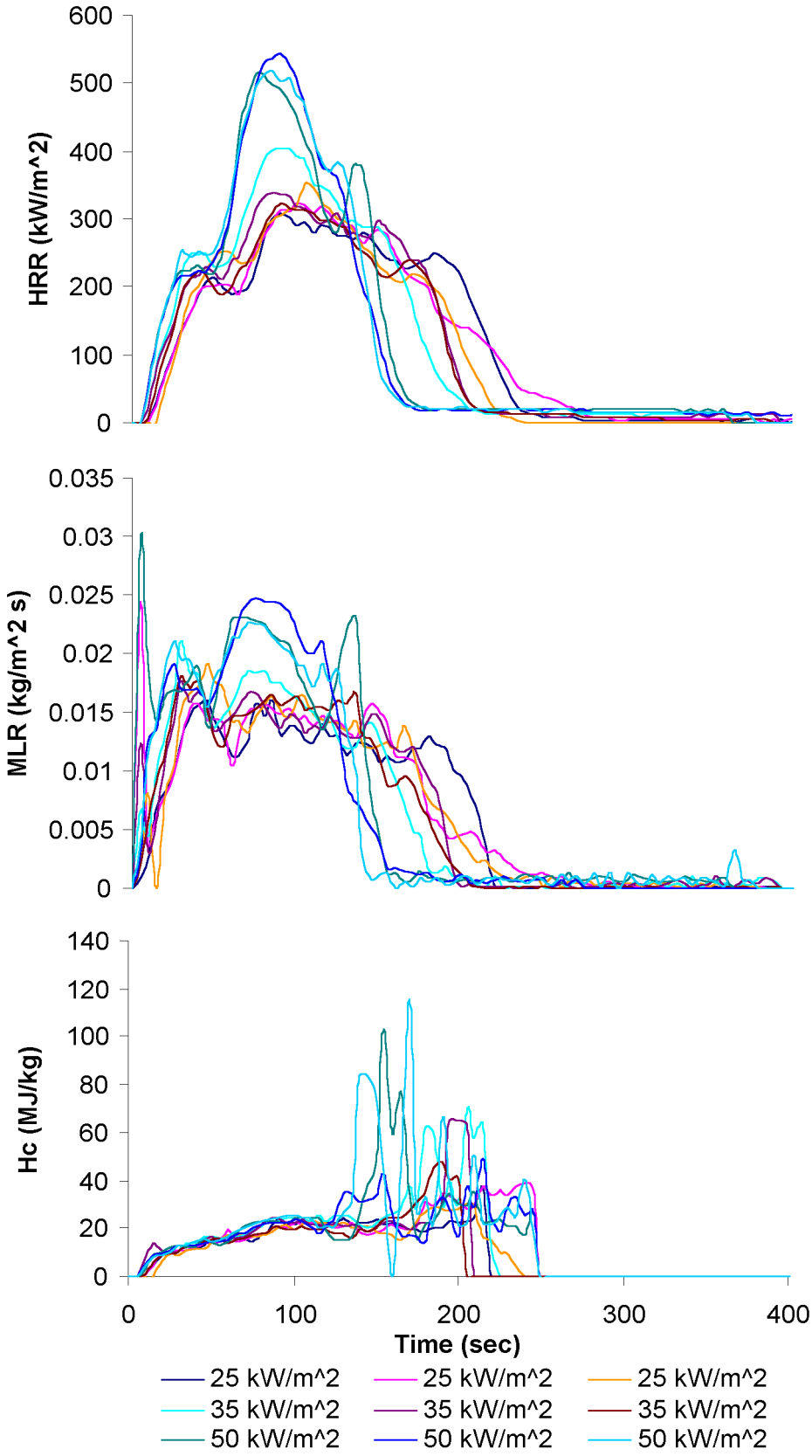


Figure 6.37: Raw cone calorimeter results for chair 3:13.

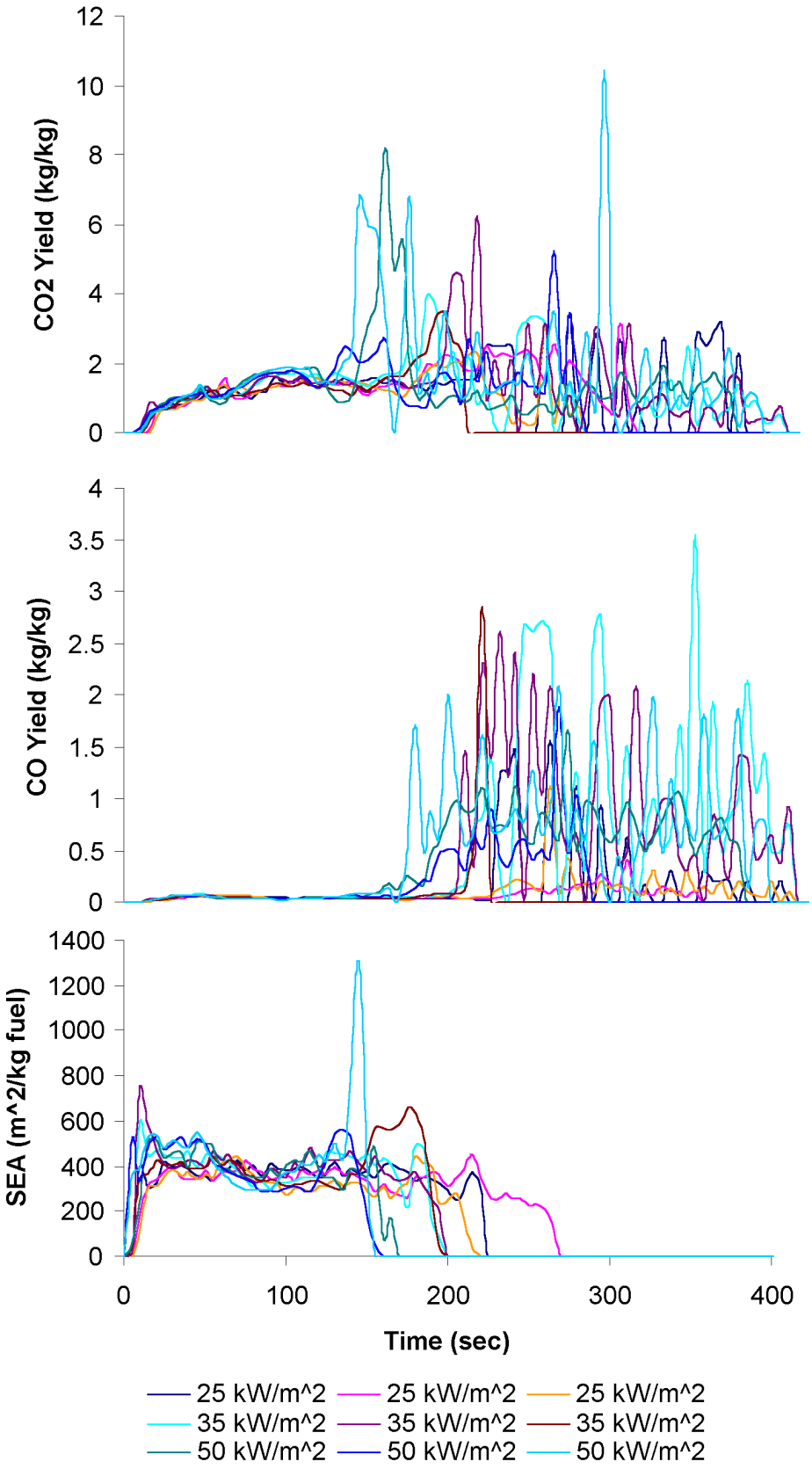


Figure 6.38: Raw cone calorimeter results for chair 3:13.

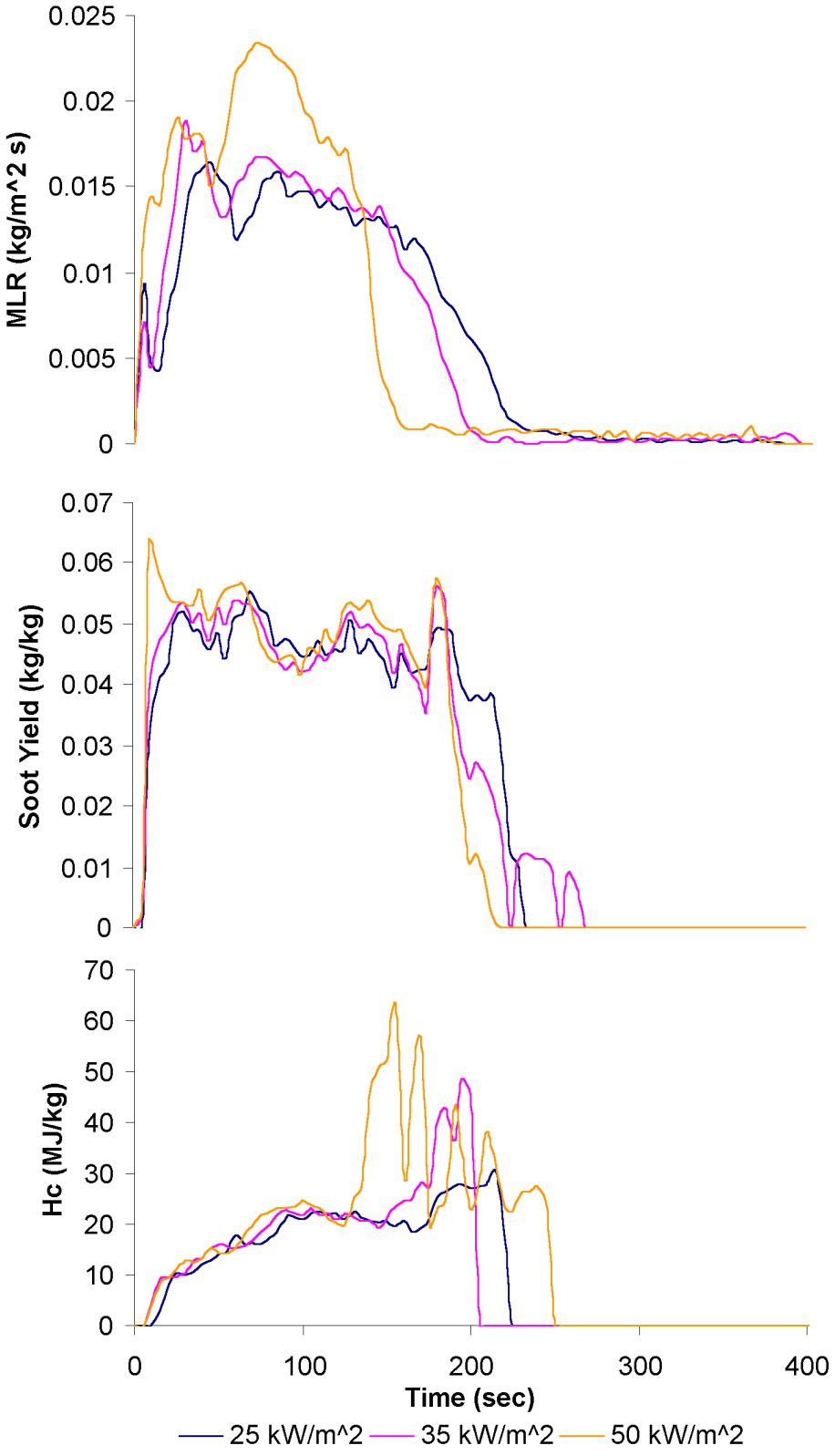


Figure 6.39: Flux averaged cone calorimeter results for chair 3:13.

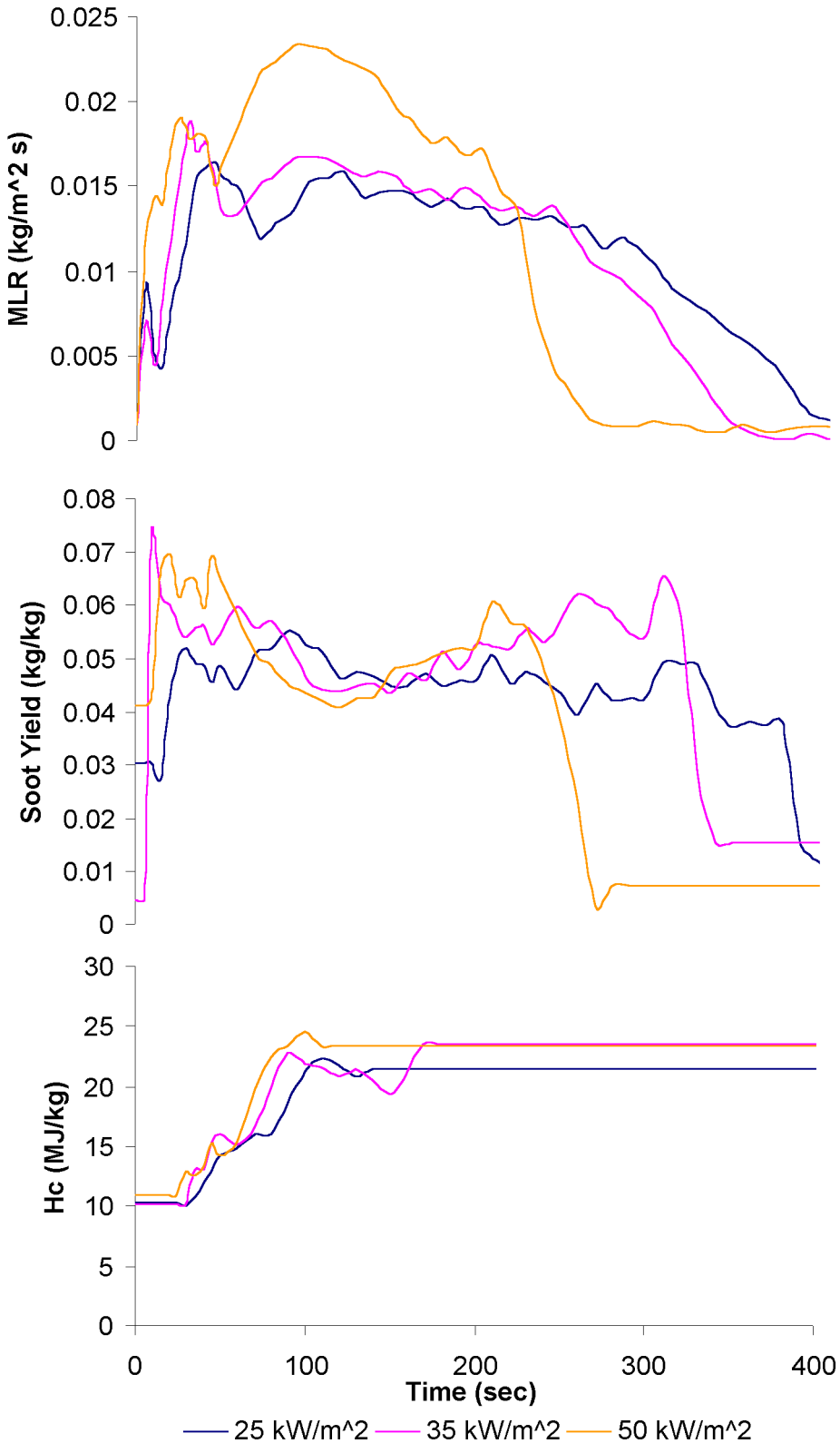


Figure 6.40: Scaled flux averaged cone calorimeter results for chair 3:13.

| Flux $\left(\frac{\mathbf{kW}}{\mathbf{m^2}}\right)$ | Time for ignition (sec) |
|---|---|
| 50 | 6 |
| 35 | 8 |
| 20 | 13 |
| 12 | $t \rightarrow \infty$ |

Table 6.20: Flux values as a function of time for ignition of chair 3:13.

- Thickness scaling was applied to account for the difference between bench and full scale foam thickness during testing.
- Multiple cone calorimeter tests at a given flux level where combined into a single data set by simple averaging.
- Very low (zero) initial heat of combustion values were reported during the first 10-20 seconds of the cone data. To prevent this physically unrealistic situation, the heat of combustion value at 30 seconds was used for times less than 30 seconds.

### Model Results

Full scale testing of this fuel package resulted in an extended fire with flame spread over the complete chair. A peak heat release rate of 235 $kW$ was observed 140 seconds into the test. A total of 126 $MJ$ of energy was released by the 6.0 $kg$ of fuel generated (60% of the original mass of the chair was consumed).

Model and experimental results for heat release rate (HRR), mass loss rate (MLR), heat of combustion ($\Delta H_c$), soot yield, total energy released, and total mass lost are given in Figures 6.41 and 6.42.

### Discussion

The model was able to capture the initial rapid spread of flame over the surface and peak burning rate. Many of the same points discussed for mattresses 1:21, 1:22, 1:23 and 1:24 would apply for chair 3:13. Analysis of the results for chair 3:13 reveals the following:

- The initial rapid fire spread across the fuel package appears to be well predicted. After the burner is turned off at 120 seconds, the model captures the decrease in HRR shown in the experiment. The greater than 75% decrease in HRR immediately after the burner is turned off is a behavior different than observed with the earlier mattress tests. For chair 3:13, the burner is placed centered on the chair and almost touches the back cushion. In this position, it exposes a large fraction of the seat and back. Without the external flux from the burner, the mass loss rate rapidly decreases until the fire redevelops during the second peak.

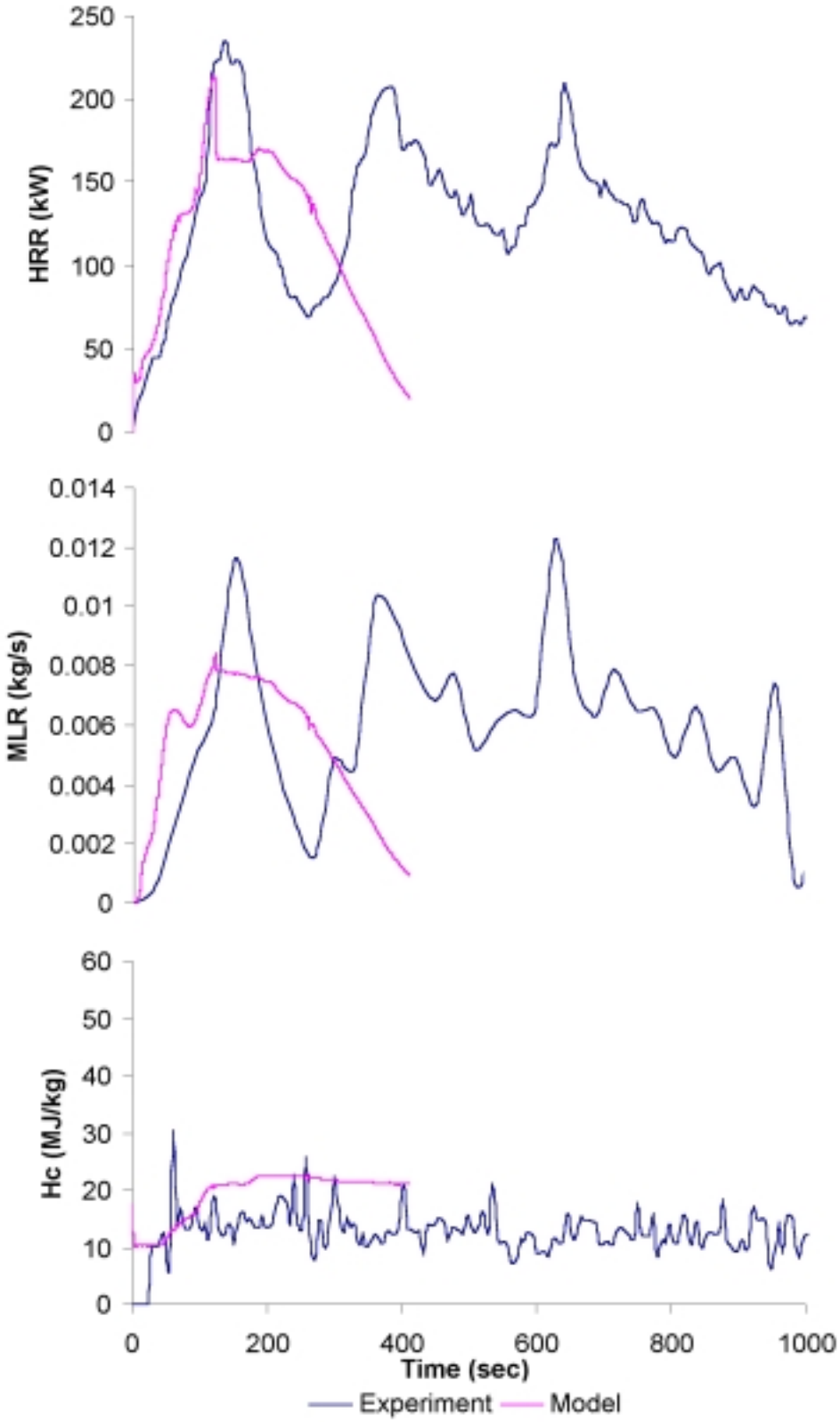


Figure 6.41: Furniture calorimeter and model results for chair 3:13.

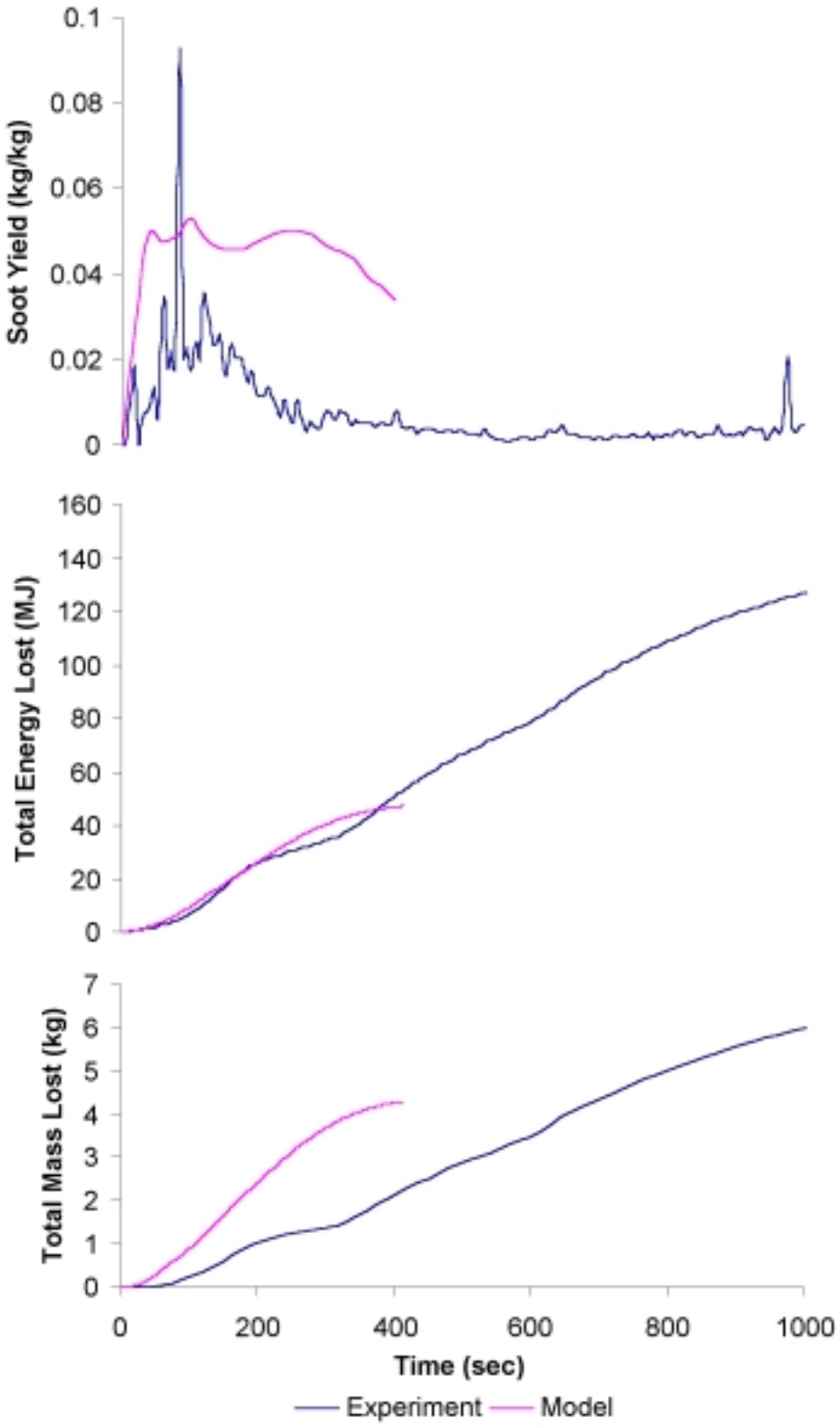


Figure 6.42: Furniture calorimeter and model results for chair 3:13.

- During the first 120 seconds, the HRR rate predicted by the model is in much better agreement with experiment than the MLR. The discrepancy appears due to differences in the actual and predicted heat of combustion.

- The model, however, fails to capture the second and third longer HRR peaks measured for the chair. By missing these peaks, the model greatly under-predicts the total energy and mass lost. Fuel pyrolysis in the model is constrained to only the surfaces defined by the user. For the chair, the top and back only, and not the sides, bottom or wood frame, where modeled. This artificially constrains the area available for pyrolysis. Difficult to predict behaviors, such as the formation of a pool fire of burning liquid foam under the chair, and involvement of the frame were not included. The resulting increase in burning area could lead to the formation of additional peaks in mass loss and resultant heat release rate.

- By the nature of how the HRR is calculated, the decrease in HRR shown by the model is much more rapid than experiment that requires the additional travel time to transport the products of combustion to the instrumentation in the hood.

- Thickness scaling of the cone calorimeter data was critical to obtaining reasonable results considering the foam in the chair was twice as thick as that tested in the cone. Runs without thickness scaling greatly under-predicted the HRR and MLR since burnout resulted prematurely.

- Utilization of ignition times at the start of a run that depend on flux as shown in Table 6.20 were important. Without this, ignition resulted instantly across the fuel surface. Such a physically impossible situation significantly over-predicted flame spread rates. The problem with the model was due to how the initial values were implemented in the .rso file.

- The reasonable agreement between fluxes from the CBUF and model burners shown in Figures 6.6 and 6.7 was necessary to allow the model to predict the ignition and beginning stages of flame spread across the chair. Without accurate initial ignition predictions, time shifting of the model results to match the experiment would have been necessary.

- Slight differences in the starting heat release rates shown in Figure 6.41 are due to how the initial guess is implemented in TASCflow. Model runs are started with the fan operating and a steady flame established on the burner. Thus the model starts out with a heat release rate of 30 $kW$ at time zero. Time shifting of the curves to a common zero would not be appropriate. Instead, both the experimental and model curves are matched at the point where the burner is turned off. If the model curve was shifted to a common starting HRR (such as 30 $kW$), then the time for burner application would be different for model and experiment. A less desirable alternative would be for the user to shut the

burner off in the model at a HRR equal to that in the furniture calorimeter when the burner is removed at 120 seconds.

- Initial flame spread over the back of the chair was more rapid than across the seat. At only 40 seconds into the model run, flame had spread over 90% and 75% of the back and seat respectively.

A total of just under 26 days of computation time was required to complete the 3:13 chair simulation. The model was executed on an Alpha EV5 (21164) processor running at 300 $MHz$ and using 512 $Mb$ of RAM. An additional 30.7 days of computation time was required for the 400 seconds of model results. The geometry for this chair permitted half symmetry to be utilized. An average of .76 hours of CPU time was used to model each second of the actual test. For the 0.25 second time step used for the model results presented, two inner loop iterations were used for each outer loop iteration. TASCflow computation time was divided approximately as shown in Figure 6.21. Net momentum, mass, species and energy values for the domain bal-

| **Component** | **Percent of CPU time** |
|---|---|
| Pre-process | 1 |
| U-V-W-P-T | 20 |
| $k_{tke} - \epsilon$ | 5 |
| Scalars | 12 |
| FV Radiation | 60 |
| Post-process | 1 |
| Miscellaneous | 1 |

Table 6.21: Breakdown of CPU usage for chair 3:13.

anced within $1E-03$ to $1E-04$ of maximum values. Reasonable levels for reacting multi-component fluid flows. Radiant heat transfer balanced globally on the order of $1E-02$ based on 65 work units per iteration. The two opposing surfaces of the chair required a much larger commitment of CPU time to provide a solution with a sufficiently small radiation transfer residual than required for a horizontal mattress.

# Chapter 7

# Conclusions

## 7.1 Summary of Results

In general, the model was found to make reasonable estimates of the mass loss from a burning piece of furniture. Heat release rates were predicted less dependably due to differences between experimental and model $\Delta H_c$ values. As expected, the more a piece of furniture deviated from predictable burning behavior, the less the model matched experiment. An overall summary of model performance is provided in Figures 7.1 and 7.2.

The top graph in Figure 7.1 shows the agreement for peak heat release rate between model and experiment. As shown in Figure 6.14 on Page 161, the experimental HRR results for mattress 1:21 show two distinct peaks. The first represents the period during which flame is spreading over the surface of the mattress. A second larger peak occurs later in the test due to the formation of a pool fire of burning polyurethane, something not addressed by the model. Considering only peak 1 for mattress 1:21, all of the peak heat release rates and time to peak for the fuels that were not highly fire retardant (1:21, 1:22, 1:23, 3:13) were predicted within ±20%. Total energy lost for the mattresses (1:21, 1:22, 1:23 and 1:24) was also predicted within ±20%. Because combustion of the wood chair frame was not included in the model, the total experimental energy and mass lost were almost twice as large.

Agreement between the experimental and model soot yields shown in Figure 7.2 are in the $20 - 50\%$ range. An accurate picture of soot production for mattress 1:22 is, however, not given. Based on Figure 6.22, the soot yield from the model is very reasonable. The greatest difference occurs both early and late in the experiment when a few discrete experimental data points fall well above the average.

Unfortunately, there is no experimental flame spread rate data to compare with the bottom graph in Figure 7.2, so there is no direct way of evaluating the model on this critical issue. In a general way, the slope of the heat release rate curve could be a representative measure of the aggregate performance of the model. Some insight, however, could be gained although it is not possible to separate the spread and pyrolysis rates. Figure 7.3 compares the slope of the experimental and model heat release rate curves measured between 10% and 90% of peak values. For the

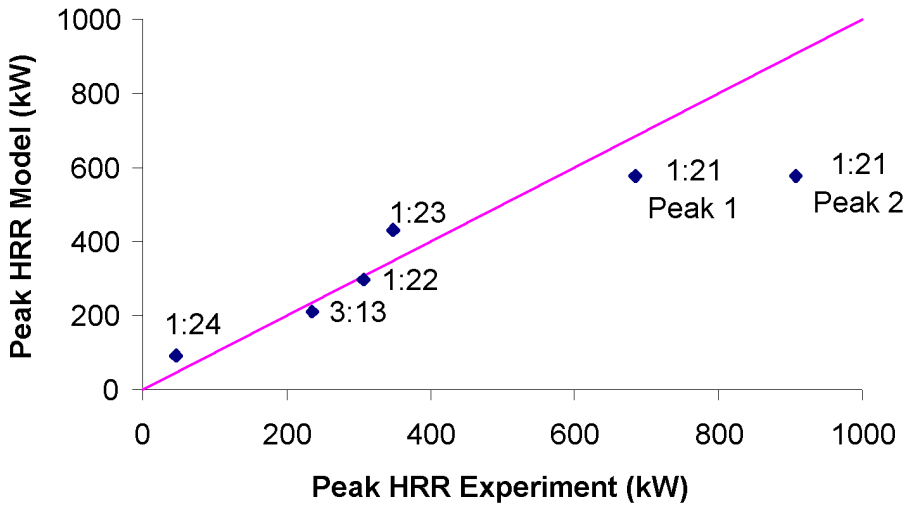


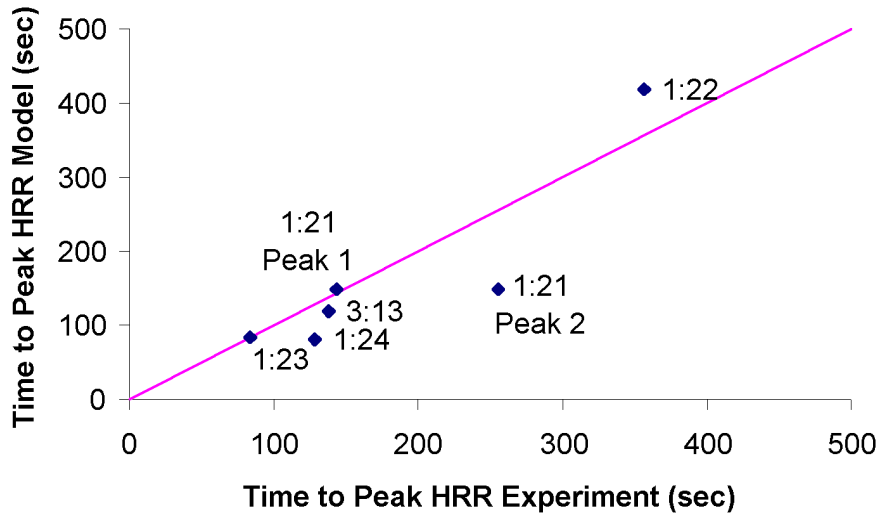


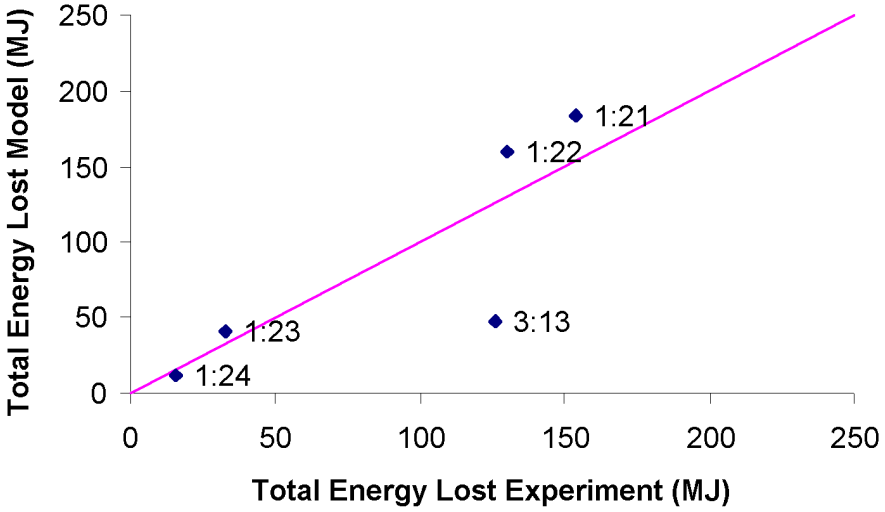


Figure 7.1: Summary of model results

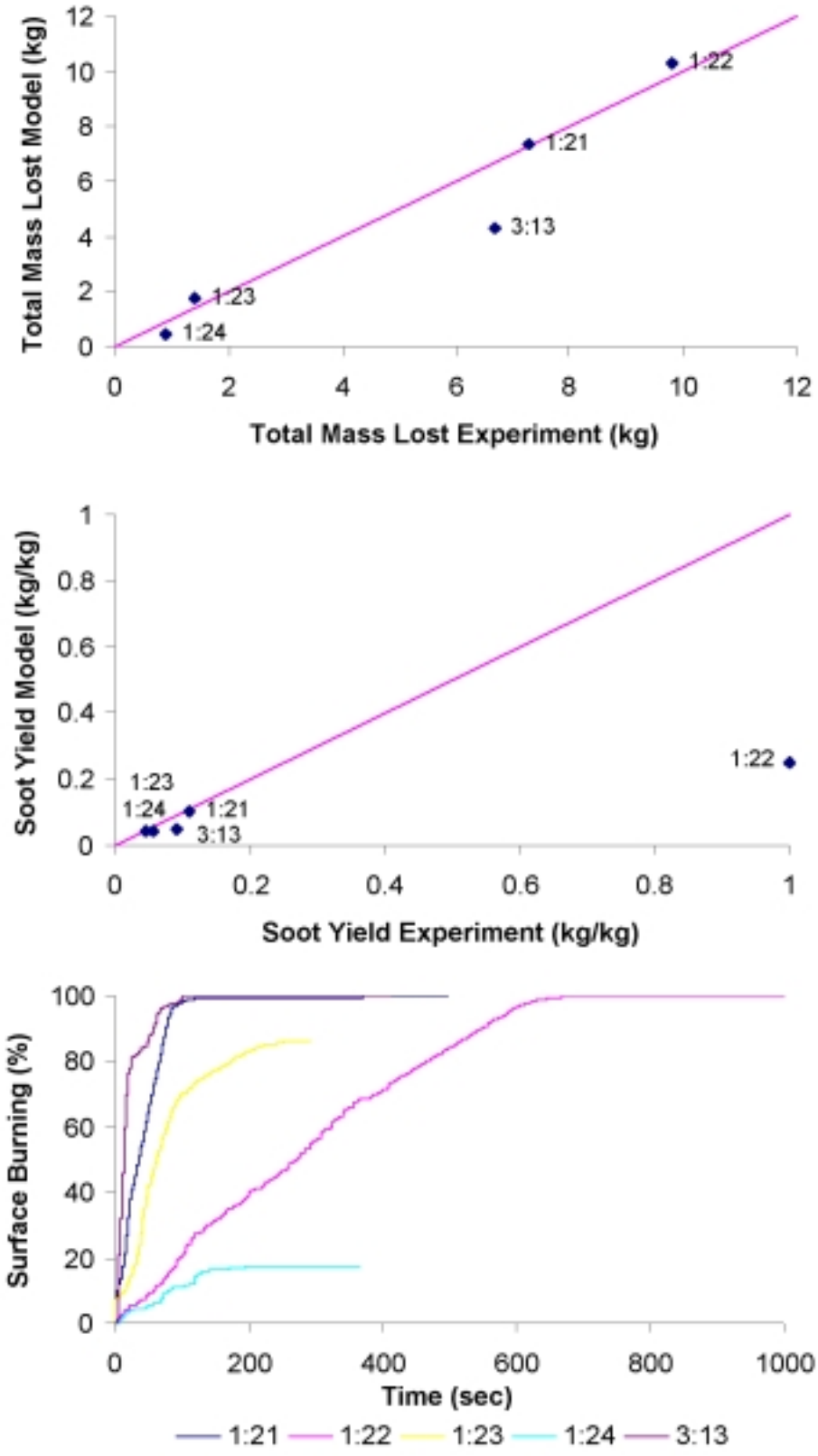


Figure 7.2: Summary of model results.

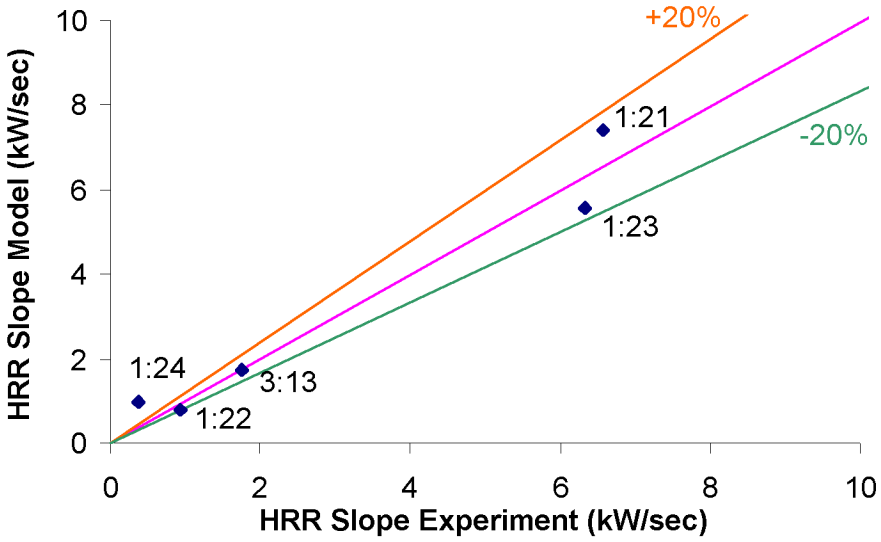


Figure 7.3: Slope of heat release rate.

furniture that was not highly fire retardant (1:21, 1:22, 1:23 and 3:13), the rate of increase in heat release rate during the spreading portion of the fire was predicted within 20% of experimental values. This important finding, although not validating the model, shows a positive overall performance of the model during the growing periods of these types of furniture fires. It does not, however, permit any evaluation of model performance when going outside the range of materials tested.

## 7.2 Accomplishments

It is important to clearly identify what has been gained by the development of a flame spread model for furniture that is incorporated within a CFD code. A number of successes were observed during model development and testing. These include:

- Flame spread modeling showed the importance of radiation calculations, especially for furniture with surfaces that face each other. Since the finite volume radiation model was the only intermediate optical behavior model investigated, it is not possible to answer the question if this is the best model. An optically thin model (surface to surface) predicted a net surface loss of energy, so ignition temperatures were never reached. At the other end of behavior, a thick environment (diffusion model) resulted in peak surface flux values of 5 $\frac{kW}{m^2}$, since the fuel is only able to see the hot gases in the control volumes directly above the surface.

- The basic flame spread models in the literature that were discussed in Chapter 2 and 3 almost without exception involve only a single surface. Flame spread is principally driven by a single flame above the fuel surface and in many cases the

flux to the fuel surface is constant or simply changing as a function of distance. Issues in predicting radiation transfer when multiple surfaces are oriented so that they view each other is clearly demonstrated in the difficulty experienced by researchers such as Dietenberger in work with the Furniture Fire Model [21]. The furniture CFD model described here has overcome many of these difficulties.

- Reasonable predictions of the ignition process were made by the Furniture CFD model. By providing sufficient detail on the burner and ignition times as a function of flux, the early periods of flame spread were generally modeled successfully. The furniture CFD model appears to be one of the few models that permit any number of surfaces at user defined locations to be involved in flame spread.

- Thickness scaling of the cone calorimeter data was very successful. Without scaling, accurate furniture fire growth predictions were not possible. The process of scaling is not difficult, since the only variable that influences the results is when burning transitions from fabric to foam.

- Support for Nam and Bill coefficients was shown by the model. Without them plume width was greatly underpredicted (velocities too high). This reduced the new radiative flux to the surface by almost a factor of 2.

- The furniture CFD model appears to be able to effectively model the interaction of two orthogonal fuel surfaces such as a chair bottom and back.

- Transient $\Delta H_c$ input values based on the cone data allow the model to overcome problems with a constant user specified value and provide results that were in better agreement with experiment.

- Distributed soot production was found to be essential to accurate radiation transfer calculations. It would be computationally inefficient to commit a large fraction of the CPU usage to radiation calculations that were based on absorption coefficients principally dependent on inaccurate soot concentrations.

- Default fluid flow and turbulence model constants specified for general CFD work are not appropriate for buoyancy driven combustion simulations. This was confirmed by reviewing the results for plume width, centerline temperature and centerline velocity.

- The solver contained in TASCflow proved to be extremely robust. Only when the model user provided incorrect input did the solver experience difficulty in completing a simulation.

- A mattress with an inner spring was successfully modeled.

However, a number of limitations of the Furniture CFD model exist and should be considered by model users when preparing a simulation, using the model and reviewing its results.

- CFD modeling of fire is still a research tool that is far from general application in engineering problems such as design. Significant development work will be necessary before CFD is expected in widespread use by fire protection engineers. The research community is the intended audience for the current work, but as CFD technology matures, fire growth predictions should move into more common use by practitioners.

- The closure models necessary to predict fire growth are computationally expensive. Long calculation times will limit the number of runs that can be completed for parameter studies and is currently the single greatest limitation to both CFD and this model.

- The model did not accurately predict the slow creeping horizontal flame spread experienced by mattress 1:24. It is expected that a much finer discretization would be necessary to capture the critical solid phase conduction. In cases such as very low HRR's, an accurate comparison between model and experiment may not be possible.

- Grid and time step independence may demand unrealistically fine discretization. The chair simulation, for example, required both a smaller time step and grid size than the mattresses to assure independent results. It is expected that the same would apply for even more complicated furniture arrangements.

- TASCflow does not allow a mass inflow boundary condition coupled with conjugate heat transfer surfaces. The Furniture CFD model addresses this issue, although the operation would be much cleaner if permitted by TASCflow source code.

- The rate of flame spread depends directly on the radiant heating from the flame to uninvolved surfaces. If the quality of the predictions by the radiation transfer and property models is not sufficient, fire growth results will suffer. The model user is cautioned to verify that the radiation calculations are providing realistic results.

- Furniture is not constructed of a single homogeneous layer, but instead involves multiple materials that char, deform and melt. These properties are not easily modeled and for the current work are assumed to not change the gross behavior of fire growth on the piece of furniture. The Furniture CFD model has shown that the spread of flame across a furniture sample can be predicted, although less success was observed for other phenomena.

- The combustion model may not provide sufficient accuracy for approximation of the sub-grid fire phenomenon. Previous predictions using the EBU combustion

model have shown good agreement between model and experiment for diffusion flames involving gas, liquid and solid fuels. In general, however, the EBU model appears to be providing reasonable predictions for the location of combustion reactions.

- As with most flame spread prediction tools, model results were sensitive to certain key fire and material properties. Unfortunately, many of these same properties are difficult to directly specify for a given fuel. Ideally, a range of values should be tested to allow assessment of the influence of a given property on the model results.

- The physics not addressed by the model as discussed in Section 5.2.3 should be considered before starting any modeling problem.

- Since flame spread rates were not measured as part of the experimental work, it was not possible to test the speed at which the pyrolysis front travels across the fuel surfaces. The slope of the HRR curve when used as a proxy for the spread rate, is within 20% of experiment for all but mattress 1:24.

- It was often difficult to get a numerically stable initial guess formulated for the start of a simulation. In many cases, more time was spent on this than the rest of the problem specification.

- The radiation calculations were found to be a CPU black hole. More and more computation time could be applied to radiation work units while at the same time never actually reaching a level of residual reduction typical of other conservation equations.

## 7.3 Future Work

The Furniture CFD model certainly shows promise for producing reasonable estimates of full scale furniture performance based on bench scale test results. To this end, a number of items that could be considered improvements are recommended:

- Multiple fuels and multiple fuel thickness values should be incorporated. Additionally, unique ignition properties should be permitted for each fuel that would allow, for example, modeling both the wood frame and the foam seat of a chair.

- The model should be tested with a data set that includes flame spread velocities. One of the weaknesses of the CBUF data set is the lack of pyrolysis front location as a function of time.

- Improvements in the furniture CFD code and TASCflow would be necessary before realistic flame spread calculations could be carried out on the $mm$ length scales necessary to capture solid phase conduction dominated horizontal flame spread.

- The instrumentation section of the furniture calorimeter should be incorporated to determine how well the model predicts the travel time for products of combustion. Improved results could be expected from the model if comparisons with experiment for HRR, soot yield etc. were made at the same location.
- Pyrolysis from multiple layers, charring and melting could be included to provide a more accurate description of fabric-foam combustion.

# Bibliography


[1] V. Babrauskas. Fire modelling tools for FSE: Are they good enough? *SFPE Journal*, 18:289–296, 1996.

[2] V. Babrauskas and S. J. Grayson, editors. *Heat Release in Fires*. Elsevier Applied Science, 1992.

[3] T. Niioka. Ignition time in the stretched flow field. In *Eighteenth Symposium (International) on Combustion*, pages 1807–1813. The Combustion Institute, 1981.

[4] G. Cox. *Combustion Fundamentals of Fire*. The Combustion Treatise Series. Academic Press, London, first edition, 1995.

[5] M. Janssens. Piloted ignition of wood: A review. *Fire and Materials*, 15:151–168, 1991.

[6] D. Drysdale. Ignition: The material, the source and subsequent fire growth. Technical Report TR83-5, Society of Fire Protection Engineers, 1983.

[7] D. Drysdale. *An Introduction to Fire Dynamics*. Wiley Interscience, first edition, 1985.

[8] H. E. Thomson and D. Drysdale. Critical mass flowrate at the firepoint of plastics. In T. Wakamatsu, editor, *Fire Safety Science–Proceedings of the Second International Symposium*, pages 67–76. International Association for Fire Safety Science, Hemisphere Publishing Corporation, 1989.

[9] H. S. Carslaw and J. C. Jaeger. *Conduction of Heat in Solids*. Oxford University Press, London, second edition, 1959.

[10] M. Janssens. A thermal model for piloted ignition of wood including variable thermophysical properties. In G. Cox and B. Langford, editors, *Fire Safety Science–Proceedings of the Third International Symposium*, New York, 1991. International Association for Fire Safety Science, Elsevier Applied Science.

[11] E. Mikkola and I. S. Wichman. On the thermal ignition of combustible materials. *Fire and Materials*, 14:87–96, 1989.

[12] J. F. Krasny and D. Huang. Small flame ignitability and flammability behavior of upholstered furniture materials. Technical Report NBSIR 88-3771, NBS, 1988.

[13] T. J. Shields, G. W. Silcock, and J. J Murray. Evaluating ignition data using the flux time product. *Fire and Materials*, 18:243–254, 1994.

[14] H. E. Thomson, D. D. Drysdale, and C. L. Beyler. An experimental evaluation of critical surface temperature as a criterion for piloted ignition of solid fuels. *Fire Safety Journal*, 13:185–196, 1988.

[15] D. J. Rasbash, D. D. Drysdale, and D. Deepak. Critical heat and mass transfer at pilot ignition and extinction of a material. *Fire Safety Journal*, 10:1–10, 1986.

[16] D. D. Drysdale and H. E. Thomson. The ignitability of flame retarded plastics. In T. Kashiwagi, editor, *Fire Safety Science–Proceedings of the Fourth International Symposium*, pages 195–204, New York, 1994. International Association for Fire Safety Science.

[17] E. E. Smith and T. J. Green. Release rate tests for a mathematical model. In *Mathematical Modeling of Fires STP 983*. ASTM, 1987.

[18] E. E. Smith and S. Satija. Release rate model for developing fires. In *ASME/AIChE National Heat Transfer Conference Paper 81-HT-4*, Milwaukee, Wisconsin, August 1981.

[19] G. W. H. Silcock and T. J. Shields. A protocol for analysis of time to ignition data from bench scale tests. *Fire Safety Journal*, 24:75–95, 1994.

[20] B. R. Toal, G. W. H. Silcock, and T. J. Shields. An examination of piloted ignition characteristics of cellulosic materials using the ISO ignitability test. *Fire and Materials*, 14:97–106, 1989.

[21] M. A. Dietenberger. Modification to furniture fire model for HAZARD system. Technical Report NBS-GCR-92-601, NBS, January 1992.

[22] B. T Amos. Ignition and flame propagation studies over a flat fuel surface. Technical Report NIST-CGR-92-604, NIST, March 1992.

[23] S. Patankar. *Numerical Heat Transfer and Fluid Flow*. Computational Methods in Mechanical and Thermal Sciences. McGraw-Hill Book Company, New York, first edition, 1980.

[24] T. Kashiwagi. A radiative ignition model of a solid fuel. *Combustion Science and Technology*, 8:225–236, 1974.

[25] L. S. Tzeng, A. Atreya, and I. S. Wichman. A one-dimensional model of piloted ignition. *Combustion and Flame*, 80:94–107, 1990.

[26] S. H. Park and C. L. Tien. Radiation induced ignition of solid fuels. *International Journal of Heat and Mass Transfer*, 33(7):1511–1520, 1990.

[27] A. C. Fernandez–Pello and T. Hirano. Controlling mechanisms of flame spread. *Combustion Science and Technology*, 32:1–31, 1983.

[28] M. Anderson, et al. An experimental study of upward flame spread on cellulosic materials. In *Conference Proceedings of the Seventh International Interflam Conference*, pages 169–178. Interscience Communications Limited, 1996.

[29] A. C. Fernandez–Pello. Fire propagation in concurrent flows, final progress report. Technical Report NIST-GCR-89-569, NIST, December 1989.

[30] A. C. Fernandez–Pello. Fire propagation in concurrent flows. Technical Report NIST-GCR-94-644, NIST, June 1994.

[31] A. C. Fernandez–Pello. Flame spread in a forward forced flow. *Combustion and Flame*, 36:63–78, 1979.

[32] L. Zhou and A. C. Fernandez-Pello. Concurrent turbulent flame spread. In *Symposium (International) on Combustion*, pages 1709–1714, 1990.

[33] L. Zhou and A. C. Fernandez-Pello. Solid fuel combustion in a forced, turbulent, flat plate flow: The effect of buoyancy. In *Twenty-Fourth Symposium (International) on Combustion*, pages 1721–1728, 1992.

[34] A. C. Fernandez–Pello. Flame spread modeling. *Combustion Science and Technology*, 39:119–134, 1984.

[35] Y. H. Chao and A. C. Fernandez-Pello. Turbulent concurrent flame spread: Effect of oxygen concentration. In *Western State Section of The Combustion Institute Spring Meeting*. University of Utah, Salt Lake City, 1993.

[36] Y. H. Chao and A. C. Fernandez-Pello. Flame spread in a vitiated concurrent flow. In A. M. Kanury and M. Q. Brewster, editors, *HTD Volume 199, Heat Transfer in Fire and Combustion Systems*. The American Society of Mechanical Engineers, 1992.

[37] M. Sibulkin, J. Kim, and J. V. Creeden. The dependence of flame propagation rates on surface heat transfer. I: Downward burning. *Combustion Science and Technology*, 14:43–56, 1976.

[38] V. Babrauskas. Flame fluxes in opposed flow flame spread: A review of the literature. Technical Report 1995:06, Swedish National Testing and Research Institute (SP), 1995.

[39] A. C. Fernandez–Pello. Fire propagation in concurrent flows. Technical Report NIST-GCR-89-560, NIST, February 1989.

[40] L. Zhou, A. C. Fernandez-Pello, and R. Cheng. Flame spread in an opposed turbulent flow. In *Fall Technical Meeting*. Western Section of the Combustion Institute, October 17-18 1988.

[41] A. K. Kulkarni. Upward flame spread on vertical walls. Technical Report NBS-GCR-89-565, NBS, 1989.

[42] J. G. Quintiere. Surface flame spread. In P. J. DiNenno, editor, *SFPE Handbook of Fire Protection Engineering*. SFPE and NFPA, second edition, 1995.

[43] G. H. Markstein and J. deRis. Upward fire spread over textiles. In *Fourteenth Symposium (International) on Combustion*, pages 1085–1097. The Combustion Institute, 1972.

[44] L. Orloff, J. deRis, and G. H. Markstein. Upward turbulent fire spread and burning of fuel surface. In *Fifteenth Symposium (International) on Combustion*. The Combustion Institute, 1975.

[45] P. H. Thomas. On concurrent upward surface spread of flame. *Fire Safety Journal*, 22:89–99, 1994.

[46] K. Saito, J. G. Quintiere, and F. A. Williams. Upward turbulent flame spread. In *Fire Safety Science–Proceedings of the First International Symposium*. International Association for Fire Safety Science, 1986.

[47] B. Karlsson. Modeling fire growth on combustible lining materials in enclosures. Technical Report TVBB-1009, Lund University Department of Fire Safety Engineering, 1992.

[48] A. K. Kulkarni, C. I. Kim, and C. H. Kuo. Upward flame spread on a vertical wall. Technical Report Annual Progress Report, NIST, 1990.

[49] J. G. Quintiere, M. Harkleroad, and Y. Hasemi. Wall flames and implications for upward flame spread. *Combustion Science and Technology*, 48:191–222, 1986.

[50] B. Sundström. CBUF fire safety of upholstered furniture - the final report on the CBUF research programme. Technical Report 3478/1/0/196/92/11-BCR-DK(30), European Commission Measurements and Testing, 1995.

[51] H Cheng Kung. A mathematical model of wood pyrolysis. *Combustion and Flame*, 18:185–195, 1972.

[52] W. Parker. Prediction of the heat release rate of wood. In *Fire Safety Science–Proceedings of the First International Symposium*, pages 207–216. International Association for Fire Safety Science, 1986.

[53] W. Parker and R. Filipczak. Modelling the heat release rate of aircraft cabin panels in the cone and OSU calorimeters. *Fire and Materials*, 19:55–59, 1995.

[54] H. E. Mitler. Algorithm for the mass–loss rate of burning wall. Technical Report NBSIR 87-3682, NBS, December 1987.

[55] H. E. Mitler. Algorithm for the mass–loss rate of burning wall. In T. Wakamatsu, editor, *Fire Safety Science–Proceedings of the Second International Symposium*, pages 179–188. International Association for Fire Safety Science, Hemisphere Publishing Corporation, 1989.

[56] L. Orloff, A. T. Modak, and R. L. Alpert. Burning of large–scale vertical surface. In *Sixteenth Symposium (International) on Combustion*. The Combustion Institute, 1977.

[57] A. K. Kulkarni, E. Brehob, S. Manohar, and R. Nair. Turbulent upward flame spread on a vertical wall under external radiation. Technical Report NIST-GCR-1994-638, NIST, 1994.

[58] J. N. deRis. Spread of a laminar diffusion flame. In *Twelfth Symposium (International) on Combustion*, pages 241–252. The Combustion Institute, 1969.

[59] S. Bhattacharjee. A comparison of numerical and analytical solution of the creeping flame spread over thermally thin material. *Combustion and Flame*, 93:434–444, 1993.

[60] C. Di Blasi, S. Crescitelli, G. Russo, and A. C. Fernandez–Pello. Predictions of the dependence on the opposed flow characteristics of the flame spread rate over thick solid fuel. In T. Wakamatsu, editor, *Fire Safety Science–Proceedings of the Second International Symposium*, pages 119–128. International Association for Fire Safety Science, Hemisphere Publishing Corporation, 1989.

[61] C. Di Blasi. Processes of flames spreading over the surface of charring fuels: Effects of the solid thickness. *Combustion and Flame*, 97:225–239, 1994.

[62] J. G. Quintiere. An approach to modeling wall fire spread in a room. *Fire Safety Journal*, 3:201–214, 1981.

[63] J. G. Quintiere, M. Harkleroad, and W. Walton. Measurement of material flame spread properties. Technical Report NBSIR-82-2557, NBS, 1982.

[64] J. G. Quintiere, M. Harkleroad, and D. Walton. Measurement of material flame spread properties. *Combustion Science and Technology*, 32:67–89, 1983.

[65] J. G. Quintiere and M. Harkleroad. New concepts for measuring flame spread properties. Technical Report NBSIR-84-2943, NBS, 1984.

[66] Q. Jianmin. Prediction of flame spread test results from the test data of the cone calorimeter. Technical Report 1990:38, Swedish National Testing and Research Institute (SP), 1990.

[67] S. M. Lai, M. C. Jeng and G. M. Faeth. An investigation of turbulent fires on vertical walls: Wall plume structure. Technical Report NBS-GCR-1985-486, NBS, 1985.

[68] B. A. Östman and R. M. Nussbaum. National standard fire tests in small scale compared with the full scale ISO room test. Technical Report 8702017, RAPPORT, 1987.

[69] B. A. Östman and R. M. Nussbaum. Correlation between small–scale rate of heat release and full–scale room flashover for surface linings. In T. Wakamatsu, editor, *Fire Safety Science–Proceedings of the Second International Symposium*. International Association for Fire Safety Science, Hemisphere Publishing Corporation, 1989.

[70] B. A. Östman and D. Tsantaridis. Correlation between cone calorimeter data and time to flashover in the room fire test. *Fire and Materials*, pages 205–209, 1994.

[71] A. W. Heskestad. Valic smoke evaluation by the cone calorimeter. In *Conference Proceedings of the Seventh International Interflam Conference*, pages 247–255. Interscience Communications Limited, 1996.

[72] R. V. Petrella. The assessment of full–scale fire hazards from cone calorimeter data. *Journal of Fire Sciences*, 12, January/February 1994.

[73] B. Karlsson and S. E. Magnusson. Combustible wall lining materials: Numerical simulation of room fire growth and the outline of a reliability based classification procedure. In G. Cox and B. Langford, editors, *Fire Safety Science–Proceedings of the Third International Symposium*, pages 667–678, New York, 1991. International Association for Fire Safety Science, Elsevier Applied Science.

[74] W. Parker, K. Tu, S. Nurbakhsh, and G. Damant. Chair burns in the TB133 room, the ASTM room, the furniture calorimeter and the cone calorimeter. In G. Cox and B. Langford, editors, *Fire Safety Science–Proceedings of the Third International Symposium*, pages 699–708, New York, 1991. International Association for Fire Safety Science, Elsevier Applied Science.

[75] V. Babrauskas and J. Krasny. Prediction of upholstered chair heat release rates from bench scale measurements. In T. Z. Harmathy, editor, *Fire Safety: Science and Engineering, STP 882*, pages 268–284. ASTM, 1985.

[76] CIB W14 Workshop. *A Thermal Model to Predict Fire Growth on a Wall*. VTT, Espoo, Finland, 1995.

[77] G. Grant and D. Drysdale. Numerical modelling of early flame spread in warehouse fires. *Journal of Fire Sciences*, 1996.

[78] E. E. Smith. Mathematical model of a fire in a compartment having combustible walls and ceiling. In *AIChE Symposium Series Number 246*, volume 81, pages 64–74, 1984.

[79] K. Saito, F. A. Williams, I. S. Wichman, and J. G. Quintiere. Upward turbulent flame spread on wood under external radiation. *Journal of Heat Transfer*, 111:438–445, May 1989.

[80] B. Karlsson. A mathematical model for calculating heat release rate in the room calorimeter. *Fire Safety Journal*, 20:93–113, 1993.

[81] B. Karlsson. Mathematical models for calculating heat release rate in the room corner test. In *Fire and Flammability of Furnishings and Contents of Buildings, STP 1233.*, pages 216–236. ASTM, 1994.

[82] M. Kokkala, U. Göransson, and J Söderbom. EUREFIC-Large scale fire experiments in a room with combustible linings. Some results from Project 3 of the EUREFIC fire research programme. Technical Report 1990:41, Swedish National Testing and Research Institute (SP), 1990.

[83] K. Opstad and L. E. Lonvik. Note: Fire test data available for your purpose. *Fire and Materials*, 17:139–143, 1993.

[84] B. J. McCaffrey, J. G. Quintiere, and M. F. Harkleroad. Estimating room temperatures and the likelihood of flashover using fire test data correlations. *Fire Technology*, 17:98–119, 1981.

[85] G. Grant and D. Drysdale. Flame spread modelling and fire growth in warehouses. unpublished.

[86] W. H. Press, S. A. Teukolsky, W. T. Vetterling, and B. P. Flannery. *Numerical Recipes in Fortran*. Cambridge University Press, second edition, 1992.

[87] H. Brunner and P. J. van der Houwen. *The Numerical Solution of Volterra Equations, CWI Monograph 3*. Elsevier Science Publishers, Amsterdam, 1986.

[88] J. Blomqvist and B. Andersson. Modelling of furniture experiments with zone models. *Fire and Materials*, 9(2):81–87, 1985.

[89] R. W. Bukowski, F. B. Clarke, J. R. Hall, and S. W. Stiefel. Fire risk assessment method: Case study 1 upholstered furniture in residences. Technical report, National Fire Protection Research Foundation, 1990.

[90] H. E. Mitler and G. Walton. A computer model of the smoldering ignition of furniture. Technical Report NISTIR 4973, NIST, 1992.

[91] H. E. Mitler and H. W. Emmons. Documentation for CFC V, the fifth Harvard fire code. Technical Report NBS GCR 81-344, NBS, 1981.

[92] H. W. Emmons. The use of fire test data in fire models. Technical Report 78, Harvard University, 1989.

[93] J. M. Sauer and E. E. Smith. Mathematical model of a ventilation controlled compartment fire. *Journal of Fire Sciences*, 1, July/August 1983.

[94] H. E. Mitler and K. D. Steckler. Comparison of wall-fire behavior with and without a ceiling. Technical Report NISTIR 5380, NIST, 1993.

[95] H. E. Mitler. Predicting the spread rates of fires on vertical surfaces. In *Twenty-Third Symposium (International) on Combustion*, pages 1715–1721. The Combustion Institute, 1990.

[96] H. E. Mitler and K. D. Steckler. SPREAD-a model of flame spread on vertical surfaces. Technical Report NISTIR 5619, NIST, 1995.

[97] H. E. Mitler. An algorithm to describe the spread of a wall fire under a ceiling. Technical Report NISTIR 5547, NIST, 1994.

[98] M. A. Dietenberger. Furniture fire model. Technical Report NBS-GCR-84-480, NBS, November 1984.

[99] M. A. Dietenberger. Mathematical modeling of furniture fires. Technical Report NBS-GCR-86-506, NBS, February 1986.

[100] M. A. Dietenberger. Description and results of furniture fire modules within FAST (HEMFAST). Technical Report UDR-TR-87-29, University of Dayton Research Institute, January 1987.

[101] M. A. Dietenberger. Improved furniture fire model within FAST: HEMFAST2. Technical Report NBS-GCR-88-545, NBS, March 1988.

[102] M. A. Dietenberger. A validated furniture fire model within FAST (HEMFAST). Technical Report NBS-GCR-89-564, NBS, June 1989.

[103] M. A. Dietenberger. Technical reference and user's guide for FAST/FFM Version 3. Technical Report NBS-GCR-91-589, NBS, May 1991.

[104] C. Beyler. Technical review of the Furniture Fire Model Version 3. Technical Report NIST-GCR-92-618, NIST, October 1992.

[105] K. Opstad. Fire modelling using cone calorimeter results. Technical Report STF25 A92028, SINTEF NBL Norwegian Fire Research Laboratory, 1992.

[106] K. Opstad. Calculation of flame spread on lining materials by the field model KAMELEON. Project 5 of the EURIFIC fire research programme. Technical Report STF A92016, SINTEF NBL–Norwegian Fire Research Laboratory, January 1993.

[107] K. Opstad. Modelling of thermal flame spread on solid surfaces in large scale fires. Technical Report 1995:114(D), Department of Applied Mechanics, Thermo and Fluid Dynamics, 1995.

[108] K. S. Pedersen and B. F. Magnussen. Field models–their present and future application in fire safety engineering. In *International Fire Safety Engineering Conference*, Sydney, Australia, 1992.

[109] B. F. Magnussen and B. H. Hjertager. On mathematical modeling of turbulent combustion with special emphasis on soot formation and combustion. In *Sixteenth Symposium (International) on Combustion*, pages 719–729. The Combustion Institute, 1976.

[110] B. F. Magnussen, B. H. Hjertager, J. B. Olsen, and D. Bhaduri. Effects of turbulent structure and local concentrations on soot formation and combustion in acetylene diffusion flames. In *Seventeenth Symposium (International) on Combustion*, pages 1383–1393. The Combustion Institute, 1978.

[111] H. Yan. CFD and experimental studies of room fire growth on wall lining materials. *Fire Safety Journal*, 27:201–238, 1996.

[112] Modak, A. T. Radiation from Products of Combustion. *Fire Research*, 1:339–361, 1979.

[113] American Society for Testing and Materials, Philadelphia. *ASTM E 1354 - Test Method for Heat and Visible Smoke Release Rates for Materials and Products Using an Oxygen Consumption Calorimeter*, 1996 edition.

[114] International Standards Organization. *ISO 5660, Reaction to fire, Part 1: Rate of heat release from building products (Cone calorimeter method)*, first edition, 1993.

[115] M. M. Hirschler. Fire tests and interior furnishings. In *Fire and Flammability of Furnishings and Contents of Buildings. STP 1233*, pages 7–31. ASTM, 1994.

[116] NORDTEST, Esbo, Finland. *NT FIRE 032 - Nordtest Method for Upholstered Furniture: Burning Behaviour - Full Scale Test*, 1991.

[117] Underwriters Laboratories Inc. *UL 1056 Standard for Fire Test of Upholstered Furniture*, second edition, 1995.

[118] British Standard BS 5852: Part 2:1982. *Fire tests for furniture. Part 2. Methods of test for the ignitability of upholstered composites for seating by flaming sources.*

[119] American Society for Testing and Materials, Philadelphia. *ASTM E 1537 - Standard Test Method for Fire Testing of Upholstered Furniture Items*, 1996 edition.

[120] T. G. Cleary and J. G. Quintiere. Flammability characterization of foam plastics. Technical Report NISTIR 4664, NIST, 1991.

[121] T. J. Ohlemiller and J. R. Shields. Behavior of mock-ups in the California Technical Bulletin 133 test protocol: Fabric and barrier effects. Technical Report NISTIR 5653, NIST, 1995.

[122] S. G. Helzer, B. Buchbinder, and F. L. Offensend. Decision analysis of strategies for reducing upholstered furniture fire losses. Technical Report Technical Note 1101, NBS, 1979.

[123] V. Babrauskas. Full-scale burning behavior of upholstered chairs. Technical Report Technical Note 1103, NBS, 1979.

[124] V. Babrauskas. Upholstered furniture room fires-measurements, comparisons with furniture calorimeter data, and flashover predictions. *Journal of Fire Sciences*, 2:5–19, 1984.

[125] J. F. Krasny and V. Babrauskas. Burning behavior of upholstered furniture mockups. *Journal of Fire Sciences*, 2:205–235, May/June 1984.

[126] V. Babrauskas, J. R. Lawson, W. D. Walton, and W. H Twilley. Upholstered furniture heat release rates measured with a furniture calorimeter. Technical Report NBSIR 82-2604, NBS, 1982.

[127] V. Babrauskas. Upholstered furniture heat release rates: Measurements and estimation. *Journal of Fire Sciences*, 1:9–32, 1983.

[128] J. R. Lawson, W. D. Walton, and W. H. Twilley. Fire performance of furnishings as measured in the NBS furniture calorimeter. Part I. Technical Report NBSIR 83-2787, NBS, 1984.

[129] G. S. Springer. Behavior of furniture frames during fire. Technical Report NBS-GCR-85-494, NBS, 1985.

[130] Department of Consumer Affairs Bureau of Home Furnishings and Thermal Insulation State of California. *Flammability Test Procedure for Seating Furniture for Use in Public Occupancies - Technical Bulletin 133*, 1988.

[131] J. G. Quintiere. Furniture flammability: An investigation of the California Technical Bulletin 133 Test. Part I: Measuring the hazards of furniture fires. Technical Report NISTIR 4360, NIST, 1990.

[132] T. J. Ohlemiller and K. Villa. Furniture flammability: An investigation of the California Bulletin 133 test. Part II: Characterization of the ignition source and a comparable gas burner. Technical Report NISTIR 4348, NIST, 1990.

[133] W. J. Parker and K Tu. Furniture flammability: An investigation of the California Technical Bulletin 133 Test. Part III: Full scale chair burns. Technical Report NISTIR 4375, NIST, 1990.

[134] A. F. Grand, D. N Priest, and H. W. Stansberry. Burning characteristics of upholstered chairs. In *Fire and Flammability of Furnishings and Contents of Buildings. STP 1233*, pages 63–82. ASTM, 1994.

[135] H. H. Forsten. Cone calorimeter studies of furniture component system. In *Fire and Flammability of Furnishings and Contents of Buildings. STP 1233*, pages 105–113. ASTM, 1994.

[136] G. H. Damant and S. Nurbakhsh. Using California Technical Bulletin 133 to measure heat release rate tests of seating furniture. In *Fire and Flammability of Furnishings and Contents of Buildings-STP 1233*, pages 83–97. ASTM, 1994.

[137] V. Beck, D. Yung, Y. He, and K. Sumathipala. Experimental validation of a fire growth model. In *Conference Proceedings of the Seventh International Interflam Conference*, pages 653–662. Interscience Communications Limited, 1996.

[138] The Association of Contract Textiles-Decorative Fabrics Association Joint Industry Upholstery Flammability Study. *Flammability Studies of Selected Fabrics, Flame Blocking Barriers and Polyurethane Foams in the California Technical Bulletin 133 and Cone Calorimeter Test Protocols*, May 1995.

[139] V. Babrauskas. Bench-scale predictions of mattress and upholstered chair fires-similarities and differences. Technical Report NISTIR 5152, NIST, 1993.

[140] B. Andersson. Fire behaviour of beds and upholstered furniture - an experimental study (second test series). Technical Report LUTVDG(TVBB-3023), Division of Building Fire Safety and Technology-Lund University, 1985.

[141] M. Harkleroad, J. Quintiere, and W. Walton. Radiative ignition and opposed flow flame spread easurements on materials. Technical Report DOT/FAA/CT-83/28, Federal Aviation Administration, 1983.

[142] R. M. Herrington. The rate of heat smoke and toxic gases release from polyurethane foams. In C. J. Hilado, editor, *Flammability of Cellular Plastics Part 2*. Technomic Publishing, 1981.

[143] A. Modak. Influence of enclosures on fire growth volume II - analysis. Technical Report 0A0R3.BU, Factory Mutual Research, July 1978.

[144] A. Modak. The third full-scale bedroom fire test of the home fire project (July 30, 1975) Volume II-Analysis of test results. Technical Report 21011.7, Factory Mutual Research, November 1976.

[145] V. Babrauskas and J. F. Krasny. Fire behavior of holstered furniture. Technical Report Monograph 173, NBS, 1985.

[146] J. G. Quintiere and B. Rhodes. Fire growth models for materials. Technical Report NIST-GCR-94-647, NIST, June 1994.

[147] M. M. Hirschler. The measurement of smoke in rate of heat release equipment in a manner related to fire hazard. *Fire Safety Journal*, 17:239–258, 1991.

[148] V. Babrauskas, et al. Fire hazard comparison of fire-retarded and non-fire-retarded products. Technical Report Special Publication 749, NBS, 1988.

[149] G. W. Mulholland, V. Henzel, and V. Babrauskas. The effect of scale on smoke emissions. In T. Wakamatsu, editor, *Fire Safety Science–Proceedings of the Second International Symposium*, pages 347–357. International Association for Fire Safety Science, Hemisphere Publishing Corporation, 1989.

[150] V. Babrauskas. Wall insulation products: Full-scale tests versus evaluation from bench-scale toxic potency data. In *Conference Proceedings of the Seventh International Interflam Conference*, pages 257–274. Interscience Communications Limited, 1996.

[151] V. Babrauskas. The generation of CO in bench-scale fire tests and the prediction for real-scale fires. *Fire and Materials*, 19:205–213, 1995.

[152] V. Babrauskas, R. H. Harris, E. Braun, B. Levin, M. Paabo, and R. Gann. The role of bench-scale test data in assessing real-scale fire toxicity. Technical Report Technical Note 1284, NIST, 1991.

[153] W. M. Pitts. Executive summary for the workshop on developing a predictive capability for CO formation in fires. Technical Report NISTIR 89-4093, NIST, 1989.

[154] N. Peters. Laminar flamelet concepts in turbulent combustion. In *Twenty-first Symposium (International) on Combustion*, pages 1231–1250. The Combustion Institute, 1986.

[155] J. B. Moss, G. Cox, and S. Kumar. Laminar flamelet models of fire–the prospect. Crown Copyright, 1987.

[156] Advanced Scientific Computing Ltd., Waterloo, Ontario, Canada. *TASCflow Documentation Version 2.4*, 1995.

[157] V. Babrauskas. Bench-scale predictions of mattress and upholstered chair fires: Similarities and differences. In *Fire and Flammability of Furnishings and Contents of Buildings - STP 1233*, pages 50–62. ASTM, 1994.

[158] J. D. Anderson. *Computation Fluid Dynamics: The Basics with Applications*. McGraw-Hill series in Aeronautical and Aerospace Engineering, 1995.

[159] J. H. Ferziger and M Peric. *Computational Methods for Fluid Dynamics*. Springer-Verlag Berlin, 1996.

[160] H. E. Mitler. Mathematical modeling of enclosure fires. Technical Report NISTIR 90-4294, NIST, 1990.

[161] H. Schlichting. *Boundary Layer Theory*. Pergamon, 1979.

[162] D. C. Wilcox. *Turbulence Modeling for CFD*. DCW Industries, Inc., 1993.

[163] S. Kumar. Mathematical modelling of natural convection in fire–a state of the art review of the field modelling of variable density turbulent flow. *Fire and Materials*, 7(1), 1983.

[164] D. A. Anderson, J. C. Tannehill, and R. H. Pletcher. *Computational Fluid Mechanics and Heat Transfer*. Hemisphere Publishing Corporation, 1994.

[165] G. Cox and S. Kumar. Field modelling of fire in forced ventilated enclosures. *Combustion Science and Technology*, 52:7–23, 1987.

[166] N. C. Markatos, M. R. Malin, and Geoff Cox. Mathematical modelling of buoyancy-induced smoke flow in enclosures. *International Journal Of Heat Mass Transfer*, 25(1):63–75, 1982.

[167] S. Nam and R. G. Bill. Numerical simulation of thermal plumes. *Fire Safety Journal*, 21:231–256, 1993.

[168] S. Kumar and G. Cox. Radiation and surface roughness effects in the numerical modelling of enclosure fires. In T. Wakamatsu, editor, *Fire Safety Science–Proceedings of the Second International Symposium*, pages 851–860. International Association for Fire Safety Science, Hemisphere Publishing Corporation, 1989.

[169] Y. Jaluria and K. E. Torrance. *Computational Heat Transfer*. Computational Methods in Mechanics and Thermal Sciences. Hemisphere Publishing Corporation, 1986.

[170] Hottel, H. C. and Sarofim, A. F. *Radiative Transfer*. McGraw-Hill, 1967.

[171] J. N. deRis. Fire radiation - a review. In *Seventeenth Symposium (International) on Combustion*, pages 1003–1015. The Combustion Institute, 1979.

[172] M. A. Delichatsios and L. Orloff. Effects of turbulence on flame radiation from diffusion flames. In *Twenty-Second Symposium (International) on Combustion*, pages 1271–1279. The Combustion Institute, 1988.

[173] R. Siegel and J. Howell. *Thermal Radiation Heat Transfer*. Hemisphere Publishing Corporation, second edition, 1981.

[174] A. Sarofim. Radiative heat transfer in combustion: Friend or foe. In *Twenty-first Symposium (International) on Combustion*, pages 1–23. The Combustion Institute, 1986.

[175] F. C. Lockwood and N. G. Shah. A new radiation solution method for incorporation in general combustion prediction procedures. In *Eighteenth Symposium (International) on Combustion*, pages 1405–1414. The Combustion Institute, 1981.

[176] S. H. Chan. Numerical methods for multidimensional radiative transfer analysis in participating media. In T. C. Chawla, editor, *Annual Review of Numerical Fluid Mechanics and Heat Transfer*. Hemisphere Publishing Corporation, 1987.

[177] G. D. Raithby and E. H. Chui. A finite-volume method for predicting radiant heat transfer in enclosures with participating media. *Journal of Heat Transfer*, 112:415–423, 1990.

[178] W. L. Grosshandler. RADCAL: A narrow band model for radiation calculations in a combustion environment. Technical Report Technical Note 1402, NIST, April 1993.

[179] W. L. Grosshandler. Radiative heat transfer in nonhomogeneous gases: A simplified approach. *International Journal of Heat and Mass Transfer*, 23:1447–1459, 1980.

[180] W. L. Grosshandler and A. T. Modak. Radiation form nonhomogeneous combustion products. In *Eighteenth Symposium (International) on Combustion*, pages 601–609. The Combustion Institute, 1981.

[181] F. C. Lockwood and M. G. Malalasekera. Fire computation: The flashover phenomenon. In *Twenty-Second Symposium (International) on Combustion*, pages 1319–1328. The Combustion Institute, 1988.

[182] M. Fairweather, W. P. Jones, H. S. Ledin, and R. P. Lindstedt. Predictions of soot formation in turbulent non-premixed propane flames. In *Twenty-Fourth Symposium (International) on Combustion*, pages 1067–1074. The Combustion Institute, 1992.

[183] P. J. DiNenno, editor. *SFPE Handbook of Fire Protection Engineering*. Society of Fire Protection Engineers and National Fire Protection Association, second edition, 1995.

[184] M. Foley and D. Drysdale. Note: Smoke measurement and the cone calorimeter. *Fire and Materials*, pages 385–387, 1994.

[185] V. Babrauskas. Describing product fire performance–manufacturers' versus modelers' needs. *Fire and Materials*, 18:289–296, 1994.

[186] J. S. Newman and J. Steciak. Characterization of particulates from diffusion flames. *Combustion and Flame*, 67:55–64, 1987.

[187] J. K. Seader and I. N. Einhorn. Some physical, chemical, toxicological and physiological aspects of fire smokes. In *Sixteenth Symposium (International) on Combustion*, pages 1423–1445. The Combustion Institute, 1976.

[188] C. L. Beyler. *Fire Dynamics and Chemistry: An Engineering Approach*. Unpublished, 1988.

[189] D. B. Spalding. Mixing and chemical reaction in steady confined turbulent flames. In *Thirteenth Symposium (International) on Combustion*, pages 649–657. The Combustion Institute, 1971.

[190] P. Cumber. A Comparison of the Three Computational Fluid Dynamics Packages JASMINE, CINA, and FLOW3D. Technical Report B0011, FRS 80/89, Fire Research Station, Borehamwood, Hertfordshire WD6 2BL, England, March 1991. Building Research Establishment Note N36/91.

[191] W. D. Davis, G. P. Forney, and J. H. Klote. Field modeling of room fires. Technical Report NISTIR 91-4673, NIST, 1991.

[192] C. Fransson and H. Vilselius. Application of a general purpose CFD code to field modelling of tunnel fires. Technical Report FOA B 20131-2.7, Forsvarets Forskningsanstalt - National Defense Research Establishment - Sweden, June 1994.

[193] G. Cox and S. Kumar. Mathematical modelling of fires in road tunnels. In *Fifth International Symposium on the Aerodynamics and Ventilation of Vehicle Tunnels*, pages 61–76. BHRA, 1985.

[194] N. Rhodes. CFD code predictions of memorial tunnel fire tests. In *Conference Proceedings of the Seventh International Interflam Conference*, pages 983–988. Interscience Communications Limited, 1996.

[195] E. R. Galea and N. C. Markatos. Modelling of aircraft cabin fires. In T. Wakamatsu, editor, *Fire Safety Science–Proceedings of the Second International Symposium*, pages 801–810. International Association for Fire Safety Science, Hemisphere Publishing Corporation, 1989.

[196] A. D. Johnson, et al. Jet fire hazards on offshore facilities-large scale experiments, modelling and fire protection. In *Conference Proceedings of the Seventh International Interflam Conference*, pages 1043–1051. Interscience Communications Limited, 1996.

[197] V. F. Nicolette and K. T. Yang. Fire modeling of the Heiss Dampf reaktor containment. Technical Report NUREG/CR-6017, U.S. Nuclear Regulatory Commission, 1995.

[198] N. C. Markatos and G. Cox. Hydrodynamics and heat transfer in enclosures containing a fire source. *Physicochemical Hydrodynamics*, 5(1):53–66, 1984.

[199] S. Kumar, G. Cox, and A. K. Gupta. Effects of thermal radiation on the fluid dynamics of compartment fires. In G. Cox and B. Langford, editors, *Fire Safety Science–Proceedings of the Third International Symposium*, pages 345–354, New York, 1991. International Association for Fire Safety Science, Elsevier Applied Science.

[200] S. Kumar, N. Hoffman, and G. Cox. Some validation of JASMINE for fires in hospital wards. In *Lecture Notes in Engineering*, pages 159–169. Springer-Verlag, New York, 1985.

[201] G. Cox, S. Kumar, and N. C. Markatos. Some field model validation studies. In *Fire Safety Science–Proceedings of the First International Symposium*. International Association for Fire Safety Science, 1986.

[202] H. Tuovinen and H. Ingason. CFD simulation of fires in two dimensional rack storage. In *Conference Proceedings of the Seventh International Interflam Conference*, pages 209–215. Interscience Communications Limited, 1996.

[203] K. A. Pericleous, D. R. E. Worthington, and G. Cox. The field modeling of fire in an air-supported structure. In T. Wakamatsu, editor, *Fire Safety Science–Proceedings of the Second International Symposium*, pages 871–880. International Association for Fire Safety Science, Hemisphere Publishing Corporation, 1989.

[204] J. S. Tubbs. Modelling the NIST high bay fire experiment with JASMINE. Master's thesis, Worcester Polytechnic Institute, 1994.

[205] S. Kumar and M. Yehia. Mathematical field modelling of transient ceiling jet characteristics in fires. Fire Research Station, Borehamwood, Hertfordshire WD6 2BL, England, 1993.

[206] F. Tamanini. Reaction rates, air entrainment and radiation in turbulent fire plumes. *Combustion and Flame*, 30:85–101, 1977.

[207] K. Satoh. Three-dimensional field model analysis of fire-induced flow in an enclosure with a doorway opening - comparison with NBS fire tests. *Report of Fire Research Institute of Japan*, 60:53–62, 1985.

[208] J. Björkman and O. Keski-Rahkonen. Simulation of the steckler room fire experiments by using SOFIE CFD model. Technical Report 265, VTT Technical Research Centre of Finland, 1996.

[209] L. Kerrison, et al. A comparison of two fire field models with experimental room fire data. In T. Kashiwagi, editor, *Fire Safety Science–Proceedings of the Fourth International Symposium*, pages 161–172, New York, 1994. International Association for Fire Safety Science.

[210] T. Joh, J. Mashige, T. Yoshikawa, and O. Sugawa. Numerical simulation of a compartment fire from burn–up to flashover. In T. Wakamatsu, editor, *Fire Safety Science–Proceedings of the Second International Symposium*, pages 861–870. International Association for Fire Safety Science, Hemisphere Publishing Corporation, 1989.

[211] R. D. Pehrson and J. R. Barnett. Who's Right? TASCflow, FLOW3D, Phoenics, JASMINE or SOFIE. In *Proceedings of the ASC TASCflow International Users Conference*, Toronto, Canada, 1996.

[212] K. D. Steckler, J. G. Quintiere, and W. J. Rinkinen. Flow induced by fire in a compartment. Technical Report NBSIR 82-2520, NBS, September 1982.

[213] H. E. Nelson. *NFPA 92B Guide for Smoke Management Systems in Malls, Atria, and Large Areas.* National Fire Protection Association, 1995.

[214] G. Cox. Fire simulation in the design evaluation process: An exemplification of the use of a computer field model. In *INTERFLAM 90'*, Fire Research Station, Borehamwood, Herts WD6 2BL, 1990. Building Research Establishment.

[215] J. G. Sanchez. Using CFD for ventilation shaft design for fire conditions. In *SFPE and WPI Technical Symposium on Computer Applications in Fire Protection Engineering*, June 1996.

[216] R. Huhtanen. Numerical fire modelling of a turbine hall. In T. Wakamatsu, editor, *Fire Safety Science–Proceedings of the Second International Symposium*, pages 771–779. International Association for Fire Safety Science, Hemisphere Publishing Corporation, 1989.

[217] N. A. Hoffmann and E. R. Galea. An extension of the fire–field modelling technique to include fire–sprinkler interaction–I. the mathematical basis. *International Journal of Heat and Mass Transfer*, 36(6):1435–1444, 1993.

[218] N. A. Hoffmann and E. R. Galea. An extension of the fire–field modelling technique to include fire–sprinkler interaction–II. the simulations. *International Journal of Heat and Mass Transfer*, 36(6):1445–1457, 1993.

[219] G. H. Hadjisophocleous, S. Cao, and Kim A. Modelling the interaction between fine watersprays and a fire plume. *Advanced Computational Methods in Heat Transfer*, pages 239–249, 1995.

[220] R. N. Mawhinney, E. R. Galea, and M. K. Patel. Fire sprinkler spray interaction modelling using an Euler Lagrange approach. In *Conference Proceedings of the Seventh International Interflam Conference*, pages 841–845. Interscience Communications Limited, 1996.

[221] J. R. Mawhinney and G. V. Hadjisophocleous. The role of fire dynamics in design of water mist fire suppression systems. In *Conference Proceedings of the Seventh International Interflam Conference*, pages 415–424. Interscience Communications Limited, 1996.

[222] W. K. Chow and N. K. Fong. Numerical simulation on cooling of the fire-induced air flow by sprinkler water sprays. *Fire Safety Journal*, 17:263–290, 1991.

[223] S. Bard, K. H. Clow, and P. J. Pagni. Combustion of cellular urethane. *Combustion Science and Technology*, 19:141–150, 1979.

[224] D. Gross. Data sources for parameters used in predictive modeling of fire growth and smoke spread. Technical Report NBSIR 85-3223, NBS, 1985.

[225] H. G. Nadean. *Materials Bank Compendium of Fire Property Data*. Products Research Committee, February 1980.

[226] Patrick Van Hees. Personal communication. March, 1999.

[227] R. Alpert, A. Modak, and J Newman. The third full-scale bedroom fire test of the home fire project (July 30, 1975). Technical Report 21011.6, Factory Mutual Research, October 1975.

[228] W. D. Woolley. Are foams a fire hazard? In J. M. Buist, S. J. Grayson, and W. D. Woolley, editors, *Fire and Cellular Polymers*. Elsevier Applied Science, 1986.

[229] W. Becker, et al. *Fire Research on Cellular Plastics: The Final Report of the Products Research Committee*. Products Research Committee. J. W. Lyons, Chairman, April 1980.

# Appendix A

# Thermal Physical Properties

## A.1 Foam and Fabric Properties

| **Fuel** | **K** $\left(\frac{\mathbf{W}}{\mathbf{m\ K}}\right)$ | $\rho$ $\left(\frac{\mathbf{kg}}{\mathbf{m^3}}\right)$ | **C** $\left(\frac{\mathbf{J}}{\mathbf{kg\ K}}\right)$ | $\mathbf{k\rho c}$ $\left(\frac{\mathbf{W^2 s}}{\mathbf{m^4 K^2}}\right)$ | **Conditions** | **Source** |
|---|---|---|---|---|---|---|
| PU | 0.04 | 50 | 1700. | | 303 K | [224] |
| PU | | | 1884<br>1884<br>1842 | | 344 K<br>378 K<br>422 K | [227] |
| PU | 0.041-0.14 | 22-30 | 1600. | | | [228] |
| PU | | 29 | 1750.-1840. | 2264. | | [225, 2, 99] |

Table A.1: PU foam thermal properties

| **Fuel** | $\mathbf{T_{ign}}$ **(K)** | $\mathbf{q''_{crit}}$ $\left(\frac{\mathbf{kW}}{\mathbf{m^2}}\right)$ | $\mathbf{\Delta H_c}$ $\left(\frac{\mathbf{MJ}}{\mathbf{kg}}\right)$ | **Comments** | **Source** |
|---|---|---|---|---|---|
| PU | | | 27.6-28.2 | | [227, 229] |
| PU | 610-680 | | | | [141] |
| PU | | | 26.15 | Stoich AF=10.32<br>Stoich OF=2.16<br>$\chi_r = .64$ | [225] |
| PU | 720.-757. | | 23.2-28.0 | | [2, 99] |
| FRPU | | 11.0 | 24.0-25.0 | | [148, 2] |

Table A.2: PU foam combustion properties

| **Fabric** | **K** $(\frac{\mathbf{W}}{\mathbf{m\ K}})$ | $\rho$ $(\frac{\mathbf{kg}}{\mathbf{m^3}})$ | **C** $(\frac{\mathbf{J}}{\mathbf{kg\ K}})$ | **K$\rho$C** $\left(\frac{\mathbf{W^2 s}}{\mathbf{m^4 K^2}}\right)$ | **Conditions** | **Source** |
|---|---|---|---|---|---|---|
| cotton | k=k(T) | | 1.32 | | 0-100 $C$ | [90] |
| NFR cotton | | | | 1042. | | [99] |
| FR cotton | | | | 1287. | | [99] |
| NFR olefin | | | | 1042. | | [99] |
| FR olefin | | | | 1287. | | [99] |
| Wool neoprene | | | | 7046. | | [99] |
| Polypropylene | | 960. | | | | [135] |
| Nylon | | 1140. | | | | [135] |
| Acrylic | | 1170. | | | | [135] |
| Modacrylic | | 1350. | | | | [135] |
| Polyester | | 1340. | | | | [135] |
| Wool | | 1310. | | | | [135] |
| Cotton | | 1350. | | | | [135] |
| Rayon | | 1500. | | | | [135] |
| Kevlar | | 1440. | | | | [135] |

Table A.3: Fabric thermal properties

| **Fabric** | $\mathbf{T_{ign}}$ $(\mathbf{K})$ | **Stoich A/F Mass Ratio** | $\mathbf{\Delta H_c(net)}$ $(\frac{\mathbf{MJ}}{\mathbf{kg}})$ | **Comments** | **Source** |
|---|---|---|---|---|---|
| NFR cotton | 565. | | | | [99] |
| FR cotton | 575. | | | | [99] |
| NFR olefin | 605. | | | | [99] |
| FR olefin | 680. | | | | [99] |
| Wool neoprene | 635 . | | | | [99] |
| NFR PU/LO | 623. | | | $\sigma_s^e = 5060.$ | [21] |
| FR PU/LO | 711. | | | $\sigma_s^e = 4740.$ | [21] |
| FR PU/HO | 711. | | | $\sigma_s^e = 5300.$ | [21] |
| FR PU/LC | 590. | | | $\sigma_s^e = 3150.$ | [21] |
| NFR PU/HC | 580. | | | $\sigma_s^e = 4690.$ | [21] |
| FR PU/HC | 590. | | | $\sigma_s^e = 3150.$ | [21] |
| NP/LO | 583. | | | | [99] |
| cotton | | 9.79 | 24.6 | $\Delta H_f = -393.6 \frac{Kcal}{mole}$ | [224] |
| Polypropylene | 623-768 | | 46.5 | | [135] |
| Nylon | 663-783 | | 33.1 | | [135] |
| Acrylic | 738-773 | | 31.8 | | [135] |
| Polyester | 663-781 | | 23.9 | | [135] |
| Wool | 843-873 | | 20.5 | | [135] |
| Cotton | 523-533 | | 17.0 | | [135] |
| Rayon | 693-843 | | 17.0 | | [135] |

# Appendix B

# User Source Code Routines

## B.1 usrsrc.f

Applies source terms to conservation equations. Also contains main controlling routines for flame spread calculations

```
C     ^^^^^^^^^^^^^^^^^^^^^^^^^^^^^^^^^^^^^^^^
C     | FURNITURE CFD FIRE MODEL VERSION 1.0 |
C     |           JANUARY 5, 1999            |
C     ^^^^^^^^^^^^^^^^^^^^^^^^^^^^^^^^^^^^^^^^
C
C     Main routine to apply user modifiable source terms which permit
C     modeling full scale flame spread based on bench scale cone
C     calorimeter data.
C
C=======================================================================
C
      SUBROUTINE USRSRC (LABEL, IWK,   RWK, DWK, CWK, LWK,
     &                          NIBLK,NRBLK,NDWK,NCWK,NLWK,
     &                             IZ,   RZ,  DZ,  CZ,  LZ, ID,JD,KD)

CSCDB
C A description of the subroutine inputs is given below.
C
C Input:
C   LABEL : character string identifying equation solved:
C           ({SCALAR_NAME}, ENERGY, ENERGY_S, MOMENTUM)
C   IWK   : is the integer temporary workspace array
C   RWK   : is the real temporary workspace array
C   DWK   : is the double precision temporary workspace array
C   CWK   : is the character temporary workspace array
C   LWK   : is the logical temporary workspace array
C   NIBLK : is the integer temporary workspace no. of IDxJDxKD blocks
C   NRBLK : is the real temporary workspace no. of IDxJDxKD blocks
C   NDWK  : is the double precision temporary workspace
C   NCWK  : is the character temporary workspace
C   NLWK  : is the logical temporary workspace
C   IZ    : global integer array
C   RZ    : global real array
C   DZ    : global double precision array
C   CZ    : global character arra
C   LZ    : global logical array
C   ID,JD,KD : dummy computational domain dimensions

C Modified:

C Local:
```

```
C   ERCODE  : integer used for error identification (=0)
C   ERSTOP  : logical used to describe the appropriate action on error
C   VEC     : 3 element real array used in derivative calculations

CSCDE

C=======================================================================

C-------------------------
C Subroutine Arguments
C-------------------------

      REAL    RZ(*),RWK(ID,JD,KD,NRBLK),DTIME, STIME

      INTEGER IZ(*),IWK(ID,JD,KD,NIBLK),ID,JD,KD,NIBLK,NRBLK,
     &        NDWK,NCWK,NLWK
      INTEGER INP,JNP,KNP,ILNB,JLNB,KLNB,NCVM,NCVP,NPMAP,LPMAP
      integer IPG(4),NPG(8)

      LOGICAL LZ(*),LWK(NLWK)

      CHARACTER*(*) LABEL, CZ(*),CWK(NCWK)

      DOUBLE PRECISION DZ(*),DWK(NDWK)

C-------------------------
C Local Variables
C-------------------------

      include 'flame.com'

      REAL VEC(3),VUSRC,R,VU,sigmar
      real BNDFLO(100),bflowe(100),bflowf(100),bflowp(100)
      parameter (sigmar=5.67E-8)
      INTEGER X,Y,U,V
      INTEGER SRCU,SRCV,ACTU,ACTV
      INTEGER ERCODE,NR,NREG,I,J,K,IB,IE,JB,JE,KB,KE
      integer ntr4,nqrad,nsrc,nfloc,lenarr
      LOGICAL ERSTOP

      DATA VEC /3*0.0/

C----------------------------
C Common Blocks
C----------------------------

      COMMON/CONTRL/ IONUM(100),IARR(200),RARR(100),CONST(100),LARR(200)
      COMMON/MAPS/ INP(8),JNP(8),KNP(8),ILNB(7),JLNB(7),KLNB(7),
     &             NCVM(12),NCVP(12),NPMAP(12,8),LPMAP(8,8)
      INTEGER IONUM,IARR
      REAL RARR,CONST
      LOGICAL LARR

      EQUIVALENCE (CONST(2),DTIME),(RARR(24),STIME)

      PARAMETER (MAXMCF = 100)
      COMMON /COMBUS/ HENTHO(MAXMCF)

C-----------------------------------------------------------------------

C-------------------------
C Executable Statements
C-------------------------

c     #@#@#@#@#@#@#@#@#@#@#@#@#
c     BEGIN MAIN
c     #@#@#@#@#@#@#@#@#@#@#@#@#
```

```
C-----Have the code shut down on encountering an error.

      ERCODE = 0
      ERSTOP = .TRUE.

c-----Set initial values
      runtime=stime
      dt=dtime

c-----unit number of .out file
      nout=21

c-----Open summary output file, 'flame.sum'
      open (unit=2, file='flame.sum', status='old')

      call getpnt (nmass,'real',1,ercode,erstop)
      call getpnt (nmom,'real',2,ercode,erstop)
      call getpnt (ndens,'real',3,ercode,erstop)
      call getpnt (nfuel,'real',4,ercode,erstop)
      call getpnt (nx,'real',5,ercode,erstop)
      call getpnt (ny,'real',6,ercode,erstop)
      call getpnt (nz,'real',7,ercode,erstop)
      call getpnt (nt,'real',8,ercode,erstop)
      call getpnt (nts,'real',9,ercode,erstop)
      call getpnt (ncp,'real',10,ercode,erstop)
      call getpnt (ncv,'real',11,ercode,erstop)
      call getpnt (neng,'real',12,ercode,erstop)
      call getpnt (nsoot,'real',13,ercode,erstop)
      call getpnt (nfspent,'real',14,ercode,erstop)
      call getpnt (nprod,'real',15,ercode,erstop)

c-----Get the temporary workspace arrays
      call getrar ('density',rwk(1,1,1,ndens),rz,ercode,erstop)
      call getrar ('X',rwk(1,1,1,nx),rz,ercode,erstop)
      call getrar ('Y',rwk(1,1,1,ny),rz,ercode,erstop)
      call getrar ('Z',rwk(1,1,1,nz),rz,ercode,erstop)
      call getrar ('T',rwk(1,1,1,nt),rz,ercode,erstop)
      call getrar ('TS',rwk(1,1,1,nts),rz,ercode,erstop)
      call getrar ('SPECIFIC_HEAT_P',rwk(1,1,1,ncp),
     &              rz,ercode,erstop)
      call getrar ('SPECIFIC_HEAT_V',rwk(1,1,1,ncv),
     &              rz,ercode,erstop)
      call getrar ('FSPENT',RWK(1,1,1,nfspent),RZ,ERCODE,ERSTOP)

c-----Get pointer to octant control volumes (8)
      CALL MPTGET('QVOL','REAL',LENARR,MQVOL)

c-----Get pointer to control volume volumes (1)
      CALL MPTGET('CVOL','REAL',LENARR,MCVOL)

c-----Get pointer to ITYPHY
      CALL MPTGET('ITYPHY','INTEGER',LENARR,MTYPHY)

c-----Get pointer to fuel reacted by EBU model for a given iteration
      CALL MPTGET('FSPENT','REAL',LENARR,MFSPNT)

c-----Begin loop that is only visited once at the start of the run
      if (ivisit.ne.1) then
        timedif=-1.0
        ttsave=-1.0
c-------Open data input file
        open (unit=10, file='flame.dat', status='unknown')

c-------Open hrr input file
        open (unit=4, file='flame.hrr',status='old')
```

```
c-------Read in data from flame.hrr and flame.dat
        call datain

c-------Close file 'flame.hrr' and 'flame.dat'
        close (unit=4)
        close (unit=10)

c-------Open FE burning time output file, 'flame.out'
        open (unit=1, file='flame.out', status='unknown')

c-------Read in tmlost values from flame.out
        call datain2

c-------Close file 'flame.out'
        close (unit=1)

c-------Write flame spread model information to output file
        call header

c-------Save type for each node
        do 2 kf=1,kd
        do 2 jf=1,jd
        do 2 if=1,id
          NODES=(IF-1)+(JF-1)*ID+(KF-1)*ID*JD
          itypef(if,jf,kf)=iz(mtyphy+nodes)
          volcv(if,jf,kf)=rz(mcvol+nodes)
 2      continue

c-------Get global coordinates
        do 1 n=1,numsurf
          if (n .eq. 1) then
            call getgbl ('surf1',1,nsurf(n,1,1),nsurf(n,2,1),
     &        nsurf(n,1,2),nsurf(n,2,2),nsurf(n,1,3),nsurf(n,2,3),
     &        ercode,erstop)
            call srcvol ('surf1',svol,rz,iz,ercode,erstop)
            volsave(n)=svol
          else if (n .eq. 2) then
            call getgbl ('surf2',1,nsurf(n,1,1),nsurf(n,2,1),
     &        nsurf(n,1,2),nsurf(n,2,2),nsurf(n,1,3),nsurf(n,2,3),
     &        ercode,erstop)
            call srcvol ('surf2',svol,rz,iz,ercode,erstop)
            volsave(n)=svol
          else if (n .eq. 3) then
            call getgbl ('surf3',1,nsurf(n,1,1),nsurf(n,2,1),
     &        nsurf(n,1,2),nsurf(n,2,2),nsurf(n,1,3),nsurf(n,2,3),
     &        ercode,erstop)
            call srcvol ('surf3',svol,rz,iz,ercode,erstop)
            volsave(n)=svol
          else if (n .eq. 4) then
            call getgbl ('surf4',1,nsurf(n,1,1),nsurf(n,2,1),
     &        nsurf(n,1,2),nsurf(n,2,2),nsurf(n,1,3),nsurf(n,2,3),
     &        ercode,erstop)
            call srcvol ('surf4',svol,rz,iz,ercode,erstop)
            volsave(n)=svol
          else
            write (6,*) 'usrsrc.f error message 107'
            write (6,*) 'write more lines in usrsrc getgbl section'
            write (nout,*) 'usrsrc.f error message 107'
            write (nout,*) 'write more lines in usrsrc getgbl section'
          endif

c---------Save loop limits for surf
          IBF(n) = MIN(nsurf(n,1,1),nsurf(n,2,1))
          JBF(n) = MIN(nsurf(n,1,2),nsurf(n,2,2))
          KBF(n) = MIN(nsurf(n,1,3),nsurf(n,2,3))
          IEF(n) = MAX(nsurf(n,1,1),nsurf(n,2,1))
          JEF(n) = MAX(nsurf(n,1,2),nsurf(n,2,2))
```

```
          KEF(n) = MAX(nsurf(n,1,3),nsurf(n,2,3))
 1      continue

c-------Evaluate allignment of surfaces
        do 5 n=1,numsurf

          dxs1=abs((rwk(nsurf(n,2,1),nsurf(n,1,2),nsurf(n,1,3),nx))-
     &             (rwk(nsurf(n,1,1),nsurf(n,1,2),nsurf(n,1,3),nx)))
          dxs2=abs((rwk(nsurf(n,1,1),nsurf(n,2,2),nsurf(n,1,3),nx))-
     &             (rwk(nsurf(n,1,1),nsurf(n,1,2),nsurf(n,1,3),nx)))
          dxs3=abs((rwk(nsurf(n,1,1),nsurf(n,1,2),nsurf(n,2,3),nx))-
     &             (rwk(nsurf(n,1,1),nsurf(n,1,2),nsurf(n,1,3),nx)))
          dys1=abs((rwk(nsurf(n,2,1),nsurf(n,1,2),nsurf(n,1,3),ny))-
     &             (rwk(nsurf(n,1,1),nsurf(n,1,2),nsurf(n,1,3),ny)))
          dys2=abs((rwk(nsurf(n,1,1),nsurf(n,2,2),nsurf(n,1,3),ny))-
     &             (rwk(nsurf(n,1,1),nsurf(n,1,2),nsurf(n,1,3),ny)))
          dys3=abs((rwk(nsurf(n,1,1),nsurf(n,1,2),nsurf(n,2,3),ny))-
     &             (rwk(nsurf(n,1,1),nsurf(n,1,2),nsurf(n,1,3),ny)))
          dzs1=abs((rwk(nsurf(n,2,1),nsurf(n,1,2),nsurf(n,1,3),nz))-
     &             (rwk(nsurf(n,1,1),nsurf(n,1,2),nsurf(n,1,3),nz)))
          dzs2=abs((rwk(nsurf(n,1,1),nsurf(n,2,2),nsurf(n,1,3),nz))-
     &             (rwk(nsurf(n,1,1),nsurf(n,1,2),nsurf(n,1,3),nz)))
          dzs3=abs((rwk(nsurf(n,1,1),nsurf(n,1,2),nsurf(n,2,3),nz))-
     &             (rwk(nsurf(n,1,1),nsurf(n,1,2),nsurf(n,1,3),nz)))

c---------Evaluate allignment of surface

          if ((dxs1.gt.dys1).and.(dxs1.gt.dzs1)) then
            ngxyzs(n,1)=1
          else if ((dys1.gt.dxs1).and.(dys1.gt.dzs1)) then
            ngxyzs(n,1)=2
          else if ((dzs1.gt.dxs1).and.(dzs1.gt.dys1)) then
            ngxyzs(n,1)=3
          else
            write (6,*) 'usrsrc.f error message 108'
            write (6,*) 'error determining surface allignment'
            write (nout,*) 'usrsrc.f error message 108'
            write (nout,*) 'error determining surface allignment'
          endif
          if ((dxs2.gt.dys2).and.(dxs2.gt.dzs2)) then
            ngxyzs(n,2)=1
          else if ((dys2.gt.dxs2).and.(dys2.gt.dzs2)) then
            ngxyzs(n,2)=2
          else if ((dzs2.gt.dxs2).and.(dzs2.gt.dys2)) then
            ngxyzs(n,2)=3
          else
            write (6,*) 'usrsrc.f error message 109'
            write (6,*) 'error determining surface allignment'
            write (nout,*) 'usrsrc.f error message 109'
            write (nout,*) 'error determining surface allignment'
          endif
          if ((dxs3.gt.dys3).and.(dxs3.gt.dzs3)) then
            ngxyzs(n,3)=1
          else if ((dys3.gt.dxs3).and.(dys3.gt.dzs3)) then
            ngxyzs(n,3)=2
          else if ((dzs3.gt.dxs3).and.(dzs3.gt.dys3)) then
            ngxyzs(n,3)=3
          else
            write (6,*) 'usrsrc.f error message 110'
            write (6,*) 'error determining surface allignment'
            write (nout,*) 'usrsrc.f error message 110'
            write (nout,*) 'error determining surface allignment'
          endif

c---------Determine direction for surfaces
c         See if distance is increasing in same direction as global coord.
          distdif(n)=0.0
```

```
      do 6 ii=1,3
        ip(1)=ibf(n)
        ip(2)=jbf(n)
        ip(3)=kbf(n)
        if ((ngxyzs(n,ii).eq.1).and.((nfeor(n).eq.1).or.
&           (nfeor(n).eq.2))) then
          ip(ii)=ip(ii)+1
          distdif(n)=rwk(ip(1),ip(2),ip(3),nx)-
&                    rwk(ibf(n),jbf(n),kbf(n),nx)
          if (distdif(n).gt.0.0) then
            if (nfeor(n).eq.1) then
              nfegb(n)=2*ii-1
            else if (nfeor(n).eq.2) then
              nfegb(n)=2*ii
            endif
          else if (distdif(n).lt.0.0) then
            if (nfeor(n).eq.1) then
              nfegb(n)=2*ii
            else if (nfeor(n).eq.2) then
              nfegb(n)=2*ii-1
            endif
          else
            write (6,*) 'usrsrc.f error number 111'
            write (6,*) 'error setting global orientation'
            write (nout,*) 'usrsrc.f error number 111'
            write (nout,*) 'error setting global orientation'
          endif
        else if ((ngxyzs(n,ii).eq.2).and.((nfeor(n).eq.3).or.
&           (nfeor(n).eq.4))) then
          ip(ii)=ip(ii)+1
          distdif(n)=rwk(ip(1),ip(2),ip(3),ny)-
&                    rwk(ibf(n),jbf(n),kbf(n),ny)
          if (distdif(n).gt.0.0) then
            if (nfeor(n).eq.3) then
              nfegb(n)=2*ii-1
            else if (nfeor(n).eq.4) then
              nfegb(n)=2*ii
            endif
          else if (distdif(n).lt.0.0) then
            if (nfeor(n).eq.3) then
              nfegb(n)=2*ii
            else if (nfeor(n).eq.4) then
              nfegb(n)=2*ii-1
            endif
          else
            write (6,*) 'usrsrc.f error number 112'
            write (6,*) 'error setting global orientation'
            write (nout,*) 'usrsrc.f error number 112'
            write (nout,*) 'error setting global orientation'
          endif
        else if ((ngxyzs(n,ii).eq.3).and.((nfeor(n).eq.5).or.
&           (nfeor(n).eq.6))) then
          ip(ii)=ip(ii)+1
          distdif(n)=rwk(ip(1),ip(2),ip(3),nz)-
&                    rwk(ibf(n),jbf(n),kbf(n),nz)
          if (distdif(n).gt.0.0) then
            if (nfeor(n).eq.5) then
              nfegb(n)=2*ii-1
            else if (nfeor(n).eq.6) then
              nfegb(n)=2*ii
            endif
          else if (distdif(n).lt.0.0) then
            if (nfeor(n).eq.5) then
              nfegb(n)=2*ii
            else if (nfeor(n).eq.6) then
              nfegb(n)=2*ii-1
            endif
```

```
              else
                write (6,*) 'usrsrc.f error number 113'
                write (6,*) 'error setting global orientation'
                write (nout,*) 'usrsrc.f error number 113'
                write (nout,*) 'error setting global orientation'
              endif
            endif
 6        continue

c---------Check to see that surface index numbers are unique
          if ((ngxyzs(n,1).eq.ngxyzs(n,2)).or.
     &        (ngxyzs(n,1).eq.ngxyzs(n,3)).or.
     &        (ngxyzs(n,2).eq.ngxyzs(n,3)).or.
     &        (ngxyzs(n,1).eq.0).or.(ngxyzs(n,2).eq.0).or.
     &        (ngxyzs(n,3).eq.0)) then
            write (6,*) 'usrsrc.f error message 114'
            write (6,*) 'surface index numbers not unique'
            write (nout,*) 'usrsrc.f error message 114'
            write (nout,*) 'surface index numbers not unique'
          endif
 5      continue

c-------Determine location of top solid FE for application of energy
c       source term to solid representing Lv
        do 7 n=1,numsurf
          ipp(1)=ibf(n)
          ipp(2)=jbf(n)
          ipp(3)=kbf(n)
          ipp(4)=ief(n)
          ipp(5)=jef(n)
          ipp(6)=kef(n)
          if (nfegb(n).eq.1) then
            ipp(4)=ibf(n)
            ipp(1)=ibf(n)-1
          else if (nfegb(n).eq.2) then
            ipp(1)=ief(n)
            ipp(4)=ief(n)+1
          else if (nfegb(n).eq.3) then
            ipp(5)=jbf(n)
            ipp(2)=jbf(n)-1
          else if (nfegb(n).eq.4) then
            ipp(2)=jef(n)
            ipp(5)=jef(n)+1
          else if (nfegb(n).eq.5) then
            ipp(6)=kbf(n)
            ipp(3)=kbf(n)-1
          else if (nfegb(n).eq.6) then
            ipp(3)=kef(n)
            ipp(6)=kef(n)+1
          endif
            nsolid(n,1,1)=ipp(1)
            nsolid(n,1,2)=ipp(2)
            nsolid(n,1,3)=ipp(3)
            nsolid(n,2,1)=ipp(4)
            nsolid(n,2,2)=ipp(5)
            nsolid(n,2,3)=ipp(6)
 7      continue

c-------Calculate FE volumes with QVOL
        do 8 kf=1,kd-1
        do 8 jf=1,jd-1
        do 8 if=1,id-1
          fevol(if,jf,kf)=0.0
        do 8 np=1,8
          NODES=((IF-1)+(JF-1)*ID+(KF-1)*ID*JD)+(np-1)*id*jd*kd
          fevol(if,jf,kf)=fevol(if,jf,kf)+rz(mqvol+NODES)
 8      continue
```

```
        do 9 n=1,numsurf
        volusum(n)=0.0
        do 9 kf=kbf(n),kef(n)-1
        do 9 jf=jbf(n),jef(n)-1
        do 9 if=ibf(n),ief(n)-1
          volusum(n)=volusum(n)+fevol(if,jf,kf)
          if (fevol(if,jf,kf).le.0.0) then
            write (6,*) 'usrsrc.f error message 115'
            write (6,*) 'QVOL.le.0.0',n,if,jf,kf,fevol(if,jf,kf)
            write (nout,*) 'usrsrc.f error message 115'
            write (nout,*) 'QVOL.le.0.0',n,if,jf,kf,fevol(if,jf,kf)
          endif
 9      continue

        do 10 n=1,numsurf
          nfloc=nfegb(n)
          areasum(n)=0.0
          do 20 kf=kbf(n),kef(n)-1
          do 20 jf=jbf(n),jef(n)-1
          do 20 if=ibf(n),ief(n)-1
            CALL BFAREA(RZ,IZ,DZ,CZ,LZ,BFACE,NFLOC,
     &                  IF,JF,KF,ID,JD,KD)
            fearea(n,if,jf,kf)=bface
            areasum(n)=areasum(n)+bface
 20       continue

c---------Compare results
          write (6,901) ' ==> Region coordinates for surf',n,': [',
     &         nsurf(n,1,1),':',nsurf(n,2,1),',',
     &         nsurf(n,1,2),':',nsurf(n,2,2),',',
     &         nsurf(n,1,3),':',nsurf(n,2,3),']'
          write (nout,901) ' ==> Region coordinates for surf',n,': [',
     &         nsurf(n,1,1),':',nsurf(n,2,1),',',
     &         nsurf(n,1,2),':',nsurf(n,2,2),',',
     &         nsurf(n,1,3),':',nsurf(n,2,3),']'
          write (6,901) ' ==> Region coordinates for solid',n,': [',
     &         nsolid(n,1,1),':',nsolid(n,2,1),',',
     &         nsolid(n,1,2),':',nsolid(n,2,2),',',
     &         nsolid(n,1,3),':',nsolid(n,2,3),']'
          write (nout,901) ' ==> Region coordinates for solid',n,': [',
     &         nsolid(n,1,1),':',nsolid(n,2,1),',',
     &         nsolid(n,1,2),':',nsolid(n,2,2),',',
     &         nsolid(n,1,3),':',nsolid(n,2,3),']'
 901      format (A,I1,A,I2,A,I2,A,I2,A,I2,A,I2,A,I2,A)
          write (6,903) '     Area for surf',n,':',areasum(n),'m^2'
          write (6,903) '     Volume for surf',n,':',volusum(n),
     &                  'm^3'
          write (nout,903) '     Area for surf',n,':',areasum(n),'m^2'
          write (nout,903) '     Volume for surf',n,':',volusum(n),
     &                  'm^3'
 903      format (A,I1,A,E12.5, 1x, a)
          if ((volusum(n).lt.(0.999*volsave(n))).or.
     &        (volusum(n).gt.(1.001*volsave(n)))) then
            write (6,*) ' '
            write (6,*) 'usrsrc.f error message 116'
            write (6,*) 'the difference between the region volume'
            write (6,*) 'calculated in qvol and that from'
            write (6,*) 'srcvol is greater than .1%'
            write (6,*) n,volusum(n),volsave(n)
            write (6,*) ' '
            write (nout,*) ' '
            write (nout,*) 'usrsrc.f error message 116'
            write (nout,*) 'the difference between the region volume'
            write (nout,*) 'calculated in qvol and that from'
            write (nout,*) 'srcvol is greater than .1%'
            write (nout,*) n,volusum(n),volsave(n)
            write (nout,*) ' '
```

```
          endif
 10     continue
        write (6,*) ' '
        write (6,*) '#$##$##$##$  End Fire Growth Input Summary ',
     &              '#$##$##$##$'
        write (6,*) '*****************************************',
     &              '**********'
        write (6,*) ' '
        write (nout,*) ' '
        write (nout,*) '#$##$##$##$  End Fire Growth Input Summary ',
     &              '#$##$##$##$'
        write (nout,*) '*****************************************',
     &              '**********'
        write (nout,*) ' '
        ivisit=1
       endif

c-----Calculate the mass loss rates at the start of each outer loop iteration

      if (runtime.ne.timedif) then

        if (LABEL.EQ.'MASS') then

c---------Calculate mass, momentum and energy source terms at the start
c         of each iteration (outter loop)

          open (unit=3, file='flame.out.tmp', status='unknown')

          write (6,*) '**************************************',
     &                '**************'
          write (6,*) '#$##$##$##$   Fire Growth Routine Running   ',
     &                '#$##$##$##$'
          write (nout,*) '**************************************',
     &                '**************'
          write (nout,*) '#$##$##$##$   Fire Growth Routine Running   ',
     &                '#$##$##$##$'

         symdot=0.0
         smdot=0.0
         hcymdot=0.0
         hcmdot=0.0
         do 40 n=1,numsurf
            ncntma(n)=0
            burnarea(n)=0.0
            nfloc=nfegb(n)

c-----------Evaluate FE average solid temperature for igntion determination
            do 42 kk=kbf(n),kef(n)-1
            do 42 jj=jbf(n),jef(n)-1
            do 42 ii=ibf(n),ief(n)-1
              if (nfegb(n).eq.1) then
                ttest=(rwk(ibf(n),jj,kk,nts)+
     &                 rwk(ibf(n),jj+1,kk,nts)+
     &                 rwk(ibf(n),jj,kk+1,nts)+
     &                 rwk(ibf(n),jj+1,kk+1,nts))/4.0
              else if (nfegb(n).eq.2) then
                ttest=(rwk(ief(n),jj,kk,nts)+
     &                 rwk(ief(n),jj+1,kk,nts)+
     &                 rwk(ief(n),jj,kk+1,nts)+
     &                 rwk(ief(n),jj+1,kk+1,nts))/4.0
              else if (nfegb(n).eq.3) then
                ttest=(rwk(ii,jbf(n),kk,nts)+
     &                 rwk(ii+1,jbf(n),kk,nts)+
     &                 rwk(ii,jbf(n),kk+1,nts)+
     &                 rwk(ii+1,jbf(n),kk+1,nts))/4.0
              else if (nfegb(n).eq.4) then
                ttest=(rwk(ii,jef(n),kk,nts)+
```

```
     &                rwk(ii+1,jef(n),kk,nts)+
     &                rwk(ii,jef(n),kk+1,nts)+
     &                rwk(ii+1,jef(n),kk+1,nts))/4.0
               else if (nfegb(n).eq.5) then
                 ttest=(rwk(ii,jj,kbf(n),nts)+
     &                rwk(ii+1,jj,kbf(n),nts)+
     &                rwk(ii,jj+1,kbf(n),nts)+
     &                rwk(ii+1,jj+1,kbf(n),nts))/4.0
               else if (nfegb(n).eq.6) then
                 ttest=(rwk(ii,jj,kef(n),nts)+
     &                rwk(ii+1,jj,kef(n),nts)+
     &                rwk(ii,jj+1,kef(n),nts)+
     &                rwk(ii+1,jj+1,kef(n),nts))/4.0
               endif

               if (ttest.le.0.0) then
                 write (6,*) 'usrsrc.f error 117'
                 write (6,*) 'There appears to be an error in the'
                 write (6,*) 'solid temperature averaging for'
                 write (6,*) 'ignition evaluation'
                 write (nout,*) 'usrsrc.f error 117'
                 write (nout,*) 'There appears to be an error in the'
                 write (nout,*) 'solid temperature averaging for'
                 write (nout,*) 'ignition evaluation'
               endif

c--------------Evaluate FE flux level for igntion
               call BFQRAD(RZ,IZ,DZ,CZ,LZ,
     &                    QRAD,NFLOC,II,JJ,KK,ID,JD,KD)
               feflux(n,ii,jj,kk)=qrad

c--------------Only update source terms for FE's that are above the
c              igntion temperature, above the flux level for igntion
c              or are already ignited (already following cone curve)
               if ((ttest.ge.tign).or.(tmlost(n,ii,jj,kk).gt.0.0).or.
     &              (feflux(n,ii,jj,kk).ge.fign)) then
                 ncntma(n)=ncntma(n)+1
                 burnarea(n)=burnarea(n)+fearea(n,ii,jj,kk)
c----------------obtain mass loss rate based on flux and total mass lost
                 tmin=tmlost(n,ii,jj,kk)
                 call polint(tmin,pout,syield,hcomb)
                 pdot=pout*fearea(n,ii,jj,kk)
c----------------save total mass lost by each FE
c                tmlost is on a per meter square basis
                 tmlost(n,ii,jj,kk)=tmlost(n,ii,jj,kk)+pout*dt
                 prate(n,ii,jj,kk)=pdot/(fevol(ii,jj,kk))
c----------------calculate momentum source, pvel
                 pvel(n,ii,jj,kk)=(pdot*pdot)/(rhofuel
     &                        *fearea(n,ii,jj,kk)*fevol(ii,jj,kk))
c----------------calculate soot source, psoot
                 symdot=symdot+syield*pdot
                 smdot=smdot+pdot
c----------------calculte heat of combustion source, hcomb
                 hcymdot=hcymdot+hcomb*pdot
                 hcmdot=hcmdot+pdot

c----------------calculate energy source using pyrolysis temperature
                 if (ttest.lt.tign) then
                   tengin=tign
                 else
                   tengin=ttest
                 endif
                 peng(n,ii,jj,kk)=rwk(ii,jj,kk,ncp)*
     &                       (tengin-303.)*pdot/fevol(ii,jj,kk)
c                 write (6,905) 'brn#',ncntma(n),ii,jj,kk,ttest,
c     &             feflux(n,ii,jj,kk),pout,
c     &             tmlost(n,ii,jj,kk),syield,hcomb
```

```
 905         format (a,4(i3),f8.3,5(1x,E10.4))

c---------------calculate the energy change due to pyrolysis
                pengs(n,ii,jj,kk)=hevap*pdot
c---------------send total mass lost to flame.out file
                write (3,*) n,ii,jj,kk,tmlost(n,ii,jj,kk)
                else
                  prate(n,ii,jj,kk)=0.0
                  pvel(n,ii,jj,kk)=0.0
                  peng(n,ii,jj,kk)=0.0
                endif
 42           continue
              write (6,907) '==> Number of burning FE on surf', n, ':',
     &                    ncntma(n)
              write (nout,907) '==> Number of burning FE on surf', n,
     &                  ':', ncntma(n)
 907          format (1x, a, i1, a, i5)
              if (areasum(n).gt.0.0) then
                write (6,909) 'Area of burning FE:',
     &                        burnarea(n), 'm^2 (',
     &                        100.0*burnarea(n)/areasum(n),
     &                        '% of surface)'
                write (nout,909) 'Area of burning FE:',
     &                        burnarea(n), 'm^2 (',
     &                        100.0*burnarea(n)/areasum(n),
     &                        '% of surface)'
              else
                write (6,*) 'Area of burning FE: 0.0 m^2 (0% of surface)'
                write (nout,*) 'Area of burning FE: 0.0 m^2',
     &                        '(0% of surface)'
              endif
 909          format (5x, a, f10.7, 1x, a, f7.2, a)
              if (n.eq.numsurf) then
                write (3,*) -999, -999, -999, -999, -999.
              endif
 40         continue

            if (smdot.le.0.0) then
              syave=.01
              write (6,*) 'resetting syave',syave
            else
              syave=symdot/smdot
            endif
            if (hcmdot.le.0.0) then
              hcave=10300000.
              write (6,*) 'resetting hcave',hcave
            else
              hcave=hcymdot/hcmdot
            endif
            write (6,*) 'syave',symdot,smdot,syave
            write (6,*) 'hcyave',hcymdot,hcmdot,hcave
            write (6,*) '#$##$##$##$## End Fire Growth Routine Summary ',
     &                  '#$##$##$##$#'
            write (6,*) '**************************************',
     &                  '**************'
            write (nout,*) '#$##$##$##$## End Fire Growth Routine Summary ',
     &                  '#$##$##$##$#'
            write (nout,*) '**************************************',
     &                  '**************'
            close (unit=3)

            timedif=runtime
          endif

c-----Now end the loop visited at the start of each outter loop iteration
        endif
```

```
c-----Start loop that is visited at the start of each inner loop iteration

      do 50 n=1,numsurf
c-----Apply source terms for every iteration (inner and outter)

        if (LABEL.EQ.'MASS') then
          do 52 kk=kbf(n),kef(n)-1
          do 52 jj=jbf(n),jef(n)-1
          do 52 ii=ibf(n),ief(n)-1
            do 54 nk=kk,kk+1
            do 54 nj=jj,jj+1
            do 54 ni=ii,ii+1
              rwk(ni,nj,nk,nmass)=prate(n,ii,jj,kk)
 54         continue
            call putsrc ('MASS',rwk(1,1,1,nmass),rz,
     &                   ii,ii+1,jj,jj+1,kk,kk+1,ercode,erstop)
            do 56 nk=kk,kk+1
            do 56 nj=jj,jj+1
            do 56 ni=ii,ii+1
              rwk(ni,nj,nk,nmass)=0.0
 56         continue
 52       continue

        else if (LABEL.EQ.'FUEL') then
          ncntfu=ncntfu+1
          do 62 kk=kbf(n),kef(n)-1
          do 62 jj=jbf(n),jef(n)-1
          do 62 ii=ibf(n),ief(n)-1
            do 64 nk=kk,kk+1
            do 64 nj=jj,jj+1
            do 64 ni=ii,ii+1
              rwk(ni,nj,nk,nfuel)=prate(n,ii,jj,kk)
 64         continue
            call putsrc ('FUEL',rwk(1,1,1,nfuel),rz,
     &                  ii,ii+1,jj,jj+1,kk,kk+1,ercode,erstop)
            do 66 nk=kk,kk+1
            do 66 nj=jj,jj+1
            do 66 ni=ii,ii+1
              rwk(ni,nj,nk,nfuel)=0.0
 66         continue
 62       continue

        ELSE IF (LABEL.EQ.'MOMENTUM') THEN

c         set enthalpies to give transient heat of combustion
          henth0(1)=hcave
          henth0(2)=0.0
          henth0(3)=0.0
          henth0(4)=0.0
          henth0(5)=0.0


c---------write HRR to output file for each iteration
          if (n.eq.1) then
            BFLOWE(1) = 0.0
            CALL STORSC('ENERGY','EBUCOMB',BFLOWE(1),2,NERR1)
            IF (NERR1.EQ.0) THEN
              write (6,*) 'EBU Energy',bflowe(1)
              write (nout,*) 'EBU Energy',bflowe(1)
c              WRITE(ITRM,*) ' Calculated heat release ',BNDFLO(1)
c              WRITE(IOUT,*) ' Calculated heat release ',BNDFLO(1)
            ENDIF
            BFLOWF(1) = 0.0
            CALL STORSC('FUEL','EBUCOMB',BFLOWF(1),2,NERR1)
            IF (NERR1.EQ.0) THEN
              write (6,*) 'EBU Fuel',bflowf(1)
              write (nout,*) 'EBU Fuel',bflowf(1)
```

```
c              WRITE(ITRM,*) ' Calculated heat release ',BNDFLO(1)
c              WRITE(IOUT,*) ' Calculated heat release ',BNDFLO(1)
            ENDIF
            BFLOWP(1) = 0.0
            CALL STORSC('PROD','EBUCOMB',BFLOWP(1),2,NERR1)
            IF (NERR1.EQ.0) THEN
              write (6,*) 'EBU Prod',bflowp(1)
              write (nout,*) 'EBU Prod',bflowp(1)
            ENDIF

            if (ttsave.ne.stime) then
              if ((burnarea(1).gt.0.0).and.(areasum(1).gt.0.0)) then
                ttba(1)=100.0*burnarea(1)/areasum(1)
              else
                ttba(1)=0.0
              endif
              if ((burnarea(2).gt.0.0).and.(areasum(2).gt.0.0)) then
                ttba(2)=100.0*burnarea(2)/areasum(2)
              else
                ttba(2)=0.0
              endif
              if ((burnarea(3).gt.0.0).and.(areasum(3).gt.0.0)) then
                ttba(3)=100.0*burnarea(3)/areasum(3)
              else
                ttba(3)=0.0
              endif
              if ((burnarea(4).gt.0.0).and.(areasum(4).gt.0.0)) then
                ttba(4)=100.0*burnarea(4)/areasum(4)
              else
                ttba(4)=0.0
              endif

              write (2,960)  stime,bflowe(1),-bflowf(1),smdot,
     &                       ttba(1),ttba(2),ttba(3),ttba(4)
              ttsave=stime
 960          format (f7.3,3(1x,e11.4),4(1x,f7.2))
            endif
          endif
          ncntmo=ncntmo+1
          do 72 kk=kbf(n),kef(n)-1
          do 72 jj=jbf(n),jef(n)-1
          do 72 ii=ibf(n),ief(n)-1
            do 74 nk=kk,kk+1
            do 74 nj=jj,jj+1
            do 74 ni=ii,ii+1
              if ((nfeor(n).eq.1).or.(nfeor(n).eq.3).or.
     &            (nfeor(n).eq.5)) then
                rwk(ni,nj,nk,nmom)=pvel(n,ii,jj,kk)
              else if ((nfeor(n).eq.2).or.(nfeor(n).eq.4).or.
     &                 (nfeor(n).eq.6)) then
                rwk(ni,nj,nk,nmom)=-pvel(n,ii,jj,kk)
              else
                write (6,*) 'usrsrc.f error message 122'
                write (6,*) 'no unique momentum vector'
                write (nout,*) 'usrsrc.f error message 122'
                write (nout,*) 'no unique momentum vector'
              endif
 74         continue

            if ((nfeor(n).eq.1).or.(nfeor(n).eq.2)) then
                call putsrc ('U',rwk(1,1,1,nmom),rz,
     &                       ii,ii+1,jj,jj+1,kk,kk+1,ercode,erstop)
            else if ((nfeor(n).eq.3).or.(nfeor(n).eq.4)) then
                call putsrc ('V',rwk(1,1,1,nmom),rz,
     &                       ii,ii+1,jj,jj+1,kk,kk+1,ercode,erstop)
            else if ((nfeor(n).eq.5).or.(nfeor(n).eq.6)) then
                call putsrc ('W',rwk(1,1,1,nmom),rz,
```

```
     &                        ii,ii+1,jj,jj+1,kk,kk+1,ercode,erstop)
           endif

           do 76 nk=kk,kk+1
           do 76 nj=jj,jj+1
           do 76 ni=ii,ii+1
             rwk(ni,nj,nk,nmom)=0.0
 76        continue
 72       continue

        else if (LABEL.EQ.'ENERGY') then
c---------add energy source term representing internal energy of fuel
          do 81 kk=kbf(n),kef(n)-1
          do 81 jj=jbf(n),jef(n)-1
          do 81 ii=ibf(n),ief(n)-1
            do 82 nk=kk,kk+1
            do 82 nj=jj,jj+1
            do 82 ni=ii,ii+1
              rwk(ni,nj,nk,neng)=peng(n,ii,jj,kk)
 82         continue
            do 83 nk=kk,kk+1
            do 83 nj=jj,jj+1
            do 83 ni=ii,ii+1
              rwk(ii,jj,kk,neng)=0.0
 83        continue
 81      continue

        else if (LABEL.EQ.'ENERGY_S') then

c---------Evaluate FE average solid temperature for igntion determination
          do 130 kk=kbf(n),kef(n)-1
          do 130 jj=jbf(n),jef(n)-1
          do 130 ii=ibf(n),ief(n)-1
            if (nfegb(n).eq.1) then
              ttest1=(rwk(ibf(n),jj,kk,nts)+
     &              rwk(ibf(n),jj+1,kk,nts)+
     &              rwk(ibf(n),jj,kk+1,nts)+
     &              rwk(ibf(n),jj+1,kk+1,nts))/4.0
              if (ttest1.gt.tign) then
                do 131 nk=kk,kk+1
                do 131 nj=jj,jj+1
                  rwk(ibf(n),nj,nk,neng)=-(ttest1-tign)*1884.*20.
     &               -pengs(n,ibf(n),jj,kk)/fevol(ibf(n),jj,kk)
                  rwk(ibf(n)-1,nj,nk,neng)=0.0
 131            continue
                call putsrc ('ENERGY_S',rwk(1,1,1,neng),rz,
     &            ibf(n)-1,ibf(n),jj,jj+1,kk,kk+1,ercode,erstop)
              else if ((ttest1.lt.tign).and.
     &                 (tmlost(n,ibf(n),jj,kk).gt.0.0)) then
                do 132 nk=kk,kk+1
                do 132 nj=jj,jj+1
                  rwk(ibf(n),nj,nk,neng)=-.5*(ttest1-tign)*1884.*20.
                  rwk(ibf(n)-1,nj,nk,neng)=-.5*(ttest1-tign)*1884.*20.
 132            continue
                call putsrc ('ENERGY_S',rwk(1,1,1,neng),rz,
     &            ibf(n)-1,ibf(n),jj,jj+1,kk,kk+1,ercode,erstop)
              endif
              do 133 nk=kk,kk+1
              do 133 nj=jj,jj+1
                rwk(ibf(n),nj,nk,neng)=0.0
                rwk(ibf(n)-1,nj,nk,neng)=0.0
 133          continue

            else if (nfegb(n).eq.2) then

              ttest1=(rwk(ief(n),jj,kk,nts)+
     &              rwk(ief(n),jj+1,kk,nts)+
```

```
     &              rwk(ief(n),jj,kk+1,nts)+
     &              rwk(ief(n),jj+1,kk+1,nts))/4.0

               if (ttest1.gt.tign) then
                 do 134 nk=kk,kk+1
                 do 134 nj=jj,jj+1
                   rwk(ief(n),nj,nk,neng)=-(ttest1-tign)*1884.*20.
     &               -pengs(n,ief(n),jj,kk)/fevol(ief(n),jj,kk)
                   rwk(ief(n)+1,nj,nk,neng)=0.0
 134             continue
                 call putsrc ('ENERGY_S',rwk(1,1,1,neng),rz,
     &             ief(n),ief(n)+1,jj,jj+1,kk,kk+1,ercode,erstop)
               else if ((ttest1.lt.tign).and.
     &                (tmlost(n,ief(n),jj,kk).gt.0.0)) then
                 do 135 nk=kk,kk+1
                 do 135 nj=jj,jj+1
                   rwk(ief(n),nj,nk,neng)=-.5*(ttest1-tign)*1884.*20.
                   rwk(ief(n)+1,nj,nk,neng)=-.5*(ttest1-tign)*1884.*20.
 135             continue
                 call putsrc ('ENERGY_S',rwk(1,1,1,neng),rz,
     &             ief(n),ief(n)+1,jj,jj+1,kk,kk+1,ercode,erstop)
               endif
               do 136 nk=kk,kk+1
               do 136 nj=jj,jj+1
                 rwk(ief(n),nj,nk,neng)=0.0
                 rwk(ief(n)+1,nj,nk,neng)=0.0
 136           continue

             else if (nfegb(n).eq.3) then

               ttest1=(rwk(ii,jbf(n),kk,nts)+
     &              rwk(ii+1,jbf(n),kk,nts)+
     &              rwk(ii,jbf(n),kk+1,nts)+
     &              rwk(ii+1,jbf(n),kk+1,nts))/4.0

               if (ttest1.gt.tign) then
                 do 137 nk=kk,kk+1
                 do 137 ni=ii,ii+1
                   rwk(ni,jbf(n),nk,neng)=-(ttest1-tign)*1884.*20.
     &               -pengs(n,ii,jbf(n),kk)/fevol(ii,jbf(n),kk)
                   rwk(ni,jbf(n)-1,nk,neng)=0.0
 137             continue
                 call putsrc ('ENERGY_S',rwk(1,1,1,neng),rz,
     &             ii,ii+1,jbf(n)-1,jbf(n),kk,kk+1,ercode,erstop)
               else if ((ttest1.lt.tign).and.
     &                (tmlost(n,ii,jbf(n),kk).gt.0.0)) then
                 do 138 nk=kk,kk+1
                 do 138 ni=ii,ii+1
                   rwk(ni,jbf(n),nk,neng)=-.5*(ttest1-tign)*1884.*20.
                   rwk(ni,jbf(n)-1,nk,neng)=-.5*(ttest1-tign)*1884.*20.
 138             continue
                 call putsrc ('ENERGY_S',rwk(1,1,1,neng),rz,
     &             ii,ii+1,jbf(n)-1,jbf(n),kk,kk+1,ercode,erstop)
               endif
               do 139 nk=kk,kk+1
               do 139 ni=ii,ii+1
                 rwk(ni,jbf(n),nk,neng)=0.0
                 rwk(ni,jbf(n)-1,nk,neng)=0.0
 139           continue

             else if (nfegb(n).eq.4) then

               ttest1=(rwk(ii,jef(n),kk,nts)+
     &              rwk(ii+1,jef(n),kk,nts)+
     &              rwk(ii,jef(n),kk+1,nts)+
     &              rwk(ii+1,jef(n),kk+1,nts))/4.0
```

```
            if (ttest1.gt.tign) then
              do 140 nk=kk,kk+1
              do 140 ni=ii,ii+1
                rwk(ni,jef(n),nk,neng)=-(ttest1-tign)*1884.*20.
     &             -pengs(n,ii,jef(n),kk)/fevol(ii,jef(n),kk)
                rwk(ni,jef(n)+1,nk,neng)=0.0
140           continue
              call putsrc ('ENERGY_S',rwk(1,1,1,neng),rz,
     &          ii,ii+1,jef(n),jef(n)+1,kk,kk+1,ercode,erstop)
            else if ((ttest1.lt.tign).and.
     &               (tmlost(n,ii,jef(n),kk).gt.0.0)) then
              do 141 nk=kk,kk+1
              do 141 ni=ii,ii+1
                rwk(ni,jef(n),nk,neng)=-.5*(ttest1-tign)*1884.*20.
                rwk(ni,jef(n)+1,nk,neng)=-.5*(ttest1-tign)*1884.*20.
141           continue
              call putsrc ('ENERGY_S',rwk(1,1,1,neng),rz,
     &          ii,ii+1,jef(n),jef(n)+1,kk,kk+1,ercode,erstop)
            endif
            do 142 nk=kk,kk+1
            do 142 ni=ii,ii+1
              rwk(ni,jef(n),nk,neng)=0.0
              rwk(ni,jef(n)+1,nk,neng)=0.0
142         continue

          else if (nfegb(n).eq.5) then

            ttest1=(rwk(ii,jj,kbf(n),nts)+
     &              rwk(ii+1,jj,kbf(n),nts)+
     &              rwk(ii,jj+1,kbf(n),nts)+
     &              rwk(ii+1,jj+1,kbf(n),nts))/4.0

            if (ttest1.gt.tign) then
              do 143 nj=jj,jj+1
              do 143 ni=ii,ii+1
                rwk(ni,nj,kbf(n),neng)=-(ttest1-tign)*1884.*20.
     &             -pengs(n,ii,jj,kbf(n))/fevol(ii,jj,kbf(n))
                rwk(ni,nj,kbf(n)-1,neng)=0.0
143           continue
              call putsrc ('ENERGY_S',rwk(1,1,1,neng),rz,
     &          ii,ii+1,jj,jj+1,kbf(n)-1,kbf(n),ercode,erstop)
            else if ((ttest1.lt.tign).and.
     &               (tmlost(n,ii,jj,kbf(n)).gt.0.0)) then
              do 144 nj=jj,jj+1
              do 144 ni=ii,ii+1
                rwk(ni,nj,kbf(n),neng)=-.5*(ttest1-tign)*1884.*20.
                rwk(ni,nj,kbf(n)-1,neng)=-.5*(ttest1-tign)*1884.*20.
144           continue
              call putsrc ('ENERGY_S',rwk(1,1,1,neng),rz,
     &          ii,ii+1,jj,jj+1,kbf(n)-1,kbf(n),ercode,erstop)
            endif
            do 145 nj=jj,jj+1
            do 145 ni=ii,ii+1
              rwk(ni,nj,kbf(n),neng)=0.0
              rwk(ni,nj,kbf(n)-1,neng)=0.0
145        continue

          else if (nfegb(n).eq.6) then

            ttest1=(rwk(ii,jj,kef(n),nts)+
     &              rwk(ii+1,jj,kef(n),nts)+
     &              rwk(ii,jj+1,kef(n),nts)+
     &              rwk(ii+1,jj+1,kef(n),nts))/4.0

            if (ttest1.gt.tign) then
              do 146 nj=jj,jj+1
              do 146 ni=ii,ii+1
```

```
                rwk(ni,nj,kef(n),neng)=-(ttest1-tign)*1884.*20.
     &             -pengs(n,ii,jj,kef(n))/fevol(ii,jj,kef(n))
                rwk(ni,nj,kef(n)+1,neng)=0.0
146             continue
                call putsrc ('ENERGY_S',rwk(1,1,1,neng),rz,
     &            ii,ii+1,jj,jj+1,kef(n),kef(n)+1,ercode,erstop)
              else if ((ttest1.lt.tign).and.
     &                 (tmlost(n,ii,jj,kef(n)).gt.0.0)) then
                do 147 nj=jj,jj+1
                do 147 ni=ii,ii+1
                  rwk(ni,nj,kef(n),neng)=-.5*(ttest1-tign)*1884.*20.
                  rwk(ni,nj,kef(n)+1,neng)=-.5*(ttest1-tign)*1884.*20.
147             continue
                call putsrc ('ENERGY_S',rwk(1,1,1,neng),rz,
     &            ii,ii+1,jj,jj+1,kef(n),kef(n)+1,ercode,erstop)
              endif
              do 148 nj=jj,jj+1
              do 148 ni=ii,ii+1
                rwk(ni,nj,kef(n),neng)=0.0
                rwk(ni,nj,kef(n)+1,neng)=0.0
148           continue

            endif
1310            format (a,4(1x,i2),5(1x,e10.3))
130       continue


          else if (LABEL.EQ.'PROD') then
            ncntfu=ncntfu+1
            do 112 kk=kbf(n),kef(n)-1
            do 112 jj=jbf(n),jef(n)-1
            do 112 ii=ibf(n),ief(n)-1
              do 114 nk=kk,kk+1
              do 114 nj=jj,jj+1
              do 114 ni=ii,ii+1
                rwk(ni,nj,nk,nprod)=0.02*prate(n,ii,jj,kk)
114                             continue
              call putsrc ('PROD',rwk(1,1,1,nprod),rz,
     &                    ii,ii+1,jj,jj+1,kk,kk+1,ercode,erstop)
              do 116 nk=kk,kk+1
              do 116 nj=jj,jj+1
              do 116 ni=ii,ii+1
                rwk(ni,nj,nk,nprod)=0.0
116           continue
112         continue
          endif

50      continue

        if (LABEL.EQ.'SOOT') then

          do 97 kk=1,kd
          do 97 jj=1,jd
          do 97 ii=1,id
            if (volcv(ii,jj,kk).gt.0.0) then
              rwk(ii,jj,kk,nsoot)=syave*
     &             rwk(ii,jj,kk,nfspent)/volcv(ii,jj,kk)
            else
              rwk(ii,jj,kk,nsoot)=0.0
            endif
97        continue
          call putsrc ('SOOT',rwk(1,1,1,nsoot),rz,
     &               1,id,1,jd,1,kd,ercode,erstop)
        endif

        return
        end
```

```
c     #################
c     BEGIN SUBROUTINES
c     #################

c     *****************
      subroutine datain
c     *****************

c-----called by main program

c-----reads in data from file flame.hrr
      include 'flame.com'
      cntime(0)=0.0
      nlist=0
      icont=1
      do while (icont .ne. -999)
        read (4,*) read1, read2, read3, read4, read5, read6, read7,
     &            read8, read9, read10
        write (6,*) 'readin',read1,read2,read3,read4,read5,read6,
     &     read7,read8,read9,read10
        if (read1 .ge. 0.0) then
          if (nlist.eq.998) then
            write (6,*) 'usrsrc.f error message 101'
            write (6,*) 'Increase cntime & cnmdot array size',
     &                  'in subroutine datain since flame.hrr has',
     &                  'more than 1000 entries'
            write (nout,*) 'usrsrc.f error message 101'
            write (nout,*) 'Increase cntime & cnmdot array size',
     &                  'in subroutine datain since flame.hrr has',
     &                  'more than 1000 entries'
            stop
          endif
          cntime(nlist)=read1
          cnmdot(nlist,1)=read2
          cnmdot(nlist,2)=read5
          cnmdot(nlist,3)=read8
          cnsoot(nlist,1)=read3
          cnsoot(nlist,2)=read6
          cnsoot(nlist,3)=read9
          cnhc(nlist,1)=read4
          cnhc(nlist,2)=read7
          cnhc(nlist,3)=read10

          nhrr=nlist
          nlist=nlist+1
        else
          icont = -999
        endif

      enddo
      summas(0,1)=0.0
      summas(0,2)=0.0
      summas(0,3)=0.0

      do 400 i=1,nhrr
        if (cntime(i).eq.cntime(i-1)) then
          write (6,*) 'usrsrc.f error message 102'
          write (6,*) 'two input hrr times are the same'
          write (nout,*) 'usrsrc.f error message 102'
          write (nout,*) 'two input hrr times are the same'
          stop
        endif

c     put in linear cnmdot
      summas(i,1)=summas(i-1,1)+(cntime(i)-cntime(i-1))*
     &                  (.5*(cnmdot(i,1)+cnmdot(i-1,1)))
```

```
      summas(i,2)=summas(i-1,2)+(cntime(i)-cntime(i-1))*
     &                  (.5*(cnmdot(i,2)+cnmdot(i-1,2)))
      summas(i,3)=summas(i-1,3)+(cntime(i)-cntime(i-1))*
     &                  (.5*(cnmdot(i,3)+cnmdot(i-1,3)))
      if (summas(i,1).lt.summas(i-1,1)) then
        write (6,*) 'error massage 103'
        write (6,*) 'sum of cone mass loss is not positive',
     &              summas(i,1),summas(i-1,1)
        write (nout,*) 'error massage 103'
        write (nout,*) 'sum of cone mass loss is not positive',
     &              summas(i,1),summas(i-1,1)
      endif
      if (summas(i,2).lt.summas(i-1,2)) then
        write (6,*) 'error massage 104'
        write (6,*) 'sum of cone mass loss is not positive',
     &              summas(i,2),summas(i-1,2)
        write (nout,*) 'error massage 104'
        write (nout,*) 'sum of cone mass loss is not positive',
     &              summas(i,2),summas(i-1,2)
      endif
      if (summas(i,3).lt.summas(i-1,3)) then
        write (6,*) 'error massage 105'
        write (6,*) 'sum of cone mass loss is not positive',
     &              summas(i,3),summas(i-1,3)
        write (nout,*) 'error massage 105'
        write (nout,*) 'sum of cone mass loss is not positive',
     &              summas(i,3),summas(i-1,3)
      endif

 400  continue

c-----read in values from flame.dat
      read (10,*) nfeor(1)
      read (10,*) nfeor(2)
      read (10,*) nfeor(3)
      read (10,*) nfeor(4)
      read (10,*) rhofuel
      read (10,*) tign
      read (10,*) fign
      read (10,*) hevap
      read (10,*) abeta
      read (10,*) wfuel
      read (10,*) wo2
      read (10,*) wprod
      read (10,*) wsoot
      read (10,*) wn2
      read (10,*) wco2
      read (10,*) wh2o
      read (10,*) zmolh2o
      read (10,*) cnglim
      read (10,*) tmps
      read (10,*) gaslim
      read (10,*) sotlim
      read (10,*) iterad
      read (10,*) flux1
      read (10,*) flux2
      read (10,*) flux3

c-----determine number of surfaces for flame spread
      numsurf=0
      do 401 i=1,4
      if (nfeor(i).gt.0) then
        numsurf=numsurf+1
      endif
 401  continue

c-----determine number of different mass loss rate curves provided
```

```
      if ((flux1.gt.0.0).and.(flux2.eq.0.0).and.(flux3.eq.0.0)) then
        nflux=1
      else if ((flux1.gt.0.0).and.(flux2.gt.0.0)
     &         .and.(flux3.eq.0.0)) then
        nflux=2
      else if ((flux1.gt.0.0).and.(flux2.gt.0.0)
     &         .and.(flux3.gt.0.0)) then
        nflux=3
      endif

      if (numsurf.lt.1) then
        write (6,*) 'usrsrc.f error message 106'
        write (6,*) 'there are no burning surfaces', numsurf
        write (nout,*) 'usrsrc.f error message 106'
        write (nout,*) 'there are no burning surfaces', numsurf
        stop
      endif

      return
      end

c     ******************
      subroutine datain2
c     ******************

c-----called by main program

c-----reads in data from file flame.out
      include 'flame.com'

      icont=1
      do while (icont .ne. -999)
        read (1,*) nr1,nr2,nr3,nr4,rr1
        if (nr1 .ge. 0) then
          tmlost(nr1,nr2,nr3,nr4)=rr1
        else
          icont = -999
        endif
      enddo

      return
      end

c     *****************
      subroutine header
c     *****************

c-----called by main program

c-----writes flame spread model information to output file
      include 'flame.com'


      write (6,*) ' '
      write (6,*) '*****************************************',
     &            '**********'
      write (6,*) '#$#$#$#$#$#   Fire Growth Routine Running   ',
     &            '#$#$#$#$#$#'
      write (6,*) ' '
      write (6,911) ' ==> Number of fuel surfaces', numsurf
      write (nout,*) ' '
      write (nout,*) '*****************************************',
     &            '**********'
      write (nout,*) '#$#$#$#$#$#   Fire Growth Routine Running   ',
     &            '#$#$#$#$#$#'
      write (nout,*) ' '
      write (nout,911) ' ==> Number of fuel surfaces', numsurf
```

```
911  format (a, 1x, i1)
     write (6,913) 'Surface orientation 1:',nfeor(1),'2:',nfeor(2),
    &               '3:',nfeor(3),'4:',nfeor(4)
     write (nout,913) 'Surface orientation 1:',nfeor(1),'2:',nfeor(2),
    &               '3:',nfeor(3),'4:',nfeor(4)
913  format (5x,4(a,i1,1x))
     write (6,915) '(1:s=-1, 2:s=1, 3:t=-1, 4:t=1'
     write (6,915) '5:u=-1, 6:u=1, 0:no flame spread)'
     write (nout,915) '(1:s=-1, 2:s=1, 3:t=-1, 4:t=1'
     write (nout,915) '5:u=-1, 6:u=1, 0:no flame spread)'
915  format (5x,a)
     write (6,917) 'Solid fuel ignition temperature:', tign, 'K'
     write (6,917) 'Solid fuel flux for ignition:', fign, 'W/m^2'
     write (nout,917) 'Solid fuel ignition temperature:', tign, 'K'
     write (nout,917) 'Solid fuel flux for ignition:', fign, 'W/m^2'
917  format (5x, a, 1x, f9.2, 1x, a)
     write (6,919) '     Density of pyrolysis products:',
    &               rhofuel, 'kg/m^3'
     write (nout,919) '     Density of pyrolysis products:',
    &               rhofuel, 'kg/m^3'
919  format (a, 1x, e10.3, 1x, a)
     write (6,921) '     Moles of H2O produced per',
    &              'mole of CO2:', zmolh2o
     write (nout,921) '     Moles of H2O produced per',
    &              'mole of CO2:', zmolh2o
921  format (a, 1x, a, 1x,f5.3)
     write (6,923) ' ==> Absorptivity values are updated every',
    &              iterad, 'iterations'
     write (nout,923) ' ==> Absorptivity values are updated every',
    &              iterad, 'iterations'
923  format (a, 1x, I2, 1x, a)
     write (6,925) 'Minumum % change in species concentration',
    &              'for'
     write (nout,925) 'Minumum % change in species concentration',
    &              'for'
925  format (5x,a, 1x, a)
     write (6,927) 'absorptivity to be recalculated:', cnglim
     write (nout,927) 'absorptivity to be recalculated:', cnglim
927  format (5x,a,f6.2)
     write (6,929) 'Minimum gas mass fraction for inclusion'
     write (6,931) 'in absorptivity calculations:', gaslim
     write (6,929) 'Minimum soot volume fraction for inclusion'
     write (6,931) 'in absorptivity calculations:', sotlim
     write (nout,929) 'Minimum gas mass fraction for inclusion'
     write (nout,931) 'in absorptivity calculations:', gaslim
     write (nout,929) 'Minimum soot volume fraction for inclusion'
     write (nout,931) 'in absorptivity calculations:', sotlim
929  format (5x, a)
931  format (5x, a, e10.3)
     write (6,933) 'Blackbody source temperature:', tmps, 'K'
     write (nout,933) 'Blackbody source temperature:', tmps, 'K'
933  format (5x, a, 1x, f6.2, 1x, a)
     write (6,935) 'Cone flux levels:', flux1, ';', flux2, ';',
    &               flux3,'w/m^2'
     write (nout,935) 'Cone flux levels:', flux1, ';', flux2, ';',
    &               flux3,'w/m^2'
935  format (5x, a, 1x, f8.2, a, 1x, f8.2, a, 1x, f8.2, 1x, a)
     return
     end

c    *****************
     subroutine polint(xin,yout,sout,hout)
c    *****************

c    Given arrays tmlost, and cnmdot, of length nhrr, and
c    given a value xin, this routine returns a value yout, and
c    an error estimate dy. If p(xin) is the
```

```
c     polynomial of degree nhrr-1 such that p(xai)=yai, i=1,..,nhrr, then the
c     returned value yout=p(xin). xin and yout are per m^2

      implicit real (a-h,o-z)
      include 'flame.com'
      integer ns

c     xin now equals the total mass lost per m^2, tmlost
c      xin=xin/areain

       if (xin.lt.summas(0,1)) then
            write (6,*) 'usrsrc.f error message 119'
            write (6,*) 'xin',xin,'is not in the flame.hrr table'
            write (nout,*) 'usrsrc.f error message 119'
            write (nout,*) 'xin',xin,'is not in the flame.hrr table'
            stop
       else if (xin.gt.summas(nhrr,1)) then
         yout=0.0
         sout=0.0
         hout=0.0
       else
       yout=0.0
       yout1=0.0
       yout2=0.0
       sout=0.0
       sout1=0.0
       sout2=0.0
       hout=0.0
       hout1=0.0
       hout2=0.0
      do 101 m=1,nhrr
        if (nflux.eq.1) then
          if ((xin.eq.0.0).and.(summas(0,1).eq.0.0)
     &             .and.(m.eq.1)) then
            yout=(cnmdot(m,1)-cnmdot(0,1))*(dt/(cntime(1)-cntime(0)))
     &           +cnmdot(0,1)
            sout=(cnsoot(m,1)-cnsoot(0,1))*(dt/(cntime(1)-cntime(0)))
     &           +cnsoot(0,1)
            hout=(cnhc(m,1)-cnhc(0,1))*(dt/(cntime(1)-cntime(0)))
     &           +cnhc(0,1)
          else if ((xin.ge.summas(m-1,1)).and.(xin.le.summas(m,1))) then
            yout=(cnmdot(m,1)-cnmdot(m-1,1))*((xin-summas(m-1,1))/
     &           (summas(m,1)-summas(m-1,1)))+cnmdot(m-1,1)
            sout=(cnsoot(m,1)-cnsoot(m-1,1))*((xin-summas(m-1,1))/
     &           (summas(m,1)-summas(m-1,1)))+cnsoot(m-1,1)
            hout=(cnhc(m,1)-cnhc(m-1,1))*((xin-summas(m-1,1))/
     &           (summas(m,1)-summas(m-1,1)))+cnhc(m-1,1)
          endif
        else if (nflux.eq.2) then
          if (feflux(n,ii,jj,kk).le.flux1) then
            if ((xin.ge.summas(m-1,1))
     &          .and.(xin.le.summas(m,1))) then
              yout=(cnmdot(m,1)-cnmdot(m-1,1))*((xin-summas(m-1,1))
     &             /(summas(m,1)-summas(m-1,1)))+cnmdot(m-1,1)
              sout=(cnsoot(m,1)-cnsoot(m-1,1))*((xin-summas(m-1,1))
     &             /(summas(m,1)-summas(m-1,1)))+cnsoot(m-1,1)
              hout=(cnhc(m,1)-cnhc(m-1,1))*((xin-summas(m-1,1))
     &             /(summas(m,1)-summas(m-1,1)))+cnhc(m-1,1)
            endif
          else if ((feflux(n,ii,jj,kk).gt.flux1).and.
     &             (feflux(n,ii,jj,kk).lt.flux2)) then
            if ((xin.ge.summas(m-1,1))
     &          .and.(xin.le.summas(m,1))) then
              yout1=(cnmdot(m,1)-cnmdot(m-1,1))*((xin-summas(m-1,1))
     &             /(summas(m,1)-summas(m-1,1)))+cnmdot(m-1,1)
              sout1=(cnsoot(m,1)-cnsoot(m-1,1))*((xin-summas(m-1,1))
     &             /(summas(m,1)-summas(m-1,1)))+cnsoot(m-1,1)
```

```
        hout1=(cnhc(m,1)-cnhc(m-1,1))*((xin-summas(m-1,1))
&              /(summas(m,1)-summas(m-1,1)))+cnhc(m-1,1)
      endif
      if ((xin.ge.summas(m-1,2))
&         .and.(xin.le.summas(m,2))) then
        yout2=(cnmdot(m,2)-cnmdot(m-1,2))*((xin-summas(m-1,2))
&              /(summas(m,2)-summas(m-1,2)))+cnmdot(m-1,2)
        sout2=(cnsoot(m,2)-cnsoot(m-1,2))*((xin-summas(m-1,2))
&              /(summas(m,2)-summas(m-1,2)))+cnsoot(m-1,2)
        hout2=(cnhc(m,2)-cnhc(m-1,2))*((xin-summas(m-1,2))
&              /(summas(m,2)-summas(m-1,2)))+cnhc(m-1,2)
      endif
    else if (feflux(n,ii,jj,kk).ge.flux2) then
      if ((xin.ge.summas(m-1,2))
&         .and.(xin.le.summas(m,2))) then
        yout=(cnmdot(m,2)-cnmdot(m-1,2))*((xin-summas(m-1,2))
&              /(summas(m,2)-summas(m-1,2)))+cnmdot(m-1,2)
        sout=(cnsoot(m,2)-cnsoot(m-1,2))*((xin-summas(m-1,2))
&              /(summas(m,2)-summas(m-1,2)))+cnsoot(m-1,2)
        hout=(cnhc(m,2)-cnhc(m-1,2))*((xin-summas(m-1,2))
&              /(summas(m,2)-summas(m-1,2)))+cnhc(m-1,2)
      endif
    endif
  else if (nflux.eq.3) then
    if (feflux(n,ii,jj,kk).le.flux1) then
      if ((xin.ge.summas(m-1,1))
&         .and.(xin.le.summas(m,1))) then
        yout=(cnmdot(m,1)-cnmdot(m-1,1))*((xin-summas(m-1,1))
&              /(summas(m,1)-summas(m-1,1)))+cnmdot(m-1,1)
        sout=(cnsoot(m,1)-cnsoot(m-1,1))*((xin-summas(m-1,1))
&              /(summas(m,1)-summas(m-1,1)))+cnsoot(m-1,1)
        hout=(cnhc(m,1)-cnhc(m-1,1))*((xin-summas(m-1,1))
&              /(summas(m,1)-summas(m-1,1)))+cnhc(m-1,1)
      endif
    else if ((feflux(n,ii,jj,kk).gt.flux1).and.
&            (feflux(n,ii,jj,kk).le.flux2)) then
      if ((xin.ge.summas(m-1,1))
&         .and.(xin.le.summas(m,1))) then
        yout1=(cnmdot(m,1)-cnmdot(m-1,1))*((xin-summas(m-1,1))
&              /(summas(m,1)-summas(m-1,1)))+cnmdot(m-1,1)
        sout1=(cnsoot(m,1)-cnsoot(m-1,1))*((xin-summas(m-1,1))
&              /(summas(m,1)-summas(m-1,1)))+cnsoot(m-1,1)
        hout1=(cnhc(m,1)-cnhc(m-1,1))*((xin-summas(m-1,1))
&              /(summas(m,1)-summas(m-1,1)))+cnhc(m-1,1)
      endif
      if ((xin.ge.summas(m-1,2))
&         .and.(xin.le.summas(m,2))) then
        yout2=(cnmdot(m,2)-cnmdot(m-1,2))*((xin-summas(m-1,2))
&              /(summas(m,2)-summas(m-1,2)))+cnmdot(m-1,2)
        sout2=(cnsoot(m,2)-cnsoot(m-1,2))*((xin-summas(m-1,2))
&              /(summas(m,2)-summas(m-1,2)))+cnsoot(m-1,2)
        hout2=(cnhc(m,2)-cnhc(m-1,2))*((xin-summas(m-1,2))
&              /(summas(m,2)-summas(m-1,2)))+cnhc(m-1,2)
      endif
    else if ((feflux(n,ii,jj,kk).gt.flux2).and.
&            (feflux(n,ii,jj,kk).le.flux3)) then
      if ((xin.ge.summas(m-1,2))
&         .and.(xin.le.summas(m,2))) then
        yout1=(cnmdot(m,2)-cnmdot(m-1,2))*((xin-summas(m-1,2))
&              /(summas(m,2)-summas(m-1,2)))+cnmdot(m-1,2)
        sout1=(cnsoot(m,2)-cnsoot(m-1,2))*((xin-summas(m-1,2))
&              /(summas(m,2)-summas(m-1,2)))+cnsoot(m-1,2)
        hout1=(cnhc(m,2)-cnhc(m-1,2))*((xin-summas(m-1,2))
&              /(summas(m,2)-summas(m-1,2)))+cnhc(m-1,2)
      endif
      if ((xin.ge.summas(m-1,3))
&         .and.(xin.le.summas(m,3))) then
```

```
          yout2=(cnmdot(m,3)-cnmdot(m-1,3))*((xin-summas(m-1,3))
     &              /(summas(m,3)-summas(m-1,3)))+cnmdot(m-1,3)
          sout2=(cnsoot(m,3)-cnsoot(m-1,3))*((xin-summas(m-1,3))
     &              /(summas(m,3)-summas(m-1,3)))+cnsoot(m-1,3)
          hout2=(cnhc(m,3)-cnhc(m-1,3))*((xin-summas(m-1,3))
     &              /(summas(m,3)-summas(m-1,3)))+cnhc(m-1,3)
        endif
      else if (feflux(n,ii,jj,kk).gt.flux3) then
        if ((xin.ge.summas(m-1,3))
     &          .and.(xin.le.summas(m,3))) then
          yout=(cnmdot(m,3)-cnmdot(m-1,3))*((xin-summas(m-1,3))
     &              /(summas(m,3)-summas(m-1,3)))+cnmdot(m-1,3)
          sout=(cnsoot(m,3)-cnsoot(m-1,3))*((xin-summas(m-1,3))
     &              /(summas(m,3)-summas(m-1,3)))+cnsoot(m-1,3)
          hout=(cnhc(m,3)-cnhc(m-1,3))*((xin-summas(m-1,3))
     &              /(summas(m,3)-summas(m-1,3)))+cnhc(m-1,3)
        endif
      endif
    endif

101  continue

     if (nflux.eq.2) then
       if ((feflux(n,ii,jj,kk).gt.flux1).and.
     &             (feflux(n,ii,jj,kk).le.flux2)) then
         yout=((feflux(n,ii,jj,kk)-flux1)/(flux2-flux1))*(yout2-yout1)+
     &          yout1
         sout=((feflux(n,ii,jj,kk)-flux1)/(flux2-flux1))*(sout2-sout1)+
     &          sout1
         hout=((feflux(n,ii,jj,kk)-flux1)/(flux2-flux1))*(hout2-hout1)+
     &          hout1
       endif
     else if (nflux.eq.3) then
       if ((feflux(n,ii,jj,kk).gt.flux1).and.
     &             (feflux(n,ii,jj,kk).le.flux2)) then
         yout=((feflux(n,ii,jj,kk)-flux1)/(flux2-flux1))*(yout2-yout1)+
     &          yout1
         sout=((feflux(n,ii,jj,kk)-flux1)/(flux2-flux1))*(sout2-sout1)+
     &          sout1
         hout=((feflux(n,ii,jj,kk)-flux1)/(flux2-flux1))*(hout2-hout1)+
     &          hout1
       else if ((feflux(n,ii,jj,kk).gt.flux2).and.
     &             (feflux(n,ii,jj,kk).le.flux3)) then
         yout=((feflux(n,ii,jj,kk)-flux2)/(flux3-flux2))*(yout2-yout1)+
     &          yout1
         sout=((feflux(n,ii,jj,kk)-flux2)/(flux3-flux2))*(sout2-sout1)+
     &          sout1
         hout=((feflux(n,ii,jj,kk)-flux2)/(flux3-flux2))*(hout2-hout1)+
     &          hout1
       endif
     endif

       if (yout.lt.0.0) then
         write (6,*) 'usrsrc.f error message 120'
         write (6,*) 'negative mass loss interpolation',xin,yout
         write (nout,*) 'usrsrc.f error message 120'
         write (nout,*) 'negative mass loss interpolation',xin,yout
         stop
       endif
       if (sout.lt.0.0) then
         write (6,*) 'usrsrc.f error message 121'
         write (6,*) 'negative soot production interpolation',xin,
     &                sout
         write (nout,*) 'usrsrc.f error message 121'
         write (nout,*) 'negative soot production interpolation',
     &                  xin,sout
         stop
```

```
   endif
   if (hout.lt.0.0) then
     write (6,*) 'usrsrc.f error message 121a'
     write (6,*) 'negative hc production interpolation',xin,
&                hout
     write (nout,*) 'usrsrc.f error message 121a'
     write (nout,*) 'negative hc production interpolation',
&                   xin,hout
     stop
   endif

 endif

 return
 end
```

## B.2 flame.dat

Flame spread routine problem input data file

```
5         ! Side of FE for flame spread
1         ! (1:s=-1, 2:s=1, 3:t=-1, 4:t=1, 5:u=-1, 6:u=1, 0:no flame spread)
0         ! These directions are for the local coordinate. The code will
0         ! account for the transition to global coordinates.
.391      ! Fuel density (kg/m^3)
543.      ! Ignition temperature (K) Value for PU/LC
15000.    ! Minimum flux for ignition (W/m^2)
605000.   ! Latent heat of vaporization (J/kg)
1.0       ! Abeta (fraction of a given control surface for pyrolsys)
20.       ! MW fuel (Scalar #1)
32.       ! MW O2   (Scalar #2)
31.4      ! MW PROD (Scalar #3)
12.       ! MW SOOT (Scalar #4)
28.       ! MW N2   (Scalar #5)
44.       ! MW CO2  (Scalar #3 component)
18.       ! MW H2O  (Scalar #3 component)
.89       ! Number of moles of H2O formed per mole of CO2
.075      ! Cnglim (fraction change in concentration for RADCAL updating)
270.0     ! Blackbody source temperature (K)
0.0001    ! Minimum mass fraction for gas calcs in RADCAL
1e-14     ! Minimum volume fraction for soot calcs in RADCAL
5         ! Iteration frequency for radcal
25000.0   ! Flux1
35000.0   ! Flux2 (0.0 if no data)
50000.0   ! Flux3 (0.0 if no data)
```

## B.3 flame.hrr

Bench scale $\dot{m}''$, $Y_{\mathrm{SOOT}}$, and $\Delta H_c$ input file

```
   25 kW/m^2                35 kW/m^2                50 kW/m^2
   mdot    Ysoot   Hc       mdot    Ysoot   Hc       mdot    Ysoot   Hc
0  0.009   0.002   23000000 0.008   0.002   23000000 0.005   0.01    23000000
5  0.00975 0.00298 23000000 0.00886 0.002   23000000 0.00597 0.01234 23000000
10 0.00721 0.04977 23000000 0.01174 0.00271 23000000 0.01386 0.09459 23000000
15 0.00953 0.04617 23000000 0.01959 0.03906 23000000 0.01531 0.14159 23000000
20 0.01262 0.23037 23000000 0.00900 0.03006 23000000 0.01694 0.12415 23000000
-999. -999. -999. -999. -999. -999. -999. -999. -999. -999.
```

## B.4 flame.out

Flame spread routine results output file

```
      -999        -999        -999        -999  -999.0000
```

## B.5 flame.sum

Flame spread routine summary of flame spread progress

| time | hrr | mdot(tot) | mdot(furn) | % burn1 | % burn2 | % burn3 | % burn4 |
|---|---|---|---|---|---|---|---|
| 0 | 0 | 0 | 0 | 0 | 0 | 0 | 0 |
| 0.3 | 1.04E+03 | 7.66E-05 | 0.00E+00 | 0 | 0 | 0 | 0 |
| 0.6 | 2.63E+03 | 1.48E-04 | 0.00E+00 | 0 | 0 | 0 | 0 |
| 0.9 | 4.92E+03 | 3.17E-04 | 0.00E+00 | 0 | 0 | 0 | 0 |
| 1.2 | 7.57E+03 | 5.57E-04 | 0.00E+00 | 0 | 0 | 0 | 0 |

## B.6 flame.com

Fortran common file that contains subroutine variable and array definitions

```
common /ra/ fluxvol, pdot,rhofuel,burnvol,abeta,fign
common /rb/ fdens,fex,fey,fez,tign,xdif,ydif,zdif,delx,dely,delz
common /rc/ delh,cntime(0:1000),cnmdot(0:1000,3),pevap1
common /rd/ fevol(90,90,90),fearea(4,90,90,90),hevap,pevap2
common /re/ pvel(4,90,90,90),areaobj,areao(4,90,90,90)
common /rf/ volo(4,90,90,90),volobj,dlim1b,dlim1e,dlim2b,dlim2e
common /rg/ dlim3b,dlim3e,areasum(4),runtime,timedif
common /rh/ read1,read2,tmlost(4,90,90,90),peng(4,90,90,90)
common /ri/ ttemp,t1(100),t2(100),tos(4,100,100,100),dt
common /rj/ sumxm,sumym,sumzm,sumnxm,sumnym,sumnzm
common /rk/ x1,x2,x3,x4,y1,y2,y3,y4,z1,z2,z3,z4,h1,h2,h3,h4
common /rl/ cnsoot(0:1000,3),psoot(4,90,90,90),syield
common /rm/ flux1, flux2, flux3, summas(0:1000,3),areatmp
common /rn/ feflux(4,90,90,90),zmolh2o,fluxip(4),volsave(4)
common /ro/ gaslim, sotlim, tmps, cnglim,burnarea(4),ttsave
common /rp/ prate(4,90,90,90),distdif(4),volusum(4),ttba(4)
common /rq/ symdot,smdot,syave,ssrc(90,90,90),volcv(90,90,90)
common /rr/ pengs(4,90,90,90),ptdif(90,90,90),ttest,ttest1
common /rs/ cnhc(0:1000,3),hcomb,hcave,hcymdot,hcmdot

common /ia/ ncntfu,ncntmo,ncntma(4), npnt1, npnt2, npnt3
common /ib/ n, nci,ncj,nck,nx,ny,nz,ii,jj,kk,indxdif(4)
common /ic/ nii,njj,nkk,ncnter,ms,mo,ijk(3),loopcnto(3)
common /id/ nmass,nvol,narea,nmom,nfevol,nflux,ndens,nfuel
common /ie/ nfex,nfey,nfez,nt,nts,ntime(90,90,90),neng
common /if/ nobj(4,2,3), nsurf(4,2,3), numsurf, ndir(4),ndirg(4)
common /ig/ nlim1b,nlim1e,nlim2b,nlim2e,ivisit,numdata,nhrr
common /ih/ ndirgo(4),ndirgs(4),ngxyzo(4,3),ngxyzs(4,3)
common /ii/ ib,ie,jb,je,kb,ke,ibe,jbe,kbe,iterad
common /ij/ ilimit,jlimit,klimit,l1,l2,l3,nfeor(4),ip(3)
common /ik/ ibf(4),ief(4),jbf(4),jef(4),kbf(4),kef(4),ipp(6)
common /il/ nfegb(4),nout,itypef(90,90,90),nsolid(4,2,3)
```

## B.7 propb.f

Calculates the buld compressibility for natural convection fluid flows

```
C     ^^^^^^^^^^^^^^^^^^^^^^^^^^^^^^^^^^^^^^^
C     | FURNITURE CFD FIRE MODEL VERSION 1.0 |
C     |           JANUARY 5, 1999           |
C     ^^^^^^^^^^^^^^^^^^^^^^^^^^^^^^^^^^^^^^^
C
C     Calculates the bulk fluid compressibility
C
C=======================================================================
C
      SUBROUTINE PROPB(BETAFL,
     &                 U,V,W,P,T,PHI,NPHI,XYZ,
     &                 ILABEL,LABEL,I,J,K,ID,JD,KD)
C
CSCDB
C  Input:
C
C      U,V,W : Cartesian velocity components
C          P : static pressure
C          T : static temperature
C        PHI : additional scalars
C       NPHI : number of additional scalars
C        XYZ : Cartesian coordinates of grid nodes
C      LABEL : character string identifying equation solved
C     ILABEL : number of the current scalar equation being solved
C      I,J,K : topological grid coordinates
C   ID,JD,KD : topological grid dimensions
C
C  Output:
C
C     BETAFL : bulk compressibility of fluid
C
C  Local:
C
C       POFF : pressure offset (level shift)
C       TOFF : temperature offset (level shift)
C       BETA : bulk compressibility of fluid
C
C  Common Blocks:
C
C  /CONTRL/ is declared so that information can be added as needed
C           for desired equation of state.
C
C     IONUM  : integer, unit numbers in CONTRL common block.
C     IARR   : integer, integer switches in CONTRL common block.
C     RARR   : real, real constants in CONTRL common block.
C     CONST  : real, property constants in CONTRL common block.
C     LARR   : logical, logical switches in CONTRL common block.
C
C  NOTE: The true levels of pressure (P) and temperature (T) are
C        assumed to be
C           P_true = P + POFF
C           T_true = T + TOFF
C        where POFF and TOFF are level shifts in the actual dependent
C        values of P and T that are solved for.
CSCDE
C
C=======================================================================
C
C---------------------------
C Subroutine Arguments
C---------------------------
C
      REAL U(ID,JD,KD),V(ID,JD,KD),W(ID,JD,KD),P(ID,JD,KD),T(ID,JD,KD),
```

```
     &     PHI(ID,JD,KD,*),XYZ(ID,JD,KD,3),BETAFL
C
      INTEGER NPHI,ILABEL,I,J,K,ID,JD,KD
C
      CHARACTER*(*) LABEL
C
C----------------------------
C Local Variables
C----------------------------
C
      REAL BETA,POFF,TOFF
C
C----------------------------
C Common Blocks
C----------------------------
C
      COMMON/CONTRL/ IONUM(100),IARR(200),RARR(100),CONST(100),LARR(200)
C
      REAL RARR,CONST
C
      INTEGER IONUM, IARR
C
      LOGICAL LARR
C
      EQUIVALENCE (CONST(19),BETA), (CONST(13),POFF),(CONST(14),TOFF)
C
C----------------------------
C Executable Statements
C----------------------------
C
      IF (ILABEL.EQ.0) THEN
c        BETAFL = BETA
        betafl=1./(T(i,j,k)+toff)
      ELSE
        betafl=1./(T(i,j,k)+toff)
c        BETAFL = 0.0
      ENDIF

      RETURN
      END
```

# B.8 propf.f

Fluid dynamic viscosity

```
C     ^^^^^^^^^^^^^^^^^^^^^^^^^^^^^^^^^^^^^^^^
C     | FURNITURE CFD FIRE MODEL VERSION 1.0 |
C     |           JANUARY 5, 1999            |
C     ^^^^^^^^^^^^^^^^^^^^^^^^^^^^^^^^^^^^^^^^
C
C     Calculates dynamic viscosity using power laws from White
C     Species #1 FUEL (CH4)
C     Species #2 O2
C     Species #3 PROD (.73 CO2  .27 H2O)
C     Species #4 SOOT (Same as fuel)
C     Species #5 N2
C=======================================================================
C
      SUBROUTINE PROPF(VISCL,
     &                 U,V,W,P,T,PHI,NPHI,XYZ,
     &                 ILABEL,LABEL,I,J,K,ID,JD,KD)
C
C  Input:
C
C     ILABEL =  0  fluid
C            >  0  MCF component index
C            <  0  solid CHT object with label given by
C                  'LABEL' (invalid)
C      LABEL : character string identifying equation solved
C      U,V,W : Cartesian velocity components
C          P : static pressure
C          T : static temperature
C        PHI : additional scalars
C       NPHI : number of additional scalars
C        XYZ : Cartesian coordinates of grid nodes
C      I,J,K : topological grid coordinates
C   ID,JD,KD : topological grid dimensions
C
C  Output:
C
C      VISCL : fluid viscosity
C
C  Local:
C
C     VISCFL : fluid viscosity
C       POFF : pressure offset (level shift)
C       TOFF : temperature offset (level shift)
C     SUTHER : logical variable indicates whether or not to use
C              Sutherland's law
C
C  Common Blocks:
C
C  /CONTRL/ is declared so that information can be added as needed
C           for desired equation of state.
C
C     IONUM  : integer, unit numbers in CONTRL common block.
C     IARR   : integer, integer switches in CONTRL common block.
C     RARR   : real, real constants in CONTRL common block.
C     CONST  : real, property constants in CONTRL common block.
C     LARR   : logical, logical switches in CONTRL common block.
C
C  /PHINUM/ contains scalar transport equation information.
C
C     IARRQ  : integer, integer switches in PHINUM common block.
C     RARRQ  : real, real constants in PHINUM common block.
C     LARRQ  : logical, logical switches in PHINUM common block.
```

```
C
C  NOTE: The true levels of pressure (P) and temperature (T) are
C        assumed to be
C           P_true = P + POFF
C           T_true = T + TOFF
C        where POFF and TOFF are level shifts in the actual dependent
C        values of P and T that are solved for.
CSCDE
C
C=======================================================================
C
C---------------------------
C Subroutine Arguments
C---------------------------
C
      REAL U(ID,JD,KD),V(ID,JD,KD),W(ID,JD,KD),P(ID,JD,KD),T(ID,JD,KD),
     &     PHI(ID,JD,KD,*),XYZ(ID,JD,KD,3),VISCL,TT
C
      INTEGER ILABEL,I,J,K,ID,JD,KD,NPHI
C
      CHARACTER*(*) LABEL
C
C---------------------------
C Local Variables
C---------------------------
C
      REAL VISCFL,POFF,TOFF
C
      LOGICAL SUTHER
C
C---------------------------
C Common Blocks
C---------------------------
C
      COMMON/CONTRL/ IONUM(100),IARR(200),RARR(100),CONST(100),LARR(200)
      REAL RARR,CONST
      INTEGER IONUM,IARR
      LOGICAL LARR
C
      EQUIVALENCE (CONST(5),VISCFL),(CONST(13),POFF),(CONST(14),TOFF),
     &            (LARR(83),SUTHER)
C
C
      COMMON/PHINUM/IARRQ(100,10),RARRQ(100,10),LARRQ(100,10)
      INTEGER IARRQ
      REAL RARRQ
      LOGICAL LARRQ
C
C---------------------------
C Executable Statements
C---------------------------
C
C------ SINGLE-COMPONENT FLUID
C
      TT=T(I,J,K)+TOFF

      IF (ILABEL.EQ.0) THEN
C
C------ USE SUTHERLAND's LAW FOR MOLECULAR VISCOSITY --
C
        IF (SUTHER) THEN
          VISCL = 1.458E-6*(T(I,J,K)+TOFF)**1.5/(T(I,J,K)+TOFF+110.4)
        ELSE
          VISCL = VISCFL
        ENDIF
C
C------ MULTI-COMPONENT FLUID
```

```
C
      ELSE IF (ILABEL.GT.0) THEN

        IF((ILABEL .EQ. 1).or.(ILABEL .EQ. 4)) THEN
          if (tt.gt.1200.) then
            viscl = 1.34e-5*(1200./293.)**0.87
          else
            viscl = 1.34e-5*(tt/293.)**0.87
          endif
        ELSE IF(ILABEL .EQ. 2) THEN
          if (tt.gt.1200.) then
            viscl = 2.0E-5*(1200./293.)**0.69
          else
            viscl = 2.0E-5*(TT/293.)**0.69
          endif
        ELSE IF(ILABEL .EQ. 3) THEN
          if (tt.gt.1200.) then
            vis1 = 1.48E-5*(1200./293.)**0.79
            vis2 = 1.02E-5*(1200./293.)**1.15
          else
            vis1 = 1.48E-5*(TT/293.)**0.79
            vis2 = 1.02E-5*(TT/293.)**1.15
          endif
c---------use mass fraction for CO2 and H2O
          viscl=.73*vis1+.27*vis2
        ELSE IF(ILABEL .EQ. 5) then
          if (tt.gt.1200.) then
            viscl = 1.76E-5*(1200./293.)**0.67
          else
            viscl = 1.76E-5*(tt/293.)**0.67
          endif
        ELSE
          write (6,*) 'propf.f error message number 101'
          write (6,*) 'stop propf', ilabel,i,j,k
          STOP 'PROPF: Invalid label'
        ENDIF
      ENDIF
C
      RETURN
      END
```

# B.9 propq.f

Calculates mass diffusion coefficient, $\Gamma_i$ for species $i$

```
C     ^^^^^^^^^^^^^^^^^^^^^^^^^^^^^^^^^^^^^^^^
C     | FURNITURE CFD FIRE MODEL VERSION 1.0 |
C     |           JANUARY 5, 1999            |
C     ^^^^^^^^^^^^^^^^^^^^^^^^^^^^^^^^^^^^^^^^
C
C     Calculates the scalar diffusion coefficient [mass/(length time)]
C     The diffusion coefficient is set equal to viscosity through a
C     Schmidt number of unity   Gam_i=mu_i/Sch

C     Species #1 FUEL (CH4)
C     Species #2 O2
C     Species #3 PROD (.73 CO2  .27 H2O)
C     Species #4 SOOT (Same as fuel)
C     Species #5 N2
C=======================================================================
C
      SUBROUTINE PROPQ(GAMAS,
     &                 U,V,W,P,T,PHI,NPHI,XYZ,
     &                 ILABEL,LABEL,I,J,K,ID,JD,KD)
C
C  ILABEL =  0   fluid
C          >0  MCF component index
C          <0  solid CHT object with label given by 'LABEL'
C
C  The common block /CONTRL/ is declared here so that information
C  can be added as needed for the desired equation of state.
C
C  NOTE: The true levels of pressure (P) and temperature (T) are
C  assumed to be
C          P_true = P + POFF
C          T_true = T + TOFF
C  where POFF and TOFF are level shifts in the actual dependent
C  values of P and T that are solved for.
C
C=======================================================================
C
      REAL U(ID,JD,KD),V(ID,JD,KD),W(ID,JD,KD),P(ID,JD,KD),T(ID,JD,KD),
     &     PHI(ID,JD,KD,NPHI),XYZ(ID,JD,KD,3),gam1,gam2,shmdt
      CHARACTER*(*) LABEL
      LOGICAL LARR,LARRQ
      COMMON/CONTRL/ IONUM(100),IARR(200),RARR(100),CONST(100),LARR(200)
      COMMON/PHINUM/IARRQ(100,10),RARRQ(100,10),LARRQ(100,10)
      EQUIVALENCE (CONST(13),POFF),(CONST(14),TOFF)

      shmdt=1.0
      IF(ILABEL.GT.0) THEN
        TT = T(I,J,K) + TOFF

        IF((ILABEL .EQ. 1).or.(ILABEL .EQ. 4)) THEN
          if (tt.gt.1200.) then
            gamas = (1.34e-5*(1200./293.)**0.87)*(1/shmdt)
          else
            gamas = (1.34e-5*(tt/293.)**0.87)*(1/shmdt)
          endif
        ELSE IF(ILABEL .EQ. 2) THEN
          if (tt.gt.1200.) then
            gamas = (2.0E-5*(1200./293.)**0.69)*(1/shmdt)
          else
            gamas = (2.0E-5*(TT/293.)**0.69)*(1/shmdt)
          endif
        ELSE IF(ILABEL .EQ. 3) THEN
          if (tt.gt.1200.) then
            gam1 = (1.48E-5*(1200./293.)**0.79)*(1/shmdt)
```

```
      gam2 = (1.02E-5*(1200./293.)**1.15)*(1/shmdt)
    else
      gam1 = (1.48E-5*(TT/293.)**0.79)*(1/shmdt)
      gam2 = (1.02E-5*(TT/293.)**1.15)*(1/shmdt)
    endif
    gamas=.73*gam1+.27*gam2
  ELSE IF(ILABEL .EQ. 5) then
    if (tt.gt.1200.) then
      gamas = (1.76E-5*(tt/293.)**0.67)*(1/shmdt)
    else
      gamas = (1.76E-5*(tt/293.)**0.67)*(1/shmdt)
    endif
  ELSE
    write (6,*) 'propq.f error message number 101'
    write (6,*) 'stop propq', ilabel,i,j,k
    STOP 'PROPQ: Invalid label'
  ENDIF

ENDIF

RETURN
END
```

## B.10 propr.f

Uses the ideal gas law to calculate density, $\rho$

```
C     ^^^^^^^^^^^^^^^^^^^^^^^^^^^^^^^^^^^^^^^^
C     | FURNITURE CFD FIRE MODEL VERSION 1.0 |
C     |           JANUARY 5, 1999            |
C     ^^^^^^^^^^^^^^^^^^^^^^^^^^^^^^^^^^^^^^^^
C
C     Calculates density for both fluid and solid node I,J,K
C     Species #1 FUEL (CH4)
C     Species #2 O2
C     Species #3 PROD (.73 CO2  .27 H2O) [R is gravimetrically based]
C     Species #4 SOOT (Same as fuel)
C     Species #5 N2
C
C=======================================================================
C
      SUBROUTINE PROPR(RHO,ARP,ARB,EQST,
     &                 U,V,W,P,T,PHI,NPHI,XYZ,
     &                 ILABEL,LABEL,I,J,K,ID,JD,KD)
C
C  Input:
C
C     ILABEL =  0  single component fluid
C            >  0  MCF component index
C            <  0  solid CHT object with label given by 'LABEL'
C      LABEL : character string identifying equation solved
C      U,V,W : Cartesian velocity components
C          P : static pressure
C          T : static temperature
C        PHI : additional scalars
C       NPHI : number of additional scalars
C        XYZ : Cartesian coordinates of grid nodes
C    ARP,ARB : coefficients in linearized equation of state
C       EQST : logical variable indicating whether or not to use the
C              equation of state
C      I,J,K : topological grid coordinates
C   ID,JD,KD : topological grid dimensions
C
C  Output:
C
C        RHO : control volume density
C
C  Local:
C
C     MAXMCF : work space parameter for multi-component fluids
C       POFF : pressure offset (level shift)
C       TOFF : temperature offset (level shift)
C         SN : small number
C      CONDL : local thermal conductivity
C         CP : specific heat at constant pressure
C         CV : specific heat at constant volume
C     RIDEAL : ideal gas constant for fluid
C     RHOSOL : solid density
C     RHOFLD : fluid density
C
C  Common Blocks:
C
C  /CONTRL/ is declared so that information can be added as needed
C           for desired equation of state.
C
C     IONUM  : integer, unit numbers in CONTRL common block.
C     IARR   : integer, integer switches in CONTRL common block.
C     RARR   : real, real constants in CONTRL common block.
C     CONST  : real, property constants in CONTRL common block.
```

```
C     LARR   : logical, logical switches in CONTRL common block.
C
C  /MULTIF/ contains information for multicomponent fluids.
C
C     DENSQ  : real, component density.
C     ZMOLQ  : real, component molecular weight.
C     CONDQ  : real, component conductivity.
C     CPHTQ  : real, component specific heat at constant pressure.
C     CVHTQ  : real, component specific heat at constant volume.
C     LMCFQ  : logical, multi-component fluid.
C     EQSTQ  : logical, equation of state.
C     NMCF   : integer, number of components.
C     NMCFNA : integer, maximum scalar which is a multi-component fluid.
C
C  NOTE: The true levels of pressure (P) and temperature (T) are
C        assumed to be
C           P_true = P + POFF
C           T_true = T + TOFF
C        where POFF and TOFF are level shifts in the actual dependent
C        values of P and T that are solved for.
CSCDE
C=======================================================================
C
C-------------------------
C Subroutine Arguments
C-------------------------
C
      INTEGER NPHI,ILABEL,I,J,K,ID,JD,KD
C
      REAL U(ID,JD,KD),V(ID,JD,KD),W(ID,JD,KD),P(ID,JD,KD),T(ID,JD,KD),
     &     PHI(ID,JD,KD,*),XYZ(ID,JD,KD,3),RHO,ARP,ARB
C
      LOGICAL EQST
C
      CHARACTER*(*) LABEL
C
C-------------------------
C Local Variables
C-------------------------
C
      INTEGER MAXMCF
      PARAMETER (MAXMCF = 100)
C
      REAL POFF,TOFF,RHOSOL,RHOFLD,SN,CONDL,CP,CV,RIDEAL
      PARAMETER (SN = 1.E-20)
C
C-------------------------
C Common Blocks
C-------------------------
C
      COMMON/CONTRL/ IONUM(100),IARR(200),RARR(100),CONST(100),LARR(200)
      INTEGER IONUM,IARR
      REAL RARR,CONST
      LOGICAL LARR
C
      EQUIVALENCE (CONST(13),POFF),(CONST(14),TOFF),
     &            (CONST(1),RHOFLD),(CONST(28),RHOSOL)
C
      COMMON /MULTIF/ DENSQ(MAXMCF),ZMOLQ(MAXMCF),
     &                CONDQ(MAXMCF),CPHTQ(MAXMCF),CVHTQ(MAXMCF),
     &                LMCFQ(MAXMCF),EQSTQ(MAXMCF),NMCF,NMCFNA
      INTEGER NMCF,NMCFNA
      REAL DENSQ,ZMOLQ,CONDQ,CPHTQ,CVHTQ
      LOGICAL LMCFQ,EQSTQ
C
C---------------------------
C Executable Statements
```

```
C----------------------------

C=============== SINGLE-COMPONENT FLUID ================
C
      IF (ILABEL.EQ.0) THEN
C
C------ Constant density ------
C       Set through PRM file parameter RHOFLD if EQUATION_OF_STATE=T
C
        IF (.NOT.EQST) THEN
          RHO = RHOFLD
C
C------ Equation of state ------
C
        ELSE
C
C  Get thermal properties of single fluid
          CALL PROPT (CONDL,CP,CV,
     &                U,V,W,P,T,PHI,NPHI,XYZ,
     &                ILABEL,LABEL,I,J,K,ID,JD,KD)
C
C  Calculate coefficients of the linearized equation of state
C  for density, such that
C         RHO = ARP*P + ARB = (P+POFF)/(RIDEAL*(T+TOFF))
C  Apply ideal gas law
C
          RIDEAL = CP - CV
          ARP = 1.0/(RIDEAL*(T(I,J,K)+TOFF+SN))
          ARB = POFF*ARP
          RHO = ARP * P(I,J,K) + ARB
        ENDIF
C
C
C============== MULTI-COMPONENT FLUID SPECIES ================
C
      ELSE IF (ILABEL.GT.0) THEN
C
C------ Constant density for species ------
C       Set though PRM file parameter DENSITYn if EQSTn=T
C
        IF (.NOT.EQSTQ(ILABEL)) THEN
          RHO = DENSQ(ILABEL)
          ARP = 0.0
          ARB = 0.0
C
C------ Equation of state for species ------
C
        ELSE

C  Get thermal properties of component and apply ideal gas law
            CALL PROPT (CONDL,CP,CV,
     &                  U,V,W,P,T,PHI,NPHI,XYZ,
     &                  ILABEL,LABEL,I,J,K,ID,JD,KD)
            RIDEAL = CP - CV

            ARP = 1.0/(RIDEAL*(T(I,J,K)+TOFF+SN))
            ARB = POFF*ARP
            RHO = ARP * P(I,J,K) + ARB
c-----------use density for soot
            if (ilabel.eq.4) then
              rho = 1100.0
            endif
        ENDIF
C
C
C=============== SOLID (CHT) DENSITY ==============
C
```

```
      ELSE
        if (label .eq. 'SKIRT') then
c          rno = density of steel
           RHO = 7854.
        elseif (label .eq. 'HOOD') then
c          rho = density of steel
          RHO = 7854.
        elseif (label .eq. 'BURNER') then
c          rho = density of steel
          RHO = 7854.
        elseif ((label .eq. 'BASE').or.
     &          (label.eq.'PU1').or.(label.eq.'PU2').or.
     &          (label.eq.'PU3').or.(label.eq.'PU4')) then
c          correct for PU foam
           RHO = 20.
        elseif (label.eq.'COTTON') then
c          rho = density of cotton fabric
           RHO = 1350.
        endif
      ENDIF

      RETURN
      END
```

## B.11 propt.f

Calculates fluid and CHT solid thermal properties such as specific heat, $c_p$, and thermal conductivity, $k$

```
C     ^^^^^^^^^^^^^^^^^^^^^^^^^^^^^^^^^^^^^^^^
C     | FURNITURE CFD FIRE MODEL VERSION 1.0 |
C     |           JANUARY 5, 1999            |
C     ^^^^^^^^^^^^^^^^^^^^^^^^^^^^^^^^^^^^^^^^
C
C     Calculates specific heat and thermal conductivity values
C     for fluid and solid nodes
C     Species #1 FUEL (CH4)
C     Species #2 O2
C     Species #3 PROD (.73 CO2  .27 H2O)
C     Species #4 SOOT (Same as fuel)
C     Species #5 N2
C=======================================================================
C
      SUBROUTINE PROPT(CONDL,CPHEAT,CVHEAT,
     &                 U,V,W,P,T,PHI,NPHI,XYZ,
     &                 ILABEL,LABEL,I,J,K,ID,JD,KD)
C
CSCDB
C  Input:
C
C     ILABEL = 0   fluid
C            > 0  MCF component index
C            < 0  solid CHT object with label given by 'LABEL'
C      LABEL : character string identifying equation solved
C      U,V,W : Cartesian velocity components
C          P : static pressure
C          T : static temperature
C        PHI : additional scalars
C       NPHI : number of additional scalars
C        XYZ : Cartesian coordinates of grid nodes
C      I,J,K : topological grid coordinates
C   ID,JD,KD : topological grid dimensions
C
C  Output:
C
C      CONDL : local thermal conductivity
C     CPHEAT : specific heat at constant pressure
C     CVHEAT : specific heat at constant volume
C
C  Local:
C
C     MAXMCF : work space parameter for multi-component fluids
C       POFF : pressure offset (level shift)
C       TOFF : temperature offset (level shift)
C     CONDFL : fluid conductivity
C     CONDSL : solid conductivity
C      CPFLD : fluid specific heat at constant pressure
C      CVFLD : fluid specific heat at constant volume
C      CCSOL : solid specific heat
C     SUTHER : logical variable indicating whether or not to use
C              Sutherland's law
C
C  Common Blocks:
C
C  /CONTRL/ is declared so that information can be added as needed
C           for desired equation of state.
C
C     IONUM  : integer, unit numbers in CONTRL common block.
C     IARR   : integer, integer switches in CONTRL common block.
```

```
C     RARR   : real, real constants in CONTRL common block.
C     CONST  : real, property constants in CONTRL common block.
C     LARR   : logical, logical switches in CONTRL common block.
C
C  /MULTIF/ contains information for multicomponent fluids.
C
C     DENSQ  : real, component density.
C     ZMOLQ  : real, component molecular weight.
C     CONDQ  : real, component conductivity.
C     CPHTQ  : real, component specific heat at constant pressure.
C     CVHTQ  : real, component specific heat at constant volume.
C     LMCFQ  : logical, multi-component fluid.
C     EQSTQ  : logical, equation of state.
C     NMCF   : integer, number of components.
C     NMCFNA : integer, maximum scalar which is a multi-component fluid.
C
C  NOTE: The true levels of pressure (P) and temperature (T) are
C        assumed to be
C           P_true = P + POFF
C           T_true = T + TOFF
C        where POFF and TOFF are level shifts in the actual dependent
C        values of P and T that are solved for.
CSCDE
C
C=======================================================================
C
C-----------------------------
C Subroutine Arguments
C-----------------------------
C
      INTEGER NPHI,I,J,K,ID,JD,KD,ILABEL
C
      REAL U(ID,JD,KD),V(ID,JD,KD),W(ID,JD,KD),P(ID,JD,KD),T(ID,JD,KD),
     &     PHI(ID,JD,KD,*),XYZ(ID,JD,KD,3),CONDL,CPHEAT,CVHEAT
C
      CHARACTER*(*) LABEL
C
C-----------------------------
C Local Variables
C-----------------------------
C
      INTEGER MAXMCF
      PARAMETER (MAXMCF = 100)
C
      REAL CONDFL,CPFLD,CVFLD,CONDSL,CCSOL,POFF,TOFF
C
      LOGICAL SUTHER
C
C-----------------------------
C Common Blocks
C-----------------------------
C
      COMMON/CONTRL/ IONUM(100),IARR(200),RARR(100),CONST(100),LARR(200)
      INTEGER IONUM,IARR
      REAL RARR,CONST
      LOGICAL LARR
C
      EQUIVALENCE (CONST(3),CONDFL),(CONST(11),CPFLD),(CONST(12),CVFLD),
     &            (CONST(29),CONDSL),(CONST(30),CCSOL),
     &            (CONST(13),POFF),(CONST(14),TOFF),(LARR(83),SUTHER)
C
      COMMON /MULTIF/ DENSQ(MAXMCF),ZMOLQ(MAXMCF),
     &                CONDQ(MAXMCF),CPHTQ(MAXMCF),CVHTQ(MAXMCF),
     &                LMCFQ(MAXMCF),EQSTQ(MAXMCF),NMCF,NMCFNA
      INTEGER NMCF,NMCFNA
      REAL DENSQ,ZMOLQ,CONDQ,CPHTQ,CVHTQ
      LOGICAL LMCFQ,EQSTQ
```

```
C
C --- Property data block
C
      PARAMETER (RGAS=8.3143)
C
      REAL CPCH4(5,2), CPO2(5,2), CPH2O(5,2), CPCO2(5,2), CPCH2O(5,2),
     &     CPN2(5,2), tmpcp1, tmpcp2, tmpcv1, tmpcv2,
     &     tmpk1, tmpk2
C
C-------------------------------
C Data Statements
C-------------------------------
      DATA CPCH4/
     &         1.63552643E+00,  1.00842795E-02, -3.36916254E-06,
     &         5.34958667E-10, -3.15518833E-14,
     &         5.14987613E+00, -1.36709788E-02,  4.91800599E-05,
     &        -4.84743026E-08,  1.66693956E-11/
      DATA CPO2/
     &         3.66096083E+00,  6.56365523E-04, -1.41149485E-07,
     &         2.05797658E-11, -1.29913248E-15,
     &         3.78245636E+00, -2.99673415E-03,  9.84730200E-06,
     &         -9.68129508E-09, 3.24372836E-12/
      DATA CPH2O/
     &         2.67703787E+00, 2.97318329E-03,-7.73769690E-07,
     &         9.44336689E-11,-4.26900959E-15,
     &         4.19864056E+00,-2.03643410E-03, 6.52040211E-06,
     &        -5.48797062E-09, 1.77197817E-12/
      DATA CPCO2/
     &         4.63659493E+00, 2.74131991E-03,-9.95828531E-07,
     &         1.60373011E-10,-9.16103468E-15,
     &         2.35677352E+00, 8.98459677E-03,-7.12356269E-06,
     &         2.45919022E-09,-1.43699548E-13/
      DATA CPCH2O/
     &         3.16952654E+00, 6.19320583E-03,-2.25056377E-06,
     &         3.65975680E-10,-2.20149470E-14,
     &         4.79372315E+00,-9.90833369E-03, 3.73220008E-05,
     &        -3.79285261E-08, 1.31772652E-11/
      DATA CPN2/
     &         2.95257626E+00, 1.39690057E-03,-4.92631691E-07,
     &         7.86010367E-11,-4.60755321E-15,
     &         3.53100528E+00,-1.23660987E-04,-5.02999437E-07,
     &         2.43530612E-09,-1.40881235E-12/

C
C-------------------------------
C Executable Statements
C-------------------------------
      TT = T(I,J,K) + TOFF

C------ SINGLE-COMPONENT FLUID

      IF (ILABEL.EQ.0) THEN

C------ USE SUTHERLAND'S LAW FOR THERMAL CONDUCTIVITY -----

        IF (SUTHER) THEN
            CONDL  = 2.502E-3*(TT)**1.5/(TT+194.4)
        ELSE
          CONDL = CONDFL
        ENDIF
        CPHEAT = CPFLD
        CVHEAT = CVFLD

C------ MULTI-COMPONENT FLUID COMPONENT

      ELSE IF (ILABEL.GT.0) THEN
c        CPHEAT = RGAS / WM(ILABEL)
```

```
C       Units on CPHEAT are j/kg K

        IF (TT .GT. 1000.) THEN
          IF((ILABEL.EQ.1) .or. (ILABEL.EQ.4)) THEN
            CPHEAT = (RGAS / .016)*
     &              (CPCH4(1,1) + TT * ( CPCH4(2,1) +
     &                           TT * ( CPCH4(3,1) +
     &                           TT * ( CPCH4(4,1) +
     &                           TT * ( CPCH4(5,1) )))))
            CVHEAT = CPHEAT - RGAS / (.016)
            if (TT.gt.1270.) then
              condl = -1.869E-3 + 8.727E-5*(1270.)
     &                +1.179E-7*(1270.**2)
     &                -3.614E-11*(1270.**3)
            else
              condl = -1.869E-3 + 8.727E-5*TT+1.179E-7*(TT**2)
     &                -3.614E-11*(TT**3)
            endif
          ELSEIF(ILABEL.EQ.2) THEN
            CPHEAT = (RGAS / .032)*
     &              (CPO2(1,1) + TT * ( CPO2(2,1) +
     &                           TT * ( CPO2(3,1) +
     &                           TT * ( CPO2(4,1) +
     &                           TT * ( CPO2(5,1) )))))
            CVHEAT = CPHEAT - RGAS / (.032)
            CONDL  = CPHEAT * 1.74E-6*TT**1.5/(TT+138.9) / 0.71
          ELSEIF(ILABEL.EQ.3) THEN
C                                    product
            tmpcp1 = (RGAS / .044)*
     &              (CPCO2(1,1) + TT * ( CPCO2(2,1) +
     &                           TT * ( CPCO2(3,1) +
     &                           TT * ( CPCO2(4,1) +
     &                           TT * ( CPCO2(5,1) )))))

            tmpcp2 = (RGAS / .018)*
     &              (CPH2O(1,1) + TT * ( CPH2O(2,1) +
     &                           TT * ( CPH2O(3,1) +
     &                           TT * ( CPH2O(4,1) +
     &                           TT * ( CPH2O(5,1) )))))

            if (TT.GT.1670.) then
              tmpk1 =-7.215E-3 + 8.015E-5*(1670.)
     &               + 5.477E-9*(1670.**2)
     &               -1.053E-11*(1670.**3)
            else
              tmpk1 =-7.215E-3 + 8.015E-5*TT +5.477E-9*(TT**2)
     &               -1.053E-11*(TT**3)
            endif
            if (TT.GT.1200.) then
              tmpk2 = 7.341E-3 - 1.013E-5*(1200)
     &               +1.801E-7*(1200.**2)
     &               -9.100E-11*(1200.**3)
            else
              tmpk2 = 7.341E-3 - 1.013E-5*TT +1.801E-7*(TT**2)
     &               -9.100E-11*(TT**3)
            endif
            cpheat = .73*tmpcp1+.27*tmpcp2
            CVHEAT = .73*(tmpcp1 - RGAS / (.044))+
     &               .27*(tmpcp2 - RGAS / (.018))
            CONDL  = .73*tmpk1+.27*tmpk2
          ELSEIF(ILABEL.EQ.5) THEN
            CPHEAT = (RGAS / .028)*
     &              (CPN2(1,1) + TT * ( CPN2(2,1) +
     &                           TT * ( CPN2(3,1) +
     &                           TT * ( CPN2(4,1) +
     &                           TT * ( CPN2(5,1) )))))
```

```
            CVHEAT = CPHEAT - RGAS / (.028)
            if (TT.gt.1470.) then
              condl=3.919E-4 + 9.816E-5*1470.
     &              - 5.067E-8*(1470.**2)
     &              + 1.504E-11*(1470.**3)
            else
              condl=3.919E-4 + 9.816E-5*TT - 5.067E-8*(TT**2)
     &              + 1.504E-11*(TT**3)
            endif
          ENDIF
C                     TT lower than 1000. K
C       Units on CPHEAT are j/kg K
          ELSE
            IF((ILABEL.EQ.1) .or. (ilabel.eq.4)) THEN
              CPHEAT = (RGAS / .016)*
     &              (CPCH4(1,2) + TT * ( CPCH4(2,2) +
     &                           TT * ( CPCH4(3,2) +
     &                           TT * ( CPCH4(4,2) +
     &                           TT * ( CPCH4(5,2) )))))
              CVHEAT = CPHEAT - RGAS / (.016)
              condl = -1.869E-3 + 8.727E-5*TT+1.179E-7*(TT**2)
     &              -3.614E-11*(TT**3)
            ELSEIF(ILABEL.EQ.2) THEN
              CPHEAT = (RGAS / .032)*
     &              (CPO2(1,2) + TT * ( CPO2(2,2) +
     &                          TT * ( CPO2(3,2) +
     &                          TT * ( CPO2(4,2) +
     &                          TT * ( CPO2(5,2) )))))
              CVHEAT = CPHEAT - RGAS / (.032)
              CONDL  = CPHEAT * 1.74E-6*TT**1.5/(TT+138.9) / 0.71
            ELSEIF(ILABEL.EQ.3) THEN
              tmpcp1 = (RGAS / .044)*
     &              (CPCO2(1,2) + TT * ( CPCO2(2,2) +
     &                           TT * ( CPCO2(3,2) +
     &                           TT * ( CPCO2(4,2) +
     &                           TT * ( CPCO2(5,2) )))))
              tmpcp2 = (RGAS / .018)*
     &              (CPH2O(1,2) + TT * ( CPH2O(2,2) +
     &                           TT * ( CPH2O(3,2) +
     &                           TT * ( CPH2O(4,2) +
     &                           TT * ( CPH2O(5,2) )))))
              tmpk1 =-7.215E-3 + 8.015E-5*TT +5.477E-9*(TT**2)
     &             -1.053E-11*(TT**3)
              tmpk2 =7.341E-3 - 1.013E-5*TT +1.801E-7*(TT**2)
     &             -9.100E-11*(TT**3)
              cpheat = .73*tmpcp1+.27*tmpcp2
              CVHEAT = .73*(tmpcp1 - RGAS / (.044))+
     &              .27*(tmpcp2 - RGAS / (.018))
              CONDL  = .73*tmpk1+.27*tmpk2
            ELSEIF(ILABEL.EQ.5) THEN
              CPHEAT = RGAS / (.028) *
     &              (CPN2(1,2) + TT * ( CPN2(2,2) +
     &                          TT * ( CPN2(3,2) +
     &                          TT * ( CPN2(4,2) +
     &                          TT * ( CPN2(5,2) )))))
              CVHEAT = CPHEAT - RGAS / (.028)
              condl=3.919E-4 + 9.816E-5*TT - 5.067E-8*(TT**2)
     &           + 1.504E-11*(TT**3)
            ENDIF
          ENDIF
C
          if (condl.le.0.0) then
            write (6,*) 'propt.f error message number 101'
            write (6,*) 'Negative thermal conductivity calculated'
            write (6,*) 'in propt.f',i,j,k,tt,condl
            write (6,*) 'Resetting to .01'
            condl=.01
```

```
          cpheat=1.
          cvheat=1.
        endif
C
C---- USE SOLID DEFAULT THERMAL PROPERTIES
C
      ELSE
C       set thermal properties for steel
        CONDL  = CONDSL
        CVHEAT = CCSOL
          if ((label .eq. 'HOOD') .or. (label .eq. 'SKIRT')
     &         .or. (label .eq. 'BURNER')) then
               IF((TT.GE.273.).AND.(TT.LT.373.)) THEN
                 CONDL  = 60.
                 cvheat = 380.
               ELSEIF((TT.GE.373.).AND.(TT.LT.473.))THEN
                 CONDL = 57.
                 cvheat = 380.
               ELSEIF((TT.GE.473.).AND.(TT.LT.573.))THEN
                 CONDL = 53.
                 cvheat = 385.
               ELSEIF((TT.GE.573.).AND.(TT.LT.673.))THEN
                 CONDL = 48.
                 cvheat = 460.
               ELSEIF((TT.GE.673.).AND.(TT.LT.773.))THEN
                 CONDL = 44.
                 cvheat = 470.
               ELSEIF((TT.GE.773.).AND.(TT.LT.873.))THEN
                 CONDL = 39.
                 cvheat = 505.
               ELSEIF((TT.GE.873.).AND.(TT.LT.973.))THEN
                 CONDL = 35.
                 cvheat = 530.
               ELSEIF((TT.GE.973.).AND.(TT.LT.1073.))THEN
                 CONDL = 30.
                 cvheat = 585.
               ELSEIF((TT.GE.1073.).AND.(TT.LT.1173.))THEN
                 CONDL = 28.
                 cvheat = 675.
               ELSEIF((TT.GE.1173.).AND.(TT.LT.1273.))THEN
                 CONDL = 27.
                 cvheat = 670.
               ELSEIF((TT.GE.1273.))THEN
                 CONDL = 27.
                 cvheat = 670.
               ELSEIF((TT.LT.273.))THEN
                 write (6,*) 'propt.f error message number 102'
                 write (6,*) 'Low Base Temp',I,J,K,TT
               ENDIF
          elseif ((label .eq. 'BASE').or.(label.eq.'PU1').or.
     &             (label.eq.'PU2').or.(label.eq.'PU3').or.
     &             (label.eq.'PU4'))then
c              properties for PU
               condl = .04
c              specific heat for PU foam is just about constant
               cvheat = 1884.
c               cvheat = 1700.
            if (tt.lt.273.) then
              write (6,*) 'propt.f error message number 103'
              write (6,*) 'Low Base Temp',I,J,K,TT
              write (6,*) xyz(i,j,k,1),xyz(i,j,k,2),xyz(i,j,k,3)
            ENDIF

          elseif (label.eq.'COTTON') then
               condl = .324
               cvheat = 1300.
            if (tt.lt.273.) then
```

```
        write (6,*) 'propt.f error message number 104'
        write (6,*) 'Low Base Temp',I,J,K,TT
        write (6,*) xyz(i,j,k,1),xyz(i,j,k,2),xyz(i,j,k,3)
      ENDIF
    endif
ENDIF

RETURN
END
```

# B.12 prpfvr.f

Controlling routine for RADCAL

```
C     ^^^^^^^^^^^^^^^^^^^^^^^^^^^^^^^^^^^^^^^^
C     | FURNITURE CFD FIRE MODEL VERSION 1.0 |
C     |           JANUARY 5, 1999            |
C     ^^^^^^^^^^^^^^^^^^^^^^^^^^^^^^^^^^^^^^^^
C
C     CONTROLLING PROGRAM FOR SUBROUTINE "RADCAL", A NARROW-BAND
C     MODEL FOR CALCULATING SPECTRAL INTENSITY (W/M-2/SR/MICRON) AND
C     SPECTRAL TRANSMITTANCE VERSUS WAVELENGTH (MICRONS) IN A NONISO-
C     THERMAL, VARIABLE COMPOSITION  MIXTURE OF CO2, H2O, CO, N2, O2,
C     CH4, AND SOOT.   FOR A HOMOGENEOUS PATH, THE PROGRAM ALSO COMPUTES
C     THE PLANCK-MEAN ABSORPTION COEF., APO, THE INCIDENT-MEAN ABSORPTION
C     COEFFICIENT, AIWALL, AND THE EFFECTIVE-MEAN ABSORPTION COEFFICIENT,
C     AMEAN, ALL IN UNITS OF INVERSE METERS.
c
C=======================================================================
C
      SUBROUTINE PRPFVR(ABSRP,QVOL,CVOL,XYZ,FEPC,ITYPHY,
     &                  U,V,W,P,T,RHO,TKE,EPS,PHI,NPHI,INTEN,
     &                  NLING,LLTOG,SANG,NLVEC,NSANGD,NILGRP,
     &                  SRFAVL,IB,IE,JB,JE,KB,KE,
     &                  ILABEL,LABEL,IWK,RWK,DWK,CWK,LWK,
     &                  NIBLK,NRBLK,NDWK,NCWK,NLWK,
     &                  RZ,IZ,CZ,LZ,DZ,ID,JD,KD)
C
CSCDT Calculates thermal radiation properties of fluid and particles
C
CSCDB
C
C  Input:
C
C     ILABEL = 0  fluid
C            < 0  solid CHT object with label given by 'LABEL'
C      LABEL : character string identifying equation solved
C          T : static temperature
C        XYZ : Cartesian coordinates of grid nodes
C   ITYPHY   : physical type of control volume .LE.2 is fluid
C   ID,JD,KD : topological grid dimensions
C   IWK   : is the integer temporary workspace array
C   RWK   : is the real temporary workspace array
C   DWK   : is the double precision temporary workspace array
C   CWK   : is the character temporary workspace array
C   LWK   : is the logical temporary workspace array
C   NIBLK : is the integer temporary workspace no. of IDxJDxKD blocks
C   NRBLK : is the real temporary workspace no. of IDxJDxKD blocks
C   NDWK  : is the double precision temporary workspace
C   NCWK  : is the character temporary workspace
C   NLWK  : is the logical temporary workspace
C   IZ    : global integer array
C   RZ    : global real array
C   DZ    : global double precision array
C   CZ    : global character array
C   LZ    : global logical array
C   SRFAVL: Surface area to volume ratio.
C   ID,JD,KD : dummy computational domain dimensions
C
C  Output:
C
C      ABCGM  : ABsorption Coefficient for Grey Medium

C  Local:
C
C      POFF : pressure offset (level shift)
```

```
C      TOFF : temperature offset (level shift)
C    ABSRBM : absorptivity of medium
C   ERCODE  : integer used for error identification (=0)
C   ERSTOP  : logical used to describe the appropriate action on error
C
C  NOTE: The true levels of pressure (P) and temperature (T) are
C        assumed to be
C           P_true = P + POFF
C           T_true = T + TOFF
C
C        where POFF and TOFF are level shifts in the actual dependent
C        values of P and T that are solved for.
CSCDE
C
C=======================================================================
C
C--------------------------
C Subroutine Arguments
C--------------------------
C
      REAL RZ(*),RWK(ID,JD,KD,NRBLK),SRFAVL(ID,JD,KD),
     &     U(ID,JD,KD),V(ID,JD,KD),W(ID,JD,KD),P(ID,JD,KD),T(ID,JD,KD),
     &     RHO(ID,JD,KD),TKE(ID,JD,KD),EPS(ID,JD,KD),PHI(ID,JD,KD,*),
     &     INTEN(ID,JD,KD,*),QVOL(ID,JD,KD,8),CVOL(ID,JD,KD),
     &     XYZ(ID,JD,KD,3),FEPC(ID,JD,KD),ABSRP(ID,JD,KD),
     &     SANG(NSANGD),NLVEC(3,NSANGD)
C
      REAL pathl(90,90,90),oldphi(90,90,90,5),oldab(90,90,90)
      INTEGER ivisit,nupdat
C
      INTEGER IZ(*),IWK(ID,JD,KD,NIBLK),ITYPHY(ID,JD,KD),
     &        NIBLK,NRBLK,NDWK,NCWK,NLWK
C
      LOGICAL LZ(*),LWK(NLWK)
C
      CHARACTER*(*) CZ(*),CWK(NCWK)
C
      DOUBLE PRECISION DZ(*),DWK(NDWK)
C
      INTEGER ID,JD,KD,NLING(NSANGD),LLTOG(NSANGD)
C
      CHARACTER*(*) LABEL
C
C--------------------------
C Local Variables
C--------------------------
C
      INTEGER nodex_fb,nplb,ni,nj,nk,ncnt,isave,jsave,ksave,
     &        ilsave,jlsave,klsave,iterad,junk(4)
C
      REAL absul, abspl, absll, x, y, z, yfuel, yo2, yprod, yn2
      real xfuel, xo2, xprod, xn2, xco2, xh2o, yco2, yh2o, tmpg, tmps
      real pph2o, ppco2, ptemp, wco2,wh2o,wfuel,wo2,wprod,wn2,xsum
      real sk,vf, ysoot, volcv,xdif,ydif,zdif,asurf,runtim,dt
      real xm,xp,ym,yp,zm,zp,cvmass,sootm,sootv,fv2,cvrho,cnglim
      real timdif,gaslim,sotlim,zmolh2o
C
      REAL POFF,TOFF,ABSRBM
C
C--------------------------
C Common Blocks
C--------------------------
C
      REAL RARR,CONST
      INTEGER IONUM,IARR
      LOGICAL LARR
      COMMON/CONTRL/ IONUM(100),IARR(200),RARR(100),CONST(100),LARR(200)
```

```
      EQUIVALENCE (CONST(13),POFF),(CONST(14),TOFF),
     &            (IONUM(20),ITRM),(IONUM(21),IOUT)
C
C     Common block for finite volume radiation model.
      REAL RARFVR
      INTEGER IARFVR
      LOGICAL LARFVR,LMPART
      COMMON/FVRAD/ RARFVR(100),IARFVR(100),LARFVR(100)
      EQUIVALENCE (LARFVR(3),LMPART),(RARFVR(9),ABSRBM)
C
C---------------------------
C Executable Statements
C---------------------------
C
c     Main body of absoptivity calulation routine
C
      nout=21

      DO 100 K=KB,KE
      DO 100 J=JB,JE
      DO 100 I=IB,IE
c        NODES=(I-1)+(J-1)*ID+(K-1)*ID*JD
        IF(ITYPHY(I,J,K).LE.2) THEN

c       This section only called once at start of run
        if (ilabel .ge. 0) then
          if (ncnt .eq. 0) then
            ncnt=1
            isave=i
            jsave=j
            ksave=k

c           open data input file
            open (unit=10, file='flame.dat', status='unknown')
c-----------read in values from flame.dat
            read (10,*) junk(1)
            read (10,*) junk(2)
            read (10,*) junk(3)
            read (10,*) junk(4)
            read (10,*) rhofuel
            read (10,*) tign
            read (10,*) fign
            read (10,*) hevap
            read (10,*) abeta
            read (10,*) wfuel
            read (10,*) wo2
            read (10,*) wprod
            read (10,*) wsoot
            read (10,*) wn2
            read (10,*) wco2
            read (10,*) wh2o
            read (10,*) zmolh2o
            read (10,*) cnglim
            read (10,*) tmps
            read (10,*) gaslim
            read (10,*) sotlim
            read (10,*) iterad
            read (10,*) flux1
            read (10,*) flux2
            read (10,*) flux3

            close (unit=10)

            nupdat=0
            timdif=-1.0
            itrcnt=iterad
            wvmin=50.
```

```
            wvmax=10000.

          endif

          if ((i.eq.isave).and.(j.eq.jsave).and.(k.eq.ksave)) then
            ncnt=ncnt+1
          endif

c---------This section visited for every fluid node during first iteration
          if (ncnt .eq. 2) then
c           calculate mean beam length, pathl
c           pl=3.6*cvol(i,j,k)/asurf
c           pathl(i,j,k)=3.6*((cvol(i,j,k))**(.333333))
            pathl(i,j,k)=3.6/srfavl(i,j,k)

            if (pathl(i,j,k) .le. 0.0) then
              write (6,*) 'prpfvr.f error message number 101'
              write (6,*) 'pl less than zero', i,j,k,
     &                    srfavl(i,j,k),pathl(i,j,k)
              write (nout,*) 'prpfvr.f error message number 101'
              write (nout,*) 'pl less than zero', i,j,k,
     &                    srfavl(i,j,k),pathl(i,j,k)
              pathl(i,j,k)=.001
            endif
            if (pathl(i,j,k) .le. 1e-4) then
              write (6,*) 'prpfvr.f error message number 102'
              write (6,*) 'small pl', i,j,k,cvol(i,j,k),pathl(i,j,k)
              write (nout,*) 'prpfvr.f error message number 102'
              write (nout,*) 'small pl', i,j,k,cvol(i,j,k),pathl(i,j,k)
            endif
            ilsave=i
            jlsave=j
            klsave=k
            nupdat=-1
          endif

c---------This section called during every iteration
          if ((i.eq.isave).and.(j.eq.jsave).and.(k.eq.ksave)) then
            write (6,*) '#$#$#$#$#$ In prpfvr.f using RADCAL #$#$#$#$#$'
            write (nout,*) '#$#$#$#$#$ In prpfvr.f using ',
     &                     'RADCAL #$#$#$#$#$'
c           control when radcal is called
            if (itrcnt.eq.iterad) then
              ivisit=1
              itrcnt=1
            else
c             do not calculate
              ivisit=0
              itrcnt=itrcnt+1
            endif
          endif

c         set gas and black body source temp equal to fluid temp
          tmpg=t(i,j,k)
          ptemp=p(i,j,k)+poff

c         convert pressure from Pa to kPa
          ptemp=ptemp/1000.

c         calc vf based on mass fraction and density
          vf=phi(i,j,k,4)*(rho(i,j,k))/(1100.)

c---------This section only called for nodes with sufficient
c         change in species concentration to warrant
c         recalculation of absorptivity
          if (((((phi(i,j,k,1).lt.(oldphi(i,j,k,1)*(1-cnglim))).or.
     &      (phi(i,j,k,1).gt.(oldphi(i,j,k,1)*(1+cnglim)))).and.
```

```
     &      (phi(i,j,k,1).gt.gaslim)).or.
     &      (((phi(i,j,k,2).lt.(oldphi(i,j,k,2)*(1-cnglim))).or.
     &      (phi(i,j,k,2).gt.(oldphi(i,j,k,2)*(1+cnglim)))).and.
     &      (phi(i,j,k,2).gt.gaslim)).or.
     &      (((phi(i,j,k,3).lt.(oldphi(i,j,k,3)*(1-cnglim))).or.
     &      (phi(i,j,k,3).gt.(oldphi(i,j,k,3)*(1+cnglim)))).and.
     &      (phi(i,j,k,3).gt.gaslim)).or.
     &      (((phi(i,j,k,4).lt.(oldphi(i,j,k,4)*(1-cnglim))).or.
     &      (phi(i,j,k,4).gt.(oldphi(i,j,k,4)*(1+cnglim)))).and.
     &      (vf.gt.sotlim))).and.(ivisit.eq.1)) then

c-----------calculate volume fractions and save species concentrations
            nupdat=nupdat+1
            yfuel=phi(i,j,k,1)
            yo2=phi(i,j,k,2)
            yprod=phi(i,j,k,3)
            ysoot=phi(i,j,k,4)
            yn2=1-yfuel-yo2-yprod-ysoot
            oldphi(i,j,k,1)=yfuel
            oldphi(i,j,k,2)=yo2
            oldphi(i,j,k,3)=yprod
            oldphi(i,j,k,4)=ysoot
            oldphi(i,j,k,5)=yn2

c-----------prevent calculation of negative mass fractions
            if (ysoot .lt. 0.0) then
              write (6,*) 'resetting ysoot',i,j,k,ysoot
              write (nout,*) 'resetting ysoot',i,j,k,ysoot
              ysoot=0.0
            endif
            if (yn2 .lt. 0.0) then
              yn2=0.0
            endif
c            yco2=(wco2/(wco2+2*wh2o))*yprod
c            yh2o=(2*wh2o/(wco2+2*wh2o))*yprod
            yco2=(wco2/(wco2+zmolh2o*wh2o))*yprod
            yh2o=(zmolh2o*wh2o/(wco2+zmolh2o*wh2o))*yprod
            xsum=yh2o/wh2o+yco2/wco2+yfuel/wfuel+yo2/wo2+yn2/wn2
     &           +ysoot/wfuel
            xfuel=(yfuel/wfuel)/xsum
            xco2=(yco2/wco2)/xsum
            xh2o=(yh2o/wh2o)/xsum
            xn2=(yn2/wn2)/xsum
            xo2=(yo2/wo2)/xsum

            ppfuel=xfuel*ptemp
            ppo2=xo2*ptemp
            ppn2=xn2*ptemp
            ppco2=xco2*ptemp
            pph2o=xh2o*ptemp

c-----------Limit fuel partial pressure below 10 kpa to prevent
c           numerical problems with radcal
            if (ppfuel.gt.10.0) then
              ppfuel=10.0
            endif

c-----------Set small species concentrations to zero. This will save
c           time by not calculating contribution by minor participants
            if (yfuel.lt.gaslim) then
              ppfuel=0.0
            endif
            if (yo2.lt.gaslim) then
              ppo2=0.0
            endif
            if (yn2.lt.gaslim) then
              ppn2=0.0
```

```
            endif
            if (yco2.lt.gaslim) then
              ppco2=0.0
            endif
            if (yh2o.lt.gaslim) then
              pph2o=0.0
            endif
            if (vf .le. sotlim) then
              vf=0.0
            endif

c-----------Call radcal with the following variables
c           pl     - pathlength (m)
c           tmpg   - gas temperature (K)
c           ppco2  - partial pressure of CO2 (kPa)
c           pph2o  - partial pressure of H2O (kPa)
c           ppfuel  - partial pressure of FUEL (kPa)
c           ppo2   - parital pressure of O2  (kPa)
c           ppn2   - parital pressure of N2  (kPa)
c           vf     - soot volume fraction ()
c           tmps   - wall (source) temperature (K)
c           wvmin  - minimum wave number (1/cm)
c           wvmax  - maximum wave number (1/cm)
c           abscof - absorption coefficient (1/m)

            pl=pathl(i,j,k)

            call gross (pl,tmpg,ppco2,pph2o,ppfuel,ppo2,ppn2,
     &                  vf,tmps,wvmin,wvmax,abscof)
            absrp(i,j,k)=abscof
            oldab(i,j,k)=abscof

            if (absrp(i,j,k).gt.15.) then
             write (6,*) 'a>15',i,j,k,vf,pl,absrp(i,j,k)
             write (nout,*) 'a>15',i,j,k,vf,pl,absrp(i,j,k)
              vf=.01*vf
              call gross (pl,tmpg,ppco2,pph2o,ppfuel,ppo2,ppn2,
     &                    vf,tmps,wvmin,wvmax,abscof)
              absrp(i,j,k)=abscof
              oldab(i,j,k)=abscof
              write (6,*) 'recalculated',absrp(i,j,k)
              write (nout,*) 'recalculated',absrp(i,j,k)
            endif

c---------absorptivity not calculated, use old value instead
          else
            absrp(i,j,k)=oldab(i,j,k)
            if ((i.eq.isave).and.(j.eq.jsave).and.(k.eq.ksave).and.
     &          (ncnt.eq.2)) then
                write (6,*) 'RADCAL is calculating absorptivity for',
     &          ' all fluid nodes this iteration #1'
                write (nout,*) 'RADCAL is calculating absorptivity',
     &          ' for all fluid nodes this iteration #1'
            endif
          endif

c---------error traps to prevent very small and very large absrp
          if (absrp(i,j,k) .le. 0.0) then
            write (6,*) 'prpfvr.f error message number 103'
            write (6,901) "absrp less than or equal zero", i,j,k,
     &                    pathl(i,j,k),absrp(i,j,k),ITYPHY(I,J,K)
            write (6,*) 'location',xyz(i,j,k,1),xyz(i,j,k,2),
     &                    xyz(i,j,k,3)
            write (nout,*) 'prpfvr.f error message number 103'
            write (nout,901) "absrp less than or equal zero", i,j,k,
     &                    pathl(i,j,k),absrp(i,j,k),ITYPHY(I,J,K)
 901        format (a,3(1x,i3),2(1x,e10.4))
```

```
            absrp(i,j,k) = .001
          elseif
     &    ((absrp(i,j,k).gt.0.0).and.(absrp(i,j,k).lt.0.000001)) then
            write (6,*) 'prpfvr.f error message number 104'
            write (6,*) 'absrp very small',i,j,k,cvol(i,j,k),pl,
     &                  absrp(i,j,k)
            write (nout,*) 'prpfvr.f error message number 104'
            write (nout,*) 'absrp very small',i,j,k,cvol(i,j,k),pl,
     &                  absrp(i,j,k)
              absrp(i,j,k)=.001
          else if (absrp(i,j,k) .ge. 20.) then
            write (6,*) 'prpfvr.f error message number 105'
            write (6,*) 'absrp greater than 20',i,j,k,cvol(i,j,k),
     &                  pl,absrp(i,j,k)
            write (nout,*) 'prpfvr.f error message number 105'
            write (nout,*) 'absrp greater than 20',i,j,k,cvol(i,j,k),
     &                  pl,absrp(i,j,k)
            absrp(i,j,k)=19.5
          endif

c---------record number of nodes updated
          if ((i.eq.isave).and.(j.eq.jsave).and.(k.eq.ksave).and.
     &        (ncnt.eq.2)) then
              write (6,*) 'RADCAL is calculating absorptivity for',
     &        ' all fluid nodes this iteration #2'
              write (nout,*) 'RADCAL is calculating absorptivity for',
     &        ' all fluid nodes this iteration #2'
          endif
          if ((i.eq.ilsave).and.(j.eq.jlsave).and.(k.eq.klsave).and.
     &      (ncnt.gt.2)) then
             write (6,900) 'RADCAL calculated absorptivity over',
     &       nupdat, 'nodes for the next iteration'
             write (nout,900) 'RADCAL calculated absorptivity over',
     &       nupdat, 'nodes for the next iteration'
             nupdat=0
 900         format (1x, a, i6, 1x, a)
          endif
        endif
      ELSE
        ABSRP(I,J,K) = 1.0
      ENDIF

  100 CONTINUE

      RETURN
      END
```